

Научном већу Института за физику у Београду

Предлог за Годишњу награду за научни рад Института за физику у Београду

Поштовани,

Велико ми је задовољство да предложим др **Игора Франовића**, вишег научног сарадника, за Годишњу награду за научни рад Института за физику у Београду, за његов допринос развоју концепта ексцитабилности и увођење нових аналитичких редукционих метода за проучавање стохастичке динамике спрегнутих ексцитабилних система.

У периоду релевантном за доделу Годишње награде, односно током **2018. и 2019. године** (претходне две календарске године), кандидат је објавио **8 радова категорије М20, од чега 3 рада категорије М21а и 3 рада категорије М21**, као и 2 рада категорије М22, на основу чега га номинујем за награду (списак радова и сви радови су у прилогу). Сем у једном раду категорије М21, др Франовић је на свим осталим радовима водећи аутор (први аутор на 3 рада и последњи аутор на 4 рада). У питању су публикације са **укупним импакт фактором 18.933** у изузетним часописима као што су *Chaos, Physical Review E, EPL*, и *Chaos, Solitons and Fractals*. Ове публикације су већ цитиране 12 пута (без аутоцитата) према бази Scopus (видети прилог). Поред тога, кандидат је у овом периоду одржао **5 предавања по позиву категорије М32** на међународним конференцијама, као и једно саопштење категорије М33 и 3 саопштења категорије М34.

Истраживачки рад др Франовића обухвата области теорије нелинеарне динамике, стохастичких процеса и теорије комплексних мрежа. Он се бави теоријском анализом самоорганизације и генеричких форми емергентног понашања у комплексним системима, чија је локална динамика представљена моделима спрегнутих осцилатора или ексцитабилних јединица. У свом раду користи концепте и методе из неколико различитих области физике, укључујући теорију нелинеарне динамике, статистичку физику и теорију комплексних мрежа, док се као главна мотивација и потенцијалне области примене добијених резултата истичу опис, предвиђање и контрола колективног понашања неуронских мрежа и других биолошких система.

У ширем контексту, проучавање емергентних феномена заснованих на синхронизацији великог броја елемената, као главном принципу самоорганизације који даје квалитативно нове форме понашања које није могуће предвидети или извести из особина локалне динамике, представља парадигму за карактеризацију макроскопске динамике бројних реалних система, од физике, хемије и биологије, преко инжењерства и технологије, до социологије и економије. При том, класа ексцитабилних система, чије је карактеристично понашање одређено тиме што им се параметри налазе у близини бифуркације која преводи систем из стационарног стања у осцилаторни режим, налази се у фокусу савремених истраживања како због теоријског значаја, тако и због могућности практичне примене, пре свега у биофизици. Комплексности колективног понашања система спрегнутих ексцитабилних јединица доприносе особине локалне динамике, која типично подразумева вишеструке временске скале, значајан утицај

шума и кашњења у интеракцијама, као и организација по схеми модуларних комплексних мрежа, како на структурном, тако и на функционалном нивоу. Проучавање емергентне динамике на оваквим системима већ је довело до настанка значајних нових теоријских концепата, као што су методе анализе различитих форми пропагативних и локализованих патерна активности, технике анализе стабилности и бифуркација система стохастичких диференцијалних једначина са и без кашњења, као и установљење појма адаптивних мрежа.

Овде су укратко истакнути најзначајнији резултати кандидата из радова на основу којих је номинован за Годишњу награду:

1. У раду *Two Scenarios for the Onset and Suppression of Collective Oscillations in Heterogeneous Populations of Active Rotators* [V. Klinshov and **I. Franović**, Phys. Rev. E **100**, 062211 (2019)], по први пут су аналитички одређени локална структура и области стабилности генеричких макроскопских режима у популацијама с динамичком хетерогеношћу, састављеним од ексцитабилних и осцилаторних јединица. Динамичка хетерогеност (алтернативно диверзитет), тј. неуниформност параметара локалне динамике, је фундаментална карактеристика неуронских и других биолошких система, чији је утицај досад третиран првенствено нумеричким, а не аналитичким методама. У раду др Франовића, као парадигматски модел посматрана је популација спрегнутих активних ротатора, при чему је диверзитет реализован тако што је уведено да су локални бифуркациони параметри, који код осцилатора представљају интринзичну фреквенцију, дистрибуирани према унапред задатој дистрибуцији вероватноће. Анализа режима макроскопске динамике обављена је екстензијом От-Антонсеновог (От-Антонсен) редукционог метода на популације с динамичком хетерогеношћу јединица, при чему су као бифуркациони параметри разматране карактеристике дистрибуције локалних фреквенција ротатора (средња вредност и ширина дистрибуције). Откривено је да постоје три режима макроскопске динамике, и то: (1) глобално хомогено стање мировања, где се сви ротатори налазе у ексцитабилном стању; (2) глобално осцилаторно стање, где су локалне осцилације ротатора парцијално синхронизоване; (3) хетерогено макроскопски стационарно стање, где се неке јединице налазе у ексцитабилном, а друге у осцилаторном режиму, при чему су њихове локалне активности несинхронизоване. Анализом стационарних решења за локални параметар поретка, добијених на основу интегро-диференцијалне От-Антонсенове једначине, као и увођењем макроскопског параметра ексцитабилности, први пут је непосредно показано како интеракције модификују локални праг ексцитабилности, доводећи до појаве различитих макроскопских режима. Детаљна бифуркациона анализа показала је да су области стабилности појединих стања задата сложеним бифуркационим сценариом, организованим око три бифуркације кодимензије два (Богданов-Такенс бифуркација, *cusp* бифуркација, *fold-homoclinic* бифуркација). Поред моностабилних домена, по први пут су пронађени бистабилни домени, који одговарају коегзистенцији између макроскопских стационарних стања, или коегзистенцији стационарног и осцилаторног режима. Такође, по први пут је показано да колективна мода може да настане путем два различита сценарија, заснованим или на Хопф-овој или седло-чвор бифуркацији на инваријантном кругу (*saddle-node on invariant circle*). При том, пронађено је и да прелазак из хомогеног у хетерогено макроскопско стационарно стање с повећањем диверзитета може да укључује хистерезис. Екстензијом методе за анализу стабилности стационарних решења От-Антонсенове једначине, показано је да сложени бифуркациони сценарио између макроскопских режима опстаје и у случају система с кашњењем у интеракцијама, а нумерички је утврђено да слично важи и у случају када је локална динамика пертурбована шумом.
2. У раду *Leap-frog Patterns in Systems of Two Coupled FitzHugh-Nagumo Units* [S. R. Eydam, **I. Franović**, and M. Wolfrum, Phys. Rev. E **99**, 042207 (2019)] показан је нови генерички механизам настанка патерна у спрегнутим ексцитабилним системима на вишеструким временским скалама, заснован на повећаној осетљивости система на пертурбацију у околини канард прелаз

између осцилација мале амплитуде (*subthreshold* осцилација) и релаксационих осцилација. Конкретно, на примеру бинарног мотива идентичних Фицхју-Нагумо (FitzHugh-Nagumo) неурона са slabим линеарним интеракцијама, демонстриран је и објашњен настанак патерна алтернирајуће активности, познатих као *leap-frogging* или *leader-switching* патерни. Истраживање др Франовића је показало да садејство локалне *multiscale* динамике и слабе одбојне интеракције у системима спрегнутих ексцитабилних јединица може да доведе до појаве периодичних или хаотичних решења карактерисаних алтернирајућим редоследом емитовања импулса између јединица. У квалитативном смислу, то представља значајан искорак у односу на класичну парадигму за проучавање неуронских система, која се типично односи на феномене синхронизације. Такође, *leap-frogging* решења су раније добијана једино у случају јаким нелинеарним интеракција између неуронских осцилатора. Насупрот томе, у раду је показан механизам настанка патерна алтернирајуће активности организован око феномена експлозије канарда у системима са једноставним линеарним интеракцијама. Појава *leap-frog* патерна квалитативно је објашњена као последица повећане осетљивости релаксационих осцилација Фицхју-Нагумо јединица на пертурбацију за вредности параметара система непосредно изнад канард прелаза. У том случају, примена чак и веома слабе пертурбације може да одведе орбиту система далеко од релаксационе осцилације, индукујући једну или серију сукцесивних *subthreshold* осцилација, због чега је заједничка карактеристика свих алтернирајућих решења је да садрже осцилације мале амплитуде, комбиноване с релаксационим осцилацијама велике амплитуде. Применом метода нумеричке континуације извршена је класификација различитих периодичних режима *leap-frogging* динамике, при чему је базична подела на асиметрична решења и решења с просторно-временском симетријом. Користећи нумеричку *path-following* методу, одређена је област стабилности најједноставнијег *leap-frog* периодичног решења, за коју је експлицитно показано да има облик *locking* конуса усмереног ка канард прелазу декуплованог система. У близини врха конуса, откривен је комплексан бифуркациони сценарио, који укључује бифуркације кодимиензије два, у којем различити типови решења с различитим симетријама мењају стабилност.

3. У раду *Phase-sensitive Excitability of a Limit Cycle* [I. Franović, O. E. Omel'chenko, and M. Wolfrum, *Chaos* **28**, 071105 (2018)] концепт ексцитабилности је први пут проширен на системе у којима је атрактор гранични круг. Као главни пример, разматране су релаксационе осцилације FitzHugh-Nagumo система, као парадигматског модела неуронске динамике. За разлику од класичног случаја ексцитабилне равнотеже, утврђено је да нови тип ексцитабилног понашања одликује неуниформност, у смислу да се ексцитабилност манифестује само ако пертурбација делује на одређеном сегменту периодичне орбите. Из тог разлога, овакав нови вид ексцитабилне динамике назван је ексцитабилност осетљива на фазу. Експлицитно је показано да ексцитабилност граничног круга укључује и универзалне особине класичног случаја, наиме нелинеарно понашање са прагом (*threshold*) и појаву карактеристичног немонотоног одговора система у присуству шума. Нелинеарно понашање са прагом објашњено је применом *slow-fast* анализе засноване на теорији сингуларних пертурбација. Утврђено је да улогу скупа за праг (*threshold set*) обавља максимални канард, експоненцијално танак слој орбита које на одређеном сегменту леже близу периодичне орбите релаксационих осцилација. У контексту немонотоног одговора система на шум, показано је да садејство ексцитабилности периодичне орбите и шума доводи до инверзне стохастичке резонанце, која подразумева да фреквенција осцилација пертурбованих шумом има минимум на интермедијерној вредности интензитета шума. Појава резонанце објашњена је на основу конкуренције два ефекта, наиме ефикасности ексцитације и деградације нелинеарног одговора система.
4. У радовима *Clustering Promotes Switching Dynamics in Networks of Noisy Neurons* [I. Franović and V. Klinshov, *Chaos* **28**, 023111 (2018)] и *Stimulus-evoked Activity in Clustered Networks of Stochastic Rate-based Neurons* [I. Franović and V. Klinshov, *Eur. Phys. J. - Spec. Top.* **227**, 1063 (2018)] објашњен је механизам настанка макроскопске варијабилности на модулларним

(кластерованим) неуронским мрежама и њен утицај на индуковану активност мреже. Макроскопска варијабилност је емергентни феномен који се опажа на временским скалама много дужим од карактеристичног времена локалне динамике неурона, а манифестује се кроз појаву спорих стохастичких флукуација средње фреквенције емитовања импулса мреже. Споре флукуације последица су кохерентних спонтаних прелазака неурона између тзв. *up*-стања повећане активности неурона и тзв. *down*-стања релативног мировања неурона. Значај овакве колективне алтернирајуће (*switching*) динамике огледа се у томе што представља динамичку парадигму за одређене процесе учења и меморије у кортексу. У радовима др Франовића су утврђени услови за појаву алтернирајуће динамике, с акцентом на садејство различитих типова шума и хетерогености у топологији мреже. Применом методе средњег поља (*mean-field method*), по први пут је развијен ефективни модел колективне динамике за модуларну неуронску мрежу, при чему је њена колективна динамика приказана преко спрегнутих стохастичких *mean-field* система који одражавају активности појединачних кластера. Бифуркационом анализом ефективних модела у термодинамичком лимесу утврђене су разлике у генеричким механизмима алтернирајуће динамике код некластерованих случајних мрежа и кластерованих мрежа. Код некластерованих мрежа, механизам је аналоган понашању стохастичке честице у потенцијалу са два минимума (*double-well potential*), тако да је зависност *switching* фреквенције од шума могуће представити Крамерсовим законом. Код модуларних мрежа, показано је да кластеровање непосредно подстиче мултистабилност колективне динамике доводећи до појаве хетерогених стања с нарушеном симетријом, што значајно утиче на повећање робусности *switching* феномена. У случају индуковане динамике, применом бифуркационе анализе на одговарајућим ефективним моделима, показано је да однос између стимулуса и одговора мреже квалитативно зависи од њене конфигурације и примењеног протокола стимулације. При том, утврђено је да су процеси ексцитације у кластерованим и статистички хомогеним разуђеним случајним мрежама значајно различити, при чему је ексцитација хомогене мреже типично нижа него код кластероване мреже. Додатно, одговор кластероване мреже фундаментално зависи од примењеног протокола стимулације, при чему тзв. „циљана стимулација“ (*targeted* или *focused stimulation*) усмерена на одређени кластер доводи до квалитативно другачијег резултата у односу на тзв. „дистрибуирану стимулацију“ (*distributed* или *diffused stimulation*), где је идентична фракција јединица мреже пертурбована независно од припадности неурона појединим кластерима.

- У раду *Inverse Stochastic Resonance in a System of Excitable Active Rotators with Adaptive Coupling* [I. Bačić, V. Klinshov, V. I. Nekorkin, M. Perc, and I. Franović, EPL **124**, 40004 (2018)] демонстриран је нови генерички сценарио инверзне стохастичке резонанце (ИСР), феномена у коме фреквенција стохастички пертурбованих осцилација постаје минимална на интермедијерној вредности шума. Ефекат је објашњен на примеру система два стохастичка активна ротатора с адаптивним интеракцијама, као парадигматског модела који укључује три типичне особине неуронских система: ексцитабилност локалне динамике, синаптичку пластичност и шум. Док су раније предложени сценарији ИСР били засновани искључиво на бистабилности локалне динамике, у раду др Франовића је утврђено да ИСР генерички настаје у системима с вишеструким карактеристичним временским скалама. У конкретном случају, раздвајање локалне динамике (брзи подсистем) и динамике јачине веза (спори подсистем) регулисано је брзином адаптације. Ефекат ИСР је уочен за интермедијерне брзине адаптације, где стохастичка динамика система подразумева алтернирање (*switching* динамичку) између метастабилних стања која одговарају коегзистентним атракторима детерминистичке верзије система (два стабилна еквилибријума и два гранична круга, при чему је сваки пар атрактора повезан изменском симетријом). Показано је да се механизам ИСР заснива на *biased switching*-у, тј. чињеници да систем значајно више времена проводи у квазистационарним стањима него у метастабилним осцилаторним стањима. Користећи методе анализе система са вишеструким временским скалама (*multiscale analysis*), укључујући разматрање тзв. *layer* и *reduced* проблема, откривено је да адаптивна динамика веза појачава резонантни ефекат, преведећи јачину веза у

област параметара у којима атрактор стационарног стања брзог подсистема мења карактер, постајући стабилни фокус уместо стабилног чвора.

- У раду *Noise-induced Switching in Two Adaptively Coupled Excitable Systems* [I. Ваћић, S. Yanchuk, M. Wolfrum, and I. Франовић, Eur. Phys. J. - Spec. Top. **227**, 1077 (2018)], применом технике стохастичког усредњавања (*stochastic averaging*), извршена је екстензија метода анализе система на вишеструким временским скалама (*multiscale analysis*) на стохастичке системе. Увођењем оваквог иновативног приступа, показано је да код неуронских мотива с адаптивним интеракцијама, коефекат шума и адаптивности доводи до два квалитативно различита, генеричка типа алтернирајуће (*switching*) динамике, у зависности од брзине адаптације. Адаптивност, чији је типичан пример пластичност синапси између неурона, подразумева да се карактеристике интеракција мењају у зависности од локалне динамике јединица, а настале промене у интеракцијама принципом повратне спреге додатно модификују динамику јединица. У случају спорије адаптације, *switching* динамика се одвија између две моде осцилација изазваних шумом (*noise-induced oscillations*), тако да шум индукује флукуације на брзој и споријој карактеристичној скали. Настанак две осцилаторне моде, које се одликују различитим редоследом емитовања импулса јединица, повезан је с инваријантношћу детерминистичке динамике система на измену индекса јединица (*exchange symmetry*). У случају интермедијерне брзине адаптације, *switching* динамика укључује метастабилна стања која одговарају коегзистентним атракторима детерминистичке верзије система (два стабилна еквилибријума и два гранична круга, при чему је сваки пар атрактора повезан изменском симетријом). Као интересантну чињеницу, показано је да се при интермедијерној адаптацији, у широкој области параметара појављује тзв. *biased switching*, при чему систем много више времена проводи у кваистационарним стањима него у осцилаторним метастабилним стањима. Интерпретација добијених резултата у контексту односа структурних неуронских мотива, задатих тополошком конфигурацијом веза, и функционалних мотива, одређених смером протока информација, указује да је у општем случају могућа коегзистенција више функционалних мотива на једном структурном мотиву. С друге стране, садејство адаптивности, шума и ексцитабилне локалне динамике омогућава споре стохастичке флукуације између различитих функционалних мотива.
- У раду *Nonlinear Dynamics Behind the Seismic Cycle: One-dimensional Phenomenological Modeling* [S. Kostić, N. Vasović, K. Todorović, and I. Франовић, Chaos Soliton. Fract. **106**, 310 (2018)], др Франовић се бавио интердисциплинарним истраживањем, које подразумева примену теорија нелинеарне динамике и стохастичких процеса на моделовање комплексног понашања сеизмичких раседа, геолошких структура одговорних за настанак земљотреса. Конкретно, увођењем меморијског ефекта у типични модел трења између масивног блока и контактне површине монокомпонентног раседа, третиран је проблем механизма настанка апериодичних временских серија на једноставним (монокомпонентним) раседима. Користећи метод бифуркационе анализе система диференцијалних једначина с кашњењем, показано је да екстензија канонског Burridge-Кнорфф модела може да генерише релевантне форме комплексне динамике, укључујући и прелаз између асеизмичког и сеизмичког понашања.

На основу описаних резултата колеге Франовића јасно је да његов досадашњи рад представља значајан допринос развоју физике комплексних система, нелинеарне динамике и статистичке физике, као и неким другим научним областима, што је доказ интердисциплинарног карактера његовог истраживања. У Институту за физику у Београду, др Франовић је увео нове методе у проучавање емергентних феномена у системима под утицајем шума и кашњења у интеракцијама. Знања и искуства које је стекао у теоријском моделирању, аналитичким методама и техникама анализе динамике комплексних система успешно преноси млађим сарадницима у Лабораторији за примену рачунара у науци у оквиру Центра изузетних вредности за изучавање комплексних система.

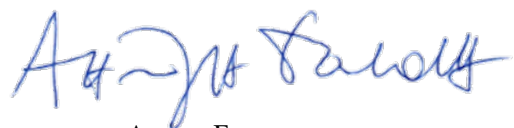
Др Игор Франовић има широку научну сарадњу са групама из Немачке, Русије и Словеније. Ментор је на докторским студијама једној студенткињи чија одбрана докторске тезе се очекује током ове године, а такође је и ментор једне мастер тезе, чија припрема је у току. Руководио је билатералним пројектом са Немачком у периоду од 2017. до 2018. године, а у оквиру Центра изузетних вредности за изучавање комплексних система руководи истраживањем на потпројекту *Емергентна динамика на комплексним мрежама: стохастички ефекти, кашњење у интеракцијама, адаптивност*.

У својој досадашњој каријери, колега Франовић је објавио 36 радова у међународним часописима категорије М20, као и једно поглавље у монографији М13. Одржао је једно предавање по позиву на међународним конференцијама категорије М31, 6 предавања по позиву на међународним конференцијама категорије М32, 6 саопштења категорије М33 и 8 саопштења категорије М34 (комплетан списак је дат у прилогу). **Од 36 радова категорије М20, др Франовић је чак 23 објавио у часописима изузетних вредности категорије М21а**, као што су *Physical Review Letters*, *Scientific Reports*, *Chaos*, *Communications in Nonlinear Science and Numerical Simulation*, *Nonlinear Dynamics* и *Physical Review E*. Према бази *Scopus*, радови др Франовића су до сада укупно цитирани 157 пута (без аутоцитата). Према бази *Web of Science*, његови радови су укупно цитирани 136 пута (без аутоцитата), уз $h=8$. Докази о цитираности према бази *Scopus* су дати у прилогу. Такође, од децембра 2017. године др Франовић је **Associate Editor** у врхунском међународном часопису *Chaos, Solitons and Fractals* (ИФ 3.064 за 2018. годину) из области нелинеарне динамике, у издању *Elsevier-a*.

На крају, желео бих да потврдим и чињеницу да колега Франовић испуњава и све формалне услове за доделу награде: сви резултати за које је номинован су остварени у целости или делимично на Институту, објављени су током претходне две календарске године и представљени су на редовном семинару на Институту (SCL семинар одржан 24. маја 2018. године).

Имајући све наведено у виду, са задовољством предлажем др Игору Франовића за Годишњу награду за научни рад Института за физику у Београду.

У Београду, 28. 04. 2020. године



др Антун Балаж, научни саветник
руководилац Центра изузетних вредности
за изучавање комплексних система

Биографија др Игора Франовића

Др Игор Франовић је рођен 25. фебруара 1979. године у Београду. Завршио је Пету београдску гимназију као ученик генерације 1997. године, након чега је уписао основне студије на Физичком факултету Универзитета у Београду, смер теоријска и експериментална физика. Дипломирао је 2002. године с просечном оценом 9.43, одбранивши дипломски рад под називом "Анализа Јан-Телеровог ефекта на примеру прелазног метал-комплекса $[\text{Cr}(\text{NH}_3)_6]^{3+}$ " под руководством проф. др Драгољуба Белића. Магистарске студије на истом факултету, смер теоријска физика кондензованог стања, завршио је с просечном оценом 10,00, а магистарску тезу под насловом *Перколациони фазни прелази на просторно-временским фракталним структурама у ex-vivo и in-vitro неуронским културама* одбранио је 2011. године под менторством доц. др Владимира Миљковића. Докторат под насловом *Collective dynamics and self-organisation of stochastic neuronal systems influenced by synaptic time delay* одбранио је 2013. године на Физичком факултету Универзитета у Београду под руководством др Николе Бурића. У оквиру тезе су анализирани аналогije у процесу самоорганизације колективне активности између система спрегнутих аутономних осцилатора и система куплованих ексциtabilних јединица, при чему је применом методе средњег поља развијен ефективни модел макроскопске динамике популације ексциtabilних јединица изложених шуму и кашњењу у интеракцијама.

Од 2004. до 2006. године Игор Франовић је на Физичком факултету, као стипендиста Министарства науке и заштите животне средине, учествовао на пројекту *Фазни прелази и нелинеарне појаве у биолошким и неорганским материјалима*, којим је руководио проф. др Сава Милошевић. Од јануара 2008. године до јануара 2011. године био је запослен као истраживач приправник на истом факултету у Београду, у оквиру пројекта *Фазни прелази и карактеризација неорганских и органских система*, којим је руководио проф. др Мићо Митровић. Од јануара 2011. до марта 2014. године био је запослен на Физичком факултету као истраживач приправник, а затим и као истраживач сарадник у оквиру пројекта ОН171015 Министарства просвете и науке Републике Србије под називом *Фазни прелази и карактеризација неорганских и органских система*, којим руководи проф. др Сунчица Елезовић-Хацић.

Др Игор Франовић је од марта 2014. године запослен у Лабораторији за примену рачунара у науци у оквиру Центра изузетних вредности за изучавање комплексних система Института за физику у Београду. Од 2014. до 2019. године је био ангажован на националном пројекту ОН171017, *Моделирање и нумеричке симулације сложених вишечестичних система*, којим је руководио др Антун Балаж. У оквиру овог пројекта, др Франовић је руководио потпројектом *Самоорганизација у спрегнутим ексциtabilним системима*. Тренутно, др Франовић руководи истраживањем на потпројекту *Емергентна динамика на комплексним мрежама: стохастички ефекти, кашњење у интеракцијама, адаптивност* у оквиру Центра изузетних вредности за изучавање комплексних система. У децембру 2014. године изабран је у звање научни сарадник, а маја 2019. године у звање виши научни сарадник.

Истраживачки рад др Франовића обухвата области теорије нелинеарне динамике, стохастичких процеса и теорије комплексних мрежа, а као водеће теме истраживања се издвајају самоорганизација у системима спрегнутих ексциtabilних јединица, развој редукционих метода и методе средњег поља за анализу стабилности и бифуркација

система обичних и стохастичких диференцијалних једначина, анализа динамике система на вишеструким временским скалама, као и коефекти топологије, шума и кашњења у интеракцијама на динамику структурних и функционалних неуронских мрежа.

Његов досадашњи рад укључује 36 радова у међународним часописима, као и једно поглавље у монографији M13, 1 предавање по позиву M31, 6 предавања по позиву M32, 6 саопштења категорије M33 и 8 саопштења категорије M34. Од 36 радова, чак 23 је објављено у часописима изузетних вредности категорије M21a, као што су *Physical Review Letters*, *Scientific Reports*, *Chaos*, *Communications in Nonlinear Science and Numerical Simulation*, *Nonlinear Dynamics* и *Physical Review E*. Према бази *Scopus*, радови др Франовића до сада имају 157 хетероцитата. Према бази *Web of Science*, његови радови су укупно цитирани 136 пута (без аутоцитата), уз $h=8$.

Др Франовић је добитник награде за најбољег младог истраживача Физичког факултета у Београду за 2013. годину. Има развијену међународну научну сарадњу с истраживачким групама из Русије, Немачке и Словеније. Ментор је на докторским студијама Иве Бачић на Физичком факултету у Београду, чија одбрана се очекује током 2020. године (тема *Self-organization in coupled excitable systems: interplay between multiple timescale dynamics and noise* је одбрањена пред Колегијумом докторских студија 2019. године), а такође је и ментор на изради мастер тезе Николе Потпаре на на Физичком факултету у Београду. Поред тога, др Франовић је јуна 2019. године био члан комисије за одбрану докторске тезе Себастијана Ејдама на Техничком универзитету у Берлину.

Др Франовић је у периоду од 2017. до 2018. био руководилац билатералног пројекта сарадње између Републике Србије и Савезне Републике Немачке *Emergent Dynamics in Systems of Coupled Excitable Units*. Такође, др Франовић је Associate Editor у врхунском међународном часопису *Chaos, Solitons & Fractals* (ИФ 3.064 за 2018. годину).

Листа публикација др Игора Франовића у периоду релевантном за награду (2018-2019)

Радови у међународним часописима изузетних вредности (M21a)

1. **I. Franović**, O. E. Omel'chenko, and M. Wolfrum:
Phase-sensitive Excitability of a Limit Cycle
Chaos **28**, 071105 (2018), ИФ 2.643 за 2018. годину
2. **I. Franović** and V. Klinshov:
Clustering Promotes Switching Dynamics in Networks of Noisy Neurons
Chaos **28**, 023111 (2018), ИФ 2.643 за 2018. годину
3. S. Kostić, N. Vasović, K. Todorović, and **I. Franović**:
Nonlinear Dynamics Behind the Seismic Cycle: One-dimensional Phenomenological Modeling
Chaos Soliton. Fract. **106**, 310 (2018), ИФ 3.064 за 2018. годину

Радови у врхунским међународним часописима (M21)

1. V. Klinshov and **I. Franović**:
Two Scenarios for the Onset and Suppression of Collective Oscillations in Heterogeneous Populations of Active Rotators
Phys. Rev. E **100**, 062211 (2019), ИФ 2.366 за 2016. годину
2. S. R. Eydám, **I. Franović**, and M. Wolfrum:
Leap-frog Patterns in Systems of Two Coupled FitzHugh-Nagumo Units
Phys. Rev. E **99**, 042207 (2019), ИФ 2.366 за 2016. годину
3. I. Bačić, V. Klinshov, V. I. Nekorkin, M. Perc, and **I. Franović**:
Inverse Stochastic Resonance in a System of Excitable Active Rotators with Adaptive Coupling
EPL **124**, 40004 (2018), ИФ 1.957 за 2016. годину

Радови у истакнутим међународним часописима (M22)

1. **I. Franović** and V. Klinshov:
Stimulus-evoked Activity in Clustered Networks of Stochastic Rate-based Neurons
Eur. Phys. J. - Spec. Top. **227**, 1063 (2018), ИФ 1.947 за 2017. годину
2. I. Bačić, S. Yanchuk, M. Wolfrum, and **I. Franović**:
Noise-induced Switching in Two Adaptively Coupled Excitable Systems
Eur. Phys. J. - Spec. Top. **227**, 1077 (2018), ИФ 1.947 за 2017. годину

Предавања по позиву с међународних скупова штампана у изводу (M32)

1. **I. Franović**

Macroscopic dynamics in heterogeneous assemblies of excitable and oscillatory Units

The 7th Conference on Information Theory and Complex Systems TINKOS 2019, Mathematical Institute of the Serbian Academy of Sciences and Arts, October 15 – 16 2019, Belgrade, Serbia

2. **I. Franović**

Macroscopic Variability in Modular Neural Networks

The 20th Symposium on Condensed Matter Physics - SFKM 2019, Serbian Academy of Sciences and Arts, 7 – 11 October 2019, Belgrade, Serbia

3. **I. Franović** and V. Klinshov

Emergence of collective oscillations in assemblies of stochastic active elements with coupling delay

PhysCon2019, The 9th International Scientific Conference on Physics and Control, 8–11 September 2019, Innopolis, Russia

4. **I. Franović:**

Switching dynamics in two adaptively coupled excitable systems

Dynamics of Coupled Oscillator Systems, 19 - 21 November 2018, Weierstrass Institute (WIAS), Berlin, Germany

5. **I. Franović:**

Switching dynamics in networks of stochastic rate-based neurons

Analysis and Modeling of Complex Oscillatory Systems (AMCOS), 19-23 March 2018, Barcelona, Spain

Саопштења с међународних скупова штампана у целини (M33)

1. S. Kostić, N. Vasović, and **I. Franović:**

Effect of viscosity of fault filling on stick-slip dynamics of seismogenic fault motion: A numerical approach

Geomechanics and Geodynamics of Rock Masses, Proceedings of the 2018 European Rock Mechanics Symposium, (Edited by Vladimir Litvinenko), 22 - 26 May 2018, St. Petersburg, Russia; DOI: 10.1201/9780429462078

Саопштења с међународних скупова штампана у изводу (M34)

1. **I. Franović**

Leap-frog patterns in motifs of two coupled FitzHugh-Nagumo units

School and Workshop on Patterns of Synchrony: Chimera States and Beyond, The Abdus Salam International Centre for Theoretical Physics, May 6 – 17 2019, Trieste, Italy

2. **I. Bačić, V. Klinshov, V. Nekorkin, and I. Franović:**
Inverse stochastic resonance in a system of active rotators with adaptive coupling
Dynamics of Coupled Oscillator Systems,
19 - 21 November 2018, Weierstrass Institute (WIAS), Berlin, Germany

3. **I. Franović, O. Omel'chenko, and M. Wolfrum:**
Phase-sensitive excitability of a limit cycle
Dynamics of Coupled Oscillator Systems,
19 - 21 November 2018, Weierstrass Institute (WIAS), Berlin, Germany

Комплетна листа публикација др Игора Франовића

Поглавље у истакнутој монографији међународног значаја (M13)

1. S. Kostić, N. Vasović, K. Todorović, and **I. Franović**:
Nonlinear Dynamics Behind The Seismogenic Fault Motion – A Review on Dynamics of Single-Array Spring-Block Models
in Wayne Coleman (ed.), “Earthquakes: Monitoring Technology, Disaster Management and Impact Assessment“, p. 1-60, Nova Science Publishers (2017)

Радови у међународним часописима изузетних вредности (M21a)

1. I. Bačić and I. Franović:
Two Paradigmatic Scenarios for Inverse Stochastic Resonance
Chaos **30**, 033123 (2020), ИФ 2.643 за 2018. годину
2. **I. Franović**, O. E. Omel'chenko, and M. Wolfrum:
Phase-sensitive Excitability of a Limit Cycle
Chaos **28**, 071105 (2018), ИФ 2.643 за 2018. годину
3. **I. Franović** and V. Klinshov:
Clustering Promotes Switching Dynamics in Networks of Noisy Neurons
Chaos **28**, 023111 (2018), ИФ 2.643 за 2018. годину
4. S. Kostić, N. Vasović, **I. Franović**, K. Todorović, V. Klinshov, and V. I. Nekorkin:
Dynamics of Fault Motion in a Stochastic Spring-slider Model with Varying Neighboring Interactions and Time-delayed Coupling
Nonlinear Dyn. **87**, 2563 (2017), ИФ 4.339 за 2017. годину
5. **I. Franović**, S. Kostić, M. Perc, V. Klinshov, V. I. Nekorkin, and J. Kurths:
Phase Response Curves for Models of Earthquake Fault Dynamics
Chaos **26**, 063105 (2016), ИФ 2.283 за 2016. годину
6. N. Vasović, S. Kostić, **I. Franović**, and K. Todorović:
Earthquake Nucleation in a Stochastic Fault Model of Globally Coupled Units with Interaction Delays
Commun. Nonlinear Sci. Numer. Simulat. **38**, 117 (2016), ИФ 2.866 за 2014. годину
7. **I. Franović**, K. Todorović, M. Perc, N. Vasović, and N. Burić:
Activation Process in Excitable Systems with Multiple Noise Sources: One and Two Interacting Units
Phys. Rev. E **92**, 062911 (2015), ИФ 2.326 за 2013. годину
8. **I. Franović**, M. Perc, K. Todorović, S. Kostić, and N. Burić:
Activation Process in Excitable Systems with Multiple Noise Sources: Large Number of Units
Phys. Rev. E **92**, 062912 (2015), ИФ 2.326 за 2013. годину

9. V. Klinshov and **I. Franović**:
Mean-field Dynamics of a Random Neural Network with Noise
Phys. Rev. E **92**, 062813 (2015), ИФ 2.326 за 2013. Годину
10. **I. Franović**, K. Todorović, N. Vasović, and N. Burić:
Stability, Coherent Spiking and Synchronization in Noisy Excitable Systems with Coupling and Internal Delays
Commun. Nonlinear Sci. Numer. Simulat. **19**, 3202 (2014), ИФ 2.866 за 2014. годину
11. S. Kostić, **I. Franović**, M. Perc, N. Vasović, and K. Todorović:
Triggered Dynamics in a Model of Different Fault Creep Regimes
Sci. Rep. **4**, 5401 (2014), ИФ 5.578 за 2014. годину
12. **I. Franović**, K. Todorović, N. Vasović, and N. Burić:
Persistence and Failure of Mean-field Approximations Adapted to a Class of Systems of Delay-coupled Excitable Units
Phys. Rev. E **89**, 022926 (2014), ИФ 2.326 за 2013. годину
13. S. Kostić, N. Vasović, **I. Franović**, D. Jevremović, D. Mitrović, and K. Todorović:
Dynamics of Landslide Model with Time Delay and Periodic Parameter Perturbations
Commun. Nonlinear Sci. Numer. Simulat. **19**, 3346 (2014), ИФ 2.866 за 2014. годину
14. S. Kostić, **I. Franović**, K. Todorović, and N. Vasović:
Friction Memory Effect in Complex Dynamics of Earthquake Model
Nonlinear Dyn. **73**, 1933 (2013), ИФ 3.009 за 2012. годину
15. **I. Franović**, K. Todorović, N. Vasović, and N. Burić:
Mean-field Approximation of Two Coupled Populations of Excitable Units
Phys. Rev. E **87**, 012922 (2013), ИФ 2.326 за 2013. годину
16. **I. Franović**, K. Todorović, N. Vasović, and N. Burić:
Cluster Synchronization of Spiking Induced by Noise and Interaction Delays in Homogenous Neuronal Ensembles
Chaos **22**, 033147 (2012), ИФ 2.188 за 2012. годину
17. **I. Franović**, K. Todorović, N. Vasović, and N. Burić:
Spontaneous Formation of Synchronization Clusters in Homogenous Neuronal Ensembles Induced by Noise and Interaction Delays
Phys. Rev. Lett. **108**, 094101 (2012), ИФ 7.943 за 2012. годину
18. **I. Franović** and V. Lj. Miljković:
The Effects of Synaptic Time Delay on Motifs of Chemically Coupled Rulkov Model Neurons
Commun. Nonlinear Sci. Numer. Simulat. **16**, 623 (2011), ИФ 2.806 за 2011. годину
19. **I. Franović**, K. Todorović, N. Vasović, and N. Burić:
Stability, Bifurcations, and Dynamics of Global Variables of a System of Bursting Neurons
Chaos **21**, 033109 (2011), ИФ 2.081 за 2010. годину

20. **I. Franović** and V. Lj. Miljković:
Functional Motifs: a Novel Perspective on Burst Synchronization and Regularization of Neurons Coupled Via Delayed Inhibitory Synapses
Chaos Soliton. Fract. **44**, 122 (2011), ИФ 3.315 за 2009. годину
21. **I. Franović** and V. Lj. Miljković:
Phase Plane Approach to Cooperative Rhythms in Neuron Motifs with Delayed Inhibitory Synapses
EPL **92**, 68007 (2011), ИФ 2.893 за 2009. годину
22. **I. Franović** and V. Lj. Miljković:
Percolation Transition at Growing Spatiotemporal Fractal Patterns in Models of Mesoscopic Neural Networks
Phys. Rev. E **79**, 061923 (2009), ИФ 2.508 за 2008. годину
23. **I. Franović** and V. Lj. Miljković:
Fractal Properties of Percolation Clusters in Euclidian Neural Networks
Chaos Soliton. Fract. **39**, 1418 (2009), ИФ 3.315 за 2009. годину

Радови у врхунским међународним часописима (M21)

1. V. Klinshov and **I. Franović**:
Two Scenarios for the Onset and Suppression of Collective Oscillations in Heterogeneous Populations of Active Rotators
Phys. Rev. E **100**, 062211 (2019), ИФ 2.366 за 2016. годину
2. S. R. Eydám, **I. Franović**, and M. Wolfrum:
Leap-frog Patterns in Systems of Two Coupled FitzHugh-Nagumo Units
Phys. Rev. E **99**, 042207 (2019), ИФ 2.366 за 2016. годину
3. I. Bačić, V. Klinshov, V. I. Nekorkin, M. Perc, and **I. Franović**:
Inverse Stochastic Resonance in a System of Excitable Active Rotators with Adaptive Coupling
EPL **124**, 40004 (2018), ИФ 1.957 за 2016. годину
4. S. Kostić, N. Vasović, K. Todorović, and **I. Franović**:
Nonlinear Dynamics Behind the Seismic Cycle: One-dimensional Phenomenological Modeling
Chaos Soliton. Fract. **106**, 310 (2018), ИФ 3.064 за 2018. годину
5. I. Bačić, **I. Franović**, and M. Perc:
Disordered Configurations of the Glauber Model in Two-dimensional Networks
EPL **120**, 68001 (2017), ИФ 1.963 за 2015. годину
6. **I. Franović**, O. V. Maslennikov, I. Bačić, and V. I. Nekorkin:
Mean-field Dynamics of a Population of Stochastic Map Neurons
Phys. Rev. E **96**, 012226 (2017), ИФ 2.366 за 2016. годину

7. **I. Franović** and V. Klinshov:
Slow Rate Fluctuations in a Network of Noisy Neurons with Coupling Delay
EPL **116**, 48002 (2016), ИФ 2.095 за 2014. годину
8. S. Kostić, N. Vasović, **I. Franović**, and K. Todorović:
Complex Dynamics of Spring-Block Earthquake Model Under Periodic Parameter Perturbations
J. Comput. Nonlin. Dyn. **9**, 031019 (2014), ИФ 1.530 за 2013. годину

Радови у истакнутим међународним часописима (M22)

1. **I. Franović** and V. Klinshov:
Stimulus-evoked Activity in Clustered Networks of Stochastic Rate-based Neurons
Eur. Phys. J. - Spec. Top. **227**, 1063 (2018), ИФ 1.947 за 2017. годину
2. I. Bačić, S. Yanchuk, M. Wolfrum, and **I. Franović**:
Noise-induced Switching in Two Adaptively Coupled Excitable Systems
Eur. Phys. J. - Spec. Top. **227**, 1077 (2018), ИФ 1.947 за 2017. годину
3. S. Kostić, N. Vasović, **I. Franović**, and K. Todorović:
Dynamics of Simple Earthquake Model with Time Delay and Variation of Friction Strength
Nonlinear Proc. Geoph. **20**, 857 (2013), ИФ 1.692 за 2013. годину
4. **I. Franović** and V. Lj. Miljković:
Possibilities of Introducing Different Functional Circuits on Top of a Structural Neuron Triplet: Where Do the Gains Lie?
Chaos Soliton. Fract. **45**, 527 (2012), ИФ 1.268 за 2010. годину
5. **I. Franović** and V. Lj. Miljković:
Power Law Behavior Related to Mutual Synchronization of Chemically Coupled Map Neurons
Eur. Phys. J. B **76**, 613 (2010), ИФ 1.575 за 2010. годину

Предавања по позиву с међународних скупова штампана у целини (M31)

1. **Igor Franović**, Kristina Todorović, Nebojša Vasović and N. Burić:
Mean Field Dynamics of Networks of Delay-coupled Noisy Excitable Units
International Conference of Numerical Analysis and Applied Mathematics (ICNAAM 2015), Minisymposium “Dynamical Networks with Complex Links“, 22–28 September 2015, Rhodes, Greece, AIP Conf. Proc. 1738, 210004 (2016);
DOI: 10.1063/1.4951987, American Institute of Physics

Предавања по позиву с међународних скупова штампана у изводу (M32)

1. **I. Franović**
Macroscopic dynamics in heterogeneous assemblies of excitable and oscillatory Units
The 7th Conference on Information Theory and Complex Systems TINKOS 2019,
Mathematical Institute of the Serbian Academy of Sciences and Arts,
Belgrade, Serbia, October 15 – 16, 2019
2. **I. Franović**
Macroscopic Variability in Modular Neural Networks
The 20th Symposium on Condensed Matter Physics - SFKM 2019,
Serbian Academy of Sciences and Arts,
Belgrade, Serbia, October 7 – 11, 2019
3. **I. Franović** and V. Klinshov
Emergence of collective oscillations in assemblies of stochastic active elements with coupling delay
PhysCon2019, The 9th International Scientific Conference on Physics and Control,
Innopolis, Russia, September 8–11, 2019
4. **I. Franović**
Switching dynamics in two adaptively coupled excitable systems
Dynamics of Coupled Oscillator Systems, 19 - 21 November 2018, Weierstrass
Institute (WIAS), Berlin, Germany
5. **I. Franović**
Switching dynamics in networks of stochastic rate-based neurons
Analysis and Modeling of Complex Oscillatory Systems (AMCOS), 19-23 March
2018, Barcelona, Spain
6. **I. Franović** and V. Klinshov
Mean-field analysis of stability and slow rate fluctuations in a network of noisy neurons with coupling delay
Topical problems of Nonlinear Wave Physics (NWP-2017), 22–28 July 2017,
Moscow - St. Petersburg, Russia

Саопштења с међународних скупова штампана у целини (M33)

1. S. Kostić, N. Vasović and **I. Franović**
Effect of viscosity of fault filling on stick-slip dynamics of seismogenic fault motion: A numerical approach
Geomechanics and Geodynamics of Rock Masses, Proceedings of the 2018 European
Rock Mechanics Symposium, (Edited by Vladimir Litvinenko), 22 - 26 May 2018, St.
Petersburg, Russia; DOI: 10.1201/9780429462078
2. K. Todorović, **I. Franović**, N. Vasović and S. Kostić
Mean-field approximation of two coupled populations of excitable units modeled by Fitzhugh-Nagumo elements
4th South-East European Conference on Computational Mechanics, isbn: 978-86-
921243-0-3, Kragujevac, 3.-4. jul 2017

3. K. Todorović, **I. Franović**, N. Vasović and S. Kostić,
Spontaneous formation of synchronization clusters in neuronal populations induced by noise and interaction delays
6th International Congress of Serbian Society of Mechanics, Tara, Serbia, isbn: 978-86-909973-6-7, 19.-21. jun 2017
4. Srđan Kostić, Nebojša Vasović, Dragutin Jevremović, Duško Sunarić, **Igor Franović** and Kristina Todorović
Complex Dynamics of Landslides with Time Delay Under External Seismic Triggering Effect
IAEG XII Congress "Engineering Geology for Society and Territory", Torino 2014, Engineering Geology for Society and Territory, vol. 2: Landslide processes, Springer (2015), p. 1353-1356, DOI: 10.1007/978-3-319-09057-3_328
5. S. Kostić, N. Vasović, **I. Franović** and K. Todorović,
Assessment of blast induced ground vibrations by artificial neural network
Proceedings of 12th Symposium on Neural Network Applications in Electrical Engineering (NEUREL) 55-60, 2014
6. **I. Franović** and V. Miljković
Percolation approach to formation of synfire chains in two dimensional neural networks
Proceedings of 8th Symposium on Neural Network Applications in Electrical Engineering (NEUREL) 69-72, 2006

Саопштења с међународних скупова штампана у изводу (М34)

1. **I. Franović**
Leap-frog patterns in motifs of two coupled FitzHugh-Nagumo units
School and Workshop on Patterns of Synchrony: Chimera States and Beyond, The Abdus Salam International Centre for Theoretical Physics, Trieste, Italy, May 6 – 17, 2019
2. I. Bačić, V. Klinshov, V. Nekorkin, and **I. Franović**
Inverse stochastic resonance in a system of active rotators with adaptive coupling
Dynamics of Coupled Oscillator Systems, 19 - 21 November 2018, Weierstrass Institute (WIAS), Berlin, Germany
3. **I. Franović**, O. Omel'chenko and M. Wolfrum:
Phase-sensitive excitability of a limit cycle
Dynamics of Coupled Oscillator Systems, 19 - 21 November, 2018, Weierstrass Institute (WIAS), Berlin, Germany
4. O.V. Maslennikov, **I. Franović** and V.I. Nekorkin
Mean-field model for a network of globally coupled stochastic map-based neurons
Topical problems of Nonlinear Wave Physics (NWP-2017), 22–28 July 2017, Moscow, St Petersburg, Russia

5. V. Klinshov and **I. Franović**
Bistability, Rate Oscillations and Slow Rate Fluctuations in a Neural Network with Noise and Coupling Delays
XXXVII Dynamics Days Europe, 5–9 June 2017, Szeged, Hungary
6. **Igor Franović**, Matjaž Perc and Kristina Todorović
Activation process in systems of excitable units with multiple noise sources
XXXVI Dynamics Days Europe, 6 June -10 June 2016, Corfu, Greece
7. **Igor Franović**, Kristina Todorović, Nebojša Vasović and Nikola Burić
Mean-field Dynamics of Systems of Delay-coupled Noisy Excitable Units
The 19th Symposium on Condensed Matter Physics – SFKM 2015,
7-11 September 2015, Belgrade, Serbia
8. **Igor Franović**, Kristina Todorović, Nebojsa Vasović and Nikola Burić
Mean-field treatment of collective motion in systems of delay-coupled stochastic excitable units
XXXIV Dynamics Days Europe, 8-12 September 2014, Bayreuth, Germany



Citation overview

Self citations of selected authors are excluded. ✕

[Back to author details](#)

[Export](#) [Print](#)

This is an overview of citations for this author.

Author *h*-index: 7 [View *h*-graph](#)

42 Cited Documents from "Franović, Igor" [+ Add to list](#)

Author ID:24461512400

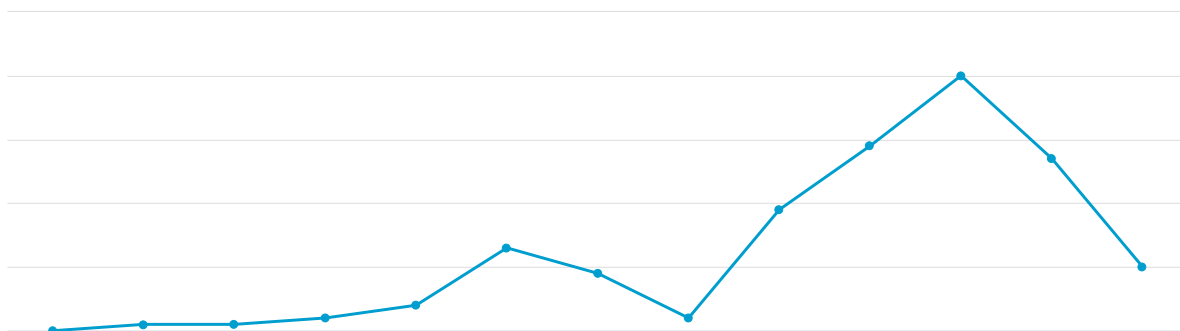
Date range: 2008 to 2020

Exclude self citations of selected author

Exclude self citations of all authors

Exclude citations from books

[Update](#)



Sort on: [Date \(newest\)](#)

Page [Remove](#)

Documents	Citations	<2008	2008	2009	2010	2011	2012	2013	2014	2015	2016	2017	2018	2019	2020	Subtotal	>2020	Total
	Total	0	0	1	1	2	4	13	9	2	19	29	40	27	10	157	0	157
<input type="checkbox"/> 1 Two paradigmatic scenarios for inverse stochastic resonance	2020															0		0
<input type="checkbox"/> 2 Two scenarios for the onset and suppression of collective os...	2019															0		0
<input type="checkbox"/> 3 Leap-frog patterns in systems of two coupled FitzHugh-Nagumo...	2019															0		0
<input type="checkbox"/> 4 Stimulus-evoked activity in clustered networks of stochastic...	2018												1			1		1
<input type="checkbox"/> 5 Noise-induced switching in two adaptively coupled excitable ...	2018												1	2		3		3
<input type="checkbox"/> 6 Phase-sensitive excitability of a limit cycle	2018													2	2	4		4
<input type="checkbox"/> 7 Clustering promotes switching dynamics in networks of noisy ...	2018												2			2		2
<input type="checkbox"/> 8 Inverse stochastic resonance in a system of excitable active...	2018														2	2		2

Documents		Citations																	Subtotal		Total	
		Total	<2008	2008	2009	2010	2011	2012	2013	2014	2015	2016	2017	2018	2019	2020	>2020	Total	Total			
<input type="checkbox"/>	9 Effect of viscosity of fault filling on stick-slip dynamics ...	2018																0	0			
<input type="checkbox"/>	10 Nonlinear dynamics behind the seismic cycle: One-dimensional...	2018																0	0			
<input type="checkbox"/>	11 Disordered configurations of the Glauber model in two-dimens...	2017																0	0			
<input type="checkbox"/>	12 Mean-field dynamics of a population of stochastic map neuron...	2017												1		1		2	2			
<input type="checkbox"/>	13 Dynamics of fault motion in a stochastic spring-slider model...	2017																0	0			
<input type="checkbox"/>	14 Nonlinear dynamics behind the seismogenic fault motion: A re...	2017																0	0			
<input type="checkbox"/>	15 Slow rate fluctuations in a network of noisy neurons with co...	2016												2		1		3	3			
<input type="checkbox"/>	16 Earthquake nucleation in a stochastic fault model of globall...	2016											1					1	1			
<input type="checkbox"/>	17 Mean field dynamics of networks of delay-coupled noisy excit...	2016																0	0			
<input type="checkbox"/>	18 Phase response curves for models of earthquake fault dynamic...	2016											2	1	2			5	5			
<input type="checkbox"/>	19 Activation process in excitable systems with multiple noise ...	2015											8	8	5	1		22	22			
<input type="checkbox"/>	20 Activation process in excitable systems with multiple noise ...	2015									1	6	7	6	1			21	21			
<input type="checkbox"/>	21 Mean-field dynamics of a random neural network with noise	2015											2	1				3	3			
<input type="checkbox"/>	22 Complex dynamics of landslides with time delay under externa...	2015																0	0			
<input type="checkbox"/>	23 Triggered dynamics in a model of different fault creep regim...	2014											4	3	2	1	2	12	12			
<input type="checkbox"/>	24 Persistence and failure of mean-field approximations adapted...	2014								1								2	2			
<input type="checkbox"/>	25 Assessment of blast induced ground vibrations by artificial ...	2014											1					1	1			
<input type="checkbox"/>	26 Dynamics of landslide model with time delay and periodic par...	2014										1	1		1			3	3			
<input type="checkbox"/>	27 Stability, coherent spiking and synchronization in noisy exc...	2014									1							1	1			
<input type="checkbox"/>	28 Complex dynamics of spring-block earthquake model under peri...	2014										1		1				2	2			
<input type="checkbox"/>	29 Dynamics of simple earthquake model with time delay and vari...	2013										1		4				5	5			
<input type="checkbox"/>	30 Friction memory effect in complex dynamics of earthquake mod...	2013							1			1	3	1	2			8	8			
<input type="checkbox"/>	31 Mean-field approximation of two coupled populations of excit...	2013								1		1	1					3	3			
<input type="checkbox"/>	32 Cluster synchronization of spiking induced by noise and inte...	2012								2	2		1	1	1	2		9	9			
<input type="checkbox"/>	33 Possibilities of introducing different functional circuits o...	2012										1						1	1			
<input type="checkbox"/>	34 Spontaneous formation of synchronization clusters in homogen...	2012								2	3	1	2	1	1	1		11	11			
<input type="checkbox"/>	35 The effects of synaptic time delay on motifs of chemically c...	2011						1	2			1		2				6	6			

		Total	0	0	1	1	2	4	13	9	2	19	29	40	27	10	157	0	157
<input type="checkbox"/>	36 Stability, bifurcations, and dynamics of global variables of...	2011										1		1			2		2
<input type="checkbox"/>	37 Functional motifs: A novel perspective on burst synchronizat...	2011						1				1		1			3		3
<input type="checkbox"/>	38 Phase plane approach to cooperative rhythms in neuron motifs...	2010						3	4			1					8		8
<input type="checkbox"/>	39 Power law behavior related to mutual synchronization of chem...	2010					1		2	1			1	1			6		6
<input type="checkbox"/>	40 Percolation transition at growing spatiotemporal fractal pat...	2009				1				1		1					3		3
<input type="checkbox"/>	41 Fractal properties of percolation clusters in Euclidian neur...	2009			1								1				2		2
<input type="checkbox"/>	42 Percolation approach to formation of synfire chains in two d...	2006															0		0

Display: 100 results per page1

^ Top of page



Citation overview results

< Back to citation overview

Stimulus-evoked activity in clustered networks of stochastic rate-based neurons

Franovic I., Klinshov V.

2018, European Physical Journal: Special Topics, (10-11) 1063-1076

Is cited 1 time in Scopus by:

Search within results...



Analyze search results

Show all abstracts Sort on: Date (newest)



Refine results

Limit to Exclude

Access type ⓘ

Year

Author name

Subject area

Document type

Publication stage

Source title

Affiliation

Funding sponsor

Country/territory

Source type

Language

Limit to Exclude

↗ Export refine

All ▾ Export Download View citation overview View cited by Add to List ...

	Document title	Authors	Year	Source	Cited by
<input type="checkbox"/> 1	Advances in nonlinear dynamics of complex networks: adaptivity, stochasticity, and delays Open Access	Nekorkin, V., Klinshov, V.	2018	European Physical Journal: Special Topics 227(10-11), pp. 995-997	0

◀ View at Publisher Related documents

Display: 20 ▾
results per page

1

^ Top of page



Citation overview results

[← Back to citation overview](#)

Noise-induced switching in two adaptively coupled excitable systems

Bacic I. , Yanchuk S. , Wolfrum M., Franovic I.

2018, European Physical Journal: Special Topics, (10-11) 1077-1090

Is cited 3 times in Scopus by:

Search within results...



Analyze search results

Show all abstracts

Sort on: Date (newest)



Refine results

Limit to Exclude

Access type ⓘ

Year

Author name

Subject area

Document type

Publication stage

Source title

Keyword

Affiliation

Funding sponsor

Country/territory

Source type

Language

Limit to Exclude

Export refine

 All Export Download View citation overview View cited by Add to List 

	Document title	Authors	Year	Source	Cited by
<input type="checkbox"/> 1	On the intersection of a chaotic attractor and a chaotic repeller in the system of two adaptively coupled phase oscillators	Emelianova, A.A. , Nekorkin, V.I.	2019	Chaos 29(11),111102	1
	View abstract	View at Publisher	Related documents		
<input type="checkbox"/> 2	Frequency entrainment and anti-entrainment of coupled active rotators synchronized by common noise	Dolmatova, A.V. , Goldobin, D.S. , Pikovsky, A.S.	2019	Izvestiya Vysshikh Uchebnykh Zavedeniy. Prikladnaya Nelineynaya Dinamika 27(6), pp. 91-113	0
	View abstract	View at Publisher	Related documents		
<input type="checkbox"/> 3	Advances in nonlinear dynamics of complex networks: adaptivity, stochasticity, and delays Open Access	Nekorkin, V. , Klinshov, V.	2018	European Physical Journal: Special Topics 227(10-11), pp. 995-997	0
		View at Publisher	Related documents		

Display: 20
results per page



Citation overview results

[← Back to citation overview](#)

Phase-sensitive excitability of a limit cycle

Franovic I., Omel'chenko O.E., Wolfrum M.

2018, Chaos, (7)

Is cited 4 times in Scopus by:

Search within results...



Refine results

Limit to Exclude

Access type

Year

Author name

Subject area

Document type

Publication stage

Source title

Keyword

Affiliation

Funding sponsor

Country/territory

Source type

Language

Limit to Exclude

[↗ Export refine](#)

Analyze search results

Show all abstracts Sort on: Date (newest)

 All Export Download View citation overview View cited by Add to List

	Document title	Authors	Year	Source	Cited by
<input type="checkbox"/> 1	Dynamics of non-autonomous oscillator with a controlled phase and frequency of external forcing	Krylosova, D.A., Seleznev, E.P., Stankevich, N.V.	2020	Chaos, Solitons and Fractals 134,109716	0
	View abstract	View at Publisher	Related documents		
<input type="checkbox"/> 2	Noise-induced early afterdepolarizations in a three-dimensional cardiac action potential model	Slepukhina, E., Ryashko, L., Kügler, P.	2020	Chaos, Solitons and Fractals 131,109515	0
	View abstract	View at Publisher	Related documents		
<input type="checkbox"/> 3	State-dependent vulnerability of synchronization	Medeiros, E.S., Medrano-T, R.O., Caldas, I.L., Tél, T., Feudel, U.	2019	Physical Review E 100(5),052201	0
	View abstract	View at Publisher	Related documents		
<input type="checkbox"/> 4	Chimera States on a Ring of Strongly Coupled Relaxation Oscillators Open Access	Rode, J., Totz, J.F., Fengler, E., Engel, H.	2019	Frontiers in Applied Mathematics and Statistics 5,31	0
	View abstract	View at Publisher	Related documents		

Display: 20
results per page



Citation overview results

< Back to citation overview

Clustering promotes switching dynamics in networks of noisy neurons

Franovic I. , Klinshov V.

2018, Chaos, (2)

Is cited 2 times in Scopus by:

Search within results...



Analyze search results

Show all abstracts

Sort on: Date (newest)



Refine results

Limit to Exclude

Access type ⓘ

Year

Author name

Subject area

Document type

Publication stage

Source title

Keyword

Affiliation

Funding sponsor

Country/territory

Source type

Language

Limit to Exclude

Export refine

All Export Download View citation overview View cited by Add to List



Document title

Authors

Year

Source

Cited by

- | | | | | | |
|----------------------------|---|---|------|--|---|
| <input type="checkbox"/> 1 | Interval stability for complex systems
Open Access | Klinshov, V.V. , Kirillov, S. , Kurths, J. , Nekorkin, V.I. | 2018 | New Journal of Physics
20(4),043040 | 2 |
|----------------------------|---|---|------|--|---|

View abstract



View at Publisher

Related documents

- | | | | | | |
|----------------------------|--|---|------|---|---|
| <input type="checkbox"/> 2 | Nonlinear dynamical models of neurons: Review
Open Access | Dmitrichev, A.S. , Kasatkin, D.V. , Klinshov, V.V. , (...), Shchapin, D.S. , Nekorkin, V.I. | 2018 | Izvestiya Vysshikh Uchebnykh Zavedeniy. Prikladnaya Nelineynaya Dinamika
26(4), pp. 5-58 | 1 |
|----------------------------|--|---|------|---|---|

View abstract



View at Publisher

Related documents

Display: 20 results per page

1

Top of page



Citation overview results

< Back to citation overview

Inverse stochastic resonance in a system of excitable active rotators with adaptive coupling

Bacic I., Klinshov V., Nekorkin V., Perc M., Franovic I.

2018, EPL, (4)

Is cited 2 times in Scopus by:

Search within results...



Analyze search results

Show all abstracts Sort on: Date (newest) ▾

All ▾ Export Download View citation overview View cited by Add to List ...

Refine results

Limit to Exclude

Access type ⓘ ▾

Year ▾

Author name ▾

Subject area ▾

Document type ▾

Publication stage ▾

Source title ▾

Keyword ▾

Affiliation ▾

Funding sponsor ▾

Country/territory ▾

Source type ▾

Language ▾

Limit to Exclude

↗ Export refine

	Document title	Authors	Year	Source	Cited by
<input type="checkbox"/> 1	Stochastic resonance in a monostable system driven by time-delayed feedback	Zhang, G., Zhou, L., Zhang, T.	2020	Indian Journal of Physics Article in Press	0
	View abstract ▾	View at Publisher	Related documents		
<input type="checkbox"/> 2	Inverse stochastic resonance in Hodgkin–Huxley neural system driven by Gaussian and non-Gaussian colored noises	Lu, L., Jia, Y., Ge, M., Xu, Y., Li, A.	2020	Nonlinear Dynamics Article in Press	1
	View abstract ▾	View at Publisher	Related documents		

Display: 20 ▾
results per page

Phase-sensitive excitability of a limit cycle

Igor Franović,^{1,a)} Oleh E. Omel'chenko,^{2,b)} and Matthias Wolfrum^{2,c)}

¹Scientific Computing Laboratory, Center for the Study of Complex Systems, Institute of Physics Belgrade, University of Belgrade, Pregrevica 118, 11080 Belgrade, Serbia

²Weierstrass Institute, Mohrenstrasse 39, 10117 Berlin, Germany

(Received 18 June 2018; accepted 6 July 2018; published online 27 July 2018)

The classical notion of excitability refers to an equilibrium state that shows under the influence of perturbations a nonlinear threshold-like behavior. Here, we extend this concept by demonstrating how periodic orbits can exhibit a specific form of excitable behavior where the nonlinear threshold-like response appears only after perturbations applied within a certain part of the periodic orbit, i.e., the excitability happens to be phase-sensitive. As a paradigmatic example of this concept, we employ the classical FitzHugh-Nagumo system. The relaxation oscillations, appearing in the oscillatory regime of this system, turn out to exhibit a phase-sensitive nonlinear threshold-like response to perturbations, which can be explained by the nonlinear behavior in the vicinity of the canard trajectory. Triggering the phase-sensitive excitability of the relaxation oscillations by noise, we find a characteristic non-monotone dependence of the mean spiking rate of the relaxation oscillation on the noise level. We explain this non-monotone dependence as a result of an interplay of two competing effects of the increasing noise: the growing efficiency of the excitation and the degradation of the nonlinear response. *Published by AIP Publishing.* <https://doi.org/10.1063/1.5045179>

The classical concept of excitability refers to a specific non-linear response of a system to perturbations of its rest state. While for small perturbations the system reacts only with a linear relaxation directly back to the rest state, for larger perturbations above a certain threshold it reacts with a large non-linear response, called excitation. Such a behavior can be observed, for example, when a neuron in the quiescent state receives a presynaptic impulse and reacts with the emission of a spike. Until the non-linear response has terminated, the system is not susceptible to further excitations. Only after the system has again reached the rest state, can it be excited again. We study here the case where the rest state is not a stationary state but a stable periodic orbit. Then, the response of the system to perturbations may be nonuniform along the orbit. Of particular interest is the case where the non-linear response to perturbations above threshold appears only in a certain part of the periodic orbit. We call this situation *phase-sensitive excitability* and demonstrate that the oscillatory regime of the FitzHugh-Nagumo system can serve as an example for this type of behavior. It is well known that for other parameter values, the FitzHugh-Nagumo system has an excitable equilibrium. In this case, a perturbation above threshold induces a response in the form of a single spike. We present a completely different scenario. Perturbations are now applied to the regime of periodic spiking. If these perturbations act close to the passage near the unstable equilibrium, they may evoke a response in the form of a subthreshold oscillation and in this way prevent the system for a certain time from spiking. There are many cases where the triggering of an excitable system by noise can result in a characteristic non-monotone

dependence of the system behavior on the noise intensity. This also holds for our example of the oscillatory regime of the FitzHugh-Nagumo system, where we can demonstrate that the spiking frequency becomes minimal at an intermediate noise level.

I. INTRODUCTION

In their groundbreaking work from 1946, Wiener and Rosenblueth,¹ having observed propagating contractions in the cardiac muscle, developed the fundamental concept of an excitable system: exciting a state of rest by perturbations above a certain threshold, the system reacts with a non-linear response. Subsequently, the system needs a certain time, called the refractory period, until it can be excited again. This concept provided an extremely successful framework for understanding a large variety of real-life systems.² Beginning from biological systems, where it describes not only cardiac tissue³ but also certain functionalities of organisms,^{4,5} and behavioral aspects of individuals, or of whole populations,^{6,7} it has been translated to gene regulatory networks,⁸ chemical reactions,⁹ laser systems,¹⁰ and semiconductors,¹¹ and last but not least, it has become one of the key principles of theoretical neuroscience.^{12–16}

We extend the concept of excitability by considering as the rest state of the system a stable periodic orbit rather than an equilibrium. In this case, the nonlinear threshold-like response may additionally depend on the phase of the oscillation at which the impulse acts such that an excitation may occur only if a super-threshold perturbation is applied within a certain part of the periodic orbit. We shall use the regime of relaxation oscillations in the FitzHugh-Nagumo system as an example

^{a)}Electronic mail: franovic@ipb.ac.rs

^{b)}Electronic mail: omelchen@wias-berlin.de

^{c)}Electronic mail: wolfrum@wias-berlin.de

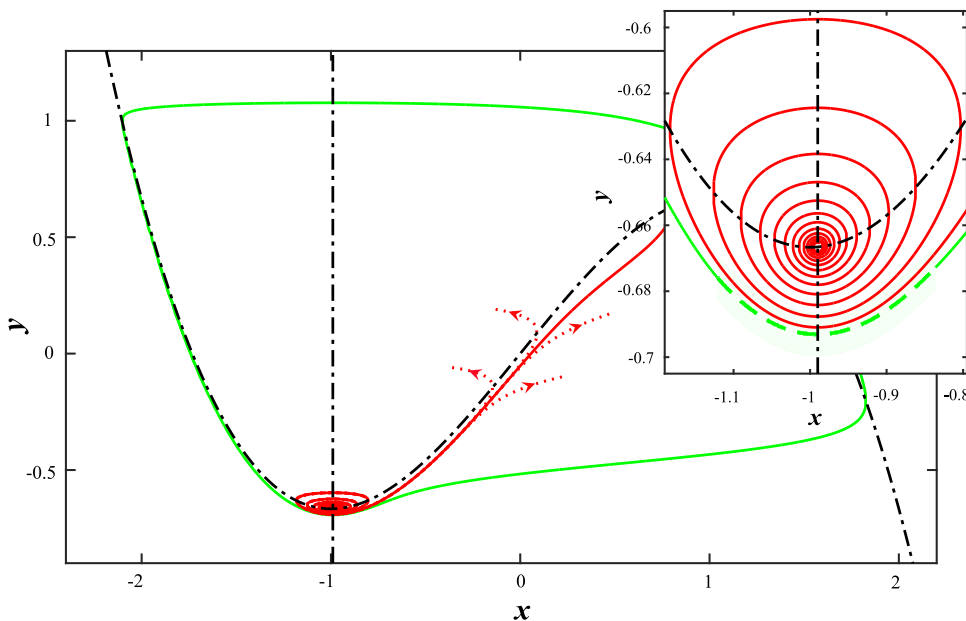


FIG. 1. Phase plane for (1) with $b = 0.99$, $\epsilon = 0.05$, $I(t) = 0$: relaxation oscillation orbit (green), maximal canard (red), and nullclines (dash-dotted). Inset: region close to the unstable equilibrium. In the region of phase-sensitive excitability (green stripe), the maximal canard passes close to the relaxation oscillation orbit such that small perturbations may deviate a solution to make an extra round trip around the unstable equilibrium.

of this general concept of phase-sensitive excitability. In the context of neuroscience, this spiking regime can already be considered as the “excited state” of a neuron. Nevertheless, here we shall consider this periodic regime as the “rest state” in the sense of Refs. 1 and 2 and shall study its nonlinear threshold-like response to perturbations, which in this case manifests as a reduced spiking activity. Note that in Ref. 17 a similar model was considered but with the rest state given by the subthreshold oscillations and with the excited state associated to the large-amplitude oscillations. Using multi-scale techniques and the canard trajectories, we shall analyze in detail the specific mechanism realizing the non-linear excitations in our system.

In Ref. 18, it has been pointed out that excitable systems can respond to noise in a specific way, showing a characteristic non-monotone dependence on the noise level. Such effects have been studied extensively and the FitzHugh-Nagumo system in the regime of an excitable equilibrium represents one of the classical examples.^{18–20} There, it is the mean spiking regularity of *noise-induced* oscillations that shows a characteristic maximum, called coherence resonance, at an intermediate noise level. Our study of the FitzHugh-Nagumo system in the oscillatory regime will demonstrate that also the relaxation oscillation shows a non-monotone response to noise: here, however, it is the mean spiking rate that shows a characteristic minimum at an intermediate noise level. This effect is most pronounced for intermediate values of the time-scale separation ($\epsilon \approx 0.05$), while in the singular limit $\epsilon \rightarrow 0$, the effect disappears. This is the reason why the effect has not been observed in the detailed study of Muratov and Vanden-Eijnden,²¹ where the behavior of the FitzHugh-Nagumo system under the influence of noise has been investigated by singular perturbation techniques. We believe that our parameter regime can be adequate in the context of neuroscience and that the effect of phase-sensitive excitability may be of importance both for deterministic inputs in coupled network systems and for the case of stochastic input signals.

II. THE FITZHUGH-NAGUMO OSCILLATOR

Our basic example for the mechanism of phase-sensitive excitability is the FitzHugh-Nagumo system

$$\begin{aligned}\epsilon \dot{x} &= x - x^3/3 - y, \\ \dot{y} &= x + b + I(t).\end{aligned}\quad (1)$$

In the context of neuroscience, x and y correspond to the neuronal membrane potential and the ion-gating channels, respectively. The time-dependent input signal $I(t)$ can be used to resemble intrinsic noise in the opening of the ion-channels.²² The smallness of the parameter ϵ reflects the time-scale separation between the dynamics of x and y . The system has been extensively studied as a slow-fast system, using the singular limit $\epsilon \rightarrow 0$, cf. Ref. 23 for an overview on the deterministic case and Refs. 2, 19, 20, and 24–26 for different scenarios with noise. Classical results for the case without input signal $I(t)$ show that system (1) undergoes a supercritical Hopf bifurcation at $b = 1$ such that for decreasing b a branch of small-amplitude oscillations of period $\mathcal{O}(\sqrt{\epsilon})$ appears. Then, for $b = b_c \approx 1 - \epsilon/8$, there is a rapid transition to large-amplitude relaxation oscillations of period $\mathcal{O}(1)$.²⁷ From the neuroscience point of view, this corresponds to the transition from the quiescent state to the spiking regime via subthreshold oscillations. In order to explain the mechanism of phase-sensitive excitability, we consider the slow-fast structures in the phase space for the relaxation oscillations at $b < b_c$ in the system (1). Figure 1 shows the relaxation oscillation orbit together with the nullclines of the vector field. During the passage close to the unstable equilibrium, located at the intersection of the nullclines, the relaxation oscillation orbit is excitable in the following sense: there is an exponentially thin layer of trajectories, called *maximal canard*, such that any perturbation large enough to elevate the state from the periodic orbit to a point above these trajectories will cause the system to make at least one loop around the unstable equilibrium before proceeding again along the relaxation oscillation orbit. Smaller perturbations or perturbations in directions below

the relaxation oscillation orbit will not give rise to such a response.

The maximal canard trajectories are characterized by the fact that they follow the whole unstable branch of the slow manifold, which in first approximation is given by the part of the nullcline $y = x - x^3/3$ lying in between the two folds, cf. Ref. 28. Already exponentially small deviations from the maximal canard cause the solutions to rapidly depart from it, traveling in either direction towards one of the stable branches of the slow manifold (dotted curves in Fig. 1). A maximal canard trajectory can readily be determined numerically by selecting an initial condition closely below the upper fold $(x, y) = (1, 2/3)$, and from there integrating backward in time. Following one of the canard trajectories in this way, one finds a region where it passes extremely close to the relaxation oscillation orbit. Along this part of the relaxation oscillation orbit, the maximal canard acts as a threshold for perturbations such that super-threshold perturbations cause a nonlinear response with an extra excitation loop around the unstable equilibrium.

III. RESPONSE TO NOISE

Having understood the response of the system to single impact perturbations of different size, we examine now the response to Gaussian white noise

$$I(t) = D\xi(t),$$

of varying amplitude D . Figure 2 shows typical realizations of trajectories for three different levels of noise. The plots show that for low noise level (a), the noise-induced excitation loops occur rarely and are well confined by the spiral structure of the maximal canard. For increasing noise level (b), they become more frequent, but at the same time they get increasingly blurred by the noise. For the largest noise level (c), the prevalence of the small excitation loops decreases again since the efficiency of the confinement by the deterministic maximal canard is reduced.

To study this process in more detail, we introduce a Poincaré section at

$$x = x_0 = -0.99, \quad y < x_0 - x_0^3/3, \quad (2)$$

i.e., we record passages through a vertical line extending below the unstable fixed point. In Fig. 3(a), we show the sampled return times ΔT between successive crossing events, obtained for the same noise levels as used in Fig. 2. The histograms show that for all three noise levels one can clearly distinguish between return times $\Delta T \approx T_R$ corresponding to relaxation oscillation cycles and those corresponding to excitation loops $\Delta T \approx T_E$. For the time trace shown in Fig. 3(b), we have shaded the corresponding time intervals accordingly. Panel (c) shows the corresponding variances $\sigma_{R,E}$ for each of the two separate peaks of the return time distribution, and panel (d) shows their relative size for varying noise level D . One can observe that there is a prevalence of excitation loops for intermediate values of the noise level $D \approx 10^{-2}$. Above this value, the variances for each of the peaks start to increase, indicating an increasing degradation of the nonlinear response by noise. The excitation loops delay the

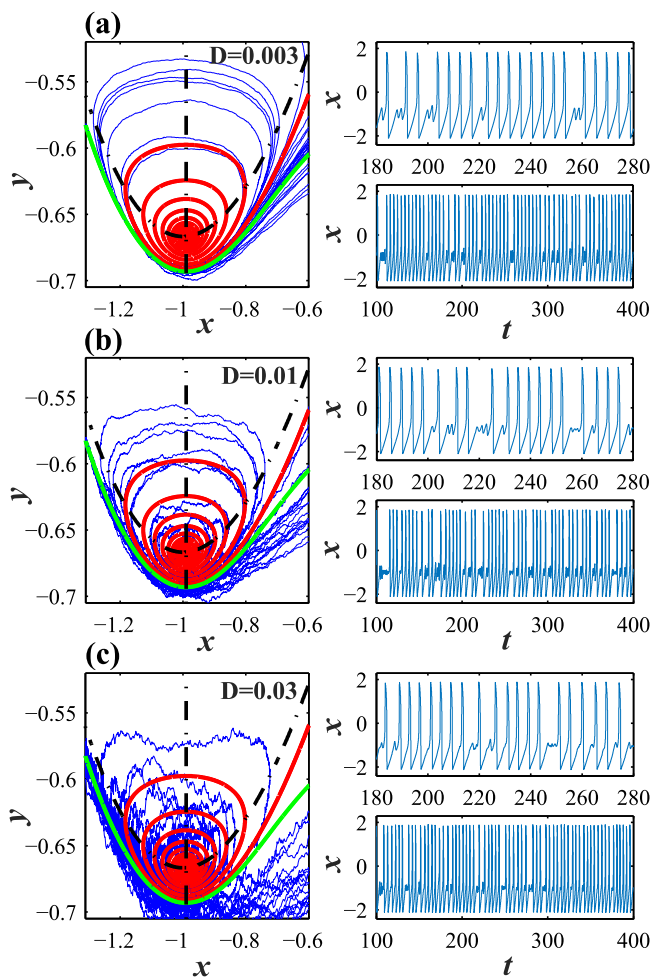


FIG. 2. Response of the relaxation oscillation to different levels of noise: (a) $D = 0.003$, (b) $D = 0.01$, and (c) $D = 0.03$. Left panels: noisy trajectories in the phase plane together with the deterministic relaxation oscillation orbit and maximal canard. Top panels: corresponding time traces $x(t)$ from the panels above. Bottom panels: longer time traces indicating the prevalence of noise induced small excitation loops for the middle noise level $D = 0.01$.

occurrence of the next spike and thus affect the mean spiking rate of the system $\langle R \rangle$, measured as the average number of large-amplitude oscillations per time. Figure 4 shows that the spiking rate exhibits a non-monotone dependence with increasing noise level D , where the minimum of $\langle R \rangle$ coincides with the maximal fraction of small excitation loops shown in Fig. 3(d).

Note that this effect is most pronounced for intermediate values $\varepsilon \approx 0.05$ of the time-scale separation. This is due to the fact that the duration of the excitation loop, given to the leading order by the linearization at the unstable equilibrium, which is a weakly undamped center, scales like $\mathcal{O}(\sqrt{\varepsilon})$. Hence, the delaying effect on the spikes and the consequent decrease of the spiking rate become small in the singular limit.

IV. EXCITATION EFFICIENCY AND DEGRADATION

The non-monotone dependence of the spiking rate $\langle R \rangle(\sigma)$ can be explained as the result of two competing effects of the increasing noise: the increasing efficiency of the excitation and the degradation of the nonlinear response. To study this competition in more detail, we consider the return times

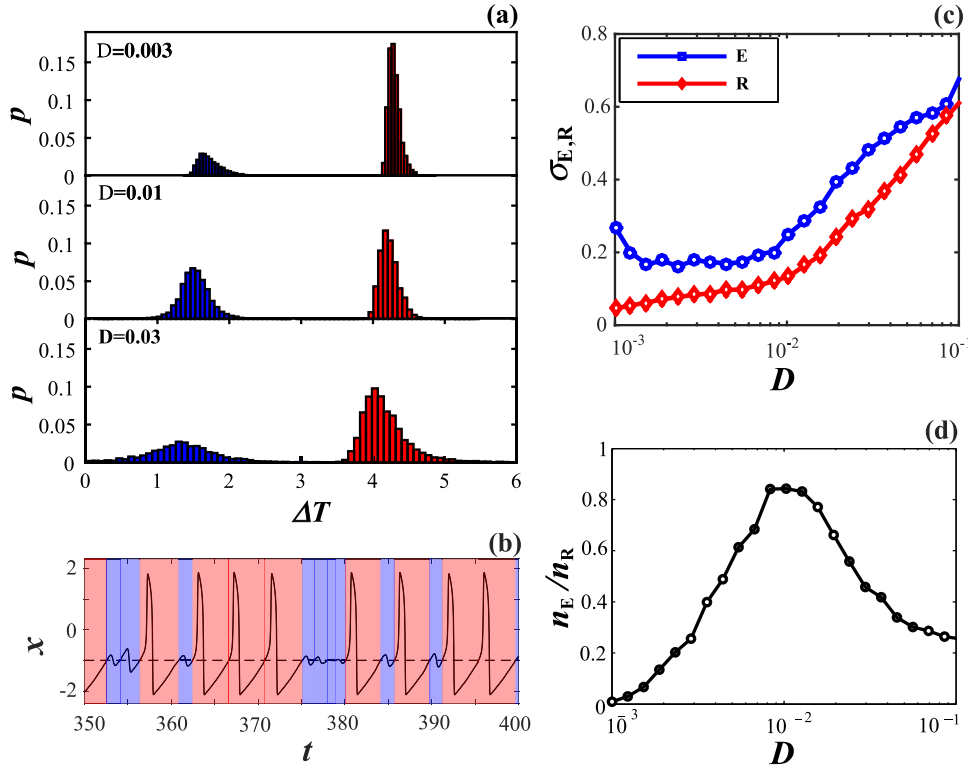


FIG. 3. (a) Sampled return times ΔT between subsequent crossings of the Poincaré section (2) for different noise levels. The two peaks in the distributions correspond to relaxation oscillations $\Delta T \approx T_R$ (red) and noise-induced excitation loops $\Delta T \approx T_E$ (blue). (b) Time trace for $D = 0.01$ with respective time intervals ΔT colored accordingly. [(c) and (d)] Variances $\sigma_{R,E}$ and relative size n_E/n_R from the two separate peaks of the return time distributions for varying noise level.

$\Delta \tilde{T}$, associated to the Poincaré section (2) with $x_0 = -0.2$. In this case, the excitation loops do not lead to additional crossing events and the corresponding return time $\Delta \tilde{T}$ measures the round trip time of each relaxation oscillation together with the included excitation loops. For small noise, the corresponding histograms in Fig. 5(a) show distributions with well separated peaks centered around $\Delta \tilde{T} \approx T_R + kT_E$, where $k \in \{0, 1, 2, 3, \dots\}$ counts the number of excitation loops between two successive Poincaré events. We observe that for $D < 10^{-2}$ there is not only an increasing number of such excitation loops, cf. Fig. 3(d) but also an increasing number of multiple successive excitation loops. This can be seen from the corresponding probabilities of successive loops for varying noise intensity D given in Fig. 5(b). It underlines the increasing efficiency of the excitation process, driven by

noise in the subcritical range $D < 10^{-2}$. Above this value, the degradation effect takes over, which consists in the loss of correlation between the number of included excitation loops and the total duration of the corresponding relaxation oscillation cycle.

In order to quantify the degradation effect, we have calculated the noise-dependence of the correlation coefficient δ between the number k of small loops the unit performs between the two successive passages of the Poincaré cross-section, and the first return time $\Delta \tilde{T}$ being in the corresponding interval $[T_R + (k - \frac{1}{2})T_E, T_R + (k + \frac{1}{2})T_E]$. Evaluating numerically this correlation coefficient, we see the onset of a strong decay above the critical noise level of $D < \approx 10^{-2}$, indicating the degradation of the nonlinear response, see Fig. 5(c). Similar effects have been described in Refs. 29 and 30 as noise-induced linearization.

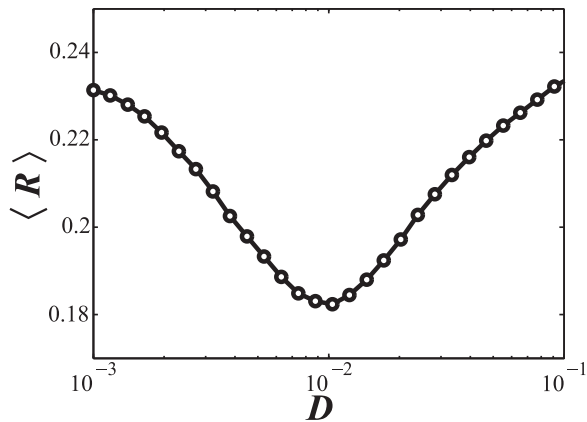


FIG. 4. Non-monotone response to noise of a phase-sensitive excitable periodic orbit: mean spiking rate $\langle R \rangle$ of the relaxation oscillations of (1) shows a characteristic minimum at an intermediate noise level $D \approx 10^{-2}$.

V. DISCUSSION AND OUTLOOK

It is important to remark that a periodic orbit emerging in a transition from an excitable equilibrium, as it happens in the FitzHugh-Nagumo system, does not necessarily inherit phase-sensitive excitability from the excitability of the preceding equilibrium. This can be seen, e.g., for the active rotator

$$\dot{\theta} = 1 + b - \sin \theta + D\xi(t), \quad \theta \in \mathbb{R}/2\pi\mathbb{Z}, \quad (3)$$

where a saddle-node infinite period (SNIPER) bifurcation at $b = 0$ mediates a transition from excitable to oscillatory behavior. However, the periodic solution at $b = 0.02$ shows no phase-sensitive excitability, and the dependence of the spiking rate on the noise level is monotone, cf. Fig. 6(a). On the other hand, for the FitzHugh-Nagumo system with a noise term $\sqrt{D/\varepsilon}\xi(t)$ added to the fast variable x so to resemble the

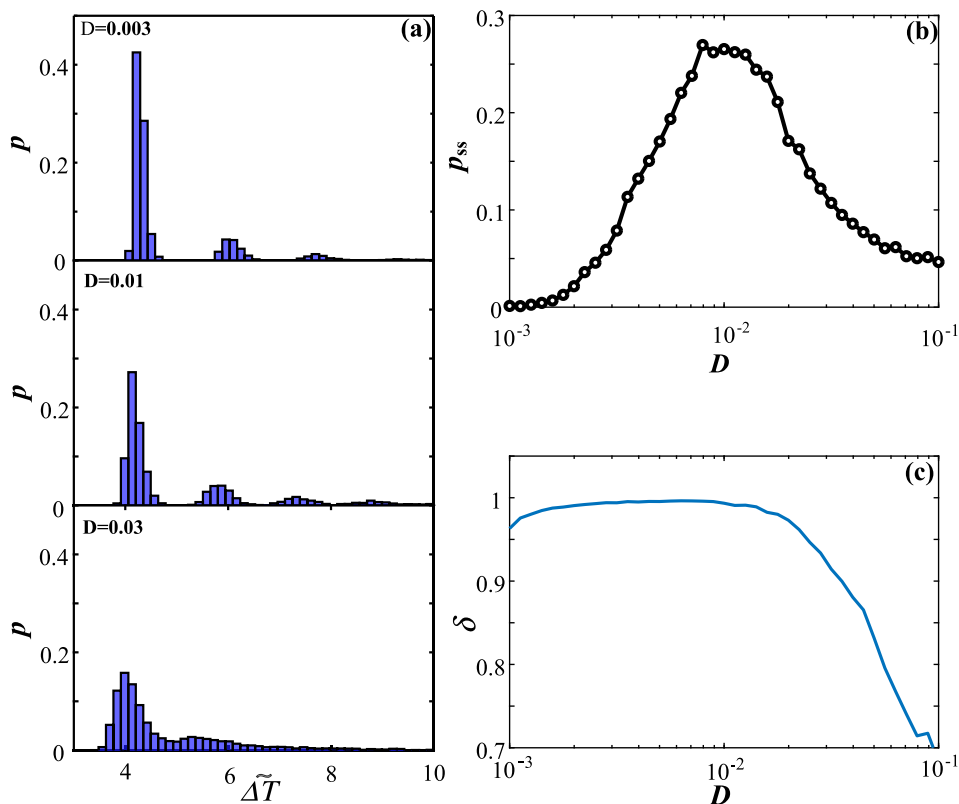


FIG. 5. (a) Histograms of first return times $\Delta\tilde{T}$ to a Poincaré section (2) with $x_0 = -0.2$. (b) Relative frequency of two successive excitation loops. (c) Correlation coefficient between the number of excitation loops in a relaxation oscillation cycle and its duration $\Delta\tilde{T}$.

action of synaptic noise,²² the excitable behavior and the non-monotone dependence can be observed in a similar way, cf. Figs. 4 and 6(b).

The presented concept of phase-sensitive excitability establishes a natural extension of the classical concept of excitability of equilibria to periodic orbits, offering a general framework for describing certain nonlinear effects in driven or interacting oscillatory systems. It resembles the main properties of the classical case:

- (i) nonlinear threshold-like response to perturbation impulses and
- (ii) non-monotone response to noisy inputs of increasing amplitude.

The nature of the non-monotone dependence on the noise level for phase-sensitive excitability in the regime of relaxation oscillations of the FitzHugh-Nagumo system is qualitatively distinct from the two classical cases concerning the FitzHugh-Nagumo model where the rest state is given by an excitable equilibrium or conforms to the regime of subthreshold oscillations before the canard explosion ($b > b_c \approx 1 - \epsilon/8$). In both the classical examples, the excited state conforms to a relaxation oscillation (spike), and the applied noise affects the *regularity* of noise-induced oscillations such that it becomes maximal for the optimal noise intensity.^{17–20} The qualitative similarity between these two cases is to be expected because the subthreshold oscillations become indistinguishable from an equilibrium in the

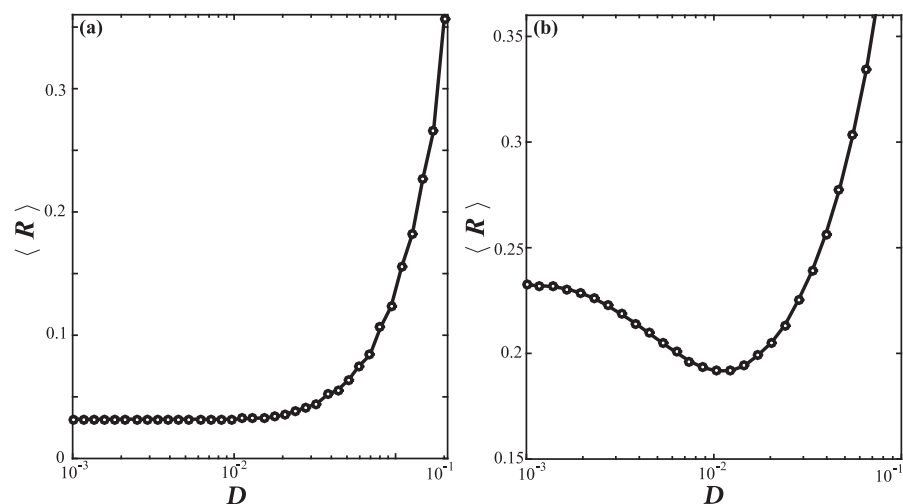


FIG. 6. (a) Monotone mean spiking rate $\langle R \rangle$ of the active rotator (3). (b) Non-monotone mean spiking rate of the relaxation oscillations of (1) with $I(t) = 0$ and adding instead noise of varying levels to the fast variable.

singular limit $\epsilon \rightarrow 0$. As opposed to that, our scenario of phase-sensitive excitability involves the regime of relaxation oscillations as the rest state, the subthreshold oscillations conform to the excited state, and the applied noise affects the *mean spiking frequency* such that it becomes minimal at an intermediate noise level.

In the context of neuroscience, the resonant effect consisting in a reduction of the spiking frequency of neural oscillators within a certain range of intermediate noise levels has been referred to as *inverse stochastic resonance*. Such an inhibitory action of noise has been observed experimentally³¹ and has also been discussed in several model studies, concerning the impact of external or intrinsic noise on single^{32–34} or coupled neurons.^{35,36} The effect has been suggested as a potential paradigm for computational tasks that either require reducing the neuronal spiking frequency without chemical neuro-modulation or involve generating episodes of bursting activity in neurons that are not endogenously bursting. The generic mechanism behind the effect has typically been linked to *bistability* of the underlying deterministic dynamics, which exhibits coexistence between an equilibrium and a stable limit cycle. For such a scenario, the noise induces a switching between the corresponding metastable states, with the spiking frequency decreasing at a certain range of intermediate noise levels where the transition rate from the quasi-stationary to oscillatory state becomes much smaller than the one in the opposite direction. The noise-driven effect reported here is based on a qualitatively distinct mechanism, because the deterministic dynamics is monostable, and the excitations off the limit cycle emerge due to phase-sensitive excitability of the associated orbit, derived from the multi-scale structure of the system.

Revisiting earlier work on coupled oscillator systems, one can find instances where effects that could be explained as a result of phase-sensitive excitability have been reported. Indeed, some of the results in Ref. 37 about space-time patterns in a coupled network of FitzHugh-Nagumo oscillators seem to be based on the phase-sensitive excitability of the relaxation oscillations. Also, the alternating behavior reported in Ref. 38 could possibly be an effect of phase-sensitive excitability. These examples may underline the importance of the abstract concept as such, offering a general framework and a unifying view for a variety of closely related phenomena.

ACKNOWLEDGMENTS

This work was supported by the Ministry of Education, Science and Technological Development of Republic of Serbia under Project No. 171017, the DAAD Serbia-Germany Bilateral Project “Emergent Dynamics in Systems of Coupled Excitable Units,” and the Deutsche Forschungsgemeinschaft (DFG) within the framework of Collaborative Research Center SFB 910.

- ¹N. Wiener and A. Rosenblueth, Arch. Inst. Cardiol. Mex. **16**, 205 (1946), available at <https://www.ncbi.nlm.nih.gov/pubmed/20245817>.
- ²B. Lindner, J. Garcia-Ojalvo, A. Neiman, and L. Schimansky-Geier, *Phys. Rep.* **392**, 321 (2004).
- ³S. Alonso and M. Bär, *Phys. Rev. Lett.* **110**, 158101 (2013).
- ⁴J. D. Murray, *Mathematical Biology* (Springer, Berlin, Heidelberg, New York, 1993).
- ⁵J. P. Keener and J. Sneyd, *Mathematical Physiology* (Springer, New York, 2009).
- ⁶I. Farkas, D. Helbing, and T. Vicsek, *Nature* **419**, 131 (2002).
- ⁷S. P. Borgatti, A. Mehra, D. J. Brass, and G. Labianca, *Science* **323**, 892 (2009).
- ⁸Y. Chen, J. K. Kim, A. J. Hirring, K. Josić, and M. R. Bennett, *Science* **349**, 986 (2015).
- ⁹A. S. Mikhailov and K. Showalter, *Phys. Rep.* **425**, 79 (2006).
- ¹⁰S. Wiecek, B. Krauskopf, T. B. Simpson, and D. Lenstra, *Phys. Rep.* **416**, 1 (2005).
- ¹¹A. M. Yacomotti, P. Monnier, F. Raineri, B. B. Bakir, C. Seassal, R. Raj, and J. A. Levenson, *Phys. Rev. Lett.* **97**, 143904 (2006).
- ¹²E. M. Izhikevich, *Dynamical Systems in Neuroscience: The Geometry of Excitability and Bursting* (MIT Press, Cambridge, 2007).
- ¹³J. White, J. Rubinstein, and A. Kay, *Trends Neurosci.* **23**, 131 (2000).
- ¹⁴I. Franović, K. Todorović, N. Vasović, and N. Burić, *Phys. Rev. E* **87**, 012922 (2013).
- ¹⁵I. Franović, K. Todorović, N. Vasović, and N. Burić, *Phys. Rev. Lett.* **108**, 094101 (2012).
- ¹⁶I. Franović, K. Todorović, N. Vasović, and N. Burić, *Chaos* **22**, 033147 (2012).
- ¹⁷V. A. Makarov, V. I. Nekorkin, and M. G. Velarde, *Phys. Rev. Lett.* **86**, 3431 (2001).
- ¹⁸A. S. Pikovsky and J. Kurths, *Phys. Rev. Lett.* **78**, 775 (1997).
- ¹⁹R. E. Lee DeVill, E. Vanden-Eijnden, and C. B. Muratov, *Phys. Rev. E* **72**, 031105 (2005).
- ²⁰C. B. Muratov, E. Vanden-Eijnden, and E. Weinan, *Physica D* **210**, 227 (2005).
- ²¹C. B. Muratov and E. Vanden-Eijnden, *Chaos* **18**, 015111 (2008).
- ²²A. Destexhe and M. Rudolph-Lilith, *Neuronal Noise* (Springer, New York, 2012).
- ²³C. Kuehn, *Multiple Time Scale Dynamics*, (Springer International Publishing, Switzerland, 2015).
- ²⁴I. Franović, K. Todorović, M. Perc, N. Vasović, and N. Burić, *Phys. Rev. E* **92**, 062911 (2015).
- ²⁵J. M. Newby and M. A. Schwemmer, *Phys. Rev. Lett.* **112**, 114101 (2014).
- ²⁶N. Berglund and D. Landon, *Nonlinearity* **25**, 2303 (2012).
- ²⁷S. M. Baer and T. Erneux, *SIAM J. Appl. Math.* **46**, 721 (1986).
- ²⁸M. Krupa and P. Szmolyan, *SIAM J. Math. Anal.* **33**, 286 (2001).
- ²⁹N. G. Stocks, N. D. Stein, H. E. Short, R. Mannella, D. G. Luchinsky, and P. V. E. McClintock, in *Fluctuations and Order: The New Synthesis* (Springer, Berlin, 1996), pp. 53–67.
- ³⁰E. Hunsberger, M. Scott, and C. Eliasmith, *Neural Comput.* **26**, 1600 (2014).
- ³¹D. Paydarfar, D. B. Forger, and J. R. Clay, *J. Neurophysiol.* **96**, 3338 (2006).
- ³²H. C. Tuckwell, J. Jost, and B. S. Gutkin, *Phys. Rev. E* **80**, 031907 (2009).
- ³³M. Uzuntarla, J. R. Cressman, M. Ozer, and E. Barreto, *Phys. Rev. E* **88**, 042712 (2013).
- ³⁴M. Uzuntarla, J. J. Torres, P. So, M. Ozer, and E. Barreto, *Phys. Rev. E* **95**, 012404 (2017).
- ³⁵B. S. Gutkin, J. Jost, and H. C. Tuckwell, *Europhys. Lett.* **81**, 20005 (2008).
- ³⁶M. Uzuntarla, E. Barreto, and J. J. Torres, *PLoS Comput. Biol.* **13**, e1005646 (2017).
- ³⁷G. Ansmann, K. Lehnertz, and U. Feudel, *Phys. Rev. X* **6**, 011030 (2016).
- ³⁸N. Semenova, A. Zakharova, V. Anishchenko, and E. Schöll, *Phys. Rev. Lett.* **117**(1), 014102 (2016).

Clustering promotes switching dynamics in networks of noisy neurons

Igor Franović^{1,a)} and Vladimir Klinshov^{2,b)}

¹Scientific Computing Laboratory, Center for the Study of Complex Systems, Institute of Physics Belgrade, University of Belgrade, Pregrevica 118, 11080 Belgrade, Serbia

²Institute of Applied Physics of the Russian Academy of Sciences, 46 Ulyanov Street, 603950 Nizhny Novgorod, Russia

(Received 30 November 2017; accepted 26 January 2018; published online 21 February 2018)

Macroscopic variability is an emergent property of neural networks, typically manifested in spontaneous switching between the episodes of elevated neuronal activity and the quiescent episodes. We investigate the conditions that facilitate switching dynamics, focusing on the interplay between the different sources of noise and heterogeneity of the network topology. We consider clustered networks of rate-based neurons subjected to external and intrinsic noise and derive an effective model where the network dynamics is described by a set of coupled second-order stochastic mean-field systems representing each of the clusters. The model provides an insight into the different contributions to effective macroscopic noise and qualitatively indicates the parameter domains where switching dynamics may occur. By analyzing the mean-field model in the thermodynamic limit, we demonstrate that clustering promotes multistability, which gives rise to switching dynamics in a considerably wider parameter region compared to the case of a non-clustered network with sparse random connection topology. *Published by AIP Publishing.* <https://doi.org/10.1063/1.5017822>

The striking feature of neuronal systems is that variability is reflected on two fundamentally different levels. While there is substantial knowledge on microscopic variability associated to spike trains of individual neurons, much less is known about macroscopic variability, which is a form of emergent behavior in neural networks. Macroscopic variability involves considerably longer timescales than the microscopic one, whereby its signature activity consists in slow rate oscillations, reflected in spontaneous alternation between the distinct network states. The latter are typically referred to as the UP and the DOWN states, such that in the UP state, both the firing rates and the synaptic conductances of neurons are elevated relative to the DOWN state. The switching dynamics between the collective states is especially relevant for activity of neocortical pyramidal neurons and is believed to facilitate or mediate different types of learning and memory. In this paper, we investigate the key ingredients behind switching dynamics, focusing on the interplay of different sources of noise and the network topology. In particular, we consider a clustered network of rate-based neurons and derive an effective model which describes its collective activity in terms of coupled second-order stochastic mean-field systems representing the particular clusters. The effective model is used to qualitatively analyze the mechanisms behind the switching dynamics in the non-clustered and clustered networks, comparing the associated parameter domains. For a homogeneous random network, where all neurons comprise a single cluster, switching is found only within a small parameter region in the vicinity of the pitchfork bifurcation, with the underlying mechanism resembling the motion of a noise-driven particle in a double-well potential. We demonstrate that clustering

plays a facilitatory role with respect to switching dynamics, enhancing the network multistability compared to the case of a homogeneous random network.

I. INTRODUCTION

The fascinating feature of neuronal dynamics is that variability appears in a twofold fashion. For single units, one observes the spike-train variability,¹ reflected in that the same input sequence applied to a given neuron under identical experimental conditions gives rise to different neuronal responses. Apart from the variability on the short timescale, one also encounters variability as an emergent network phenomenon²⁻⁴ associated to much longer timescales.⁵ The hallmark of macroscopic variability is irregular slow rate oscillations,^{6,7} alternatively called up-down states (UDS),⁸⁻¹⁰ which comprise large amplitude, low frequency (0.1–2 Hz) spontaneous fluctuations between the collective UP and DOWN states.¹¹ These states are characterized by clearly distinct firing rates and synaptic conductances, whereby the UP state involves neurons with depolarized membrane potential, elevated firing rates, and increased synaptic conductances relative to those in the DOWN state.¹²⁻¹⁵ Switching is induced by coherent activity of a large number of neurons and has been observed in cortical assemblies *in-vivo* during quiet wakefulness, sleep, and under the influence of anesthetic agents, as well as in certain *in-vitro* preparations.^{8,10,16-18} UDS are the prominent form of spontaneous activity of neocortical pyramidal neurons, facilitating coordination of temporal interactions between neocortex and hippocampus,^{12,19,20} which is fundamental to several types of learning and memory.^{19,21-23}

The issue of the mechanisms that give rise to macroscopic variability as an emergent network phenomenon has remained unresolved, but there are two general directions of

^{a)}Electronic mail: franovic@ipb.ac.rs

^{b)}Electronic mail: vladimir.klinshov@ipfran.ru

research.²⁴ One connects the slow rate fluctuations to deterministic networks with balanced massive excitation and inhibition,^{4,25,26} which leaves the collective dynamics highly sensitive to fluctuations. The other direction relates slow rate oscillations to bistability or multistability in attractor model networks where alternation between the coexisting states emerges due to noise,^{27,28} which acts as the finite-size effect.^{29–31} In this paper, we develop the latter framework by examining the interplay of stochastic neuronal dynamics and heterogeneous network topology on the onset and robustness of slow rate oscillations. In particular, we consider a network of rate-based neurons, focusing on how the different sources of noise, combined with the clustered network topology, give rise to slow stochastic fluctuations of the mean-rate. A qualitative insight into the mechanisms behind the slow fluctuations and the associated parameter domains is gained by developing an effective model of network activity, where the collective dynamics is described by coupled stochastic mean-field systems representing each of the clusters. The effective model for the clustered network with *random* inter- and intra-cluster connectivity is derived here for the first time, using the approach which incorporates the Gaussian closure hypothesis.^{32–34} As an intermediate result, we determine how the different sources of noise from local dynamics as well as statistical heterogeneity of the connection topology contribute to noise at the macroscopic level. This presents generalization of our previous work, where we have considered bistability and slow fluctuations in a network with simple random connection topology.^{30,35}

Investigating the impact of clustered topology on collective dynamics is biologically plausible, given that neural networks with statistically inhomogeneous wiring are inherent to mammalian neocortex,^{36,37} where the clustered structures with stronger synapses and increased connection probability make up the so-called cell assemblies. Earlier studies have indicated that clustered connectivity could give rise to bistability or multistability,^{4,25,38} potentially allowing for switching dynamics between interacting populations, considered as a likely paradigm for decision-making processes during perception or cognition. In this study, we demonstrate that clustering promotes multistability, thereby substantially enhancing the parameter domain admitting the slow rate fluctuations, as compared to a network with simple random connection topology.

The paper is organized as follows. In Sec. II, we present the key points of the derivation of the effective model for collective dynamics of the clustered network, explicitly demonstrating how the neuronal noise and network heterogeneity contribute to different finite-size effects. In Sec. III, we analyze how the network multistability and switching dynamics are influenced by the clustered topology. It is first indicated that in the absence of clustering, switching occurs in a relatively narrow parameter domain, whereby its mechanism resembles the noise-driven motion of a particle in a double-well potential. Then, we show that by introducing clustering, one enhances the network multistability, which ultimately makes the switching phenomenon considerably more robust. In Sec. IV, we provide a brief summary and discussion of the results obtained.

II. DERIVATION OF THE MEAN-FIELD MODEL

We consider a network comprising N neurons arranged into clusters, such that intra-cluster connectivity is larger than the connectivity between neurons from different clusters. The local dynamics of a given neuron i from cluster X follows the rate model^{30,35,39,40}

$$\frac{dr_{Xi}}{dt} = -\lambda_X r_{Xi} + H(v_{Xi}) + \sqrt{2D_X} \xi_{Xi}(t), \quad (1)$$

where λ_X defines the rate relaxation time, $\xi_{Xi}(t)$ denotes the intrinsic neuronal noise which typically derives from stochastic opening of ion-gating channels, whereas H is the nonlinear gain function, whose form will be specified further below. The total input to a neuron $v_{Xi} = u_{Xi} + I_X + \sqrt{2B_X} \eta_{Xi}(t)$ consists of a synaptic input $u_{Xi} = \sum_Y \kappa_{YX} \sum_j a_{YXji} r_{Yj}$ and the external bias current I_X , while fluctuations in the embedding environment are accounted for by synaptic (external) noise $\eta_{Xi}(t)$, characterized by B_X . The coupling scheme is given by the adjacency matrix $a_{YXji} \in \{0, 1\}$, with the notation a_{YXji} referring to the link which projects from neuron j in cluster Y to neuron i from cluster X . Coupling weights between two clusters or within a single cluster are assumed to be homogeneous, whereby we adopt the scaling $\kappa_{YX} = K_{YX}/N$. To improve readability, a summary of the most relevant notation is provided in Table I. Both external and intrinsic fluctuations are represented by Gaussian white noise terms which satisfy $\langle \langle \xi_{Xi}(t) \xi_{Yj}(t') \rangle \rangle = \langle \langle \eta_{Xi}(t) \eta_{Yj}(t') \rangle \rangle = \delta_{XY} \delta_{ij} \delta(t-t')$ and $\langle \langle \xi_{Xi}(t) \eta_{Yj}(t') \rangle \rangle = 0$.

The mean-field model involves a Gaussian closure hypothesis,^{32–34,41} such that the collective dynamics of each cluster X is described by the mean-rate R_X and the associated variance S_X

$$R_X = \frac{1}{N_X} \sum_i r_{Xi} \equiv \langle r_{Xi} \rangle, \\ S_X = \langle r_{Xi}^2 \rangle - R_X^2, \quad (2)$$

where $N_X = n_{xN}$ is the size of the cluster X , whereas $\langle \cdot \rangle$ refers to averaging over the neurons within the given cluster. The network behavior will be represented in terms of dynamics of interacting mean-field systems, each attributed to the

TABLE I. Summary of notation in Sec. II.

λ_X	Relaxation time of units in cluster X
D_X	Intensity of internal noise in cluster X
B_X	Intensity of external noise in cluster X
I_X	External current to cluster X
U_X	Average input to cluster X
$N_X \equiv n_{xN}$	Size of cluster X
K_{YX}	Strength of couplings projecting from cluster Y to cluster X
$\kappa_{YX} \equiv K_{YX}/N$	Normalized coupling strength
a_{YXji}	Element of adjacency matrix characterizing links projecting from neuron j of cluster Y to neuron i in cluster X
p_{YX}	Connection probability from cluster Y to cluster X
R_X	Mean rate of cluster X
S_X	Rate variance in cluster X

particular cluster. Our immediate goal is to derive a second-order stochastic mean-field (macroscopic) model for an arbitrary cluster by appropriately averaging the local (microscopic) neuronal dynamics. To this end, we first introduce an Ansatz regarding the local variables,^{30,35} which will ultimately allow us to treat the nonlinear threshold term $H(v_{Xi})$. In particular, one assumes that r_{Xi} may be written as $r_{Xi} = R_X + \sqrt{S_X} \rho_{Xi}$,⁴² where ρ_{Xi} is a set of variables that satisfies $\langle \rho_{Xi} \rangle = 0$, $\langle \rho_{Xi}^2 \rangle = 1$, as follows from definition (2). Using the Ansatz, the total input v_{Xi} to the neuron may be rewritten as $v_{Xi} = U_X + \delta v_{Xi}$, where

$$U_X = I_X + \frac{1}{N} \sum_Y K_{YX} p_{YX} N_Y R_Y, \quad (3)$$

$$\delta v_{Xi} = \frac{1}{N} \sum_Y K_{YX} R_Y \nu_{YXi} + \frac{1}{N} \sum_Y K_{YX} \sqrt{S_Y} \sigma_{YXi}. \quad (4)$$

In particular, Eq. (3) presents the assembly-averaged input to cluster X , with p_{YX} denoting the connectedness probability from cluster Y to cluster X . The deviation δv_{Xi} from the average input U_X contains two terms, namely, the ‘‘topological’’ and the ‘‘dynamical’’ one, whereby $\nu_{YXi} = \sum_j a_{YXji} - p_{YX} N_Y$ accounts for the deviation from the average number of connections $p_{YX} N_Y$, and $\sigma_{YXi} = \sum_j a_{YXji} \rho_{Yj}$ describes the effect of local rate fluctuations. Equations (3) and (4) enable one to expand $H(v_{Xi})$ about U_X , which proves crucial for deriving the reduced system for cluster dynamics. In particular, one obtains $H(v_{Xi}) = H_{0X} + H_{1X} \delta v_{Xi} + H_{2X} \delta v_{Xi}^2$, where we have introduced notation $H_{0X} \equiv H(U_X)$, $H_{1X} = \frac{dH}{dv_{Xi}}(U_X)$, $H_{2X} = \frac{d^2H}{2dv_{Xi}^2}(U_X)$. From the latter expression and the definition of R_X , one obtains

$$\begin{aligned} \frac{dR_X}{dt} = & -\lambda_X \langle r_{Xi} \rangle + H_{0X} + 2B_X H_{2X} + H_{1X} \langle \Gamma_{1X} \rangle \\ & + H_{2X} \langle \Gamma_{2X} \rangle + \sqrt{2D_X} \langle \zeta_{Xi}(t) \rangle, \end{aligned} \quad (5)$$

with $\langle \Gamma_{1X} \rangle$ and $\langle \Gamma_{2X} \rangle$ given by

$$\begin{aligned} \langle \Gamma_{1X} \rangle = & \frac{1}{N} \sum_Y K_{YX} R_Y \langle \nu_{YXi} \rangle + \frac{1}{N} \sum_Y K_{YX} \sqrt{S_Y} \langle \sigma_{YXi} \rangle \\ & + \sqrt{2B_X} \langle \eta_{Xi} \rangle, \end{aligned} \quad (6)$$

$$\begin{aligned} \langle \Gamma_{2X} \rangle = & \frac{1}{N^2} \sum_{YZ} K_{YX} K_{ZX} R_Y R_Z \langle \nu_{YXi} \nu_{ZXi} \rangle \\ & + \frac{1}{N^2} \sum_{YZ} K_{YX} K_{ZX} \sqrt{S_Y S_Z} \langle \sigma_{YXi} \sigma_{ZXi} \rangle \\ & + \frac{2}{N^2} \sum_{YZ} K_{YX} K_{ZX} R_Y \sqrt{S_Z} \langle \nu_{YXi} \sigma_{ZXi} \rangle \\ & + \frac{2\sqrt{2B_X}}{N} \sum_Y K_{YX} R_Y \langle \nu_{YXi} \eta_{Xi}(t) \rangle \\ & + \frac{2\sqrt{2B_X}}{N} \sum_Y K_{YX} \sqrt{S_Y} \langle \sigma_{YXi} \eta_{Xi}(t) \rangle. \end{aligned} \quad (7)$$

In order to calculate the final expression for the cluster mean-rate, one has to estimate the terms containing ν_{YXi} and σ_{YXi} and the associated averages. We have been able to carry this

out in a systematic fashion, assessing the order of each term. Ultimately, the stochastic mean-field model will include stochastic terms as finite-size effects, whereby we neglect the terms whose order is higher than $\mathcal{O}(1/N)$. In Subsection II A, we briefly discuss how one may determine the contributions from each term comprising $\langle \Gamma_{1X} \rangle$ and $\langle \Gamma_{2X} \rangle$.

A. Evaluating the finite-size effects

Let us first address the terms ν_{YXi} , which by definition present the deviation from the average number of links $p_{YX} N_Y$ projecting from cluster Y to a given node i of subassembly X . From the theory of complex networks, it is known that the average over the ensemble of different network configurations, which we denote by $[\cdot]$, is $[\nu_{YXi}] = 0$, whereas the associated variance is $[\nu_{YXi}^2] = p_{YX}(1 - p_{YX})N_Y$. By these arguments, it follows that $\langle \nu_{YXi} \rangle$ contributes to a constant random parameter dependent on the particular network configuration, which is manifestation of the quenched randomness introduced by fixing the given configuration. The variance of such a term between the different configurations is approximately $[\langle \nu_{YXi} \rangle^2] = \frac{p_{YX}(1-p_{YX})N_Y}{N_X} \approx \widetilde{p}_{YX} N_Y / N_X$, where $\widetilde{p}_{YX} = p_{YX}$ for the sparse connectivity $p_{YX} \ll 1$ and $\widetilde{p}_{YX} = 0$ in the limit of strong connectivity $p \sim 1$. Note that the division by N_X comes from the fact that the variance of a sum of independent random variables is equal to the sum of variances of the given variables. The terms $\langle \nu_{YXi} \nu_{ZXi} \rangle$ may be treated in a similar fashion, though one has to distinguish between the cases $Y = Z$ and $Y \neq Z$. If $Y = Z$, one may clearly use the estimate $[\langle \nu_{YXi}^2 \rangle] = p_{YX}(1 - p_{YX})N_Y \approx p_{YX} N_Y$, while if $Y \neq Z$, the terms $\langle \nu_{YXi} \nu_{ZXi} \rangle$ contribute to a random constant parameter, whose variance over the ensemble of different network configurations may be evaluated as $[\langle \nu_{YXi} \nu_{ZXi} \rangle^2] = p_{YX} N_Y p_{ZX} N_Z / N_X$.

The terms containing σ_{YXi} may heuristically be approached as follows. From the definition, it follows that $\sigma_{YXi} = \sum_j a_{YXji} \rho_{Yj} = \sum_{j \in \mathcal{C}_{YXi}} \rho_{Yj}$, i.e., the sum runs over the subassembly of neurons from cluster Y which project to neuron i from cluster X . By construction, such subassembly contains a small number of units $p_{YX} N_Y$, if the connectivity between clusters Y and X is sparse ($p_{YX} \ll 1$). In the limit of strong connectivity ($p_{YX} \sim 1$), one has the sum $\sigma_{YXi} \approx 0$, because the departure from the limit case $p_{YX} = 1$ due to the subset of neurons that do not project from Y to Xi is small. Though one cannot say *a priori* anything regarding the distribution of ρ_{Yj} , in the first approximation, one may consider them as a set of normally distributed random variables of zero mean and unit variance. This enables us to treat σ_{YXi} as a set of normally distributed random variables of zero mean and variance $p_{YX} N_Y$. Also note that the correlation $\sigma_{YXk} \sigma_{YXi} = \sum_{i,j} a_{YXik} a_{YXjl} = p_{YX}^2 N_Y$, which is small due to smallness of p_{YX} , such that all the terms σ_{YXi} may be taken as uncorrelated.

The above arguments imply that $\langle \sigma_{YXi} \rangle$ may be evaluated as effective noisy terms of zero mean and variance $[\langle \sigma_{YXi} \rangle^2] = (1 - \widetilde{p}_{YX}) N_Y / N_X$. By the above line of arguments, it may explicitly be shown that the variables σ_{YXi}^2 can effectively be

treated as random variables whose mean and variance satisfy $[\sigma_{YXi}^2] = p_{YX}N_Y$ and $[\sigma_{YXi}^4] - [\sigma_{YXi}^2]^2 = 2p_{YX}^2N_Y^2$, respectively.

B. Equations of the mean-field model

The results from Subsection II A enable us to systematically evaluate the contributions from all the terms on the r.h.s. of (6) and (7). Focussing on (6) first, one finds that the three associated terms give rise to finite-size effects of different nature. In particular, the first term contains an effective random parameter associated to the given network configuration and may be written as $\frac{1}{N}K_{YX}R_Y\sqrt{p_{YX}N_Y/N_X}\gamma_1$, where γ_1 is a $\mathcal{N}(0, 1)$ variable. The latter should not be confound with noise, as γ_1 can be treated as a random parameter. The second element from the r.h.s. of (6) contributes to pseudo-noise of the order $\mathcal{O}(1/N)$, which is given by $\frac{1}{N}K_{YX}\sqrt{S_Y}\sqrt{p_{YX}N_Y/N_X}\gamma_2(t)$. One refers to it as pseudo-noise because it fluctuates randomly in time, but does not derive from the actual microscopic noise. The third term on the r.h.s. of (6) presents the sum of local external noises, which gives rise to a genuine macroscopic noise $\sqrt{2B_X/N_X}\zeta_X(t)$.

As far as $\langle \Gamma_{2X} \rangle$ is concerned, the terms containing $\langle \nu_{YXi}\nu_{ZXi} \rangle$ and $\langle \sigma_{YXi}\sigma_{ZXi} \rangle$ for $Y=Z$ together provide the $\mathcal{O}(1/N)$ deterministic finite-size effect of the form $\frac{1}{N}K_{YX}^2p_{YX}n_Y(R_Y^2 + S_Y)$. The remaining contribution from such terms for $Y=Z$ and $Y \neq Z$ amounts to random constant parameters and pseudo-noises, respectively, whose intensity is of the order $\mathcal{O}(N^{-3/2})$ and as such can be neglected. As an illustration, we state that the terms involving $\langle \nu_{YXi}\nu_{ZXi} \rangle$ for $Y \neq Z$ may be evaluated as $\frac{1}{N^2}K_{YX}K_{ZX}R_YR_Z\sqrt{p_{YX}p_{ZX}N_YN_Z/N_X}$, which is indeed $\mathcal{O}(N^{-3/2})$. Finally, averaging over all the terms at the r.h.s. of (7) containing the genuine noises $\eta_{Xi}(t)$ at the macroscopic level provides stochastic effects of the order $\mathcal{O}(1/N^2)$, which can also be neglected within our mean-field model.

Collecting all the results stated so far, one arrives at the following equation for the dynamics of the cluster mean-rate:

$$\begin{aligned} \frac{dR_X}{dt} = & -\lambda_X R_X + H_{0X} + 2B_X H_{2X} \\ & + H_{2X} \sum_Y K_{YX}^2 p_{YX} n_Y (R_Y^2 + S_Y) / N \\ & + \sqrt{\Psi_X} \beta(t) + \sqrt{\Omega_X} \eta, \end{aligned} \quad (8)$$

where the ‘‘macroscopic’’ noise is of intensity $\Psi_X = \frac{1}{N}(2D_X + 2B_X H_{1X}^2) + \frac{1}{N} H_{1X}^2 \sum_Y K_{YX}^2 p_{YX} \frac{N_Y}{N_X} S_Y$, and the associated random variable $\beta(t)$ is Gaussian distributed. The macroscopic noise is made up of three terms which may be interpreted as follows. The two terms in the first bracket represent the contribution from the local intrinsic and external noise translated to macroscopic level, whereby the latter is manifested as multiplicative, rather than the additive noise. The third term is of different character and essentially reflects the impact of local fluctuations in the input provided to each neuron within the cluster. Apart from this, Eq. (8) also contains a random term where η is just a constant random number $\mathcal{N}(0, 1)$, whereas the associated intensity is $\Omega_X = \frac{1}{N} H_{1X}^2 \sum_Y K_{YX}^2 p_{YX} \frac{N_Y}{N_X} R_Y^2$. Note that the latter factor derives

from the topological ‘‘uncertainty’’ effect related to quenched randomness, in a sense that each particular network realization is characterized by distinct deviations from the average connectivity degree.

Starting from the definition and applying the Itô derivative, one may use analogous methods to obtain the final equation for the variance S_X . We omit the details of the lengthy calculation, but just state that here we also neglect the deterministic finite-size correction of the order of $\mathcal{O}(1/N)$, as well as all the noisy terms and the terms related to uncertainty parameter derived from the particular network realization. The final equation for the variance then becomes

$$\frac{dS_X}{dt} = -2\lambda_X S_X + 2B_X H_{1X}^2 + 2D_X. \quad (9)$$

Equations (8) and (9) make up the second-order stochastic mean-field model describing the collective activity of each cluster within the network. To complete the model, it is necessary to specify the gain function H . In general, the gain function should meet the requirements that it is zero for sufficiently small input and that it saturates for large enough input, whereas for intermediate input values, H should just be smooth and monotonous. For convenience of analytical study,^{30,35} we adopt the following form of H :

$$H(Q) = \begin{cases} 0, & Q \leq 0, \\ 3Q^2 - 2Q^3, & 0 < Q < 1, \\ 1, & Q \geq 1. \end{cases} \quad (10)$$

III. ANALYSIS OF THE MEAN-FIELD MODEL AND SWITCHING DYNAMICS

In order to demonstrate the facilitatory role of clustering on switching dynamics more explicitly, we first investigate how the switching emerges in case of statistically homogeneous random network and then draw comparison to scenario the involving clustered network topology. In both instances, the analysis of the mean-field model in the thermodynamic limit $N \rightarrow \infty$ is used to gain qualitative insight into the parameter domains supporting coexistence of different stationary states. The latter is a necessary ingredient for the onset of slow rate fluctuations, which emerge due to the finite-size effect. It will be demonstrated that the switching dynamics in clustered and non-clustered networks are based on different mechanisms, which we relate to the finding that clustering promotes network multistability.

A. Slow rate fluctuations in a non-clustered network

Let us first consider the deterministic dynamics of the non-clustered network with uniform coupling strengths. Given that this case has been analyzed in detail in our previous papers,^{30,35} here we provide only a brief summary of the main results.

The network behavior is described by the deterministic part of the system Eqs. (8) and (9), whereby (4) implies that the average input to each neuron amounts to $U = I + KpR = I + \alpha R$, with $\alpha = Kp$ being the connectivity parameter. Note that S generally affects the R dynamics only via $\mathcal{O}(1/N)$

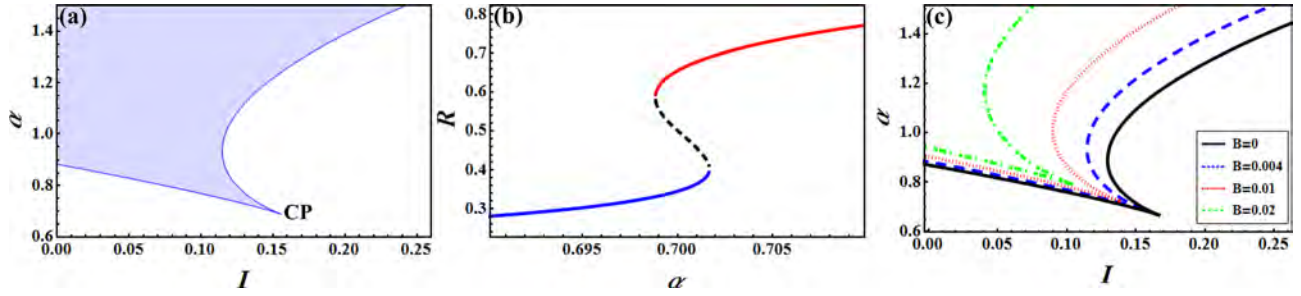


FIG. 1. Analysis of the mean-field model of a non-clustered random network in the thermodynamic limit $N \rightarrow \infty$. (a) Bistability domain (highlighted region) in the $(I - \alpha)$ plane is bounded by two branches of saddle-node bifurcations. The latter meets at the cusp point CP, located at (I_p, α_p) , where the pitchfork bifurcation occurs. External noise is set to $B = 0.004$, whereas $D = 0.02$. (b) $R(\alpha)$ dependence within the bistability tongue ($I = 0.15, B = 0.004$) shows coexistence between the UP and the DOWN state. (c) Shift of bistability domain for increasing $B \in \{0, 0.004, 0.01, 0.02\}$.

terms, which contribute to the small deterministic correction term and the macroscopic noise. Thus, in the thermodynamic limit, one may neglect the S evolution and replace it with the corresponding stationary value $S_0 = (B_\chi H_1^2 + D)/\lambda$. For simplicity, we adopt $\lambda = 1$ in the remainder of the paper. In order to analyze the stability of (8) in the limit $N \rightarrow \infty$, it is convenient to rewrite it in terms of the average input U as^{30,35}

$$\frac{dU}{dt} = -2\alpha U^3 + 3\alpha U^2 - 12\alpha B U - U + 6\alpha B + I. \quad (11)$$

Equation (11) always admits at least one stable stationary state. For the given external noise B , the onset of bistable regime is associated to the pitchfork bifurcation that occurs at $\alpha_p = 2/(3(1 - 8B))$ and $I_p = (1 - \alpha_p)/2$. From this cusp point emanate two branches of saddle-node bifurcations, which outline the bistability “tongue” where the UP and the DOWN states characterized by the high and low mean-rates coexist, cf. Fig. 1(a). In particular, the upper curve corresponds to creation of the UP state, whereas the lower curve coincides with annihilation of the DOWN state. Within the coexistence region, the two stable states are separated by the unstable state, cf. Fig. 1(b), whereby the level of the unstable state decreases with α . This confines the attraction basin of the DOWN state, facilitating the prevalence of the UP state at higher connectivity. Figure 1(c) further shows that for increasing B , the bistability domain gets shifted toward larger α . Note that the change of α is achieved by increasing the coupling strength K while the connectedness probability $p = 0.2$ is kept fixed to conform to the case of sparse random network, which maintains certain biological plausibility.

The mechanism behind switching dynamics in the non-clustered network may be explained by analyzing the finite-size effect and is reminiscent of the noise-driven motion of a

particle in a double-well potential. The analogy lies in the fact that the macroscopic noise, as the finite-size effect, allows for the network mean-rate to jump between the minima of the potential, which correspond to the two stationary levels of the deterministic part of the mean-field model, see the example of $R(t)$ series in Fig. 2(a). Replacing S by its stationary value, Eq. (8) for the stochastic dynamics of the mean-rate may be written in term of U as

$$\frac{dU}{dt} = -\frac{dV}{dU} + \sqrt{\Psi}\xi, \quad (12)$$

where V presents the potential $V(U) = \alpha U^4/2 - \alpha U^3 + (6\alpha B + 1/2)U^2 - (6\alpha B + I)U + \mathcal{O}(1/N)$, whereas the macroscopic noise amounts to $\Psi = \alpha^2(2 + \alpha^2)[36B U^2(1 - U)^2 + D]/N$. In the vicinity of the pitchfork bifurcation, V indeed has the shape of a double-well potential, as illustrated in Fig. 2(b).

The described switching mechanism is generic, in a sense that one expects to observe it close to bifurcation inducing the bistability, but is not robust, given that the physically meaningful switching rates are obtained in the sufficiently small parameter domain about the bifurcation value. Beyond this area, the potential barrier becomes too high for the noise to overcome it, making the switching events extremely unlikely.

In principle, the macroscopic noise $\Psi(U)$ is multiplicative, which makes finding the analytical expression for the underlying transition rates extremely difficult. Nevertheless, in a first approximation, the setup may be reduced to the classical Kramers problem⁴³ if Ψ is replaced by its mean Ψ_m obtained by averaging over the U values between the two potential wells. Figure 3(a) illustrates that Ψ_m may be considered representative for the whole range of $\Psi(U)$ values,³⁰ especially given that the macroscopic noise is well bounded

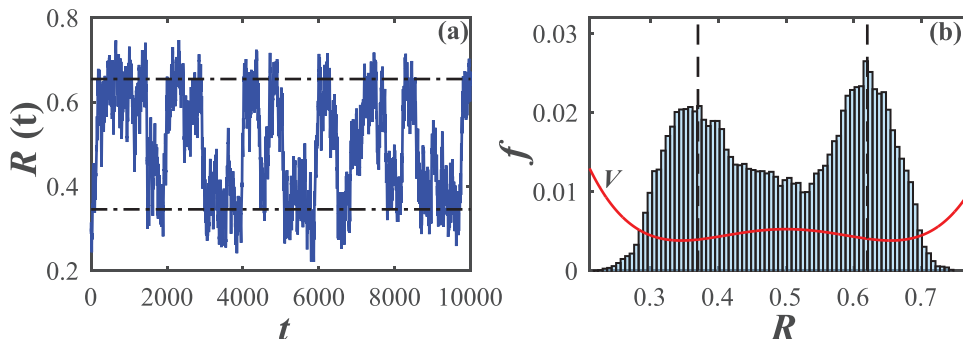


FIG. 2. Slow rate fluctuations illustrated by the $R(t)$ series in (a) and the associated stationary probability distribution $f(R)$ in (b). The results are obtained numerically for $I = 0.15, \alpha = 0.7, B = 0.004, D = 0.02$ and the network size $N = 400$. The dashed-dotted lines in (a) indicate the UP and DOWN levels of the corresponding mean-field model in the thermodynamic limit. The solid line in (b) presents the double-well potential V , cf. Eq. (12).

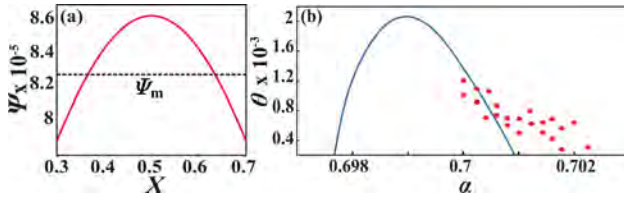


FIG. 3. (a) Macroscopic noise Ψ as a function of the mean-input X . The dotted line indicates the average Ψ_m over the relevant X range. (b) The solid line shows $\theta(\alpha)$ dependence obtained for the mean-field model via the Kramers formula (13). Dots denote the switching rates obtained numerically for $I = 0.15$, $B = 0.004$, $D = 0.02$, and $N = 400$.

within the relevant U interval. Within this framework, the first passage time between the two wells can be determined via the Kramers formula^{44–46}

$$T_{U_{\pm} \rightarrow U_{\pm}} \approx \frac{\pi}{\sqrt{|V''(U_{max})| |V''(U_{\pm})|}} \exp \left[\frac{V(U_{max}) - V(U_{\pm})}{\Psi_m} \right], \quad (13)$$

where U_{\pm} refer to the two minima of the double-well potential, whereas U_{max} denotes the location of its maximum. The total transition rate is then given by $\theta = 1/(T_{U_{+} \rightarrow U_{-}} + T_{U_{-} \rightarrow U_{+}})$. For α values in vicinity of the pitchfork bifurcation, the last expression may be used to compare with the numerical findings, cf. Fig. 3(b). One finds qualitative matching of the prediction derived from the mean-field model and the simulation within two aspects: (i) the region where $\theta(\alpha)$ is positive corresponds well to the region where the exact system exhibits slow rate fluctuations, and (ii) the order of the predicted θ values is the same as the one obtained from simulations.

B. Switching dynamics in clustered networks

In Subsection III A, we have shown that switching in homogeneous random networks is confined to the parameter domain in close vicinity of the pitchfork bifurcation. The main goal here is to demonstrate that switching in clustered networks is based on the paradigm that clustering promotes networks multistability. The outcome is that the switching phenomenon gains on robustness, in a sense that it can be found for parameter regions where it cannot be observed in statistically homogeneous random networks.

We shall show that sufficiently strong clustering supports multistability by giving rise to network states which do not exist in the non-clustered case. The increased number of network levels derives from the states with broken symmetry, where *subsets of clusters* occupy different levels, lying either in the UP or the DOWN state. By analyzing the mean-field model in the thermodynamic limit, we find that such multistability can be achieved only by varying the connectivity features of the network (topological heterogeneity), rather than by introducing the parameter heterogeneity over the subsets of network clusters. With increased multistability, the stochastic terms contributing to finite-size effect may cause the network to cross to another level just by inducing the switching event within a single cluster. The slow rate oscillations are then naturally supported by the fact that the

impact of the finite-size effect is more pronounced for individual clusters than for the entire network.

Though the system Eqs. (8) and (9) are quite general in a sense that they may be applied to a network comprising an arbitrary number of clusters of arbitrary sizes, for simplicity, we address here the case where the network consists of m equal clusters of size $N_c = N/m$. Clustering algorithm consists in rearranging the links from the homogeneous random network, such that the average connectedness probability $p = 0.2$ is preserved. We introduce additional clustering parameter g to characterize topological heterogeneity, cf. Table II for the summary of notation relevant for Sec. III B. Parameter g presents the ratio between the intra-cluster and cross-cluster connectivity, α_{in} and α_{out} , respectively, such that $\alpha_{in} = g\alpha_{out}$ with $g > 1$. Larger g implies stronger clustering, whereby the limiting case $g = 1$ describes the non-clustered network, whereas the case $g \rightarrow \infty$ corresponds to the network of disconnected clusters. One may show that α_{in} and α_{out} can be expressed in terms of the connectivity of the original homogeneous network α as

$$\alpha_{in} = \frac{gm}{m-1+g}\alpha, \quad \alpha_{out} = \frac{m}{m-1+g}\alpha. \quad (14)$$

This allows us to compare the relevant parameter domains between the homogeneous and the clustered networks.

Let us now focus on the scenario where l clusters occupy state R_a , and $m-l$ clusters lie at R_b . While the homogeneous state has the permutation symmetry Σ_m with respect to exchange of all the cluster indices, the solutions we consider now have a reduced symmetry $\Sigma_l \otimes \Sigma_{m-l}$. One may analyze the stability and bifurcations of the corresponding mean-field model in the thermodynamic limit $N \rightarrow \infty$, cf. (11). The model is given by

$$\begin{aligned} \frac{dR_a}{dt} &= -2U_a^3(R_a, R_b) + 3U_a^2(R_a, R_b) \\ &\quad + 6B(1 - 2U_a(R_a, R_b)) - R_a \\ \frac{dR_b}{dt} &= -2U_b^3(R_a, R_b) + 3U_b^2(R_a, R_b) \\ &\quad + 6B(1 - 2U_b(R_a, R_b)) - R_b, \end{aligned} \quad (15)$$

where the average input to the two groups of clusters reads

$$\begin{aligned} U_a(R_a, R_b) &= I + \frac{\alpha}{m-1+g} [(g+l-1)R_a + (m-l)R_b], \\ U_b(R_a, R_b) &= I + \frac{\alpha}{m-1+g} [lR_a + (g+m-l-1)R_b]. \end{aligned} \quad (16)$$

As for the non-clustered network, the variances S_a and S_b can be substituted by their respective stationary values

TABLE II. Summary of notation in Sec. III B.

$\alpha \equiv Kp$	Connectivity parameter of the homogeneous network
m	Total number of clusters
α_{in}	Intra-cluster connectivity
α_{out}	Inter-cluster connectivity
$g \equiv \alpha_{in}/\alpha_{out}$	Clustering parameter
$\delta \equiv 1/(g-1)$	Inverse clustering parameter

$S_i^* = (B_x H_i^2 + D)/\lambda$, with $i \in \{a, b\}$. Using (16), one may express R_a and R_b in terms of U_a and U_b via

$$\begin{aligned} R_a &= \frac{U_a - I}{\alpha} + \frac{m - l}{\alpha(g - 1)}(U_a - U_b), \\ R_b &= \frac{U_b - I}{\alpha} + \frac{l}{\alpha(g - 1)}(U_b - U_a). \end{aligned} \tag{17}$$

Inserting the latter expressions into (15), we obtain that the steady states of the mean-field model satisfy

$$\begin{aligned} I - f(U_a) + \delta(m - l)(U_b - U_a) &= 0, \\ I - f(U_b) + \delta l(U_b - U_a) &= 0. \end{aligned} \tag{18}$$

In (18), $f(U_i)$ is given by $f(U_i) = 2\alpha U_i^3 - 3\alpha U_i^2 + (1 + 12B\alpha)U_i - 6B\alpha$, which implies that the terms $I - f(U_i)$ have exactly the same form as the r.h.s. of (11) for the homogeneous random network. For convenience, we have introduced the inverse clustering parameter $\delta = (g - 1)^{-1}$, whereby the limit $\delta \rightarrow \infty$ corresponds to the non-clustered network, while the case $\delta \rightarrow 0$ coincides with ultimate clustering, i.e., the scenario where the network comprised effectively independent clusters. The system (18) naturally possesses the symmetry with respect to exchanging l and $m - l$ together with U_a and U_b ($l \leftrightarrow m - l, U_a \leftrightarrow U_b$).

Our interest lies with the inhomogeneous states where the respective stationary levels of the two groups of clusters are different, $R_a^* \neq R_b^*$. The analysis of (18) reveals that apart from the homogeneous states described in Sec. III A, one may indeed find one or two coexisting inhomogeneous states depending on the inverse clustering parameter δ under fixed (m, l, I, B) . While the system (15) and the subsequent Eqs. (16)–(18) can describe a network of arbitrary number of equal clusters, the analysis below is focused on the network of $m = 5$ clusters. This is chosen as a minimal paradigmatic example, convenient since due to symmetry, the cases $l = 1$ and $l = 2$ exhaust all the possible inhomogeneous solutions.

Onset of inhomogeneous states is investigated in detail by constructing the $\delta - I$ bifurcation diagrams (see Fig. 4). The left and the right plots refer to cases $l = 1$ and $l = 2$, respectively, with the remaining network parameters fixed to $\alpha = 0.8, B = 0.004$. For δ values less than the level indicated by the red dotted line in Fig. 4(b), there exists an I interval where two inhomogeneous solutions can coexist, whereas above the given δ , one can find only monostable inhomogeneous states.

Note that the region of coexistence between the two inhomogeneous states admits a total of 9 solutions of the mean-field model (15), cf. the notation in Fig. 4(b), whereas in the two domains with a single genuine clustered regime, one finds a total of 7 solutions of the mean-field model. Most of the curves indicated in Fig. 4 correspond to saddle-node bifurcations. In particular, the transitions from regions with 1 to regions with 3 solutions and *vice versa* coincide with creation or annihilation of the homogeneous states already described in Sec. III A. Also, the boundary between regions with 5 and 7 solutions is given by the branches of saddle-node bifurcations which meet at the cusp point where the pitchfork bifurcation occurs. Exceptions to this paradigm are the transitions involving regions with 3 and 5 solutions of the mean-field model. The latter present fold bifurcations of the inhomogeneous states within the symmetry subgroup $\Sigma_l \otimes \Sigma_{m-l}$, whereby the emanating branches correspond to an unstable fixed point and a saddle point.

A more detailed picture of the inhomogeneous states and their stability domains relative to homogeneous states may be obtained by analyzing the corresponding $R(I)$ bifurcation diagrams for fixed $(m, l, B, \delta, \alpha)$. The plots in Fig. 5 are provided for (δ, I) values supporting the coexistence of two inhomogeneous states. The top and the bottom panels refer to cases $l = 1$ and $l = 2$, respectively. In each panel, the left and the middle plots indicate the states occupied by the groups of l and $m - l$ clusters, respectively, whereas the right plot concerns the entire network (left and middle plots superimposed).

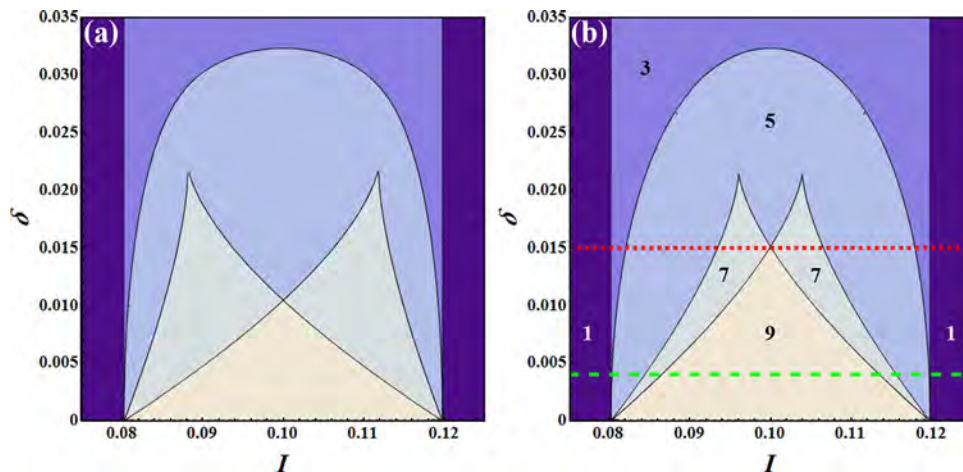


FIG. 4. Bifurcation diagrams $\delta(I)$ for the inhomogeneous solutions of the mean-field model (15). (a) corresponds to case $l = 1$, whereas (b) refers to case $l = 2$. In (b), the total number of solutions obtained for the mean-field model within the different parameter domains is indicated. The regions with 1 and 3 solutions admit only homogeneous states, while the region with 5 solutions contains unstable inhomogeneous states. The regions with 7 and 9 solutions facilitate monostable inhomogeneous states and coexistence between the two inhomogeneous states, respectively. The bistability between inhomogeneous states arises only for sufficiently strong clustering below the red dotted line, cf. the bifurcation diagrams in Fig. 5 and Fig. 6 obtained for the δ level just above the red line and the δ value indicated by the green dashed line, respectively. The remaining network parameters are $m = 5, B = 0.004, \alpha = 0.8$.

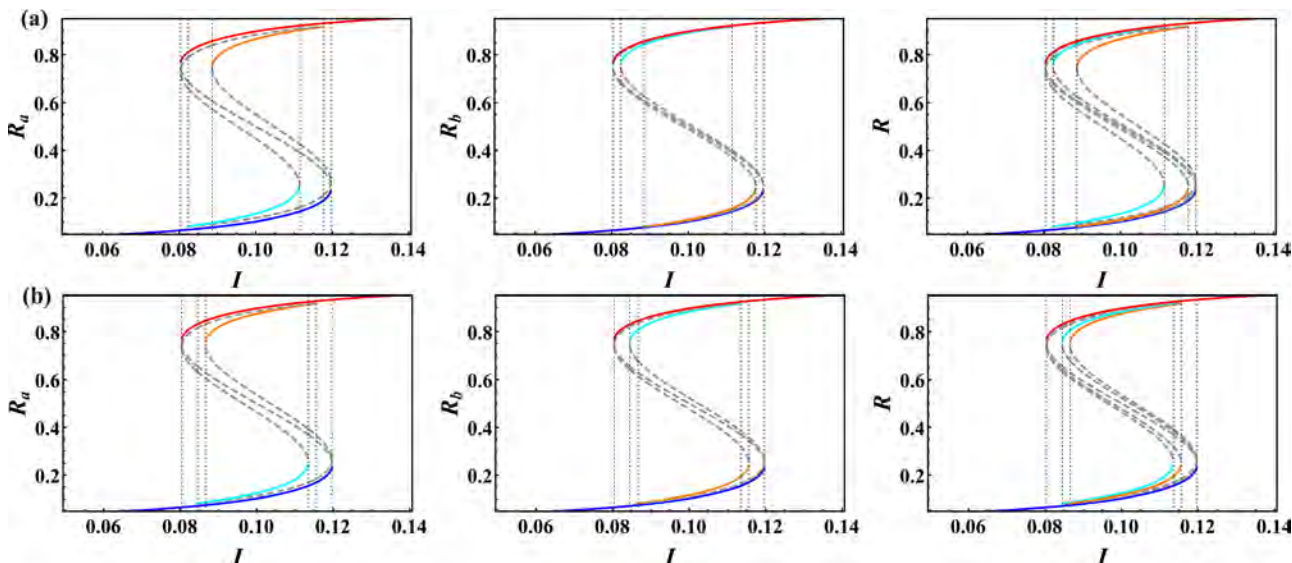


FIG. 5. Bifurcation diagrams $R(I)$ for strong clustering $\delta = 0.004$, cf. the level denoted by the green dashed line in Fig. 4(b). Panels (a) and (b) correspond to cases $l = 1$ and $l = 2$, respectively. The left and middle columns refer to states of particular groups of clusters R_a and R_b . The latter are superimposed in the right column to indicate the possible network states. The stable solutions are given by the solid lines, and the unstable branches are shown by the gray dashed lines. The R_a and R_b states corresponding to the same solution are presented by the same color. The remaining system parameters are $m = 5$, $B = 0.004$, $\alpha = 0.8$.

One clearly distinguishes between the regions where only one inhomogeneous solution is stable (either l clusters in the DOWN state and $m - l$ in the UP state or *vice versa*) and the central I region where two inhomogeneous solutions coexist. For instance, in the bottom panel, coexistence of two inhomogeneous states is found for $I \in (0.0866, 0.1135)$, whereas the regions with l clusters UP or DOWN as the only inhomogeneous solutions are given by $I \in (0.0845, 0.0866)$ and $I \in (0.1135, 0.1156)$. The presentation scheme is such that the solid (dashed) lines indicate the stable (unstable) branches of solutions. Note that the top-most (red solid line) and the bottom-most curves (blue solid line) in both panels

indicate the homogeneous states. In case of inhomogeneous states, the color coding is such that R_a and R_b corresponding to the same solution are assigned with the same color. As expected, the stability domains of the inhomogeneous states are smaller than the regions supporting the homogeneous states.

In Fig. 6, the $R(I)$ bifurcation diagrams for lower clustering (larger δ) are shown, which no longer admits bistability between the inhomogeneous states. The top and the bottom panels again refer to cases $l = 1$ and $l = 2$, respectively. From both panels, one learns that the two I intervals, where single inhomogeneous solutions exist, are separated by the I interval

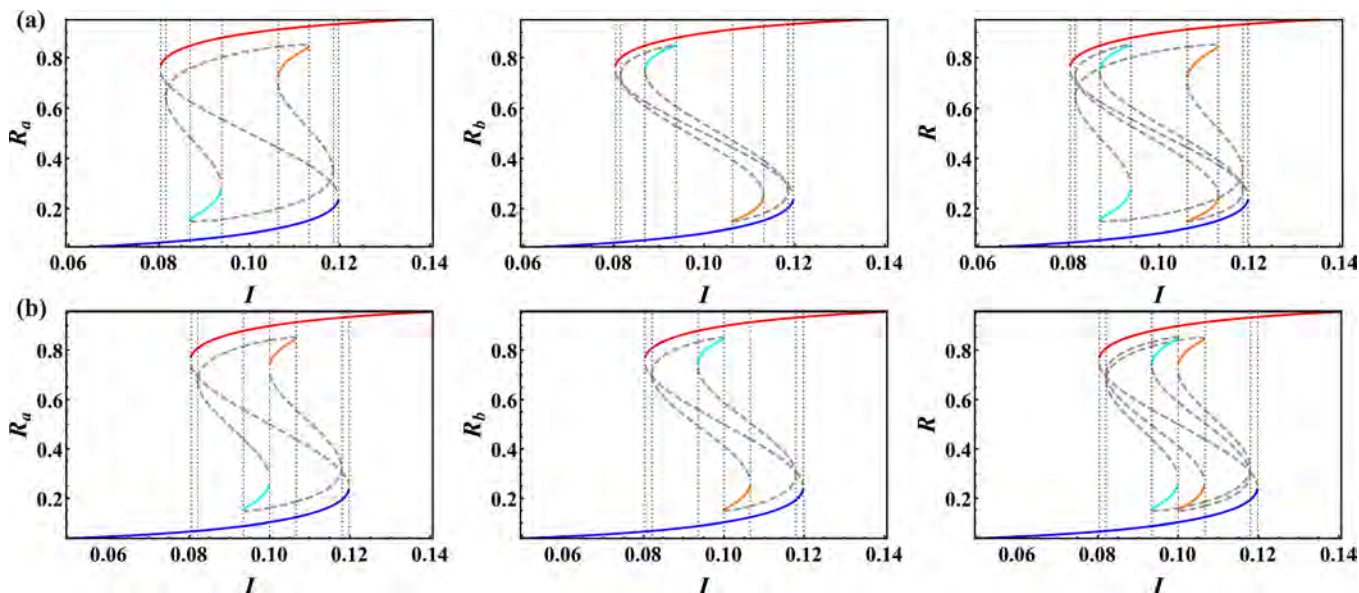


FIG. 6. Bifurcation diagrams $R(I)$ in case of weak clustering $\delta = 0.0151$, the value just above the level indicated by the red dotted line in Fig. 4(b). The top and bottom panels correspond to cases $l = 1$ and $l = 2$, respectively. The presentation style is the same as in Fig. 5. The remaining network parameters are $m = 5$, $B = 0.004$, $\alpha = 0.8$.

where only the two homogeneous states are available. A more detailed view of the basins of attraction of the particular states can be obtained by examining the vector fields for the relevant I values, cf. Fig. 7.

To gain a more general understanding of the multistability of the mean-field model (15), one should note that it is affected by two types of parameters, namely (i) the ones associated to homogeneous network and (ii) those characterizing the clustering. System (18) implies that the case of ultimate clustering ($\delta = 0$) leads to the same type of dynamics as that of a homogeneous network. Consequently, the area of bistability of the homogeneous network corresponds to the maximal multistability of the clustered network: each cluster may either be in the UP or the DOWN state, which yields $m + 1$ different stable solutions in total. Bistability of the homogeneous network has been addressed in Fig. 1 and has been examined in greater detail in our earlier papers.^{30,35}

The main novelty here concerns the impact of the clustering degree and its interplay with α, B , and m . As already indicated in Fig. 4, reduction of the clustering degree, i.e., increase of δ , leads to gradual extinction of the inhomogeneous states via saddle-node bifurcations. Nevertheless, we have established that the stronger average network connectivity α allows for the inhomogeneous states to occur at lower clustering, as corroborated by the shift of the relevant δ region to higher values when α is increased under all the other parameters fixed (not shown). Also, one finds that the δ region admitting inhomogeneous states reduces under increasing noise B .

In order to investigate the effect of the number of clusters m , one may introduce the ratio $\mu = l/m$ and rewrite Eq. (18) as

$$\begin{aligned} I - f(U_a) + \delta m(1 - \mu)(U_b - U_a) &= 0, \\ I - f(U_b) + \delta m\mu(U_b - U_a) &= 0. \end{aligned} \quad (19)$$

It follows that for the given ration μ , the bifurcations in the system depend only on the product $m\delta$. The latter implies that the increase in the number of clusters m leads to the onset of the relevant bifurcations for smaller δ . In other words, the more clusters present in the network, the stronger clustering is required to support the same level of multistability.

The analysis on multistability of the clustered network derived from the mean-field model is qualitative in character, but allows one to classify all the network states and gain understanding of the mechanism behind the switching dynamics.

The qualitative character of the predictions is reflected in that the mean-field model becomes the least accurate in vicinity of bifurcations where fluctuations are most pronounced, such that the finite-size effect prevails. Nevertheless, via the mean-field approach, one is also able to compare the effect of certain system parameters on the dynamics of the homogeneous and the clustered network. In particular, we are interested in comparison with respect to parameters I and α . For the homogeneous network, one finds the bistability tongue, whereby the switching dynamics occurs in close vicinity of the cusp. Using the model (15), we have constructed analogous $\delta - I$ bifurcation diagrams for the clustered network with fixed α . Our goal is to apply these results to explicitly demonstrate that multistability promoted by the clustered topology plays the facilitatory role with respect to switching dynamics. This is easily understood intuitively, as additional multistability induced by clustering implies more network levels distributed less widely. Then, switching between different levels becomes more efficient because it may be achieved just by alternations within individual clusters, and the finite-size effect within the clusters is more pronounced given their smaller size compared to the whole network.

To illustrate the impact of clustering on the onset of slow rate oscillations, we consider an example where the system parameters B, I, α are fixed to $B = 0.01, I = 0.0513, \alpha = 0.9$, respectively. For the given B , the selected (α, I) values lie deep within the bistability tongue of the homogeneous random network, viz., far from the cusp point, cf. Figure 1(c). The corresponding time series of the network mean-rate $R_N(t)$ and the associated stationary probability distribution obtained for the *full* system Eq. (1) are shown in Fig. 8. The latter corroborates that indeed no switching can be observed for the given parameter set in case of the homogeneous network. Nevertheless, for the sufficiently large g (small δ), the clustered network exhibits strong switching dynamics for the same (I, α) values, see the results for the *full* system Eq. (1) in Fig. 9. In Fig. 9(a), the sequences from the mean-rate dynamics of individual clusters $R_i(t)$ and the network rate $R_N(t)$ are shown, whereas in panel (b), the corresponding probability distributions are provided. Note that the network parameters are selected from the domain supporting maximal multistability, i.e., the region where the mean-field model (15) admits 9 different solutions, allowing for the coexistence of two inhomogeneous states within the same $\Sigma_l \otimes \Sigma_{m-l}$ symmetry subgroup.

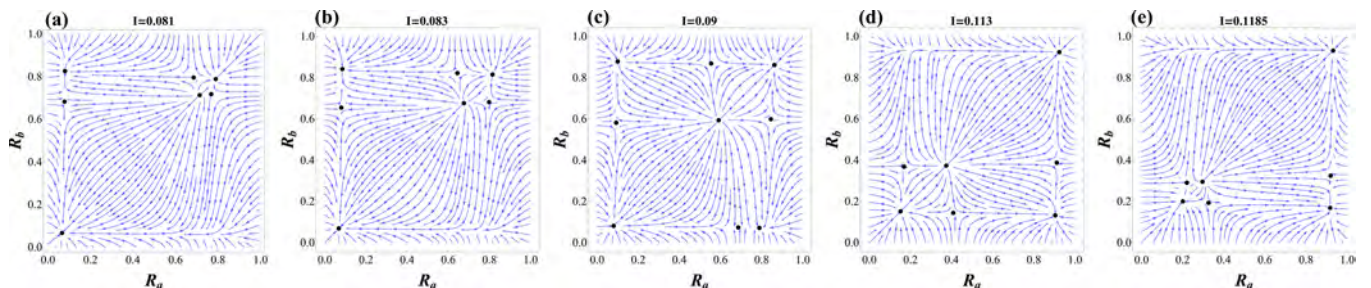


FIG. 7. Vector field plots indicating basins of attraction for the different types solutions of the mean-field model (15) in the (R_a, R_b) plane. The bias current I increases systematically from (a)-(e). The plots correspond to the example indicated in Fig. 5(b). The network parameters are $m = 5, B = 0.004, \delta = 0.004, \alpha = 0.8$.

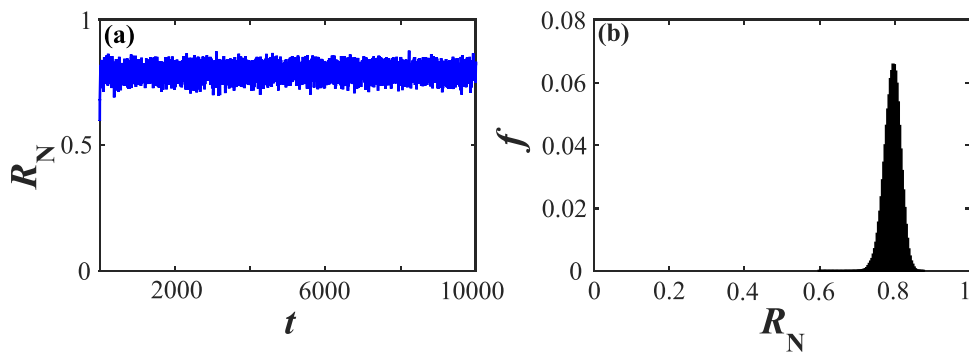


FIG. 8. Absence of switching dynamics for the *non-clustered* network beyond the vicinity of pitchfork bifurcation. In (a), the time trace of the network mean-rate $R_N(t)$ for the full system (1) is shown, whereas in (b), the corresponding stationary probability distribution $f(R)$ is provided. The network parameters are $\alpha = 0.9$, $I = 0.05$, $B = 0.01$, $N = 500$. Note that the selected (α, I) values lie within the $B = 0.01$ bistability tongue, but far from the cusp point, cf. Fig. 1(c).

The results in Figs. 8 and 9 indicate a good qualitative agreement between the dynamics of the full system and the effective model, in a sense that the analysis of the mean-field model can anticipate the parameter values where one may observe the switching dynamics in the full system. Naturally, the levels of the effective model obtained for the clustered network correspond to metastable states of the full system, whereby switching between them occurs due to the finite-size effects.

IV. CONCLUSION

In this paper, we have analyzed the interplay of clustered topology and different types of noise on the spontaneous activity of networks of rate-based neurons. Clustered topology appears to be biologically relevant,^{4,25,49} as the recent research on the microstructure of cortical networks has indicated that the small clusters of excitatory neurons are significantly over-represented.^{36,47} In real neural networks, the clusters may be important as functional units performing certain tasks⁴⁸ or may constitute processing units adapted to receiving a certain type of stimuli.^{50–52} We have demonstrated that clustering affects the collective dynamics of neural networks in a nontrivial fashion by promoting multistability such that spontaneous slow rate fluctuations gain on robustness.

From the theoretical perspective, our main contribution consists in derivation of the reduced system which describes the network activity in terms of interacting mean-field models representing each of the clusters. Typically, the reduced models address the two limit cases of a globally connected network^{32–34} or a network with the random sparse connectivity,^{30,35} such that the fluctuations of input between the units are small. The model presented here interpolates between these two scenarios, as the intra-cluster connectivity is strong, whereas the inter-cluster connectivity is weaker. We have identified three types of finite-size effects, including the small deterministic correction term, the macroscopic noise, and the topological uncertainty derived from the fact that each particular network realization features distinct deviations from the average connectivity degree. The macroscopic noise is a multiplicative one and incorporates three different sources of randomness, describing the impact of local neuronal noise on collective activity and the fluctuations in the input received by each of the units. Interestingly, the local intrinsic noise translates to additive macroscopic noise, whereas the microscopic external noise is reflected as multiplicative noise at the macroscopic level.

It has been demonstrated that the mean-field model can be used to qualitatively analyze the spontaneous activity of

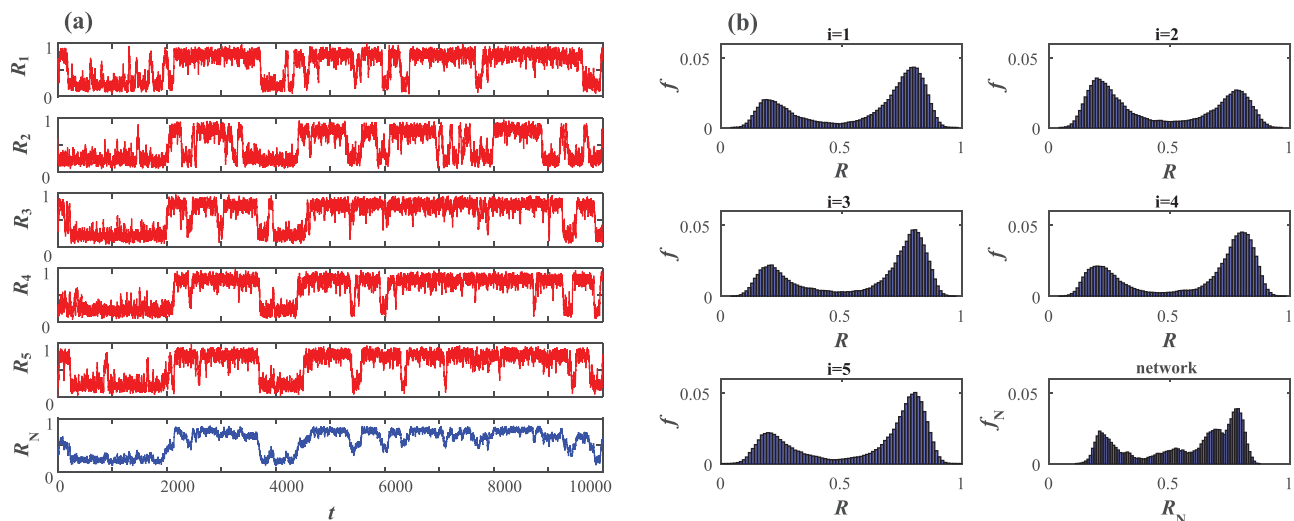


FIG. 9. Example of switching dynamics in the clustered network. Panel (a) shows the time traces of mean-rates of individual clusters $R_i(t)$, $i \in \{1, \dots, 5\}$ and the network $R_N(t)$ obtained by simulating the full system (1). In panel (b), the corresponding probability distributions $f(R)$ for the single clusters and the network are presented. The network parameters are $m = 5$, $B = 0.01$, $\alpha = 0.9$, $I = 0.0513$, $\delta = 0.01$, $N = 500$. The fact that clustering promotes multistability allows for the switching dynamics to occur in the much broader (I, α) domain than for the homogeneous random network, cf. Fig. 1(c) and the time series in Fig. 8.

the clustered network. The mechanism behind slow rate fluctuations has been explained by considering the stability and bifurcations of the mean-field model in the thermodynamic limit. The latter also allowed us to contrast the cases of the non-clustered and clustered network. In the non-clustered network, the crucial ingredient to slow rate fluctuations is that the network parameters lie close to pitchfork bifurcation. The evolution of the mean-rate may then locally be described by the paradigm of noise-driven motion of a particle in a double-well potential, so that its local minima coincide with the UP and DOWN states of the network. Such mechanism is *per se* generic, but lacks robustness, as it is confined to a small vicinity of the pitchfork bifurcation. The key effect of introducing clustering consists in the increased multistability of the network, facilitated by the onset and coexistence of states where different groups of clusters lie in the UP or the DOWN states. This promotes the switching dynamics, making it more efficient in a sense that alternation between the different network levels can be achieved just by changing the states of individual clusters rather than the whole network. Alternations within single clusters are naturally more likely since the finite-size effect associated to macroscopic noise is more pronounced. This way, the switching phenomenon gains on robustness, extending into the parameter domains where it cannot be observed for the non-clustered network.

The importance of clustered topology for macroscopic variability has earlier been indicated for the networks of spiking neurons with *balanced* excitatory-inhibitory input.^{4,24,25,53} However, with such local dynamics, slow fluctuations of the mean network activity cannot even be observed for a simple random network topology, which implies that clustering indeed plays the crucial role in inducing the switching behavior. Thus, our results on the rate-based neurons together with the previous work on spiking neurons suggest that promoting of slow rate fluctuations by clustered topology may indeed be a universal phenomenon independent on the particular model of local neuronal dynamics.

In view of the fact that the spontaneous activity of real neurons may indeed be described as a doubly stochastic process,^{54–56} combining the fluctuations on short and long timescales, the presented work has been aimed at providing theoretical tools for analysis of macroscopic variability in neural networks and its relation to microscopic dynamics and the network topology. We believe that the same method can be used to analyze the evoked activity of the network, examining the impact of clustering on the network's response to external stimulation. Also, our research so far has been confined to networks of excitatory neurons, but we believe that the same theoretical framework can readily be used to analyze the complex behavior of networks with both excitatory and inhibitory neurons. One expects that the presence of inhibitory subassembly should have a nontrivial impact both to spontaneous and evoked network activities.

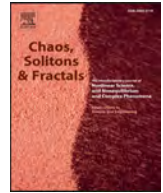
ACKNOWLEDGMENTS

This work was supported by the Ministry of Education, Science and Technological Development of Republic of Serbia

under Project No. 171017 and by the Russian Foundation for Basic Research under Project No. 17-02-00904.

- ¹A. Destexhe, M. Rudolph, and D. Paré, *Nat. Rev. Neurosci.* **4**, 739 (2003).
- ²M. R. Cohen and A. Kohn, *Nat. Neurosci.* **14**, 811 (2011).
- ³B. B. Averbeck, P. E. Latham, and A. Pouget, *Nat. Rev. Neurosci.* **7**, 358 (2006).
- ⁴A. Litwin-Kumar and B. Doiron, *Nat. Neurosci.* **15**, 1498 (2012).
- ⁵M. Smith and A. Kohn, *J. Neurosci.* **28**, 12591 (2008).
- ⁶G. Buzsáki, C. A. Anastassiou, and C. Koch, *Nat. Rev. Neurosci.* **13**, 407 (2012).
- ⁷G. Buzsáki, *Rhythms of the Brain* (Oxford University Press, Oxford, 2006).
- ⁸T. T. G. Hahn, J. M. McFarland, S. Berberich, B. Sakmann, and M. R. Mehta, *Nat. Neurosci.* **15**, 1531 (2012).
- ⁹A. Destexhe, D. Contreras, and M. Steriade, *J. Neurosci.* **19**, 4595 (1999); available at <http://www.jneurosci.org/content/19/11/4595>.
- ¹⁰C. C. H. Petersen, T. T. G. Hahn, M. Mehta, A. Grinvald, and B. Sakmann, *Proc. Natl. Acad. Sci. U. S. A.* **100**, 13638 (2003).
- ¹¹V. V. Vyazovskiy and K. D. Harris, *Nat. Rev. Neurosci.* **14**, 443 (2013).
- ¹²T. T. G. Hahn, B. Sakmann, and M. R. Mehta, *Nat. Neurosci.* **9**, 1359 (2006).
- ¹³G. Gigante, G. Deco, S. Marom, and P. Del Giudice, *PLoS Comput. Biol.* **11**, e1004547 (2015).
- ¹⁴R. Cossart, D. Aronov, and R. Yuste, *Nature* **423**, 283 (2003).
- ¹⁵R. L. Cowan and C. J. Wilson, *J. Neurophysiol.* **71**, 17 (1994).
- ¹⁶D. Millman, S. Mihalas, A. Kirkwood, and E. Niebur, *Nat. Phys.* **6**, 801 (2010).
- ¹⁷M. Steriade, D. A. McCormick, and T. J. Sejnowski, *Science* **262**, 679 (1993).
- ¹⁸J. Anderson *et al.*, *Nat. Neurosci.* **3**, 617 (2000).
- ¹⁹D. Ji and M. A. Wilson, *Nat. Neurosci.* **10**, 100 (2007).
- ²⁰Y. Isomura *et al.*, *Neuron* **52**, 871 (2006).
- ²¹M. Remondes and E. M. Schuman, *Nature* **431**, 699 (2004).
- ²²S. Diekelmann and J. Born, *Nat. Rev. Neurosci.* **11**, 114 (2010).
- ²³D. Miyamoto, *et al.*, *Science* **352**, 1315 (2016).
- ²⁴F. Lagzi and S. Rotter, *PLoS ONE* **10**, e0138947 (2015).
- ²⁵B. Doiron and A. Litwin-Kumar, *Front. Comput. Neurosci.* **8**, 56 (2014).
- ²⁶M. D. McDonnell and L. M. Ward, *PLoS One* **9**, e88254 (2014).
- ²⁷M. D. McDonnell and L. M. Ward, *Nat. Rev. Neurosci.* **12**, 415 (2011).
- ²⁸A. A. Faisal, L. P. J. Selen, and D. M. Wolpert, *Nat. Rev. Neurosci.* **9**, 292 (2008).
- ²⁹R. Moreno-Bote, J. Rinzel, and N. Rubin, *J. Neurophys.* **98**, 1125 (2007).
- ³⁰I. Franović and V. Klinshov, *Europhys. Lett.* **116**, 48002 (2016).
- ³¹L. Albantakis and G. Deco, *PLoS Comput. Biol.* **7**, e1002086 (2011).
- ³²B. Lindner, J. Garcia-Ojalvo, A. Neiman, and L. Schimansky-Geier, *Phys. Rep.* **392**, 321 (2004).
- ³³M. A. Zaks, X. Sailer, L. Schimansky-Geier, and A. B. Neiman, *Chaos* **15**, 026117 (2005).
- ³⁴I. Franović, K. Todorović, N. Vasović, and N. Burić, *Phys. Rev. E* **87**, 012922 (2013).
- ³⁵V. Klinshov and I. Franović, *Phys. Rev. E* **92**, 062813 (2015).
- ³⁶R. Perin, T. K. Berger, and H. Markram, *Proc. Natl. Acad. Sci. U. S. A.* **108**, 5419 (2011).
- ³⁷L. Zemanová, C. Zhou, and J. Kurths, *Physica D* **224**, 202 (2006).
- ³⁸W. Gerstner, W. M. Kistler, R. Naud, and L. Paninski, *Neuronal Dynamics: From Single Neurons to Networks and Models of Cognition* (Cambridge University Press, Cambridge, 2014).
- ³⁹H. Hasegawa, *Phys. Rev. E* **75**, 051904 (2007).
- ⁴⁰R. A. Anderson, S. Musallam, and B. Pesaran, *Curr. Opin. Neurobiol.* **14**, 720 (2004).
- ⁴¹I. Franović, K. Todorović, N. Vasović, and N. Burić, *Phys. Rev. Lett.* **108**, 094101 (2012).
- ⁴²A. N. Burkitt, *Biol. Cybern.* **95**, 1 (2006).
- ⁴³V. I. Mel'nikov, *Phys. Rep.* **209**, 1 (1991).
- ⁴⁴C. W. Gardiner, *Handbook of Stochastic Methods for Physics, Chemistry and the Natural Sciences* (Springer-Verlag, Berlin, 2004).
- ⁴⁵A. Bovier and F. den Hollander, *Metastability, a Potential-Theoretic Approach* (Springer International Publishing, Switzerland, 2015).
- ⁴⁶G. A. Pavliotis, *Stochastic Processes and Applications* (Springer, New York, 2014).
- ⁴⁷S. Song, P. Sjöström, M. Reigl, S. Nelson, and D. Chklovskii, *PLoS Biol.* **3**, e68 (2005).

- ⁴⁸L. Yassin, B. L. Benedetti, J. Jouhanneau, J. A. Wen *et al.*, *Neuron* **68**, 1043 (2010).
- ⁴⁹E. L. Lameu, C. A. Batista, A. M. Batista, K. Iarosz, R. L. Viana, S. R. Lopes, and J. Kurths, *Chaos* **22**, 043149 (2012).
- ⁵⁰S. B. Hofer, H. Ko, B. Pichler, J. Vogelstein, H. Ros *et al.*, *Nat. Neurosci.* **14**, 1045 (2011).
- ⁵¹H. Ko, S. B. Hofer, B. Pichler, K. A. Buchanan, P. J. Sjöström, and T. D. Mrsic-Flogel, *Nature* **473**, 87 (2011).
- ⁵²Y. Yoshimura, J. L. M. Dantzker, and E. M. Callaway, *Nature* **433**, 868 (2005).
- ⁵³G. Deco and E. Hugues, *PLoS Comput. Biol.* **8**, e1002395 (2012).
- ⁵⁴M. Churchland and L. Abbott, *Nat. Neurosci.* **15**, 1472 (2012).
- ⁵⁵A. Ponce-Alvarez, A. Thiele, T. D. Albright, G. R. Stoner, and G. Deco, *Proc. Natl. Acad. Sci. U. S. A.* **110**, 13162 (2013).
- ⁵⁶B. M. Yu, J. P. Cunningham, G. Santhanam, S. I. Ryu, K. V. Shenoy, and M. Sahani, *J. Neurophysiol.* **102**, 614 (2009).



Nonlinear dynamics behind the seismic cycle: One-dimensional phenomenological modeling



Srdan Kostić^{a,*}, Nebojša Vasović^b, Kristina Todorović^c, Igor Franović^d

^a Department for Scientific Research and Informatics, Institute for Development of Water Resources “Jaroslav Černi”, Jaroslava Černog 80, Belgrade 11226, Serbia

^b Department of Applied Mathematics, University of Belgrade Faculty of Mining and Geology, Serbia

^c Department of Physics and Mathematics, University of Belgrade Faculty of Pharmacy, Serbia

^d Scientific Computing Lab, University of Belgrade, Institute of Physics, Serbia

ARTICLE INFO

Article history:

Received 12 July 2017

Revised 27 November 2017

Accepted 30 November 2017

Keywords:

Spring-block model

Time delay

Rate-and-state dependent friction law

Seismic cycle

ABSTRACT

In present paper, authors examine the dynamics of a spring-slider model, considered as a phenomenological setup of a geological fault motion. Research is based on an assumption of delayed interaction between the two blocks, which is an idea that dates back to original Burridge–Knopoff model. In contrast to this first model, group of blocks on each side of transmission zone (with delayed interaction) is replaced by a single block. Results obtained indicate predominant impact of the introduced time delay, whose decrease leads to transition from steady state or aseismic creep to seismic regime, where each part of the seismic cycle (co-seismic, post-seismic and inter-seismic) could be recognized. In particular, for coupling strength of order 10^2 observed system exhibit inverse Andronov–Hopf bifurcation for very small value of time delay, $\tau \approx 0.01$, when long-period ($T = 12$) and high-amplitude oscillations occur. Further increase of time delay, of order 10^{-1} , induces an occurrence of a direct Andronov–Hopf bifurcation, with short-period ($T = 0.5$) oscillations of approximately ten times smaller amplitude. This reduction in time delay could be the consequence of the increase of temperature due to frictional heating, or due to decrease of pressure which follows the sudden movement along the fault. Analysis is conducted for the parameter values consistent with previous laboratory findings and geological observations relevant from the seismological viewpoint.

© 2017 Elsevier Ltd. All rights reserved.

1. Introduction

It is generally considered that process of accumulation and release of stress along the seismogenic faults always obeys the same rule: period with no movement along the fault (or with aseismic creep), when the stress is being accumulated, is followed by its sudden release, which could be further succeeded by the partial emission of the remained stored energy. These three periods, formally known as inter-seismic, co-seismic and post-seismic, respectively, constitute a single seismic cycle, which could be manifested at regular time intervals (for the strongest seismic events), or, more likely, occurrence of seismic events appears as a random process following Poisson distribution [1]. From the seismological viewpoint previous studies on properties of a seismic cycle resulted in sufficiently accurate characterization of each of the aforementioned periods. It is well known that inter-seismic deformation indicates depth of the zone that will eventually rupture seismically [2] and

the rate at which stress is accumulating along the fault zone [3]. The very end of this inter-seismic period could be marked by the occurrence of foreshocks as small partial releases of the stored potential energy before the main event. On the other hand, post-seismic deformation is usually driven by the preceding co-seismic stress change [3] and it could be as large as the fault slip during the main seismic event. Observed post-seismic behavior includes poroelastic deformation [4], frictional afterslip [5] and viscoelastic relaxation [6]. Similarly to the inter-seismic period, post-seismic part of the seismic cycle could be marked by the occurrence of aftershocks, as sudden releases of the remaining stored energy with significantly smaller magnitude in comparison to the main seismic event.

From the purely mechanical viewpoint, it is commonly considered that alternation of seismic cycles could be described by irregular stick-slip behavior [7]. For a simple frictional system, like commonly used spring-block model, the occurrence of stick-slip is due to a difference in static and kinetic friction, i.e. once the block starts to slide the friction drops suddenly to a lower level [8]. It is generally considered that surface roughness and normal

* Corresponding author.

E-mail address: srdjan.kostic@jcerni.co.rs (S. Kostić).

stress level play main role in “pushing” the spring-block model into stick-slip regime [9]. In present analysis, we analyze only the effect of friction on dynamics of spring-block model, by assuming some small constant value of normal stress which does not significantly affect the dynamics of the model. This could correspond to shallow parts of the Earth’s crust, or parts where horizontal stresses are much higher than vertical ones, due to significant effect of tectonics and surface erosion which reduced the thickness of the overlying layers.

Results of the pioneer work of Burridge and Knopoff [10] on dynamics of a simple spring-block model set a solid base for succeeding laboratory and theoretical research of seismogenic fault motion. The main outcome of their work is that distribution of displacement sums (i.e. earthquake magnitudes) follows two key macroseismological laws: Gutenberg–Richter and Omori–Utsu power law distribution. This finding enabled succeeding researchers a wide specter of additional analyzes, from the purely seismological [11,12], across the tribological [13,14] to purely dynamical [15]. These “dynamical” research are primarily in our focus, since they showed that for a certain parameter range, dynamics of spring-block models exhibit a regular transition between different dynamical regimes, with the eventual occurrence of chaotic dynamics [16,17]. Nevertheless, former studies did not treat the problem of seismic cycle *per se*, except from our previous paper, where we analyzed the impact of transient seismic wave on the dynamics of spring-block model, which resulted in transition between different seismic cycles [18]. One of the goals of the present analysis is to match different dynamical regimes of a spring-block model to appropriate phases of seismic cycles. In particular, the performed analysis should provide answers to the following questions: (1) what are the relevant parameter ranges for which the dynamic of the spring-block model enters the stick-slip regime, (2) what are the main dynamical features of that regime and (3) what does it mean for the real conditions in Earth’s crust. In that way, we will be able to reveal the main controlling mechanism behind the regularity of seismic cycle. One should note that, besides seismology, nonlinear models in general have been successively applied in other areas of natural sciences, as well [19–24].

Besides the analogy with the macroseismological laws, another important outcome of the original work of Burridge and Knopoff concerns a delayed transition of motion among two sets of blocks, indicating possible highly complex dynamical behavior. In particular, they showed that displacement among two boundary group of blocks in an one-dimensional chain is being transmitted with a certain time delay, whose order of unit corresponds to the viscosity of the middle set of blocks. Although this finding opened a lot of possibilities for investigating the cause and consequences of such a feature, it was not taken into consideration in succeeding studies. Effect of time delay was previously only implicitly introduced in friction term [25,26], and between the neighboring blocks in an one-dimensional chain of blocks with rate-dependent friction law [27]. In present paper, we analyze the transition between different seismic cycles considering the delayed interaction among the blocks with a rate- and state-dependent friction law. In contrast to our previous work, delayed interaction is assumed between the blocks exhibiting rate- and state-dependent friction law, which corresponds well to the laboratory observations of rock friction. Also, present analysis is conducted for the values of parameters which are either observed in reality or in laboratory conditions. We consider that this behavior is also relevant from the viewpoint of seismology, since different friction conditions along the fault (e.g. different thickness and physico-mechanical properties of fault gouge, impact of pore fluid, etc.) could cause a delayed transition of motion among different parts of the active seismogenic fault.

To sum up, the main idea of the present study is to determine the main dynamical mechanism by which the fault motion model reaches stick-slip like oscillations, as an appropriate dynamical state of a seismic fault motion which includes the inter-seismic, co-seismic and post-seismic regime. Thereby, dynamics of the relevant model is examined for the parameter values meaningful from the viewpoint of seismology, under the influence of the assumed delayed interaction of variable strength. Introduction of new influential parameters is motivated by the previous laboratory findings, with the aim of modeling the effect of changeable friction properties along the fault. The analysis is conducted using both analytical and numerical methods, former of which involved the application of local bifurcation analysis for the model with constant time delay whose results are corroborated numerically.

2. Model development

2.1. Original model of fault motion

Our numerical simulations of a spring-block model are based on the system of equations coupled with Dieterich–Ruina rate- and state-dependent friction law [16]:

$$\begin{aligned}\dot{\theta} &= -\left(\frac{v}{L}\right)\left(\theta + B \log\left(\frac{v}{v_0}\right)\right) \\ \dot{u} &= v - v_0 \\ \dot{v} &= \left(-\frac{1}{M}\right)\left(ku + \theta + A \log\left(\frac{v}{v_0}\right)\right)\end{aligned}\quad (1)$$

where parameter M is the mass of the block and the spring stiffness k corresponds to the linear elastic properties of the rock mass surrounding the fault [28]. According to Dieterich and Kilgore [29] the parameter L corresponds to the critical sliding distance necessary to replace the population of asperity contacts. The parameters A and B are empirical constants, which depend on material properties. Variables u and v represent displacement and velocity, while θ denotes the state variable describing the state of the rough surface along which blocks are moving [30]. Parameter v_0 represents the constant background velocity of the upper plate Fig. 1). For convenience, system ((2) is non-dimensionalized by defining the new variables θ' , v' , u' and t' in the following way: $\theta = A\theta'$, $v = v_0v'$, $u = Lu'$, $t = (L/v_0)t'$, after which we return to the use of θ , v , u and t . This non-dimensionalization puts the system into the following form:

$$\begin{aligned}\dot{\theta} &= -v(\theta + (1 + \varepsilon) \log(v)) \\ \dot{u} &= v - 1 \\ \dot{v} &= -\gamma^2[u + (1/\xi)(\theta + \log(v))]\end{aligned}\quad (2)$$

where $\varepsilon = (B - A)/A$ measures the sensitivity of the velocity relaxation, $\xi = (kL)/A$ is the nondimensional spring constant, and $\gamma = (k/M)^{1/2}(L/v_0)$ is the nondimensional frequency [16]. As it was previously shown [18], a supercritical direct Andronov–Hopf bifurcation curve occurs for the following parameter values $\varepsilon = 0.27$, $\xi = 0.5$ and $\gamma = 0.8$, leading from equilibrium state to regular periodic oscillations.

2.2. Fault motion model under study

We analyze the dynamics of two coupled blocks Fig. 1), whose motion is governed by the following system of first-order ordinary

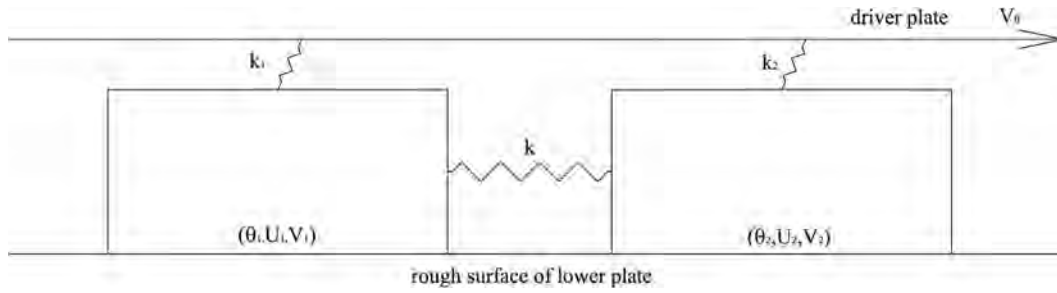


Fig. 1. Setup of the analyzed model.

differential equations, starting from the original system (1):

$$\begin{aligned}\dot{\theta}_1 &= -\left(\frac{V_1}{L_1}\right) \cdot \left(\theta_1 + B_1 \ln\left(\frac{V_1}{V_0}\right)\right) \\ \dot{U}_1 &= V_1 - V_0 \\ \dot{V}_1 &= (-1/M_1)[k_1 U_1 - k(U_2(t - \tau) - U_1(t)) + \theta_1 + A_1 \ln(V_1/V_0)] \\ \dot{\theta}_2 &= -\left(\frac{V_2}{L_2}\right) \cdot \left(\theta_2 + B_2 \ln\left(\frac{V_2}{V_0}\right)\right) \\ \dot{U}_2 &= V_2 - V_0 \\ \dot{V}_2 &= (-1/M_2)[k_2 U_2 - k(U_1(t - \tau) - U_2(t)) + \theta_2 + A_2 \ln(V_2/V_0)]\end{aligned}\quad (3)$$

Here we introduced time delay between the two coupled blocks. In this way, we simulate the original model of Burridge and Knopoff [10], where two blocks actually represent two boundary sets of blocks, and the effect of the middle set of blocks (with different viscosity properties in comparison to other two sets) is replicated by the delayed interaction between the two blocks.

Appropriate non-dimensionalization puts the system (3) into the following form:

$$\begin{aligned}\theta_1 &= -V_1 \cdot (\theta_1 + (1 + \varepsilon_1) \ln V_1) \\ U_1 &= V_1 - 1 \\ V_1 &= \gamma_1^2 \left(-U_1 + c_1 (U_2(t - \tau) - U_1(t)) - \left(\frac{1}{\xi_1}\right) (\theta_1 + \ln(V_1)) \right) \\ \theta_2 &= -V_2 \cdot (\theta_2 + (1 + \varepsilon_2) \ln V_2) \\ U_2 &= V_2 - 1 \\ V_2 &= \gamma_2^2 \left(-U_2 + c_2 (U_1(t - \tau) - U_2(t)) - \left(\frac{1}{\xi_2}\right) (\theta_2 + \ln(V_2)) \right)\end{aligned}\quad (4)$$

where $c_i = k/k_i$, $i = 1, 2$; $\theta_{1new} = \theta_{1old}/A$, $V_{new} = V_{old}/V_0$, $U_{new} = U_{old}/L$, $t_{new} = (L/V_0)t_{old}$, $\varepsilon = (B - A)/A$, $\xi = (kL)/A$, $\gamma = (k/M)^{1/2}(L/V_0)$. In present paper, we consider that $\varepsilon_1 = \varepsilon_2 = \varepsilon$, $\gamma_1 = \gamma_2 = \gamma$, $\xi_1 = \xi_2 = \xi$ and $c_1 = c_2 = c$.

3. Choice of the relevant parameter values

As it is commonly known, dynamics of any system is predominantly controlled by an action of a few control parameters, whose tuning induce corresponding transitions between different dynamical regimes. Thereby, variations of control parameters should be performed within the relevant intervals, i.e. by taking the parameter values which are of interest either from theoretical viewpoint, or which are observed in laboratory conditions or *in situ*.

Original model (2) has three main control parameters that predetermine its dynamics. As it was previously indicated, parameter ε denotes the ratio of stress drop and stress increase during the fault motion (Fig. 2). According to the results of previous studies [5], this ratio needs to be positive in order to capture the velocity-weakening behavior, i.e. for $(B - A) > 0$ one could observe the unsta-

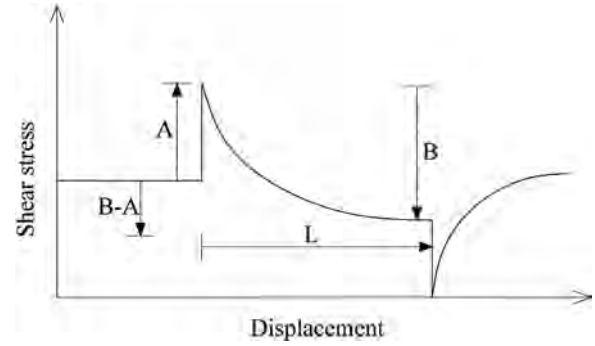


Fig. 2. General scheme of a shear stress variation during the motion of analyzed model shown in Fig. 1.

ble dynamics relevant from the viewpoint of seismology. Previous research showed that this condition is fulfilled at depths in Earth's crust where the most crustal earthquake foci are located, approximately between 5 and 15 km [5]. Below and above this zone, parameter ε has negative values, indicating velocity-strengthening behavior, which secures the stable dynamics of fault motion. Regarding the relevant values of parameter ε , preceding laboratory findings on friction properties of granite samples (since continental crust is mostly composed of granite) indicated that parameters A and B are of the order of magnitude 10^{-3} [31], with ratio $(B - A)/A$ in the interval $[-0.17, 0.36]$, which indicates that meaningful values of ε could be taken from the interval $[-1, 1]$ (Table 1). One should note that present analysis is constrained only to the dynamics of crustal faults, since fault motion in the subduction zones is under prevailing gravitational influence, which is not examined in this study. It should also be emphasized that in present analysis we observe only the velocity weakening behavior, so negative values of dimensionless stress ratio are not examined.

Parameter ξ is defined as a function of spring stiffness k_L , block mass M and stress increase A. Stiffness k_L is related to the spring by which blocks are attached to the upper moving plate, which according to Brown et al. [32] needs to be much more flexible than spring connecting the blocks (whose stiffness is described by k_C), since the distance between the interacting blocks along the fault is much smaller than the dimension of the driving plate. In present analysis if one takes that the value of k_C is around 1, than parameter k_L could take values two order of units smaller, $k_L = 10^{-2}$. This further means that relevant values of parameter c (k_C/k_L) are of 10^2 order of unit. Regarding the block mass, we assume that M takes very small values (order of unit of 10^{-6}), since, in present analysis, we do not analyze the effect of gravity (normal stress), but dynamic instability is assumed to occur due to effect of friction and delayed interaction. Hence, analysis is conducted for almost massless blocks. When all of these assumptions, constraints and previously obtained results are taken into consideration, one arrives at the relevant values of ξ of the order of 10^{-1} (Table 1).

Table 1
Relevant parameter values for the analysis.

Parameter	Relevant value from the previous studies (order of unit)	Reference
Stress increase: A	$10.3 - 19.9 \times 10^{-3}$	[25]
Stress drop: B	$12.1 - 20.3 \times 10^{-3}$	[25]
Spring stiffness between the upper plate and the block: k_L	$k_L \ll k_C (10^{-2})$	[26]
Critical slip distance: L	10^{-2}	[27]
Velocity of the driving plate: V_0	1	[16]
Controlling parameters		
Parameter	Relevant value from the previous studies (order of unit)	Adopted interval for present analysis
$\varepsilon = (B-A) / A$	[-0.17,0.36]	[-1,1]
$\xi = k_L \times M/A$	10^{-1}	[0,1]
$\gamma = (k_L/M)^{1/2} \times (L/V_0)$	1	[0,2]

Relevant values of parameter γ are determined by taking into the consideration the spring stiffness k_L , block mass M , critical slip distance L and velocity of the upper driving plate V_0 . According to Scholz [33], critical slip distance L represents a displacement needed to make a transition between the steady-state friction regimes (Fig. 2). Its recommended value is 10^{-2} order of unit. Regarding the velocity of the upper driving plate, V_0 , its relevant value is determined by the stationary solution of system (2), which is $(\theta, U, V) = (0, 0, 1)$ according to Erickson et al. [16]. Hence, we take $V_0 = 1$ as a meaningful value of the upper plate velocity. Concerning these appropriate values of k_L , M , L and V_0 , one finds that relevant value of γ is of a single order of unit (Table 1).

One should note that the value of time delay is observed in comparison with the oscillation period relevant from the seismological viewpoint. In present paper, authors consider time delay as relevant for those values which are significantly smaller than the corresponding oscillation period. This is in correspondence with the proposal by Burridge and Knopoff, who took time delay significantly smaller for the part of the fault that exhibits viscous slipping rather than the parts that move by fracture.

4. Results

Regarding the local bifurcation analysis, the considered delay differential equation (DDE) system is treated numerically using DDE BIFTOOL, having the obtained results further corroborated by the Runge-Kutta 4th order numerical method. System (4) has only one stationary solution, namely $(\theta_1, U_1, V_1, \theta_2, U_2, V_2) = (0, 0, 1, 0, 0, 1)$, which corresponds to steady sliding. We proceed in the standard way to determine and analyze the characteristic equation of (4) around a stationary solution $(0, 0, 1, 0, 0, 1)$. Details of the analysis are given in Appendix.

Next we shall analyze the effect of stationary time delay coupled with the influence of coupling strength c and the main control parameters of the observed system, namely ε , ξ and γ . All the analyzes were done for the limit cycle as the starting dynamical regime of the initial observed system ($\tau = 0$), which is considered as a co-seismic regime.

Fig. 3 shows the Hopf bifurcation curves in τ - c diagram. For the relevant range of values for coupling strength (10^2 order of unit), observed system exhibit inverse Andronov–Hopf bifurcation, from the initial oscillatory regime, with period $T \approx 12$, to equilibrium state (fixed point), for very small value of time delay, $\tau \approx 0.01$. Increase of time delay, e.g. $\tau = 0.3$, for $c = 100$, induces an occurrence of a direct Andronov–Hopf bifurcation, with the appearance of regular periodic oscillations, with period $T = 0.5$. Regarding the oscillation amplitudes, direct Andronov–Hopf bifurcation triggers approximately ten times smaller displacements.

Effect of the interaction of time delay and dimensionless stress ratio ε is given in Fig. 4. As in the previous case, an inverse supercritical Andronov–Hopf bifurcation curve occurs with the in-

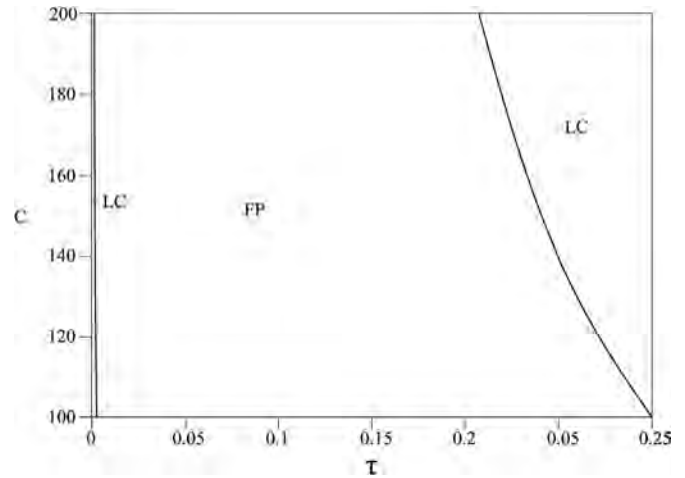


Fig. 3. Diagram $\tau(c)$, for the fixed values of parameters $\varepsilon = 0.4$, $\xi = 0.5$ and $\gamma = 0.8$ (limit cycle of the starting system). Andronov–Hopf bifurcation curves denotes the transition from limit cycle (LC) to equilibrium state (EQ) and again to limit cycle (LC). Qualitatively similar diagrams are obtained for other parameter values for the initial conditions near the equilibrium point.

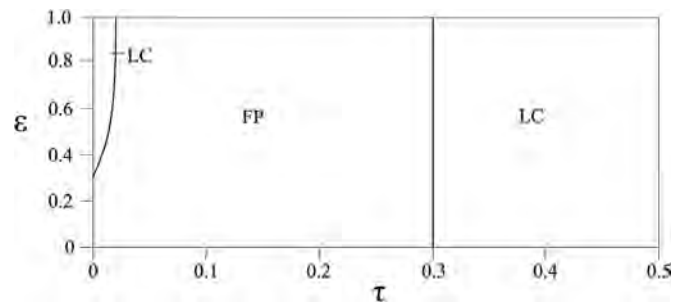


Fig. 4. Diagram $\tau(\varepsilon)$, for the fixed values of parameters $c = 100$, $\xi = 0.5$ and $\gamma = 0.8$ (limit cycle of the starting system). Andronov–Hopf bifurcation curve denotes the transition from the initial limit cycle (LC) across the equilibrium state (EQ) and again to limit cycle (LC). Qualitatively similar diagrams are obtained for other parameter values for the initial conditions near the equilibrium point.

crease of τ , introducing the change of dynamical regime from the limit cycle (for the values of $\varepsilon > 0.27$) to equilibrium state, and further again to regular periodic oscillations (for $\tau > 0.3$), with the occurrence of direct bifurcation. Qualitatively similar behavior is observed when τ and nondimensional frequency γ are simultaneously varied (Fig. 5). With the increase of time delay, for constant value of γ , both inverse and direct supercritical Andronov–Hopf bifurcation occurs.

In the case when τ and ξ are varied, while other parameters are held fixed for the equilibrium state of the original system (2),

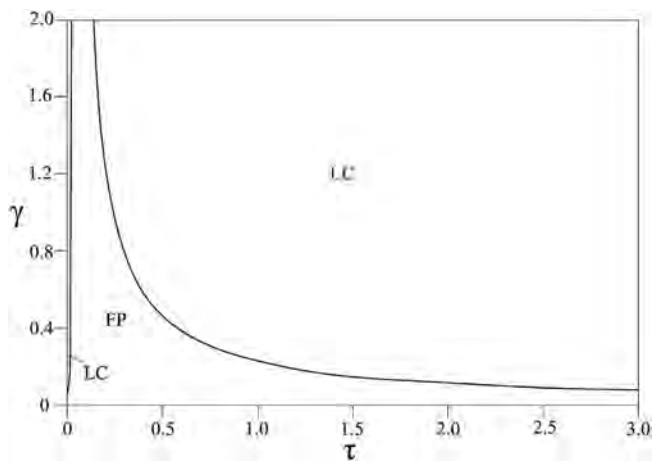


Fig. 5. Diagram $\tau(\gamma)$, for the fixed values of parameters $c=100$, $\xi=0.5$ and $\varepsilon=0.4$ (limit cycle of the starting system). Andronov–Hopf bifurcation curve denotes the transition from equilibrium state (EQ) to limit cycle (LC). Qualitatively similar diagrams are obtained for other parameter values for the initial conditions near the equilibrium point.

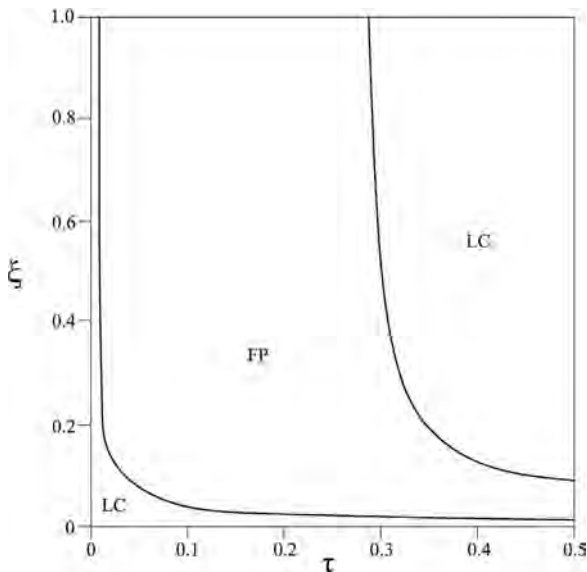


Fig. 6. Diagram $\tau(\xi)$, for the fixed values of parameters $c=100$, $\varepsilon=0.4$ and $\gamma=0.8$ (limit cycle of the starting system). Andronov–Hopf bifurcation curve denotes the transition from the limit cycle (LC) across the equilibrium state (EQ) to limit cycle (LC). Qualitatively similar diagrams are obtained for other parameter values for the initial conditions near the equilibrium point.

there is an Andronov–Hopf bifurcation curve occurs from the equilibrium state to regular periodic oscillations (Fig. 6).

5. Discussion

Results of the performed analysis are new and meaningful for both the nonlinear dynamics and seismology. From the viewpoint of nonlinear dynamics, present analysis is relevant from the phenomenological aspect. In particular, the obtained results indicate that by assuming the delayed interaction between the blocks, one can observe two phenomena: inverse and direct Andronov–Hopf bifurcation. It should be emphasized that this feature is observed for the values of time delay about 4×10^2 order of unit smaller than the corresponding period of regular oscillations of the starting system (for $\tau \approx 0$).

From the seismological aspect, interpretation could be interesting if one looks in the opposite direction. In particular, if the ex-

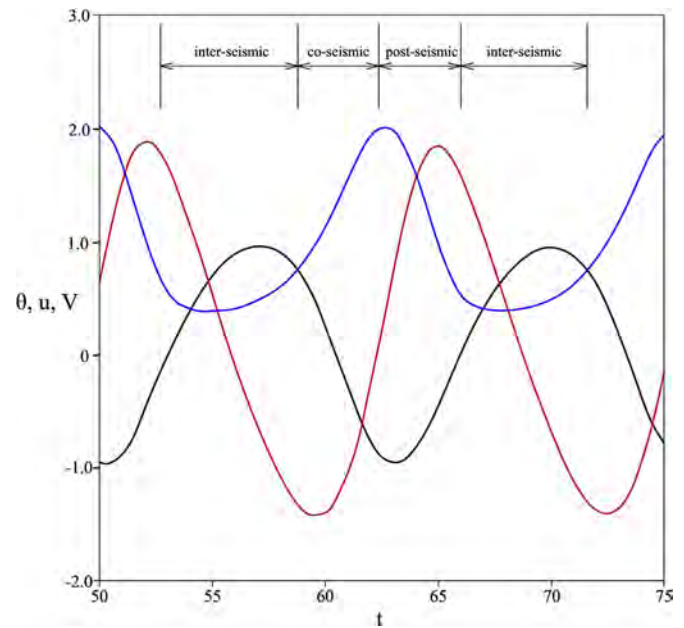


Fig. 7. Transition between seismic cycles in oscillatory regime of spring-slider dynamics. Black line denotes the change of friction (state variable), red line is for displacement, while blue line indicates the change of velocity.

istence of delayed interaction among different fault segments is justified, considering different viscous properties of fault gouge, than starting dynamical regime should be with introduced positive value of time delay. This means that the starting system is probably in equilibrium state (fixed point), which is proved to occur with the introduction of time delay. However, further increase of time delay induces the transition to regular periodic oscillations, which certainly could not be considered as the onset of co-seismic regime, for two main reasons. Firstly, frequency of displacements is very high, i.e. oscillation period is approximately 0.5, which is near the value of time delay (0.3), where the bifurcation point occurs. Such large value of time delay could hardly be expected in natural conditions. Secondly, displacement amplitude is about ten times smaller than for the starting system, which is also not likely to happen, since the majority of displacement along the fault takes place during the earthquakes, i.e. in the co-seismic regime. Hence, in order to “force” the examined system with the included time delay to enter the co-seismic regime, one needs to analyze the conditions which lead to the reduction of viscosity effect. Certainly, weaker impact of viscosity is expected in high temperature and low pressure conditions, which are the two conditions usually satisfied during the fault movement. In particular, the unconsolidated angular shaped rock material that constitutes the fault gouge exhibits high friction, which further induces the increase in temperature. Also, during the fault movement, fault itself is released of the pressure generated by the strong tectonic forces acting in opposite directions along the fault. In particular, heat generated during frictional sliding is a substantial component of the energy budget of earthquakes [34,35]. When time delay is significantly small ($\tau \ll 0.01$), fault enters the co-seismic dynamical regime, where regular periodic oscillations have low-frequency (i.e. high period, $T \approx 12$), and rather large amplitude (around 1.2–2.0 in our numerical simulations). Certainly, case with $\tau=0$ is out of the question, since main assumption of the analysis is that delayed interaction is inherent property of the compound fault.

Once the examined model is in oscillatory regime, one could easily recognize the co-seismic, post-seismic and inter-seismic regime, latter of which represent short-term occurrence (Fig. 7).

One should note that such dynamics, relevant from the viewpoint of seismology, is observed for the parameter values adopted using the previous laboratory findings.

6. Conclusion

In present paper, authors examine dynamics of a spring-slider model as a setup of fault movement. Examined model is composed of two blocks with delayed interaction, which mimics delayed interaction among a group of blocks from the original Burridge–Knopoff model. Analysis is conducted for the parameter values relevant from the seismological viewpoint, based on the previous laboratory findings and seismological observations. Main goal of the research was to establish the background dynamics of a seismic cycle, including the transition from steady state or aseismic creep to stick-slip-like seismic regime, with alternation of inter-seismic, co-seismic and post-seismic cycles.

Results of the performed analysis indicate the following. Introduction of small time delay, significantly smaller when compared to the period of oscillatory regime, leads to transition from fixed point (equilibrium state) to periodic oscillations (limit cycle). From the viewpoint of seismology, these findings indicate a key role of the interaction among different parts of a compound fault in generation of seismogenic motion. More closely, effect of viscosity of a fault zone plays a crucial role in transmission of a movement along the fault. From the standpoint of earthquake phenomenology, one could consider regular periodic oscillations as an example of stick-slip like regime, with the successive shifts between the co-seismic regime (increasing velocity branch and decreasing friction), post-seismic regime (decreasing velocity branch and increasing friction) and inter-seismic regime (quasi-stationary velocity branch). On the other hand, some authors could consider the whole oscillatory regime as a representative of a co-seismic fault movement [36].

Another interesting outcome of the present research lies in the specific effect of the main controlling parameters, which were previously indicated as the most relevant for the modeled fault dynamics [16]. Apparently, ratio of stress drop to stress increase (parameter ε), for the range of other parameters' values relevant from the seismological viewpoint and for the assumed delayed interaction as inherent property of fault dynamics, induces the transition from equilibrium state to periodic oscillations. Regarding the effect of other two parameters, γ and ξ , related to the stiffness of the spring connecting the blocks and the upper driving plate, results obtained imply that a change from steady state or aseismic creep to seismic fault motion occurs with the increase of γ and ξ . However, these parameters are considered as constants for the observed system, so it is highly unlikely to expect their significant changes during the fault motion. The expected changes of these parameters are either small or these changes are slow from the viewpoint relevant for the duration of seismogenic fault motion.

As for the effect of coupling strength c , increase of c for the relevant range of parameter values ($>10^2$) leads to the change of dynamical regime only for rather high values of time delay, which is certainly not expected in the real conditions along the fault zone in the Earth's crust. Hence, in this case, time delay plays again the significant role, in a way that the reduction of time delay could lead to the onset of co-seismic regime.

Concerning the predominant effect of delayed coupling on dynamics of fault motion, further research could include the analysis of time varying delay on fault motion. Such an assumption is justified from the seismological viewpoint, since one could expect changes of friction properties along the fault zone in a reasonable period of time. From the standpoint of nonlinear dynamics, introduction of coupling with variable delay would certainly induce

more complex behavior and, maybe, indicate some new dynamical mechanisms in the background of earthquake nucleation.

Acknowledgments

This research was partly supported by the Ministry of Education, Science and Technological Development of the Republic of Serbia (Contract Nos. 176016 and 171017).

Appendix

Linearization of the system (4) and substitution $\theta_1 = A_1 e^{\lambda t}$, $U_1 = B_1 e^{\lambda t}$, $V_1 = C_1 e^{\lambda t}$, $\theta_2 = A_2 e^{\lambda t}$, $U_2 = B_2 e^{\lambda t}$, $V_2 = C_2 e^{\lambda t}$ and with $U_1(t-\tau) = B_1 e^{\lambda(t-\tau)}$ and $U_2(t-\tau) = B_2 e^{\lambda(t-\tau)}$ results in a system of algebraic equations for the constants A_1 , B_1 , C_1 , A_2 , B_2 and C_2 . This system has a nontrivial solution if the following is satisfied:

$$\begin{aligned}
 & -(\lambda + 1) \left[\lambda \left(\lambda + \gamma_1^2 \left(\frac{1}{\xi_1} \right) \right) \cdot D \right. \\
 & \left. + \gamma_1^2 (1 + c_1) \cdot D + \gamma_1^2 c_1 e^{-\lambda \tau} (\lambda + 1) \gamma_2^2 c_2 e^{-\lambda \tau} \right] \\
 & + \lambda (1 + \varepsilon_1) \gamma_1^2 \left(\frac{1}{\xi_1} \right) \cdot D = 0
 \end{aligned} \tag{1A}$$

where:

$$D = \begin{vmatrix} -(\lambda + 1) & 0 & -(1 + \varepsilon_2) \\ 0 & -\lambda & 1 \\ -\gamma_2^2 \left(\frac{1}{\xi_2} \right) & -\gamma_2^2 (1 + c_2) & -\left(\lambda + \gamma_2^2 \left(\frac{1}{\xi_2} \right) \right) \end{vmatrix}$$

The Eq. (1A) is the characteristic equation of the system (4) and can be written in the following form:

$$\begin{aligned}
 & \left\{ -(\lambda + 1) \left[\lambda \left(\lambda + \gamma_1^2 \left(\frac{1}{\xi_1} \right) \right) + \gamma_1^2 (1 + c_1) \right] + \lambda (1 + \varepsilon_1) \gamma_1^2 \left(\frac{1}{\xi_1} \right) \right\} \cdot \\
 & D = (\lambda + 1)^2 \gamma_1^2 \gamma_2^2 c_1 c_2 e^{-2\lambda \tau}
 \end{aligned} \tag{2A}$$

in which we substitute $\lambda = i\omega$ to obtain:

$$\begin{aligned}
 & \frac{\left[\omega^2 \gamma_1^2 \left(\frac{1}{\xi_1} \right) + \omega^2 - \gamma_1^2 (1 + c_1) \right] + i\omega \left[\omega^2 - \gamma_1^2 (1 + c_1) - \gamma_1^2 \left(\frac{1}{\xi_1} \right) + (1 + \varepsilon_1) \gamma_1^2 \left(\frac{1}{\xi_1} \right) \right]}{\gamma_1^2 \gamma_2^2 c_1 c_2 [-\omega^2 + 1 + i2\omega]} D = \\
 & = \cos(2\omega\tau) - i \sin(2\omega\tau)
 \end{aligned} \tag{3A}$$

The resulting two equations for the real and imaginary part of (3A) after squaring and adding give an equation for each of the parameters, c_1 , c_2 , ε_1 and ε_2 in terms of the other parameters, ω , μ , γ_1 and γ_2 , and after division, an equation for τ in terms of the parameters ω , μ , γ_1 , γ_2 , ε_1 , ε_2 , ξ_1 and ξ_2 . In this way, one obtains parametric representations of the relations between τ and the parameters, which correspond to the bifurcation values $\lambda = i\omega$. The general form of such relations is illustrated by the following formula for ε_1 as a function of ω :

$$(1 + \varepsilon_1)_{1/2} = - \frac{F \pm \sqrt{F^2 - G^2}}{H} \tag{4A}$$

where F, G and H are abbreviations for the following terms:

$$\begin{aligned}
 F = & \left(\omega \left[\left(\omega^2 - \gamma_1^2 (1 + c_1) - \gamma_1^2 \left(\frac{1}{\xi_1} \right) \right) B + AD \right] (-\omega^2 + 1) \right. \\
 & \left. - 2 \left[AB - \omega^2 \left(\omega^2 - \gamma_1^2 (1 + c_1) - \gamma_1^2 \left(\frac{1}{\xi_1} \right) \right) D \right] \right) \cdot \\
 & \omega \gamma_1^2 \left(\frac{1}{\xi_1} \right) \{ B(-\omega^2 + 1) + 2\omega^2 D \} \\
 & + \left(\left(AB - \omega^2 \left(\omega^2 - \gamma_1^2 (1 + c_1) - D \gamma_1^2 \left(\frac{1}{\xi_1} \right) \right) \right) (-\omega^2 + 1) \right. \\
 & \left. + B\omega^2 \left(2 \left(\omega^2 - \gamma_1^2 (1 + c_1) - \gamma_1^2 \left(\frac{1}{\xi_1} \right) \right) + AD \right) \right)
 \end{aligned}$$

$$\begin{aligned}
G &= \left[\left(\omega \gamma_1^2 \left(\frac{1}{\xi_1} \right) \{ B(-\omega^2 + 1) + 2\omega^2 D \} \right)^2 \right. \\
&\quad \left. + \left(\omega^2 \gamma_1^2 \left(\frac{1}{\xi_1} \right) \left\{ B \left(1 + \frac{1}{\mu} \right) - D(-\omega^2 + 1) \right\} \right)^2 \right] \cdot \\
&\quad \left[\left(\left(\omega \left[\left(\omega^2 - \gamma_1^2 (1 + c_1) - B \gamma_1^2 \left(\frac{1}{\xi_1} \right) \right] + AD \right) (-\omega^2 + 1) \right. \right. \right. \\
&\quad \left. \left. - 2 \left[AB - D \omega^2 \left(\omega^2 - \gamma_1^2 (1 + c_1) - \gamma_1^2 \left(\frac{1}{\xi_1} \right) \right) \right] \right) \right)^2 + \\
&\quad \left. + \left(\left(AB - \omega^2 \left(\omega^2 - \gamma_1^2 (1 + c_1) - D \gamma_1^2 \left(\frac{1}{\xi_1} \right) \right) \right) \right) (-\omega^2 + 1) \right. \right. \\
&\quad \left. \left. + \omega^2 \left(2 \left(\omega^2 - \gamma_1^2 (1 + c_1) - B \gamma_1^2 \left(\frac{1}{\xi_1} \right) \right) + AD \right) \right)^2 - \right. \\
&\quad \left. - \left(\left((-\omega^2 + 1)^2 + 2\omega^2 \right) \left(\gamma_1^2 \gamma_2^2 c_1 c_2 \right) \right)^2 \right] \\
H &= \left(\gamma_1^2 \left(\frac{1}{\xi_1} \right) \omega \{ B(-\omega^2 + 1) + 2\omega^2 D \} \right)^2 \\
&\quad + \left(\omega^2 \gamma_1^2 \left(\frac{1}{\xi_1} \right) \{ 2B - D(-\omega^2 + 1) \} \right)^2 \quad (5A)
\end{aligned}$$

and A, B and D are:

$$\begin{aligned}
A &= \omega^2 \gamma_1^2 \left(\frac{1}{\xi_1} \right) + \omega^2 - \gamma_1^2 (1 + c_1) \\
B &= \omega^2 \cdot \left(\gamma_2^2 \left(\frac{1}{\xi_2} \right) + 1 \right) - \gamma_2^2 (1 + c_2) \quad (6A) \\
D &= \omega^2 - \gamma_2^2 (1 + c_2) - \gamma_2^2 \left(\frac{1}{\xi_2} \right) + \gamma_2^2 (1 + \varepsilon_2) \left(\frac{1}{\xi_2} \right)
\end{aligned}$$

On the other hand, for c_1 as a function of ω :

$$(c_1)_{1/2} = \frac{-F \pm \sqrt{F^2 - GH}}{H} \quad (7A)$$

where F, G and H are the same as in (7).

For τ as a function of ω :

$$\tau = \frac{1}{2\omega} \left\{ \arctan \left(-\frac{J}{K} \right) + k\pi \right\} \quad (8A)$$

where k is any nonnegative integer such that $\tau_k \geq 0$, and J and K are the abbreviations for the following terms:

$$\begin{aligned}
J &= \frac{\omega}{(-\omega^2 + 1)^2 + 4\omega^2} \{ [CB + AD](-\omega^2 + 1) - [2AB - \omega^2 CD] \} \\
K &= \frac{1}{(-\omega^2 + 1)^2 + 4\omega^2} \{ [AB - \omega^2 CD](-\omega^2 + 1) + 2\omega^2 [CB + AD] \} \quad (9A)
\end{aligned}$$

where A, B and D are the same as in (8), and C stands for the following term:

$$C = \omega^2 - \gamma_1^2 (1 + c_1) - \gamma_1^2 \left(\frac{1}{\xi_1} \right) + (1 + \varepsilon_1) \gamma_1^2 \left(\frac{1}{\xi_1} \right). \quad (10A)$$

References

- [1] Ayyub BM, McCuen RH. Probability, statistics and reliability for engineers and scientists. Boca Raton, Florida, USA: CRC Press; 2000. p. 628.
- [2] Ito T, Hashimoto M. Spatiotemporal distribution of interplate coupling in southwest Japan from inversion of geodetic data. *J Geophys Res* 2004;109.
- [3] Thatcher W. The earthquake deformation cycle at the Nankai trough, southwest Japan. *J Geophys Res* 1984;89:3087–101.

- [4] Jonsson S, Segall P, Pedersen R, Bjornsson G. Post-earthquake ground movements correlated to pore-pressure transients. *Nature* 2003;424:179–83.
- [5] Scholz CH. Earthquakes and friction laws. *Nature* 1998;391:37–42.
- [6] Hetland EA, Hager BH. Postseismic relaxation across the central Nevada seismic belt. *J Geophys Res* 2003;108. doi:10.1029/2002JB002257.
- [7] Brace WF, Byerlee JD. Stick-slip as a mechanism for earthquakes. *Science* 1966;153(3739):990–2.
- [8] Byerlee JD. The mechanics of stick-slip. *Tectonophys* 1970;9(5):475–86.
- [9] Gobel THW. Microseismicity, fault structure, & the seismic cycle. University of Southern California; 2013. p. 172.
- [10] Burridge R, Knopoff L. Model and theoretical seismicity. *Bull Seismol Soc Am* 1967;57(3):341–71.
- [11] Winter ME. The plausibility of long-wavelength stress correlation or stress magnitude as a mechanism for precursory seismicity: results from two simple elastic models. *Pure Appl Geophys* 2000;157(11–12):2227–48.
- [12] Mori T, Kawamura H. Spatiotemporal correlations of earthquakes in the continuum limit of the one-dimensional Burridge–Knopoff model. *J Geophys Res* 2008;113(11):B11305.
- [13] Amundsen DS, Scheibert J, Thøgersen K, Trømborg J, Malthe-Sørensen A. 1D model of precursors to frictional stick-slip motion allowing for robust comparison with experiments. *Tribol Lett* 2012;45(2):357–69.
- [14] Ichinose S. Non-equilibrium statistical approach to friction models. *Tribol Int* 2016;93:446–50.
- [15] Ueda Y, Morimoto S, Kakui S, Yamamoto T, Kawamura H. Dynamics of earthquake nucleation process represented by the Burridge–Knopoff model. *Eur Phys J B* 2015;88(9):235.
- [16] Erickson B, Birnir B, Lavalley D. A model for aperiodicity in earthquakes. *Non-linear Process Geophys* 2008;15:1–12.
- [17] Caldeira B, Silva HG, Borges JF, Tlemçani M, Bezzeghoud M. Chaotic behavior of seismic mechanisms: experiment and observation. *Ann Geophys* 2012;55(1):57–62.
- [18] Kostić S, Franović I, Perc M, Vasović N, Todorović K. Triggered dynamics in a model of different creep regimes, 4. *Scientific Reports: Nature Publishing Group*; 2014. p. 5401.
- [19] Valipour M, Asghar Montazar A. An evaluation of SWDC and WinSRFR models to optimize of infiltration parameters in furrow irrigation. *American J Sci Res* 2012;69:128–42.
- [20] Valipour M. Increasing irrigation efficiency by management strategies: cutback and surge irrigation. *ARPN J Agri Biol Sci* 2013;8:35–43.
- [21] Valipour M. Application of new mass transfer formulae for computation of evapotranspiration. *J Appl Water Eng Res* 2014;2:33–46.
- [22] Valipour M. Use of surface water supply index to assessing of water resources management in Colorado and Oregon, US. *Adv Agri Sci Engineering Res* 2013;3:631–40.
- [23] Valipour M, Ali Gholami Defidkouhi M, Raeini Sarjaz M. Selecting the best model to estimate potential evapotranspiration with respect to climate change and magnitudes of extreme events. *Agri Water Manage* 2017;180:50–60.
- [24] Valipour M. Number of required observation data for rainfall forecasting according to the climate conditions. *Am J Sci Res* 2012;74:79–86.
- [25] Kostić S, Franović I, Todorović K, Vasović N. Friction memory effect in complex dynamics of earthquake model. *Nonlinear Dyn* 2013;73(3):1933–43.
- [26] Kostić S, Vasović N, Franović I, Todorović K. Dynamics of simple earthquake model with time delay and variation of friction strength. *Nonlinear Process Geophys* 2013;20:857–65.
- [27] Vasović N, Kostić S, Franović I, Todorović K. Earthquake nucleation in a stochastic fault model of globally coupled units with interaction delays. *Commun Nonlinear Sci Numer Simul* 2016;38:117–29.
- [28] Scholz CH. The mechanics of earthquake and faulting. Cambridge: Cambridge University Press; 2002. p. 504.
- [29] Dieterich JH, Kilgore BD. Direct observation of frictional contacts: new insights for state dependent properties. *Pure Appl Geophys* 1994;143:283–302.
- [30] Clancy I, Corcoran D. State-variable friction for the Burridge–Knopoff model. *Phys Rev E Stat Nonlin Soft Matter Phys* 2009;80:016113.
- [31] Kilgore BD, Blanpied ML, Dieterich JH. Velocity dependent friction of granite over a wide range of conditions. *Geophys Res Lett* 1993;20:903–6.
- [32] Brown SR, Scholz CH, Rundle JB. A simplified spring-block model of earthquakes. *Geophys Res Lett* 1991;18:215–18.
- [33] Scholz CH. The critical slip distance for seismic faulting. *Nature* 1988;336:761–3.
- [34] McGarr A, Fletcher JB, Beeler NM. Attempting to bridge the gap between laboratory and seismic estimates of fracture energy. *Geophys Res Lett* 2004;31:L14606. doi:10.1029/2004GL020091.
- [35] Venkataraman A, Kanamori H. Observational constraints on the fracture energy of subduction zone earthquakes. *J Geophys Res* 2004;109:B05302. doi:10.1019/2003JB002549.
- [36] Vasudevan K, Cavers M, Ware A. Earthquake sequencing: chimera states with Kuramoto model dynamics on directed graphs. *Nonlinear Process Geophys* 2015;22:499–512.

Two scenarios for the onset and suppression of collective oscillations in heterogeneous populations of active rotators

Vladimir Klinshov*

*Institute of Applied Physics of the Russian Academy of Sciences, 46 Ulyanov Street, 603950 Nizhny Novgorod, Russia*Igor Franović[†]*Scientific Computing Laboratory, Center for the Study of Complex Systems, Institute of Physics Belgrade, University of Belgrade, Pregrevica 118, 11080 Belgrade, Serbia*

(Received 28 June 2019; revised manuscript received 11 October 2019; published 27 December 2019)

We consider the macroscopic regimes and the scenarios for the onset and the suppression of collective oscillations in a heterogeneous population of active rotators composed of excitable or oscillatory elements. We analyze the system in the continuum limit within the framework of Ott-Antonsen reduction method, determining the states with a constant mean field and their stability boundaries in terms of the characteristics of the rotators' frequency distribution. The system is established to display three macroscopic regimes, namely the *homogeneous stationary state*, where all the units lie at the resting state, the *global oscillatory state*, characterized by the partially synchronized local oscillations, and the *heterogeneous stationary state*, which includes a mixture of resting and asynchronously oscillating units. The transitions between the characteristic domains are found to involve a complex bifurcation structure, organized around three codimension-two bifurcation points: a Bogdanov-Takens point, a cusp point, and a fold-homoclinic point. Apart from the monostable domains, our study also reveals two domains admitting bistable behavior, manifested as coexistence between the two stationary solutions or between a stationary and a periodic solution. It is shown that the collective mode may emerge via two generic scenarios, guided by a saddle-node of infinite period or the Hopf bifurcation, such that the transition from the homogeneous to the heterogeneous stationary state under increasing diversity may follow the classical paradigm, but may also be hysteretic. We demonstrate that the basic bifurcation structure holds qualitatively in the presence of small noise or small coupling delay, with the boundaries of the characteristic domains shifted compared to the noiseless and the delay-free case.

DOI: [10.1103/PhysRevE.100.062211](https://doi.org/10.1103/PhysRevE.100.062211)

I. INTRODUCTION

The onset of a collective mode mediated via a transition to synchrony is a fundamental paradigm of macroscopic behavior in a broad variety of fields, ranging from neuroscience and other biologically inspired models to chemistry, technology, and social science [1,2]. A classical approach within the theory of nonlinear dynamics is to regard populations exhibiting a collective mode as macroscopic oscillators [3–5], which can then interact with other populations or be subjected to external stimuli. In this context, we investigate an important problem of the emergence and the suppression of collective oscillations in populations comprised of units with nonuniform intrinsic parameters, which are drawn from a certain probability distribution. Such nonuniformity is a manifestation of variability [6–9], a ubiquitous feature that often makes it more realistic to consider heterogeneous rather than homogeneous assemblies. Depending on the particular application, variability may alternatively be referred to as diversity, heterogeneity, impurities, or quenched noise. In many cases, the diversity can be large

enough to give rise to qualitative differences in individual dynamics of units, such that some of the active elements within a population may be self-oscillating while the others are excitable.

The classical Kuramoto paradigm [10] addresses the scenario where the diversity is manifested at the quantitative level alone, since all the units are considered to be self-oscillating. There, the continuous transition to synchrony occurs once the coupling between the oscillators becomes strong enough to overcome the effects of diversity [2,11]. Nevertheless, the diversity alone has been shown to be capable, under appropriate conditions, to enhance the response of an assembly to external forcing or to promote synchronization [7,8,12]. Moreover, in the case of heterogeneous assemblies made up of excitable and oscillatory units rather than the oscillators alone, it has been demonstrated that the transition to synchrony with increasing diversity may be classical or reentrant, depending on the particular form of the units frequency distribution [13]. For such a setup, it has also been indicated that the collective firing emerges via a generic mechanism where the entrainment of units is degraded by increasing diversity [8].

In the present paper, we investigate the regimes of macroscopic behavior, as well as the scenarios for the onset and the suppression of collective oscillations in a heterogeneous

*vladimir.klinshov@ipfran.ru

†franovic@ipb.ac.rs

population made up of oscillatory and excitable units, considering a model of active rotators with global sine coupling. Our analysis relies on the Ott-Antonsen reduction method [14,15], based on the ansatz that the long-term macroscopic dynamics of such systems settles on a particular invariant attractive manifold. We first provide an exact description of macroscopic stationary states featuring a *constant mean field* and then determine the bifurcations that outline the stability boundaries of the characteristic domains. While the stationary states and the associated self-consistency equation are obtained for an arbitrary distribution of natural frequencies, the subsequent bifurcation analysis is carried out for a *uniform* frequency distribution on a bounded interval, which has the advantage of allowing for analytical tractability. We establish the complete bifurcation structure and demonstrate two generic scenarios for the emergence and the suppression of the collective mode. While the scenario featuring the successive onset and suppression of oscillations under increasing diversity has earlier been reported to be universal for heterogeneous populations with various distributions of the units' frequencies [12,13], the other scenario, which involves a hysteretic behavior due to existence of bistability regions, is reported here for the first time, as far as we know.

Apart from diversity, the two additional ingredients influencing the dynamics in neuronal and other biophysical systems are coupling delays and noise [16–18]. In particular, realistic models often have to include explicit coupling delays in order to describe the effects of finite velocity of signal propagation or the latency in information processing [17,19–23]. On the other hand, creating coarse-grained models inevitably requires one to incorporate different sources of noise [24–31]. Both coupling delay and noise may play an important role in the collective dynamics of a population. For example, in systems consisting just of excitable units, it is well known that the noise may play a constructive role, contributing to the onset of collective firing via synchronization of local noise-induced oscillations [32–35]. Concerning the effect of coupling delays, the standard Kuramoto model with uniform delays has been shown to exhibit the discontinuous rather than the continuous transition between the incoherent and coherent states, further having the synchronization frequency suppressed by the delay [11,36].

Our study evinces the robustness of the general physical picture, inherited from the noiseless and the delay-free case, in the presence of *small* coupling delay and *small* noise. While the impact of small delay may be analyzed within the local stability approach we developed, the Ott-Antonsen method in principle does not allow one to treat stochastic assemblies. Only quite recently, an approach involving the so-called circular cumulants [37,38] has been developed to incorporate a first-order correction to the Ott-Antonsen theory, which accommodates for the effects of noise. We perform numerical analysis of the system dynamics in presence of small noise and complement it with qualitative arguments.

The paper is organized as follows. In Sec. II, we present the details of the model and provide the continuum limit formulation for the delay- and the noise-free setup, obtaining the Ott-Antonsen equation for the local order parameter. Section III comprises the analytical results on the local structure of the macroscopic stationary states and the related self-consistency

equation, derived for an arbitrary frequency distribution. In Sec. IV, the stability and bifurcation analysis of the stationary states is carried out for a particular distribution of frequencies, comparing the stability boundaries of the characteristic domains to those obtained in numerical experiments. In Sec. V, it is shown that the basic bifurcation scenario persists in presence of small noise or small coupling delay. Section VI contains our concluding remarks.

II. MODEL DYNAMICS AND THE CONTINUUM LIMIT FORMULATION

We consider a heterogeneous assembly of N globally coupled active rotators described by:

$$\dot{\theta}_i(t) = \omega_i - a \sin \theta_i(t) - \frac{K}{N} \sum_j \sin[\theta_j(t) - \theta_i(t - \tau) + \alpha] + \sigma \eta_i(t), \quad i = 1, \dots, N, \quad (1)$$

where the phase variables are $\theta_i \in S^1$ and the local dynamics is governed by the nonisochronicity parameter a and the natural frequency ω_i . Regarding the term “natural frequency,” note that it will be used for convenience to describe the intrinsic parameter involving the quenched randomness, even though some units may exhibit excitable, rather than oscillatory, behavior. The frequencies are distributed according to the probability density function $g(\omega)$ that satisfies $\int_{-\infty}^{\infty} g(\omega) d\omega = 1$ and is characterized by the mean value Ω and the width Δ , which we here explicitly refer to as the *diversity* parameter. The individual unit rotates uniformly with the frequency ω_i for $a = 0$ only, whereas for $a > 0$ its rotation becomes nonuniform, having the rotation direction dependent on the sign of ω_i . The relation between ω_i and the parameter a underlies the excitability feature of autonomous dynamics. In particular, ω_i constitutes the bifurcation parameter, such that for fixed a , an isolated unit lies in the excitable regime if $|\omega_i| < a$. In this case, the unit possesses a stable node, whereas the characteristic nonlinear threshold-like response is mediated by an unstable steady state. At $|\omega_i| = a$, an isolated unit undergoes a saddle-node of infinite period (SNIPER) bifurcation toward the oscillatory regime. The interactions are assumed to be uniform across the population, and are characterized by the coupling strength K , the coupling phase-lag α , and the coupling delay τ . The effect of random fluctuations is represented by the white Gaussian random forces η_i of intensity σ^2 , which act independently on each unit [$\langle \eta_i(t) \rangle = 0$, $\langle \eta_i(t) \eta_j(t) \rangle = \delta_{ij} \delta(t - t)$].

As already indicated, in this and the following section we apply the Ott-Antonsen framework [14,15] to investigate the collective dynamics of an heterogeneous assembly of active rotators in the delay- and the noise-free case $\tau = \sigma = 0$. To this end, let us introduce the Kuramoto complex order parameter, which represents the center of mass of all rotators:

$$R(t) = \rho(t) e^{i\psi(t)} = \frac{1}{N} \sum_j e^{i\theta_j(t)}, \quad (2)$$

such that (1) can be rewritten as

$$\dot{\theta}_i = \omega_i - \frac{a}{2i} (e^{i\theta_i} - e^{-i\theta_i}) + \frac{K}{2i} [R e^{-i(\theta_i + \alpha)} - \bar{R} e^{i(\theta_i + \alpha)}], \quad (3)$$

where the bar denotes the complex conjugate. In the thermodynamic limit $N \rightarrow \infty$, the macroscopic state of the system can be described by the probability density function $f(\theta, \omega, t)$, which, for the considered moment t , gives the relative number of oscillators whose phases and frequencies are $\theta_i(t) \approx \theta$, $\omega_k \approx \omega$. The normalization condition required for the probability density function is $\int_0^{2\pi} f(\theta, \omega, t) d\theta = g(\omega)$. Given the conservation of oscillators, $f(\theta, \omega, t)$ has to fulfill the continuity equation

$$\frac{\partial f}{\partial t} + \frac{\partial}{\partial \theta}(fv) = 0, \quad (4)$$

where the velocity is just

$$v(\theta, \omega, t) = \omega - \frac{a}{2i}(e^{i\theta} - e^{-i\theta}) + \frac{K}{2i}[Re^{-i(\theta+\alpha)} - \bar{R}e^{i(\theta+\alpha)}]. \quad (5)$$

In the last expression, we have used the form of the Kuramoto mean field in the thermodynamic limit $N \rightarrow \infty$,

$$R(t) = \int_{-\infty}^{\infty} d\omega \int_0^{2\pi} f(\theta, \omega, t) e^{i\theta} d\theta, \quad (6)$$

According to the Ott-Antonsen ansatz [14,15], the long-term dynamics of the continuity equation (8) settles on a particular manifold of the form

$$f(\theta, \omega, t) = \frac{g(\omega)}{2\pi} \left\{ 1 + \sum_{n=1}^{\infty} [z^n(\omega, t) e^{in\theta} + z^n(\omega, t) e^{-in\theta}] \right\}, \quad (7)$$

where the complex amplitude $z(\omega, t)$ is such that $|z(\omega, t)| \leq 1$. Introducing the assumption (7) into (4), one finds that $z(\omega, t)$ satisfies the Ott-Antonsen equation

$$\dot{z}(\omega, t) = i\omega z + (1 - z^2) \frac{a}{2} + \frac{K}{2} R e^{-i\alpha} - \frac{K}{2} \bar{R} e^{i\alpha} z^2. \quad (8)$$

Quantity $z(\omega, t)$ should be interpreted as the frequency-dependent *local order parameter*, in the sense that it quantifies the degree of synchrony of oscillators whose intrinsic frequencies ω_i lie within a small interval around the given frequency ω . In the continuum limit, the global and the local order parameter are connected by the self-consistency condition

$$R = \mathcal{G}z = \int_{-\infty}^{\infty} g(\omega) z(\omega) d\omega, \quad (9)$$

which follows from the definition (6) and the ansatz (7). Note that (8) presents a generalization of the corresponding result in Ref. [13] for $a \neq 1$, $\alpha \neq 0$.

III. STATIONARY SOLUTIONS OF THE OTT-ANTONSEN EQUATION

Within this section, our aim is to characterize the microscopic structure of the stationary solutions, finding the means to classify them by applying the self-consistency condition (9). To do so, one first looks for the solutions of the Ott-Antonsen equation (8) for which the Kuramoto mean field $R(t) = \rho(t) e^{i\psi(t)}$ is constant. In particular, we substitute the solution of the form $z(\omega, t) = r(\omega, t) e^{i\varphi(\omega, t)}$ into (8), which

ultimately results in

$$\begin{aligned} \dot{r} &= \frac{B}{2}(1 - r^2) \cos \phi, \\ r\dot{\phi} &= \omega r - \frac{B}{2}(1 + r^2) \sin \phi, \end{aligned} \quad (10)$$

having introduced the notation

$$\begin{aligned} B &= \sqrt{a^2 + K^2 \rho^2 + 2aK\rho \cos(\psi - \alpha)}, \\ \beta &= \arctan \frac{K\rho \sin(\psi - \alpha)}{a + K\rho \cos(\psi - \alpha)}, \\ \phi &= \varphi - \beta. \end{aligned} \quad (11)$$

From the system (10), one infers that the quantity B , which depends only on the coupling strength and the mean field, plays the role of the *macroscopic excitability parameter*. This follows from the fact that the microscopic structure of the stationary state is self-organized in a way that the assembly splits into two groups, according to the relation between the respective natural frequencies ω_i and B . In particular, one group is comprised of rotators in the *excitable regime*, whose intrinsic frequencies satisfy $|\omega| < B$, whereas the other group consists of rotating units, whose intrinsic frequencies satisfy $|\omega| > B$. Another indication on the role of B can be obtained if the definitions of B and β from (11) are applied to transform the original equation for the dynamics of rotators (1) into $\dot{\theta}_i = \omega_i - B \sin(\theta_i - \beta)$, which just conforms to a set of forced active rotators. From the level of single unit's dynamics, B is then classically referred to as the *resistivity parameter* in the sense that it reflects the rotator's ability to modify its natural frequency.

Taking a closer look into the dynamics of the two sub-assemblies following from (10), one finds that for $|\omega| < B$ there exist two steady states, given by

$$r^*(\omega) = 1, \quad \phi^*(\omega) = \arcsin \frac{\omega}{B}, \quad (12)$$

and

$$r^*(\omega) = 1, \quad \phi^*(\omega) = \pi - \arcsin \frac{\omega}{B}, \quad (13)$$

whereby our latter stability analysis will show that only the solution (12) is stable. For the units within the rotating group $|\omega| > B$, the only steady state reads

$$\begin{aligned} r^*(\omega) &= \frac{|\omega|}{B} - \sqrt{\frac{\omega^2}{B^2} - 1} \\ \phi^*(\omega) &= \frac{\pi}{2} \operatorname{sgn} \omega. \end{aligned} \quad (14)$$

In order to fully quantify the stationary solutions of the Ott-Antonsen equation (8), one has to obtain an explicit expression for the macroscopic excitability parameter B . In order to do so, we invoke the self-consistency equation (9). Applying the latter to the stationary state $z^*(\omega) = r^*(\omega) e^{i\phi^*(\omega) + i\beta}$ given by (12) and (14), one obtains

$$\begin{aligned} \rho e^{i(\psi - \beta)} &= \frac{i\Omega}{B} + \int_{|\omega| < B} d\omega g(\omega) \sqrt{1 - \frac{\omega^2}{B^2}} \\ &\quad - \frac{i}{B} \int_{|\omega| > B} d\omega g(\omega) \omega \sqrt{1 - \frac{B^2}{\omega^2}}, \end{aligned} \quad (15)$$

where $\Omega = \int_{-\infty}^{\infty} \omega g(\omega) d\omega$ refers to the mean value of the frequency distribution. Separating for the real and the imaginary part of (15) and after some algebra, one ultimately arrives at the self-consistency equation for B of the form:

$$f(B) = B^2 - a^2 - 2K[f_1(B) \sin \alpha + f_2(B) \cos \alpha] + K^2 \frac{f_1^2(B) + f_2^2(B)}{B^2} = 0, \quad (16)$$

where

$$f_1(B) = \Omega - \int_{|\omega| > B} d\omega g(\omega) \omega \sqrt{1 - \frac{B^2}{\omega^2}},$$

$$f_2(B) = \int_{|\omega| < B} d\omega g(\omega) \sqrt{B^2 - \omega^2}. \quad (17)$$

Note that the analogous expression has been obtained in Ref. [13] but only for the particular case $a = 1$, $\alpha = 0$. The results so far apply for an arbitrary distribution of natural frequencies $g(\omega)$. In order to carry out an explicit analysis on the stability of stationary states, including determining the associated stability boundaries and characterization of the transitions between the different collective regimes, we confine the remainder of the study to a particular case of $g(\omega)$, namely a *uniform* distribution of frequencies on a bounded interval.

IV. STABILITY OF THE STATIONARY SOLUTIONS OF THE OTT-ANTONSEN EQUATION

Within this section, we specify the general results from Sec. III to an example of a uniform distribution of natural frequencies $g(\omega)$ defined on an interval $\omega \in [\omega_1, \omega_2]$:

$$g(\omega) = \begin{cases} 0, & \omega < \omega_1 \\ \gamma, & \omega_1 < \omega < \omega_2, \\ 0, & \omega > \omega_2 \end{cases} \quad (18)$$

where $\gamma = 1/(\omega_2 - \omega_1)$ derives from the normalization condition. The given distribution is characterized by an average $\Omega = \frac{\omega_1 + \omega_2}{2}$ and the width $\Delta = \omega_2 - \omega_1$. The advantage of making such a choice of frequency distribution is that it allows for a full analytical treatment of the self-consistency equation (16) for the macroscopic excitability parameter. In particular, the integrals (17) then read

$$f_1(B) = \begin{cases} \Omega - \gamma[F_1(\omega_2) - F_1(\omega_1)], & B < \omega_1 \\ \Omega - \gamma F_1(\omega_2), & \omega_1 < B < \omega_2, \\ \Omega, & B > \omega_2 \end{cases} \quad (19)$$

where

$$F_1(\omega) = \frac{|\omega|}{2} \sqrt{\omega^2 - B^2} + \frac{B^2}{2} \ln \frac{B}{|\omega| + \sqrt{\omega^2 - B^2}}, \quad (20)$$

and

$$f_2(B) = \begin{cases} 0, & B < \omega_1 \\ \gamma \left[\frac{\pi}{4} B^2 - F_2(\omega_1) \right], & \omega_1 < B < \omega_2, \\ \gamma [F_2(\omega_2) - F_2(\omega_1)], & B > \omega_2 \end{cases} \quad (21)$$

with

$$F_2(\omega) = \frac{|\omega|}{2} \sqrt{B^2 - \omega^2} + \frac{B^2}{2} \arcsin \frac{\omega}{B}. \quad (22)$$

Considering the uniform frequency distribution (18), we have carried out the stability and bifurcation analysis of the Ott-Antonsen equation (8). The main control parameters are the characteristics of $g(\omega)$, namely its mean Ω and the width Δ , while the remaining system parameters a , K , and α are kept fixed. Note that the stability analysis of (8) requires one to rewrite it as a real system in order to eliminate the complex conjugation [39–41]. The analysis *per se* involves linearization of the Ott-Antonsen equation for variations around the stationary solution (12)–(14) and consists in determining how the Lyapunov spectra of the stationary states depend on Ω and Δ . While the technical details of the calculation are elaborated in the Appendix, the analysis we provide below will include characterization of the stationary solutions of the Ott-Antonsen equation (8) and the associated stability domains, as well as the description of the mechanisms behind the onset and the suppression of collective oscillations. The analytical results are corroborated by numerical experiments carried out on a heterogeneous assembly of $N = 10^4$ active rotators.

The microscopic structure of the stationary regimes and the fashion in which their number and stability depend on the characteristics of $g(\omega)$ may conveniently be explained in terms of the solutions of the self-consistency equation (16) for the parameter B . A typical form of the function $f(B)$ for the considered domain of (Ω, Δ) values is illustrated in Fig. 1. The three roots of $f(B)$, denoted by $B_1 > B_2 > B_3$, correspond to the stationary solutions of the Ott-Antonsen equation (8). In particular, the macroscopic regime associated to B_1 presents a global rest state, because the macroscopic excitability parameter is so large that the frequencies of all the units lie below it. Given its microscopic structure, where the local dynamics is solely excitable, this state can also be termed a *homogeneous stationary state*. The corresponding time series $\theta_i(t)$ and the evolution of the modulus of the Kuramoto order parameter $\rho(t) = |R(t)|$ are illustrated in

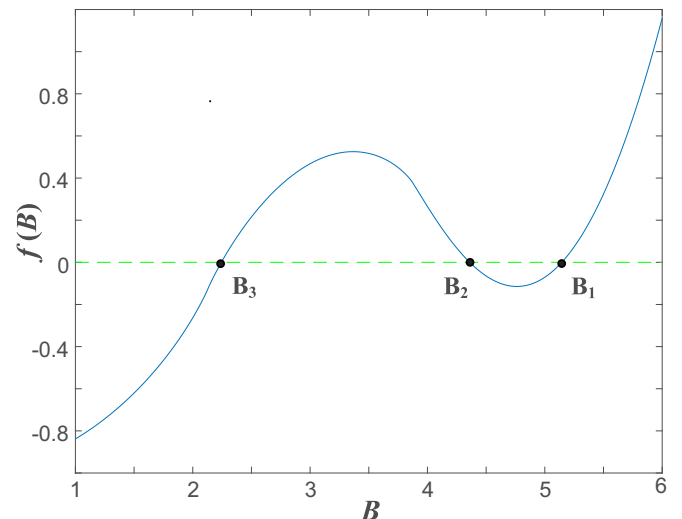


FIG. 1. Typical form of the function $f(B)$ and the three solutions $B_1 > B_2 > B_3$ of the self-consistency equation (16). The system parameters are as follows: $a = 1$, $K = 5$, $\alpha = 0$, $\Omega = 0.87$, and $\Delta = 6$.

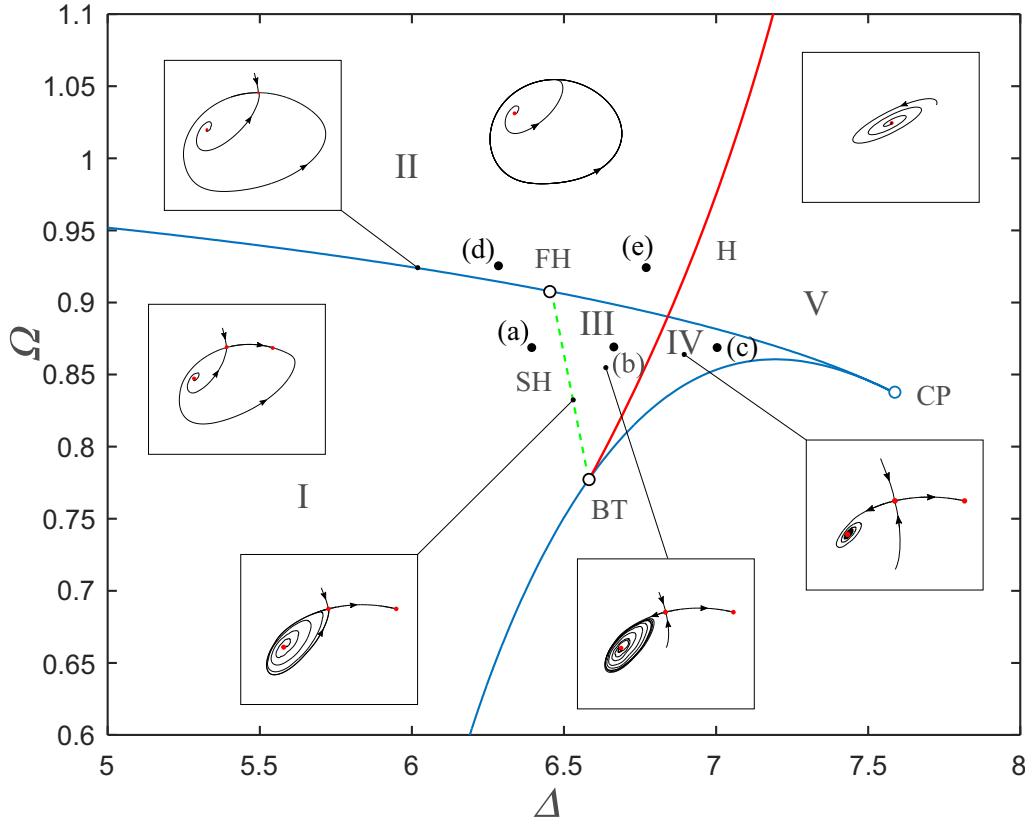


FIG. 2. Bifurcation diagram in the (Ω, Δ) plane, constructed by the method of stability analysis described in the Appendix. The remaining system parameters are fixed to $a = 1$, $K = 5$, $\alpha = 0$. The two branches of saddle-node bifurcations (blue solid lines) emanate from the cusp point CP, where the pitchfork bifurcation occurs. From the Bogdanov-Takens point (BT) emanate the Hopf bifurcation curve (H), indicated by the red solid line, and a branch of saddle-homoclinic bifurcations (SH), shown by the green dashed line. The upper branch of folds meets SH at the fold-homoclinic point (FH). The bullets indicate the parameter values associated to the time series in Fig. 4.

Fig. 4(a). We shall demonstrate below that the global rest state may disappear in a fold bifurcation. In contrast to the macroscopic regime given by B_1 , the stationary state corresponding to B_3 is typically a heterogeneous one, involving a subassembly of excitable units ($|\omega_i| < B_3$) and a subassembly of oscillating units ($|\omega_i| > B_3$), see the example of the time series in Fig. 4(c). In Ref. [13], the heterogeneous stationary state is referred to as the asynchronous state, because spiking activity may be observed at the level of single units, but the macroscopic dynamics *per se* does not exhibit a collective mode. The heterogeneous state, as shown in greater detail below, may undergo either a fold or Hopf bifurcation scenario. The stationary state associated to B_2 conforms to a saddle within the relevant (Ω, Δ) domain, undergoing fold bifurcations either with B_1 or B_3 or providing for the separatrices in case of the two observed bistable regimes.

The bifurcation diagram in Fig. 2 shows how the number and stability of the stationary solutions of the Ott-Antonsen equation (8) changes under variation of the parameters of the frequency distribution Ω and Δ . The diagram features five characteristic domains I–V and is organized around three codimension-2 bifurcation points, namely (i) the cusp point (CP), which corresponds to a symmetry-breaking pitchfork bifurcation; (ii) the Bogdanov-Takens point (BT), which unfolds into Hopf (H) and saddle-homoclinic (SH) bifurcation curves; and (iii), the fold-homoclinic point (FH), where a branch of

saddle-node bifurcations meets a curve of homoclinic tangencies of a limit cycle. The upper and the lower branch of folds, which emanate from the cusp, correspond to the coalescence of the state B_2 with B_1 and B_3 , respectively. The former or latter branch has been obtained by solving for the parameters where the local minimum or maximum of the function $f(B)$ crosses the zero level. The Hopf bifurcation curve has been determined by the local stability analysis of the stationary state B_3 . While such local analysis cannot provide for the saddle-homoclinic branch, its existence follows from the general structure of the Bogdanov-Takens bifurcation [42,43].

In the following, we provide a detailed description of the regimes underlying domains I–V, illustrating the associated phase portraits, cf. Fig. 2, and explaining the bifurcations that outline their stability boundaries. At the cusp point CP, the two branches of saddle-node bifurcations coalesce, cf. the two blue solid lines in Fig. 2. In terms of the stationary states B_1 – B_3 from Fig. 1, to the right of CP there exists only a stable fixed point B_2 . Following the pitchfork bifurcation, B_2 becomes a saddle, whereas two stable nodes, B_1 and B_3 , are created. The parameter region admitting only a single stable stationary state, be it B_1 , B_2 , or B_3 , is denoted by V in Fig. 2. Decreasing the diversity, the stability of B_1 is influenced only by a fold bifurcation, whereas the character and stability of B_3 are influenced by the fold and Hopf bifurcations, derived from the Bogdanov-Takens point. We have evinced that while

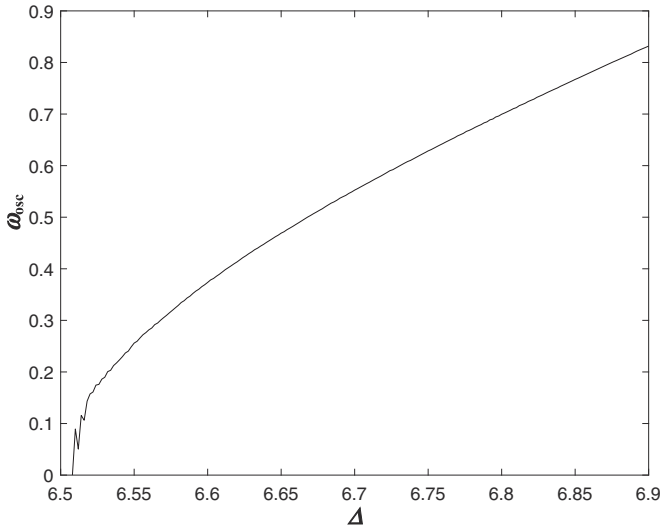


FIG. 3. Oscillation frequency of the periodic solution ω_{osc} in terms of diversity Δ , calculated along the Hopf bifurcation curve. One observes that the frequency tends to zero while approaching the Bogdanov-Takens point. The parameters a , K , and α are the same as in Fig. 2.

approaching BT, the frequency of oscillations ω_{osc} expectedly tends to zero, see Fig. 3. Along the lower branch of folds B_2 and B_3 get annihilated, so that from the right of this curve and to the cusp point, the only stable stationary state of the system is the node B_1 . The Hopf bifurcation curve that emanates from the BT point affects the stability of the stationary state B_3 , such that it becomes unstable for smaller diversities. This implies that within the region IV, bounded by the Hopf curve to the right and the two fold curves on the left, one observes *bistability between two stationary states*, namely the stable node B_1 and the stable focus B_3 , which

are separated by the stable manifold of the saddle B_2 , cf. the corresponding phase portrait in Fig. 2. Reducing diversity, B_3 undergoes a supercritical Hopf bifurcation (H), whereby immediately to the left of the Hopf curve (region III), one finds *bistability between a small limit cycle and the stable node* B_1 , again separated by the stable manifold of the saddle B_2 . The time series illustrating the microscopic and macroscopic dynamics of the oscillatory states born from the Hopf bifurcation for two different parameter sets, $(\Omega_1, \Delta_1) = (0.87, 6.76)$ and $(\Omega_2, \Delta_2) = (0.93, 6.78)$, are provided in Fig. 4(b) and Fig. 4(e).

Consistent with the Bogdanov-Takens scenario, the limit cycle born from the Hopf bifurcation is destabilized via a homoclinic tangency to the saddle B_2 , which is reflected by a branch of saddle-homoclinic bifurcations (SH) emanating from BT, see the green dashed line in Fig. 2. Using the local stability approach described in the Appendix, we are not able to trace the stability of a limit cycle *per se* but have been able to qualitatively verify the disappearance of the limit cycle by numerical means. The SH curve terminates at the fold-homoclinic point (FH), where it meets the upper branch of fold bifurcations. At FH, the stable manifold of the saddle B_2 touches the invariant circle. Decreasing diversity further away from the saddle-homoclinic bifurcation, cf. region I, the system exhibits a stable node B_1 and has two additional unstable fixed points, namely the saddle B_2 and the unstable focus B_3 .

At the upper branch of folds, under increasing diversity, the stable node B_1 and the saddle B_2 collide and disappear. For Δ values less than that of the FH point, the fold takes place on the invariant circle, giving rise to a SNIPER bifurcation. Crossing the SNIPER bifurcation either by increasing Ω or Δ , the collective dynamics of the system exhibits a transition toward the macroscopic oscillatory state. The latter is characterized by synchronous local oscillations of a large period, cf. the

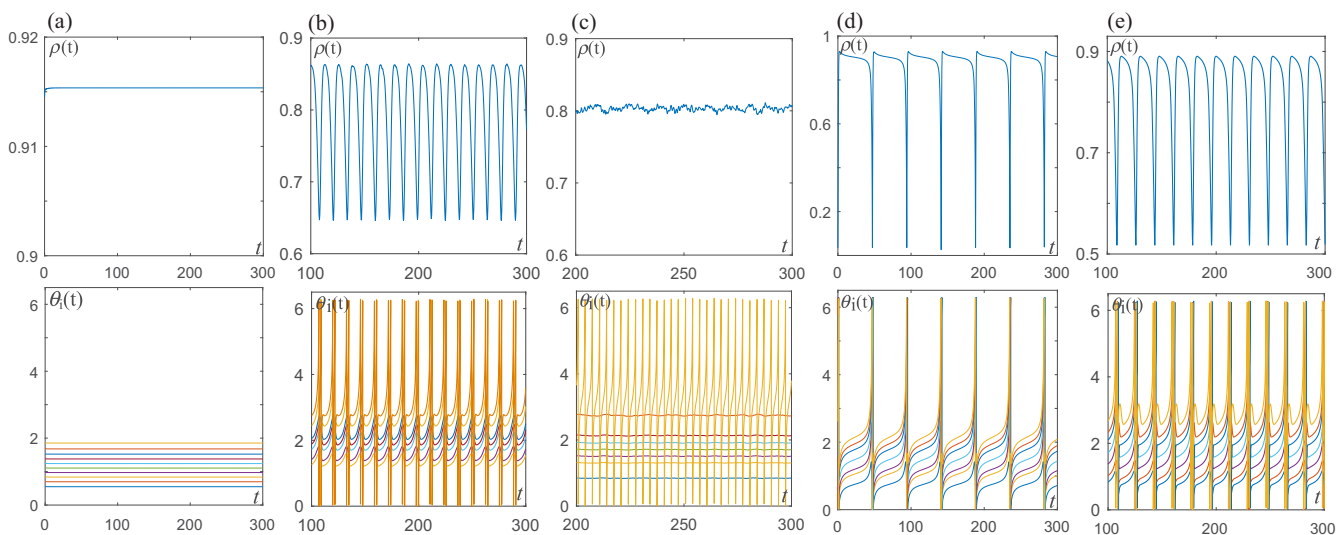


FIG. 4. Local and collective dynamics within the characteristic parameter domains indicated in Fig. 2. In the top row are provided the examples of the time series $\rho(t) = |R(t)|$, while in the bottom row are shown the corresponding local time series $\theta_i(t)$ normalized over 2π . The particular parameter values of the frequency distribution (indicated by bullets in Fig. 2) are $(\Omega, \Delta) = (0.87, 6.64)$ in (a), $(\Omega, \Delta) = (0.87, 6.76)$ in (b), $(\Omega, \Delta) = (0.87, 7)$ in (c), $(\Omega, \Delta) = (0.93, 6.6)$ in (d), and $(\Omega, \Delta) = (0.93, 6.78)$ in (e). The remaining system parameters are the same as in Fig. 2.

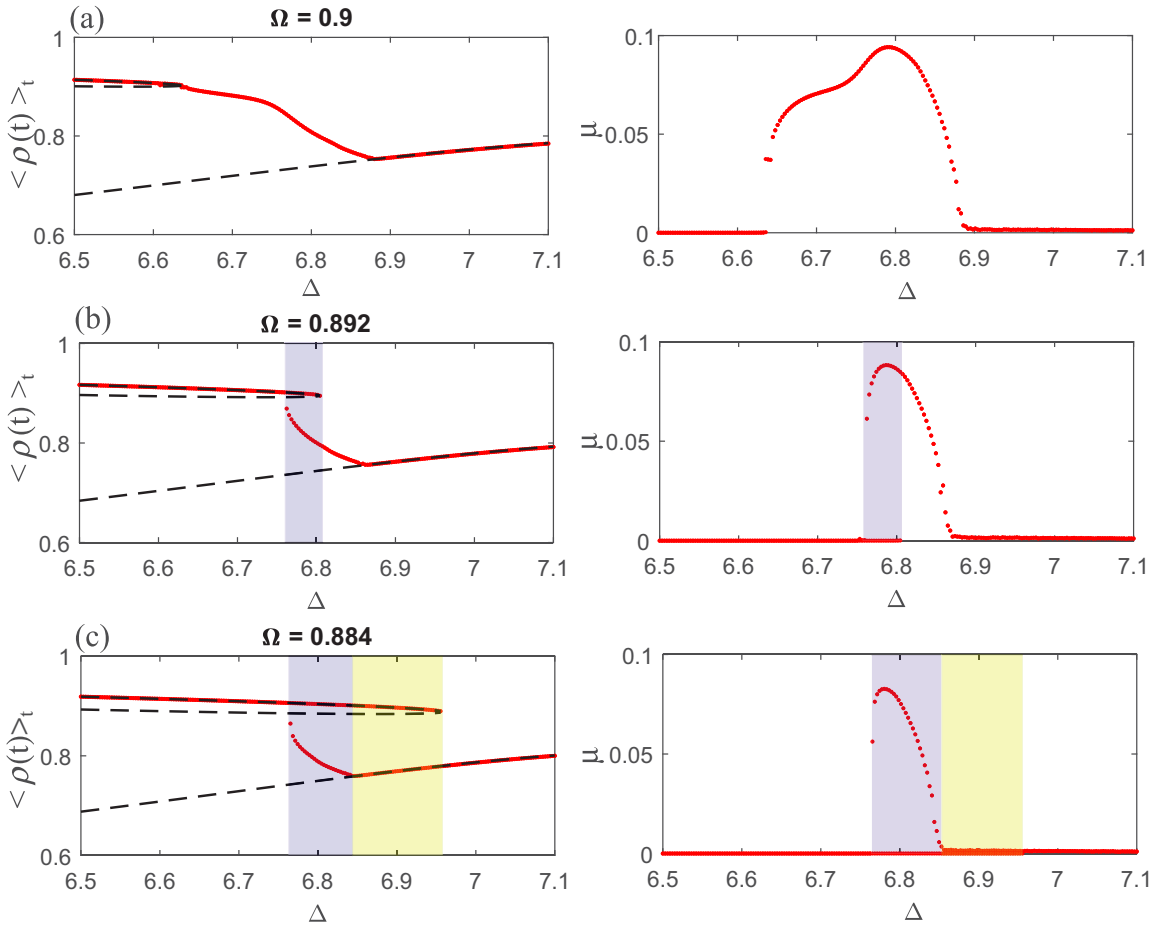


FIG. 5. Characteristic transition sequences between the different macroscopic regimes under increasing diversity for a fixed value of Ω . The states are described by the time-averaged modulus of the Kuramoto order parameter $\langle \rho(t) \rangle_t$ (left column) and the associated variance μ (right column). The mean frequencies are $\Omega = 0.9$ in (a), $\Omega = 0.892$ in (b), and $\Omega = 0.884$ in (c). The classical scenario of transitions is recovered in (a), whereas the two hysteretic scenarios involving passage over one or two bistability regions, indicated by shading in (b) and (c), are reported for the first time as far as we know.

time series in Fig. 4(e). For this reason, it is also called the *synchronous* state in Ref. [13]. For diversities to the right of the FH point, the saddle-node annihilation of B_1 and B_2 no longer occurs on an invariant circle. Thus, the only attractor within region VI corresponds to a small limit cycle emerging from Hopf destabilization of B_3 . For increasing diversity, B_3 gains stability by undergoing the inverse Hopf bifurcation, as already indicated above.

A. Classical and hysteretic transitions between macroscopic regimes

Having characterized all the regimes of macroscopic activity and the associated stability domains, we focus on the scenarios leading to the onset and the suppression of the collective mode in heterogeneous populations, an issue of outstanding importance in the theory of coupled dynamical systems. By the classical paradigm [13], the systematic increase of diversity under fixed mean frequency induces a sequence of transitions between the three regimes of collective dynamics, namely the global rest state, the synchronous state (corresponding to macroscopic oscillations), and the asynchronous

state (a heterogeneous state displaying mixed excitable and oscillatory local dynamics). Our study demonstrates that, apart from this, there exist two novel generic scenarios of transitions involving a *hysteretic behavior*. To gain a deeper insight into this problem, we have plotted how the time-averaged modulus of the Kuramoto mean-field $\rho(t) = |R(t)|$ and the associated variance $\mu = \sqrt{\langle \rho^2 \rangle_t - \langle \rho \rangle_t^2}$ change under variation of the diversity Δ for the three characteristic mean frequencies $\Omega \in \{0.9, 0.892, 0.884\}$, cf. Fig. 5. In order to reveal the potential bistable behavior, we have carried out sweeps in the directions of the increasing and the decreasing Δ applying the method of numerical continuation, where the initial conditions for the system with incremented Δ coincide with the final state at the previous Δ value.

The classical sequence of transitions is indeed recovered for $\Omega = 0.9$, see Fig. 5(a). There the onset of the collective mode is guided by a SNIPER bifurcation, mediating a transition from the homogeneous stationary state B_1 to a periodic solution. The suppression of the collective mode is induced by an inverse Hopf bifurcation that stabilizes the heterogeneous stationary state B_3 , which is analogous to the Kuramoto-type scenario where the system desynchronizes under increasing

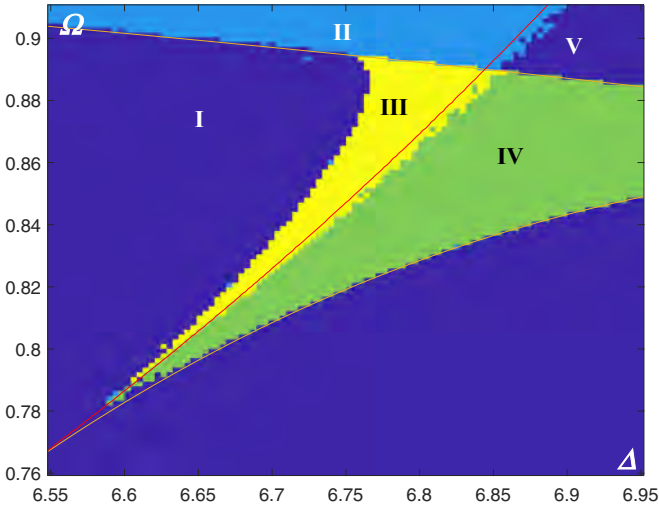


FIG. 6. The (Δ, Ω) parameter plane divided into regions with different macroscopic dynamics: the monostable stationary state (dark blue, regions I and V), monostable limit cycle (light blue, region II), bistability with two coexisting stationary states (green, region IV), and bistability between a stationary state and a limit cycle (yellow, region III). The parameter values are the same as in Fig. 2. Superimposed are the corresponding bifurcation curves obtained analytically within the Ott-Antonsen framework.

disorder. For $\Omega = 0.892$, we have established a hysteretic transition scenario, emerging due to a passage through a bistability region III from Fig. 2, which admits coexistence between the homogeneous stationary state B_1 and the periodic solution created from B_3 , cf. Fig. 5(b). In this case, the onset of a collective mode is induced by a Hopf bifurcation, while its suppression is controlled by the homoclinic tangency of the limit cycle. For $\Omega = 0.884$, the sequence of transitions remains hysteretic but becomes more complex, see Fig. 5(c). In particular, by increasing the diversity, one traverses over two bistability regions, denoted by III and IV in Fig. 2. While the first one is qualitatively the same as for $\Omega = 0.892$, the second one supports two coexisting stationary states, associated to B_1 and B_3 . Nevertheless, the onset and the suppression of the collective mode *per se* follow the same scenario as the one described in Fig. 5(b). Note that the described transition sequences are observed if the mean frequency Ω is sufficiently large.

In order to evince the generic character of the described scenarios and confirm the theoretical predictions regarding the parameter domains supporting the collective oscillations, we have carried out an extensive numerical study of the system's dynamics in terms of the parameters Δ and Ω , see Fig. 7. In particular, using numerical continuation, we have performed bidirectional sweeps over the (Ω, Δ) plane, keeping one of the parameters fixed while the other one was varied, in analogy to the method already described in relation to Fig. 6. This allowed us to partition the (Ω, Δ) plane into different regions according to the number and the type of the supported attractors. Comparison of the boundaries of these regions with the bifurcation curves from Fig. 2, which are shown overlaid, corroborates an excellent agreement between the theory and the numerical results.

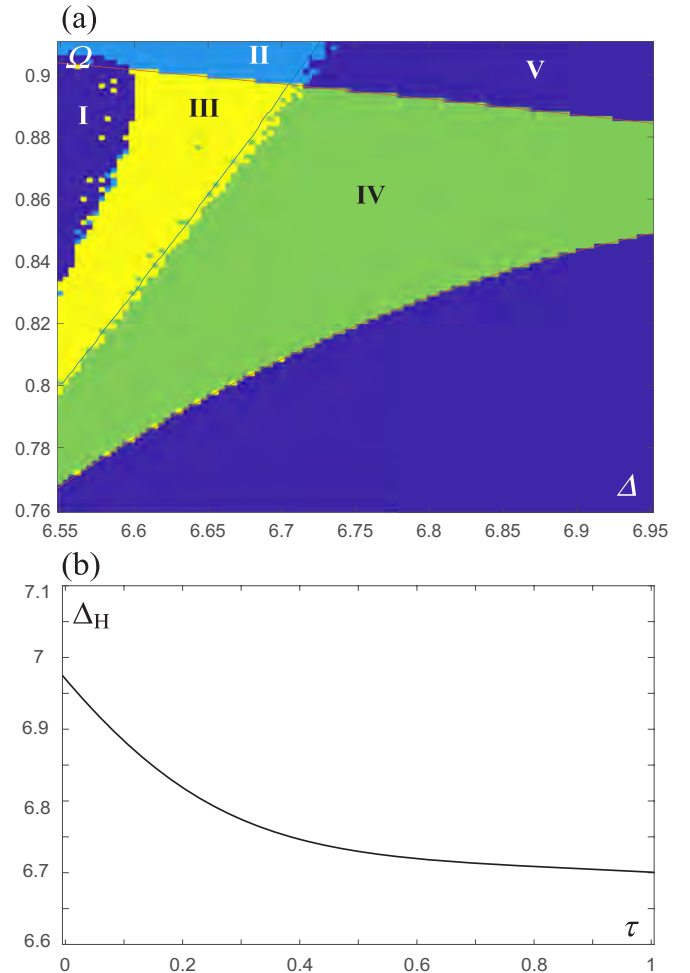


FIG. 7. (a) Characteristic domains of macroscopic behavior in the (Ω, Δ) plane for coupling delay $\tau = 0.3$. Color coding, as well as the remaining system parameters, are the same as in Fig. 6. Superimposed are the bifurcation curves obtained by the local stability approach described in the Appendix. (b) Critical diversity Δ_H corresponding to the Hopf destabilization of the state B_3 in dependence of τ for fixed $\Omega = 0.88$.

We have also examined whether the qualitative picture described so far persists under variation of the coupling strength K . It turns out that the general bifurcation structure holds qualitatively, which indicates the robustness of the scenarios underlying the transitions between the different collective regimes. Still, one notes that under increasing coupling strength, the cusp point and the Hopf bifurcation curve shift to a larger diversity (not shown).

V. IMPACT OF SMALL COUPLING DELAY AND SMALL NOISE

In this section, the goal is to demonstrate that the physical picture described so far for the noiseless and the delay-free case qualitatively also holds in presence of *small* noise or *small* coupling delay. The small-noise scenario concerns a range of noise levels where the applied perturbation typically cannot give rise to noise-induced oscillations but may rather evoke only rare spikes, so that the prevalent fraction

of units within the excitable subassembly remains at the quasistationary state. The small-delay scenario refers to delay values which are significantly less than the typical period of local oscillations, such that no delay-induced oscillations or multistability can emerge [44–46]. Essentially, our intention is not to perform an exhaustive exploration of the effects of noise or coupling delay but rather to confine the analysis to the cases where these two ingredients cannot evoke qualitatively new forms of collective behavior compared to the noiseless and delay-free case. We have carried out extensive numerical simulations to establish how the boundaries of the five characteristic domains in the (Ω, Δ) plane are modified due to the action of small noise or small coupling delay.

A. Effects of small coupling delay

The effects of small coupling delay are illustrated in Fig. 7(a), which shows the characteristic domains of macroscopic behavior in the (Ω, Δ) plane for the delay $\tau = 0.3$. One observes an excellent agreement between the bifurcation curves, obtained analytically by the local stability approach described in the Appendix, and the associated stability boundaries of the domains. In particular, introducing the coupling delay does not affect the very coordinates of the stationary states of the Ott-Antonsen equation (8), meaning that the branches of fold bifurcations remain unchanged relative to the delay-free case. Nevertheless, the key effect of the delay is that the Hopf bifurcation of the state B_3 , which underlies one of the scenarios for the onset of the collective mode, shifts to a smaller diversity compared to the delay-free case. This implies that the delay promotes multistable behavior, in the sense that the bistability domain IV, characterized by the coexistence between the stable stationary states B_1 and B_3 , becomes broader due to the impact of delay, cf. the green highlighted region in Fig. 7(a). From another point of view, the latter also suggests that the coupling delay promotes the onset of the collective mode via Hopf destabilization of the stationary state B_3 but suppresses the scenario where B_1 and B_2 undergo the SNIPER bifurcation. In Fig. 7(b) it is explicitly shown how the critical diversity Δ_H associated to Hopf bifurcation decreases with τ when Ω is kept fixed.

B. Effects of small noise

In contrast to the impact of coupling delay, the small noise is found to influence the effective positions of both the fold and the Hopf bifurcation curves, cf. Fig. 8(a), where the five characteristic domains for the noise level $\sigma = 0.3$ are shown together with the analytical curves for the *noiseless* case. The primary effect of small noise is to promote the onset of the collective mode mediated via the SNIPER bifurcation, in the sense that for a fixed mean frequency Ω , macroscopic oscillations can be observed for the diversity Δ smaller than those in the noiseless case. As a consequence, one observes that the critical diversity Δ_{SN} at which the fold between the states B_1 and B_2 takes place reduces under increasing σ , as indeed shown in Fig. 8(b) for the fixed $\Omega = 0.88$. Nonetheless, noise also shifts the location of the Hopf bifurcation relevant for the stability of the state B_3 , see Fig. 8(a). This may be interpreted as a disordering effect of noise, in the sense

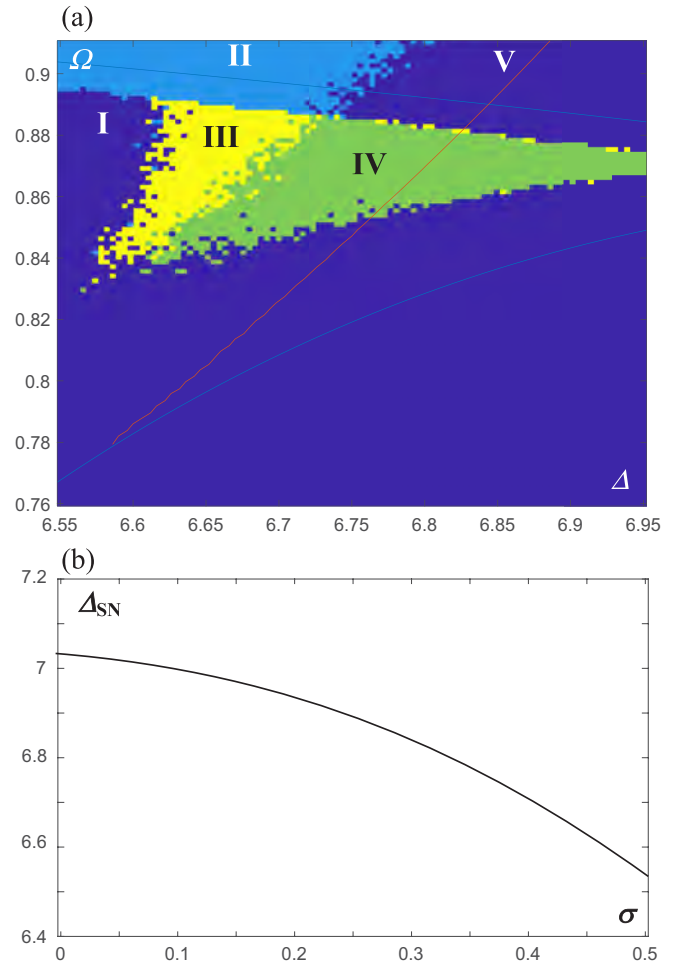


FIG. 8. (a) Characteristic domains of macroscopic dynamics in the (Ω, Δ) plane for the noise level $\sigma = 0.3$. The color coding and the remaining system parameters are the same as in Fig. 6. Superimposed are the bifurcation curves obtained analytically for the *noise-free* case $\sigma = 0$. (b) Decrease of the critical diversity Δ_{SN} with σ , corresponding to the saddle-node annihilation of the states B_1 and B_2 for fixed $\Omega = 0.88$.

that the transition from the regime of macroscopic oscillations (domain II) to the asynchronous regime (domain V) occurs at the diversity smaller than that for the noise-free case. Also note that the bistability regions III and IV shrink as compared to the noiseless case.

In principle, one observes that the structure of the characteristic domains is qualitatively preserved with introduction of small noise, but the associated stability boundaries shift to the left with respect to the noiseless case. This can be understood by the following qualitative reasoning. The impact of small noise on the local dynamics of the nodes can roughly be interpreted as a perturbation of the intrinsic frequency ω_i . To corroborate this, in Fig. 9 we illustrate how the *effective* oscillation frequencies of single units $\omega_{\text{eff},i}$, calculated numerically as the inverse of the respective mean oscillation periods, change in the presence of noise $\sigma = 0.3$. One finds that a certain fraction of units whose intrinsic frequencies ω_i lie closest to the excitability threshold $\omega = 1$ acquire a nonzero effective frequency, i.e., manifest noise-induced oscillations,

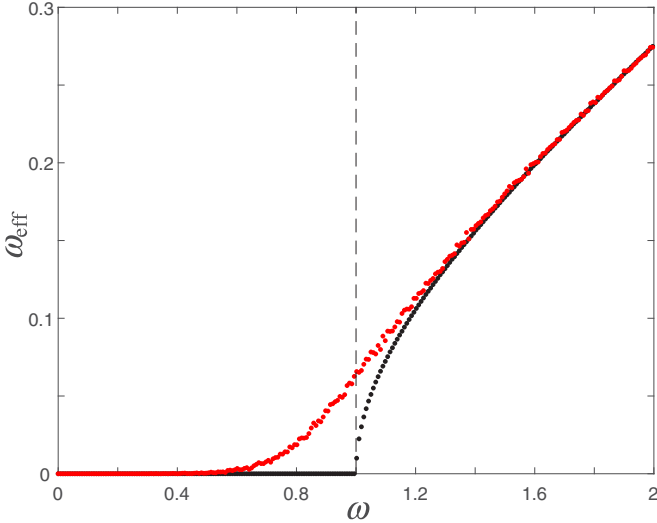


FIG. 9. Effective oscillation frequencies of uncoupled units ω_{eff} for the noiseless case (black dots) and under noise intensity $\sigma^2 = 0.09$ (red dots) as a function of the intrinsic parameters ω_i . The dashed line indicates the excitability threshold $\omega = 1$. The frequency distribution $g(\omega)$ is characterized by $\Omega = 2$, $\Delta = 4$.

while the excitable units further away from the threshold remain quasistationary. Nonetheless, the impact of noise on the self-oscillating units is reflected as a small increase of their effective frequency. Thus, in qualitative terms, the effect of small noise amounts to enhancing the effective frequency of the units near the threshold $\omega = 1$. Since this effect is symmetrical for positive and negative ω , the average assembly frequency Ω remains unchanged, whereas the variance of the associated distribution increases proportionally to the noise intensity. Therefore the introduction of small noise should lead to similar effects as the increase of diversity Δ .

VI. SUMMARY AND CONCLUSION

Considering a heterogeneous assembly of active rotators displaying excitable or oscillatory local dynamics, we have classified the associated macroscopic regimes and have demonstrated the generic scenarios for the onset and the suppression of collective oscillations. The analytical part of the study has been carried out within the framework of Ott-Antonsen theory applied for the delay- and noise-free system in the continuum limit, which enabled us to determine the three macroscopic stationary states in case of an arbitrary distribution of natural frequencies. The main qualitative insight into the microscopic structure of stationary states is that the population may in principle split into the excitable and the rotating subassembly, with the division depending on the relationship between the respective natural frequency of a rotator and the macroscopic excitability parameter. In this context, we have identified a homogeneous equilibrium where the units typically lie at rest, as well as a heterogeneous (mixed) collective stationary state, composed of units either in the excitable regime or the oscillatory regime. The local approach to stability and bifurcation analysis of the stationary states we have derived allowed us to address both the delay-free case and the case where the system's behavior is

influenced by coupling delay. The analysis has been specified to the particular case of a uniform frequency distribution on a bounded interval. While the stationary states have been determined earlier for a similar, but a less general model [13], the stability analysis, as presented here, has been carried out for the first time.

We have demonstrated that the complex bifurcation structure underlying the stability boundaries of the different macroscopic regimes is organized by three codimension-two bifurcation points, including the Bogdanov-Takens point, the cusp point, and the fold-homoclinic point. Our analysis has revealed the existence of five characteristic domains, three of which support the monostable collective behavior, while two admit bistability, involving either the coexistence between two stable stationary states or the coexistence between a stationary and a periodic solution. We have found that, depending on the mean frequency, the onset and the suppression of the collective mode may emerge via two qualitatively different scenarios under variation of diversity. In particular, for a smaller mean frequency, the onset of collective oscillations under decreasing diversity occurs due to a Hopf destabilization of a stationary state, whereas the oscillations are terminated via a saddle-homoclinic bifurcation. Nevertheless, for a sufficiently large mean frequency, increasing the diversity gives rise to collective oscillations in a SNIPER bifurcation, while the suppression of oscillations is due to an inverse Hopf bifurcation.

The classical paradigm concerning the sequence of transitions between the collective regimes in heterogeneous systems under increasing diversity involves three characteristic states, namely the global rest state; the synchronous state, characterized by macroscopic oscillations; and the asynchronous state, based on mixed excitable and oscillatory local dynamics [13]. In addition to this paradigm, our analysis has revealed two novel scenarios, which are hysteretic and involve a passage through one or two bistable domains. By the first scenarios, the transition from the global rest state to the asynchronous state occurs via two bistable regimes, the first involving a coexistence between a periodic solution and the rest state and the second one featuring coexistence between the rest state and the asynchronous state. The second hysteretic scenario is similar, but the intermediate stage involves only the coexistence between the homogeneous and the oscillatory state.

Combining theoretical methods and numerical experiments, we have shown that the basic bifurcation structure from the delay- and noiseless case persists in the presence of small noise or small coupling delay. Nevertheless, these two ingredients are found to modify the stability boundaries of the five characteristic domains. In particular, due to coupling delay, the position of the Hopf bifurcation curve is shifted toward the smaller diversity, which effectively promotes the Hopf-mediated onset of macroscopic oscillations and also enhances the parameter domain supporting bistability. Noise is seen to affect both the fold and the Hopf bifurcations, whereby the effective position of the fold or Hopf curve is shifted to smaller mean frequency or smaller diversity. At the level of macroscopic behavior, this is reflected as the promotion or suppression of the onset of macroscopic oscillations via SNIPER or Hopf bifurcation scenario, contributing in

addition to a reduction of the two bistability domains. While the described bifurcation structure appears to be generic for the considered type of frequency distribution, remaining qualitatively similar under the influence of small noise or small coupling delay, it would be interesting to examine whether and how it is modified for a substantially different form of a frequency distribution, such as a bimodal one.

ACKNOWLEDGMENTS

The work on Secs. III and IV was supported by the Russian Foundation for Basic Research under Project No. 17-02-00904. The work on Sec. V was supported by the Russian Foundation for Basic Research under Project No. 19-52-10004. The numerical simulations were supported by the Russian Science Foundation under Project No. 19-72-10114. I.F. acknowledges the support from the Ministry of Education, Science and Technological Development of the Republic of Serbia under Project No. 171017. The authors thank Matthias Wolfrum for fruitful discussions during the various stages of the study.

APPENDIX: CALCULATION OF THE STABILITY OF THE STATIONARY SOLUTION OF THE OTT-ANTONSEN EQUATION

Here we elaborate on the method applied to calculate the stability of the stationary solutions of the Ott-Antonsen equation (8). In particular, we first introduce the expressions $z(\omega, t) = x(\omega, t) + iy(\omega, t)$ and $R(\omega, t) = X(\omega, t) + iY(\omega, t)$ for the local and the global order parameters, respectively, transforming (8) to

$$\begin{aligned} \dot{x} = F(x, y, X, Y) = & \frac{a}{2}(y^2 - x^2 + 1) - \omega y \\ & - Kxy(Y \cos \alpha - X \sin \alpha) - \frac{K}{2}(X \cos \alpha + Y \sin \alpha) \\ & \times (x^2 - y^2) + \frac{K}{2}(X \cos \alpha + Y \sin \alpha) \end{aligned}$$

$$\begin{aligned} \dot{y} = G(x, y, X, Y) = & -axy + \omega x - Kxy(Y \sin \alpha + X \cos \alpha) \\ & + \frac{K}{2}(Y \cos \alpha - X \sin \alpha)(x^2 - y^2) \\ & + \frac{K}{2}(Y \cos \alpha - X \sin \alpha). \end{aligned} \quad (\text{A1})$$

The linearization of Ott-Antonsen equation (8) for variations $\xi = (\delta x, \delta y)^T$, $\Xi = (\delta X, \delta Y)^T$ of the stationary solution (x_0, y_0) can then succinctly be written in the matrix form as

$$\frac{d\xi(\omega, t)}{dt} = A(\omega)\xi(\omega, t) + B(\omega)\Xi(t), \quad (\text{A2})$$

where the matrices of derivatives are

$$A(\omega) = \begin{pmatrix} \frac{\partial F}{\partial x} & \frac{\partial F}{\partial y} \\ \frac{\partial G}{\partial x} & \frac{\partial G}{\partial y} \end{pmatrix}, \quad B(\omega) = \begin{pmatrix} \frac{\partial F}{\partial X} & \frac{\partial F}{\partial Y} \\ \frac{\partial G}{\partial X} & \frac{\partial G}{\partial Y} \end{pmatrix}. \quad (\text{A3})$$

Assuming that the variation $\xi(\omega, t)$ satisfies the ansatz $\xi(\omega, t) = \xi(\omega)e^{\lambda t}$, and similarly $\Xi(t) = \Xi e^{\lambda t}$, (A2) becomes

$$[A(\omega) - \lambda I]\xi(\omega) + B(\omega)\Xi = 0, \quad (\text{A4})$$

where I denotes the identity matrix. As shown in Ref. [40], the continuous Lyapunov spectrum consists of the eigenvalues of the matrix $B(\omega)$ for all $\omega \in [\omega_1, \omega_2]$. In our case, the continuous spectrum turns out to be always stable or marginally stable, such that the stability of the stationary solutions is determined by the discrete spectrum. In order to obtain the discrete spectrum, we multiply (A4) from the left by $g(\omega)[A(\omega) - \lambda I]^{-1}$ and integrate over ω obtaining $C(\lambda)\Xi = 0$, where

$$C(\lambda) = I + \int_{-\infty}^{\infty} d\omega g(\omega)[A(\omega) - \lambda I]^{-1}B(\omega). \quad (\text{A5})$$

The discrete Lyapunov spectrum can then be calculated by numerically solving the system $\det C(\lambda) = 0$.

In the case of nonzero coupling delay, the same type of analysis remains valid, while one has to replace X and Y in the r-hand side of (A1) by their delayed counterparts $X(t - \tau)$ and $Y(t - \tau)$. This leads to the same matrix $C(\lambda)$ as in (A5), with the only difference being the substitution of $B(\omega)$ by $B(\omega)e^{-\lambda\tau}$.

-
- [1] A. Pikovsky, M. Rosenblum, and J. Kurths, *Synchronization: A Universal Concept in Nonlinear Sciences* (Cambridge University Press, Cambridge, 2003).
- [2] J. A. Acebrón, L. L. Bonilla, C. J. P. Vicente, F. Ritort, and R. Spigler, *Rev. Mod. Phys.* **77**, 137 (2005).
- [3] Y. Baibolatov, M. Rosenblum, Z. Z. Zhanabaev, M. Kyzgarina, and A. Pikovsky, *Phys. Rev. E* **80**, 046211 (2009).
- [4] I. Franović, K. Todorović, N. Vasović, and N. Burić, *Phys. Rev. E* **87**, 012922 (2013).
- [5] S. Olmi, R. Livi, A. Politi, and A. Torcini, *Phys. Rev. E* **81**, 046119 (2010).
- [6] S. Strogatz, *Physica D (Amsterdam)* **143**, 1 (2000).
- [7] N. Komin and R. Toral, *Phys. Rev. E* **82**, 051127 (2010).
- [8] C. J. Tessone, A. Scirè, R. Toral, and P. Colet, *Phys. Rev. E* **75**, 016203 (2007).
- [9] D. Pazo and E. Montbrió, *Phys. Rev. E* **73**, 055202(R) (2006).
- [10] Y. Kuramoto, *Chemical Oscillations, Waves, and Turbulence* (Springer-Verlag, Berlin, 1984).
- [11] F. A. Rodrigues, T. K. DM. Peron, P. Ji, and J. Kurths, *Phys. Rep.* **610**, 1 (2016).
- [12] C. J. Tessone, C. R. Mirasso, R. Toral, and J. D. Gunton, *Phys. Rev. Lett.* **97**, 194101 (2006).
- [13] L. F. Lafuerza, P. Colet, and R. Toral, *Phys. Rev. Lett.* **105**, 084101 (2010).
- [14] E. Ott and T. M. Antonsen, *Chaos* **18**, 037113 (2008).
- [15] E. Ott and T. M. Antonsen, *Chaos* **19**, 023117 (2009).
- [16] L. S. Tsimring and A. Pikovsky, *Phys. Rev. Lett.* **87**, 250602 (2001).
- [17] A. Pototsky and N. B. Janson, *Phys. Rev. E* **77**, 031113 (2008).

- [18] A. Zakharova, S. A. M. Loos, J. Siebert, A. Gjurchinovski, J. C. Claussen, and E. Schöll, Controlling chimera patterns in networks: Interplay of structure, noise, and delay, in *Control of Self-Organizing Nonlinear Systems*, edited by E. Schöll, S. H. L. Klapp, and P. Hövel (Springer International Publishing, Cham, Switzerland, 2016).
- [19] F. M. Atay (ed.), *Complex Time-Delay Systems: Theory and Applications* (Springer, Berlin, 2010).
- [20] E. Schöll, G. Hiller, P. Hovel, and M. A. Dahlem, *Philos. Trans. R. Soc. Lond. A* **367**, 1079 (2009).
- [21] A. Takamatsu, T. Fujii, and I. Endo, *Phys. Rev. Lett.* **85**, 2026 (2000).
- [22] M. G. Rosenblum and A. S. Pikovsky, *Phys. Rev. Lett.* **92**, 114102 (2004).
- [23] P. Perlikowski, S. Yanchuk, O. V. Popovych, and P. A. Tass, *Phys. Rev. E* **82**, 036208 (2010).
- [24] B. Lindner, J. García-Ojalvo, A. Neiman, and L. Schimansky-Geier, *Phys. Rep.* **392**, 321 (2004).
- [25] V. Klinshov and I. Franović, *Phys. Rev. E* **92**, 062813 (2015).
- [26] I. Franović and V. Klinshov, *Chaos* **28**, 023111 (2018).
- [27] I. Franović and V. Klinshov, *Europhys. Lett.* **116**, 48002 (2016).
- [28] I. Franović and V. Klinshov, *Eur. Phys. J.- Spec. Top.* **227**, 1063 (2018).
- [29] I. Franović, K. Todorović, M. Perc, N. Vasović, and N. Burić, *Phys. Rev. E* **92**, 062911 (2015).
- [30] I. Franović, M. Perc, K. Todorović, S. Kostić, and N. Burić, *Phys. Rev. E* **92**, 062912 (2015).
- [31] I. Bačić, V. Klinshov, V. I. Nekorkin, M. Perc, and I. Franović, *Europhys. Lett.* **124**, 40004 (2018).
- [32] S. Kadar, J. Wang, and K. Showalter, *Nat. Lond.* **391**, 770 (1998).
- [33] S. Alonso, I. Sendina-Nadal, V. Perez-Munuzuri, J. M. Sancho, and F. Sagues, *Phys. Rev. Lett.* **87**, 078302 (2001).
- [34] D. E. Postnov, S. K. Han, T. G. Yim, and O. V. Sosnovtseva, *Phys. Rev. E* **59**, R3791 (1999).
- [35] M. A. Zaks, A. B. Neiman, S. Feistel, and L. Schimansky-Geier, *Phys. Rev. E* **68**, 066206 (2003).
- [36] M. Y. Choi, H. J. Kim, D. Kim, and H. Hong, *Phys. Rev. E* **61**, 371 (2000).
- [37] I. V. Tyulkina, D. S. Goldobin, L. S. Klimenko, and A. Pikovsky, *Phys. Rev. Lett.* **120**, 264101 (2018).
- [38] D. S. Goldobin, I. V. Tyulkina, L. S. Klimenko, and A. Pikovsky, *Chaos* **28**, 101101 (2018).
- [39] M. Wolfrum, S. V. Gurevich, and O. E. Omel'chenko, *Nonlinearity* **29**, 257 (2016).
- [40] O. E. Omel'chenko, and M. Wolfrum, *Physica D (Amsterdam)* **263**, 74 (2013).
- [41] O. E. Omel'chenko and M. Wolfrum, *Phys. Rev. Lett.* **109**, 164101 (2012).
- [42] H. Sakaguchi, S. Shinomoto, and Y. Kuramoto, *Prog. Theor. Phys.* **79**, 600 (1988).
- [43] B. Sonnenschein, M. A. Zaks, A. B. Neiman, and L. Schimansky-Geier, *Eur. Phys. J. Spec. Top.* **222**, 2517 (2013).
- [44] S. Yanchuk and P. Perlikowski, *Phys. Rev. E* **79**, 046221 (2009).
- [45] V. Klinshov, L. Lüicken, D. Shchapin, V. Nekorkin, and S. Yanchuk, *Phys. Rev. Lett.* **114**, 178103 (2015).
- [46] M. Wolfrum, S. Yanchuk, P. Hövel, and E. Schöll, *Eur. Phys. J. Spec. Top.* **191**, 91 (2010).

Leap-frog patterns in systems of two coupled FitzHugh-Nagumo units

Sebastian Eydam,^{1,*} Igor Franović,² and Matthias Wolfrum¹

¹Weierstrass Institute for Applied Analysis and Stochastic, Mohrenstrasse 39, 10117 Berlin, Germany

²Scientific Computing Laboratory, Center for the Study of Complex Systems, Institute of Physics Belgrade, University of Belgrade, Pregrevice 118, 11080 Belgrade, Serbia



(Received 17 January 2019; published 12 April 2019)

We study a system of two identical FitzHugh-Nagumo units with a mutual linear coupling in the fast variables. While an attractive coupling always leads to synchronous behavior, a repulsive coupling can give rise to dynamical regimes with alternating spiking order, called leap-frogging. We analyze various types of periodic and chaotic leap-frogging regimes, using numerical path-following methods to investigate their emergence and stability, as well as to obtain the complex bifurcation scenario which organizes their appearance in parameter space. In particular, we show that the stability region of the simplest periodic leap-frog pattern has the shape of a locking cone pointing to the canard transition of the uncoupled system. We also discuss the role of the timescale separation in the coupled FitzHugh-Nagumo system and the relation of the leap-frog solutions to the theory of mixed-mode oscillations in multiple timescale systems.

DOI: [10.1103/PhysRevE.99.042207](https://doi.org/10.1103/PhysRevE.99.042207)

I. INTRODUCTION

The FitzHugh-Nagumo system is a classical model of neuronal dynamics. As the simplest, yet paradigmatic example of a coupled neuronal system, we investigate here a pair of two identical FitzHugh-Nagumo units with a weak mutual coupling. Such a network motif of two coupled neurons has been considered as a basic building block of central pattern generators [1] and the complex neural networks of the cortex [2–5]. The dynamics of such systems has typically been investigated in the framework of the synchronization paradigm [6–8], focusing on the stability of states with phase-locked firing and their potential role in rhythmogenesis [9]. Nevertheless, a remarkable property of these simple circuits is that they are also able to generate complex activity patterns where the interspike intervals show complex dynamics. A typical example of such patterns is the so-called leap-frog dynamics [10], sometimes also called leader-switching dynamics [11], where the units exchange their order of firing within each oscillation cycle. Such a regime has so far been associated exclusively to class I neural oscillators coupled via strong synapses with complex nonlinear dynamics [12–16]. In the present paper, we investigate the emergence of leap-frogging dynamics in a system of two classical FitzHugh-Nagumo units interacting only via a small linear coupling. The emerging complex dynamical patterns can be explained as a result of the timescale separation between the activator and the recovery variable. For a single unit, the timescale separation is crucial for the mechanism inducing the rapid change in the amplitude from small subthreshold oscillations to large relaxation oscillations. Introducing a repulsive coupling in the

fast variables, the leap-frog patterns emerge in locking cones generated by a complex bifurcation scenario immediately at this transition. The alternation in the spiking order of the units arises from trajectories containing both the small-amplitude subthreshold oscillations and the large-amplitude relaxation oscillations. Such a behavior involving interspersed small- and large-amplitude oscillations, called *mixed-mode oscillations* [17–20], is a typical phenomenon in slow-fast systems with at least two slow variables and has been studied extensively by geometric singular perturbation methods for the limit of infinite timescale separation. In particular, a three-dimensional version of the FitzHugh-Nagumo system has been used as a classical example for mixed-mode oscillations, see, e.g., Ref. [20] and references therein. Singular perturbation techniques have been also applied to coupled nonidentical mixed-mode oscillators [21] and for the synchronization of weakly coupled slow-fast oscillations [22].

Coupled systems of two identical oscillators have specific symmetry properties, which at vanishing coupling induce an additional degeneracy. First numerical studies of coupled slow-fast oscillators can already be found in Refs. [23,24], where a detailed exposition of the four-dimensional slow-fast structure is given. Due to the symmetry-induced degeneracy, for such systems the existing theoretical results for mixed-mode oscillations do not apply directly. We will present here a first numerical exploration of a system of two identical FitzHugh-Nagumo units with symmetric mutual coupling. Our approach will be a detailed bifurcation analysis using path-following methods at finite values of the timescale separation. We perform this both for the degenerate case of small coupling, where we find an essentially new dynamical scenario, and for larger coupling, where the leap-frog dynamics is organized in a way that conforms to the general results on mixed-mode oscillations.

*sebastian.eydam@wias-berlin.de

The dynamics of the considered system of two identical FitzHugh-Nagumo units is given by

$$\begin{aligned}\frac{dv_{1,2}}{dt} &= v_{1,2} - v_{1,2}^3/3 - w_{1,2} + c(v_{2,1} - v_{1,2}), \\ \frac{dw_{1,2}}{dt} &= \varepsilon(v_{1,2} + b),\end{aligned}\quad (1)$$

where the symmetric linear coupling acts in the fast variables $v_{1,2}$. The small parameter ε facilitates the timescale separation between the fast variables v_i and the slow variables w_i . In the context of neuroscience, the former represent the neuronal membrane potentials, whereas the latter correspond to the coarse-grained activities of the membrane ion-gating channels. For a single unit, the parameter b mediates the transition from the quiescent regime for $b > 1$ to the oscillatory regime for $-1 < b < 1$. Due to the timescale separation, this is accompanied by a *canard transition* from small-amplitude subthreshold oscillations to the large-amplitude relaxation oscillations. We invoke some basic results derived from singular perturbation theory about the slow-fast structure of the uncoupled FitzHugh-Nagumo unit in Sec. II.

Since the parameters b and ε are taken to be identical for both units, system Eq. (1) possesses a \mathbb{Z}_2 -symmetry, being equivariant with respect to exchanging the indices by

$$\sigma : (v_1, w_1, v_2, w_2) \mapsto (v_2, w_2, v_1, w_1).$$

This leads to the appearance of solutions with different symmetry types, reflecting the different states of in-phase and anti-phase synchronization, which will be discussed in Sec. II which concerns the basic types of solutions bifurcating from the stationary regime. Close to the canard transition of the uncoupled system, there appear various types of periodic and chaotic leap-frog patterns in the system with repulsive coupling. Using the software package AUTO [25] for numerical bifurcation analysis by continuation methods, in Sec. III we investigate in detail the complex bifurcation scenarios responsible for the onset of the different types of leap-frogging dynamics. We conclude the paper with an outlook in Sec. IV, discussing the relation of our results to earlier findings on leap-frog dynamics in models of neuronal systems.

II. BASIC DYNAMICAL REGIMES

We begin our investigation of system Eq. (1) by collecting simple stationary and periodic solutions together with their stability and symmetry properties. In the symmetric regime

$$v_1 = v_2 \quad \text{and} \quad w_1 = w_2, \quad (2)$$

the coupling term vanishes and the dynamics Eq. (1) is governed by a single FitzHugh-Nagumo system, where the units display simultaneously the well-known transition from the quiescent regime with a unique stable equilibrium for $b > 1$ to the oscillatory regime for $b < 1$, mediated by a supercritical Hopf bifurcation at $b = 1$. Due to the timescale separation $0 < \varepsilon \ll 1$, the bifurcating branch of periodic solutions displays a characteristic transition from small-amplitude harmonic oscillations of period $O(1/\sqrt{\varepsilon})$ to large-amplitude relaxation oscillations of period $O(1/\varepsilon)$, called a *canard transition*. This scenario has been extensively studied within the framework of singular perturbation theory, viz. in the

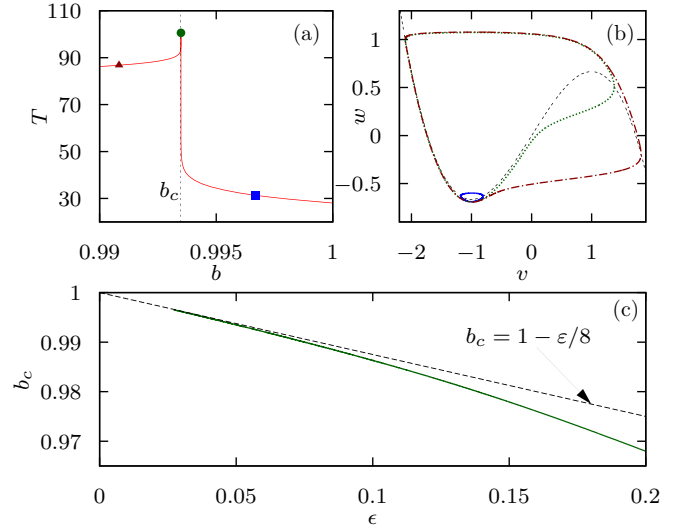


FIG. 1. (a) Variation of the period T along the branch of synchronous periodic solutions for varying b and fixed $\varepsilon = 0.05$. (b) Phase portraits of selected periodic solutions: a subthreshold oscillation for $b_c < b < b_H$ (blue solid), the canard trajectory $b_c = b$ (green dotted), a relaxation oscillations with $b_c > b$ (red dotted-dashed), corresponding to the square, the triangle, and the disk, in (a) respectively, and the cubic nullcline (dashed black). The corresponding values of b are indicated by the colored dots in (a). (c) Location of the canard transition b_c for varying ε . Numerical path-following of the periodic solution with maximal period (green line) is compared to asymptotic formula Eq. (3), shown dashed.

limit $\varepsilon \rightarrow 0$; see, e.g., Ref. [18] for a recent overview. In Fig. 1 we illustrate the canard transition in the symmetric regime, showing numerical results obtained by path-following methods [25]. In Fig. 1(a) we have fixed $\varepsilon = 0.05$, displaying the varying period along the branch of periodic orbits emerging from the Hopf-bifurcation at $b = b_H = 1$. Note the nearly vertical transition from small to large periods at the canard transition $b = b_c$. The phase portraits of the three orbits shown in Fig. 1(b), selected before, after, and immediately at the transition, indicate that the change in the period is accompanied by a transition from small to large amplitudes via *canard trajectories* that follow the unstable part of the slow manifold, which is close to the critical manifold $w = v - v^3/3$. From the neuroscience perspective, this corresponds to a transition route from the quiescent state to the spiking regime via subthreshold oscillations. A detailed asymptotic analysis reveals that the leading order approximation for the location b_c of the canard transition is given by

$$b_c \approx (1 - \varepsilon/8), \quad (3)$$

see Ref. [26]. In Fig. 1(c) we show that for small $\varepsilon > 0$ this expression (dashed line) provides indeed a good approximation for the actual location of the canard transition (solid green line), which we obtained numerically by path-following in ε the trajectory of maximal period, sometimes called *maximal canard* [green curve in Fig. 1(b)]. Recall that both the regimes of stable equilibrium and of subthreshold oscillations are excitable [27,28] in a sense that a strong enough perturbation

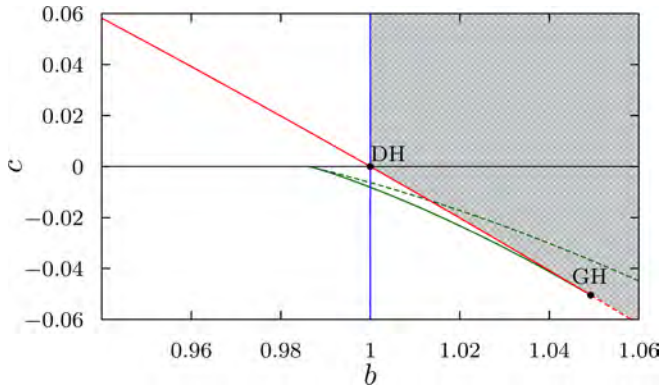


FIG. 2. Stability region (checked pattern) of the symmetric equilibrium Eq. (5) in the (b, c) plane, bounded by in-phase Hopf instability (vertical blue line) and antiphase Hopf instability (diagonal red line). The antiphase Hopf bifurcation changes from supercritical to subcritical in a generalized Hopf point (GH), where a fold curve of the antiphase synchronous limit cycles emerges (green line). DH denotes the resonant double Hopf point for the decoupled system at $(b, c) = (1, 0)$.

may elicit a large excursion in phase space, i.e., a spiking response in the form of a single relaxation oscillation.

The full system Eq. (1), which can be rewritten in coordinates longitudinal and transversal to the symmetry subspace Eq. (2),

$$v_{L,T} = v_1 \pm v_2, \quad w_{L,T} = w_1 \pm w_2, \quad (4)$$

has a slow-fast structure with two fast and two slow variables. For small coupling c , the corresponding critical manifolds and fast fibers are given trivially as a direct sum of the corresponding objects for each of the units. It can be easily seen that the only stationary state of Eq. (1) is the symmetric equilibrium

$$(v_1, w_1, v_2, w_2) = (-b, -b + b^3/3, -b, -b + b^3/3), \quad (5)$$

obtained from the single FitzHugh-Nagumo unit. While the symmetry-preserving Hopf bifurcation at $b = 1$ in the coupled system is analogous to the Hopf bifurcation of the single FitzHugh-Nagumo unit and does not depend on the coupling parameter c , in the coupled system the symmetric equilibrium may also undergo symmetry-breaking bifurcations. In particular, it may become unstable via a Hopf bifurcation to antiphase synchronized periodic solutions of the form

$$v_1(t) = v_2\left(t + \frac{T}{2}\right), \quad w_1(t) = w_2\left(t + \frac{T}{2}\right), \quad (6)$$

where $T > 0$ is the period. Using the longitudinal and transversal coordinates Eq. (4) one obtains the condition

$$c = \frac{1 - b^2}{2} \quad (7)$$

for this antiphase Hopf instability of the synchronous equilibrium Eq. (5). In Fig. 2, the associated bifurcation curve is shown in the (b, c) plane together with the in-phase Hopf instability at $b = 1$. For attractive coupling $c > 0$, the stability region (checked pattern) of the symmetric equilibrium Eq. (5) is bounded by the in-phase Hopf instability, shown by

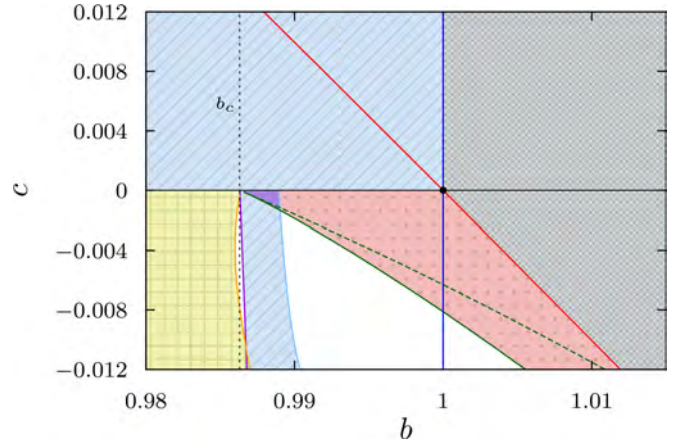


FIG. 3. Stability regions of basic periodic solutions in the (b, c) plane for $\epsilon = 0.1$: in-phase synchronous oscillations (blue diagonal stripes); antiphase synchronous subthreshold oscillations (red dotted); coexistence of in-phase and antiphase subthreshold oscillations (purple filled); asynchronous oscillations—successive spiking (yellow squared). Bifurcation curves delineating the stability boundaries: in-phase Hopf instability (vertical blue line); antiphase Hopf instability (diagonal red line); fold of antiphase synchronous limit cycles (left boundary of the lower dotted region, green); subcritical period doubling of in-phase subthreshold oscillations (left boundary of the lower striped region, purple); subcritical symmetry breaking pitchfork of in-phase subthreshold oscillations (right boundary of the lower striped region, light blue); supercritical period doubling of asynchronous oscillations (boundary of the squared region, orange). Canard transition at $b = b_c$ (black dashed); see Fig. 1.

the blue line, while for repulsive coupling $c < 0$, the stability boundary is given by the antiphase Hopf Eq. (7). For larger negative values of c , this bifurcation is subcritical, such that no stable branch of antiphase synchronized oscillations emerges. The criticality changes in a generalized Hopf (Bautin) point, labeled as GH in Fig. 2. From this point emanates a curve of folds of limit cycles, shown by the green line in Fig. 2. The two Hopf bifurcation curves intersect in the resonant double Hopf point (DH) located at $(b, c) = (1, 0)$. Note that this point belongs to the line $c = 0$ where the system decouples, thus behaving neutral with respect to all symmetry-breaking perturbations.

Figure 3 shows the stability regions and the associated stability boundaries of the periodic solutions. For attractive coupling $c > 0$, all synchronous oscillations are stable (blue diagonal striped region), undergoing at $b = b_c$ the canard transition from small- to large-amplitude oscillations as in the case of a single unit; cf. Fig. 1. For repulsive coupling $c < 0$, the situation is more complicated. There is a small region (red dotted in Fig. 3) above the generalized Hopf point and the emanating fold of limit cycles (green curve) where one finds stable antiphase synchronized oscillations. Note that after a secondary bifurcation, the fold of limit cycles (green curve) is no longer a stability boundary of the antiphase synchronized oscillations (dashed part of the curve). Surprisingly, there are also stable in-phase synchronized solutions for repulsive coupling $c < 0$. They are confined to a narrow region immediately below the canard transition, which is bounded by a curve of period doubling (left, purple line) and

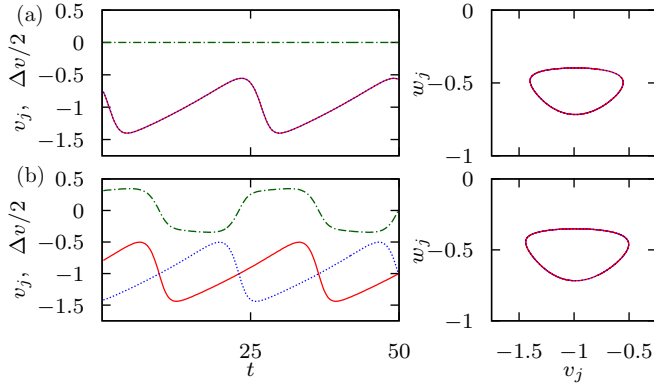


FIG. 4. Time traces and phase portraits of stable coexisting in-phase synchronous (a) and antiphase synchronous (b) subthreshold oscillations. Parameters $(\varepsilon, b, c) = (0.1, 0.9885, -0.0005)$ belong to the coexistence region (purple in Fig. 3). Variables $v_{1,2}(t)$ are shown in red (solid) and blue (dotted), whereas the coupling term $\Delta v = c(v_2 - v_1)$ is indicated in green color (dash-dotted).

a curve of symmetry-breaking pitchfork bifurcations (right, light blue line). In particular, for small negative coupling, one encounters a region of bistability, where both the in-phase and antiphase synchronized oscillations are stable (purple-shaded region in Fig. 3). Figure 4 illustrates coexisting stable in-phase and antiphase synchronous solutions computed for the parameters $(\varepsilon, b, c) = (0.1, 0.9885, -0.0005)$ from this region. Note that the coexistence region is confined to subthreshold oscillations prior to the canard transition at $b = b_c$.

Apart from the in-phase and antiphase synchronous regimes, there may also appear periodic solutions without any symmetry. For repulsive coupling $c < 0$ and beyond the canard transition, i.e., $b < b_c$, there is a large parameter region admitting a stable regime of *successive spiking*, with both units performing relaxation oscillations shifted in phase. The stability region of this successive spiking, shown in yellow (square pattern) in Fig. 3, is bounded by a curve of supercritical period doubling (right, orange line). Figures 5(a) and 5(b) provide the time traces and phase portraits for the regime of

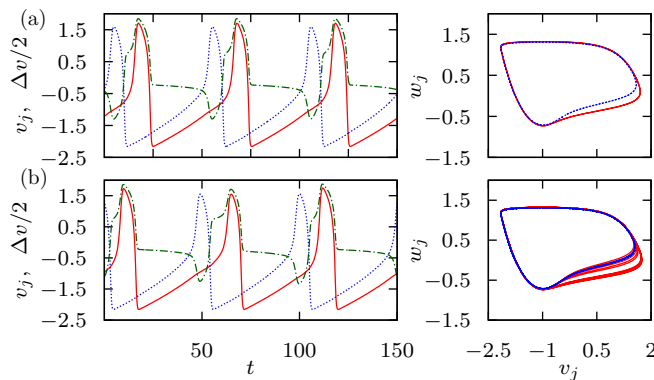


FIG. 5. Time traces and phase portraits of stable asymmetric successive spiking: (a) before period doubling ($b = 0.98625$) and (b) after several period doubling bifurcations ($b = 0.98692$). The remaining parameters are $(c, \varepsilon) = (-0.01, 0.1)$. Colors and line styles are as described in the caption of Fig. 4.

successive spiking before period doubling and after several period doubling bifurcations, respectively. Note that in Fig. 3 several bifurcation curves point toward the canard transition, thus creating a complex scenario where the different dynamical regimes with different symmetry properties bifurcate and interchange their stability. This indicates that a detailed study of the limit $\varepsilon \rightarrow 0, c \rightarrow 0$ could reveal the dependence of all these bifurcations on ε and in this way explain the whole scenario by an unfolding of the corresponding singularity.

Moreover, there is a region, indicated in white in Fig. 3, where none of the periodic solutions described above is stable. We demonstrate below that in this region the system exhibits several periodic or chaotic regimes characterized by the fact that the trajectory of each unit comprises large relaxation oscillation loops as well as smaller loops of a size comparable to that of subthreshold oscillations. This phenomenon of such so called mixed-mode oscillations has been extensively studied using geometric singular perturbation methods for the limit $\varepsilon \rightarrow 0$. They are known to arise generically in slow-fast systems with two slow variables and a folded node singularity. Let us very briefly recall the corresponding slow-fast geometry of system Eq. (1), see also Ref. [24]. Following the classical approach (see, e.g., Ref. [18]), we find the fold condition for the two-dimensional critical manifold as

$$(1 - v_1^2)(1 - v_2^2) = c(2 - v_1^2 - v_2^2).$$

For $c = 0$, this provides two lines of folds, intersecting at the point $v_1 = v_2 = -1$. At $b = 1$, the symmetric equilibrium Eq. (5) passes through this intersection of folds (DH point in Fig. 2). At the same time, the slow flow across the folds vanishes along the whole pair of intersecting lines of folds and hence violates also the usual genericity assumption on a folded singularity. An unfolding at small $c \neq 0$ of this degenerate situation involves the interplay of two small quantities. As a first step, we will explore these mixed-mode type dynamics without invoking the singular limit where these two quantities tend to zero. Instead, we use simulations and numerical path-following techniques to describe the bifurcation scenario for finite values of ε . Comparing the results of the numerical bifurcation analysis for different values of ε will also provide some information about possible scalings between the two small quantities.

III. COMPLEX DYNAMICAL REGIMES AT THE CANARD TRANSITION

To numerically examine the different types of solutions of system Eq. (1), we have performed a parameter sweep with respect to b at fixed $c = -0.01$ and $\varepsilon = 0.1$; see Fig. 6. The scan is performed by a numerical continuation according to the following procedure: after each increment in the sweeping parameter b , we use the final state of the preceding simulation as an initial condition, then discard a transient, and sample the return times T_n between consecutive crossings of the Poincaré section $w_1 = -2/3$. The robustness of the numerical results has been verified for different simulation step sizes of the fourth-order Runge-Kutta scheme, which has been used in all of our simulations. Sweeping has been carried out in forward (increasing b , red points) and backward direction (decreasing b , black points), allowing us to detect potential coexisting

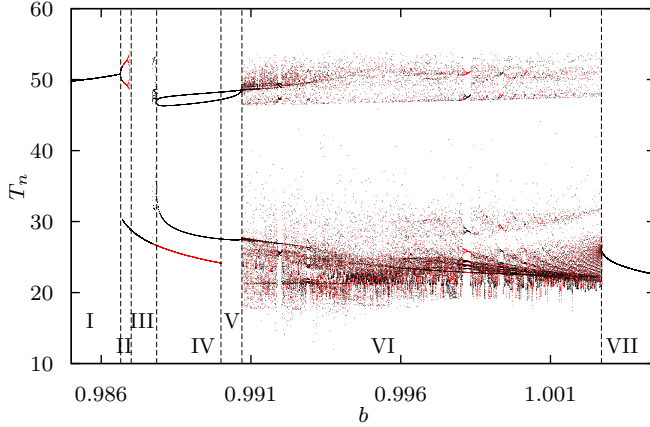


FIG. 6. Sampled return times T_n between consecutive crossings of the hyperplane $w_1 = -2/3$ for varying b and $(c, \varepsilon) = (-0.01, 0.1)$. Red and black points correspond to different sweeping directions in b .

stable regimes. Note that the return times $T_n \approx 50$ correspond to a single round trip of the unit $j = 1$ along the relaxation oscillation orbit, while the return times $T_n < 30$ correspond to a round trip following a subthreshold oscillation orbit. In Fig. 6, one can identify the regime of successive spiking in regions I and II, the in-phase subthreshold oscillations in regions II–IV, and the antiphase subthreshold oscillations in region VII. In addition, we find the periodic regime displayed in Fig. 7(a), which is the only attractor in region V and coexists with the in-phase subthreshold oscillations in region IV. Note that due to the space-time symmetry Eq. (6), the phase portraits of the trajectories of both units in the (v, w)

plane coincide. This periodic regime can be characterized as follows. Within one period, each unit performs two round trips along the relaxation oscillation orbit and one round trip along a subthreshold oscillation orbit. The spikes of the two units again occur with a phase shift as in the successive spiking regime. However, as a result of the inlaid subthreshold oscillations, the spiking order gets reversed for every pair of successive relaxation oscillations. This regime of alternating spiking order with a single subthreshold oscillation performed between each pair of successive spikes is referred to as *simple leap-frogging*. We shall discuss the underlying bifurcation scenario and its dependence on the slow-fast structure of the system in the following section.

In region VI, one observes chaotic behavior, interrupted by some small parameter intervals of more complicated periodic behavior. Chaotic mixed-mode oscillations have already been numerically observed in Ref. [29] for a periodically forced slow-fast oscillator. Examples of chaotic orbits are shown in Figs. 7(e) and 7(f). More complicated periodic orbits from some of the periodic windows in region VI are provided in Figs. 7(b)–7(d). The periodic orbits in Figs. 7(b) and 7(d) carry the space-time symmetry Eq. (6), which leads to a similar exchange in the spiking order as the leap-frog orbit in Fig. 7(a). The periodic solution in Fig. 7(c) is asymmetric, displaying successive spikes with fixed spiking order similar to Fig. 4(a), but interspersed with several almost antiphase subthreshold oscillations.

A. Simple leap-frogging

The dynamical regime of leap-frogging illustrated in Fig. 7(a) is a periodic regime where successive spikes occur with an alternating spiking order. The alternation is induced

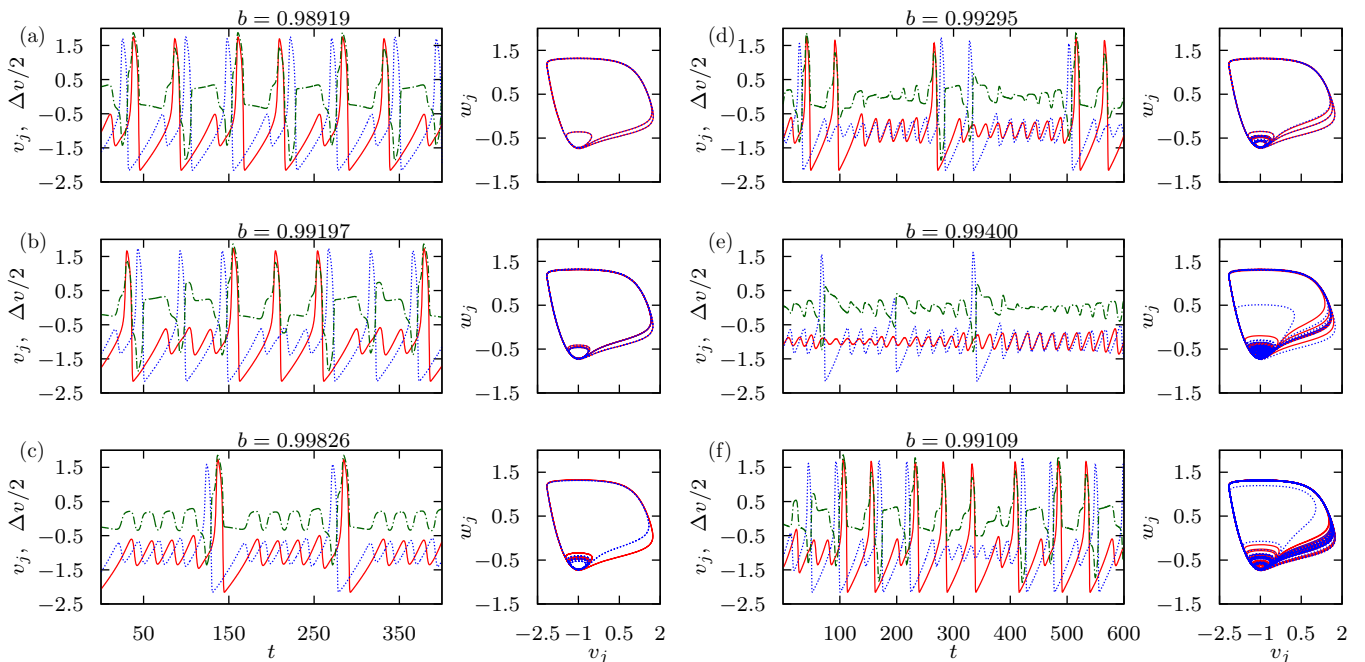


FIG. 7. Time traces and phase portraits of selected trajectories from regions V and VI in Fig. 6: Simple leap frogging in (a); periodic orbits with space-time symmetry in (b) and (d); asymmetric periodic orbit with several subthreshold oscillations in between successive spikes in (c); chaotic regimes in (e) and (f). Other parameters and colors and line styles are as described in the caption of Fig. 4.

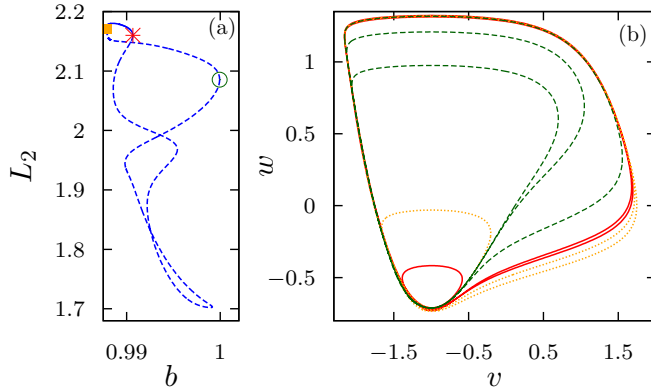


FIG. 8. (a) Branch of simple leap-frog solutions for varying b and fixed $c = -0.01$, $\varepsilon = 0.1$. The stability region (solid curve) is bounded by two folds of limit cycles (yellow square and red cross). At all other folds (e.g., green circle) both branches are unstable (dashed curves). (b) Phase portraits of limit cycles at the folds from panel (a), square (dotted), cross (solid), and circle (dashed).

by a subthreshold oscillation of the leading unit, whereby the lagging unit, passing without such a small loop, can overtake the current leader and spike the next time first. During the next spiking event, the units follow an analogous scenario but with interchanged roles, which results in the space-time symmetry Eq. (6). Figure 8(a) provides the branch of leap-frogging solutions for varying b and fixed $(c, \varepsilon) = (-0.01, 0.1)$. The branch has the shape of a closed curve and is stable only within a small region bounded by two folds of limit cycles. A continuation of these folds in the two parameters (b, c) , shown as black curves, provides the purple stability region shown in Fig. 9(a). The latter has the shape of a linear cone and points to the canard transition of the uncoupled periodic regime at $(b, c) = (b_c, 0)$. However, for the chosen value of $\varepsilon = 0.1$, the exact bifurcation structure in the vicinity of this point could not be reliably resolved numerically. Therefore, to gain a better understanding of the bifurcation structure at the tip of the stability cone, we increased the value of ε . Figure 9(b) shows the associated stability region in the (b, ε) plane. For the fixed values of $\varepsilon = 0.15$ and $\varepsilon = 0.2$, we calculated again the stability cones in the (b, c) plane, see the green and blue regions in Fig. 9(a). For these larger values of ε , it becomes apparent that the cones are clearly detached from the line $c = 0$, and that the sharp tip of the cone is actually formed by a single smooth curve of fold bifurcations. However, there is a codimension-two point close to the tip where a curve of symmetry-breaking pitchfork bifurcations crosses through the fold and becomes the stability boundary of the leap-frogging regime. The pitchfork curves are plotted in red in Fig. 9. For larger $\varepsilon = 0.15$ [see the green stability cone in Fig. 9(a)], we observe another cusp point where the branch of stable leap-frogging folds over, such that its stability region is again delineated by a fold (black curves in Fig. 9).

For $\varepsilon = 0.2$ we were able to completely resolve the bifurcation scenario in the vicinity of the tip; see Fig. 10. At small coupling $c = -0.00195$ the branch of leap-frogging solutions emerges as a small bubble [panel (I)]. For stronger coupling, this closed branch folds over and a further pair of folds

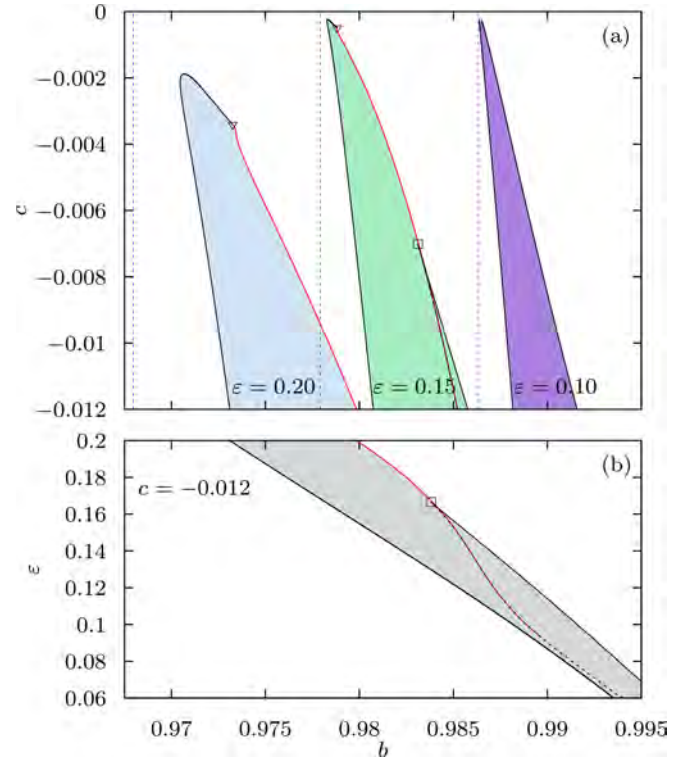


FIG. 9. (a) Stability regions of the simple leap-frog solutions in the (b, c) plane for fixed $\varepsilon \in \{0.2, 0.15, 0.1\}$ are shown in blue, green, and purple, respectively. The vertical dashed lines of corresponding color indicate the location $b_c(\varepsilon)$ of the canard transition of the synchronous oscillations. (b) Stability regions of the simple leap-frog solutions in the (b, ε) plane for fixed $c = -0.012$. In both panels, the stability regions are bounded by curves of fold bifurcations (solid black lines) and curves of pitchfork bifurcations (shown by red color). Triangles and squares indicate pitchfork-fold interaction and cusp points.

emanates from a cusp point. Moreover, through symmetry-breaking pitchfork bifurcations, there appears a branch of *asymmetric* leap-frogging solutions, which is also folded in an increasingly complex fashion, sometimes even featuring a small region of stability [see panel (II)]. Another type of codimension-two bifurcation points are 1:1 resonances, which give rise to branches of torus bifurcations. Figure 9 shows that for smaller ε , this complicated bifurcation scenario is contracted to a small vicinity of the canard transition of the uncoupled periodic regime at $(b, c) = (b_c, 0)$. The presumably exponential scaling of this contraction would clarify why already for $\varepsilon = 0.1$ the bifurcations at the tip of the cone could not be reliably resolved by our numerics.

B. Multiple leap-frogging

We have observed that the stable simple leap-frog solutions emerge already at very weak negative coupling and are accompanied with a regime of complicated or chaotic mixed-mode oscillations. However, for stronger negative coupling, one finds a different scenario. In Fig. 11 we show different dynamical regimes for varying parameter b , now with $c = -0.1$, while ε is fixed again to 0.1. Similar to Fig. 6, we

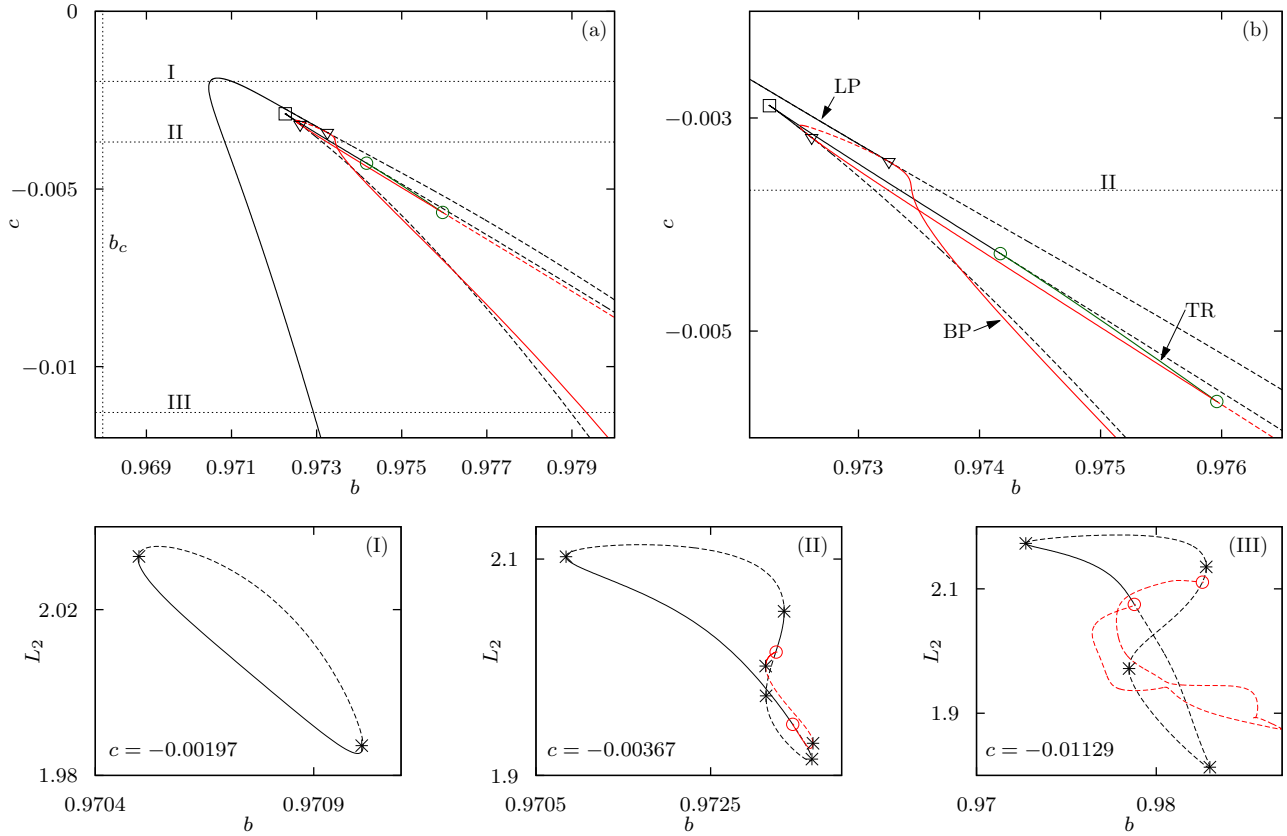


FIG. 10. (a) Bifurcations of the simple leap-frogging solutions in the (b, c) plane for $\varepsilon = 0.2$. (b) Enlarged view of the region where the complexity of the bubble increases. Bifurcation curves: folds of limit cycles (black), pitchfork bifurcations (red), torus bifurcations (green), also indicated by the labels LP, BP, and TR in panel (b), respectively. Solid curves indicate bifurcations delimiting the stability region; Dashed bifurcation curves involve only unstable states. Codimension-two bifurcations: cusps of limit cycles (squares), pitchfork-fold (triangles), torus (green circles). (I)–(III) Solid curves indicate stable branches of leap-frogging solutions with folds points (stars) and pitchfork bifurcations (circles), dashed curves indicate unstable branches. Asymmetric branches emerging from pitchfork bifurcations (red circles) are shown in red. The chosen values of c are indicated in panels (a) and (b).

have for each b value sampled the return times between consecutive Poincaré events where one of the units crosses $v_j = -b$ in increasing direction. For this stronger repulsive coupling we find a sequence of periodic patterns with a

gradually increasing number of subthreshold oscillations between two subsequent relaxation oscillations. Beginning from the regime of successive spiking at the left edge of the diagram, the system switches to the simple leap-frogging regime, characterized by two slightly different return times $T_n \approx 50$ corresponding to round trips along the relaxation oscillation orbit and a single return time $T_n < 30$ corresponding to the subthreshold oscillation following only after every second spike. Due to the symmetry Eq. (6) and the alternating spiking order, the units leave an identical trace in the respective return times. The time traces typical for the subsequent dynamical regime at larger b are shown in Fig. 12(a). Here, the subthreshold oscillations follow after each spike, which results in an asymmetric solution with fixed leader and laggard unit, distinguished by slightly different return times for the small loop and the relaxation oscillation. Note that the subthreshold oscillations, performed almost in antiphase, allow for the units to interchange the leadership twice. This is why we call this regime *double leap-frogging*. Increasing b further, we find another regime, again with the space-time symmetry Eq. (6) and an alternating spiking order, now caused by a triple interchange of leadership while performing the small loops; see Fig. 12(b). The following periodic regimes for larger b exhibit a further increasing number of subthreshold oscillations and

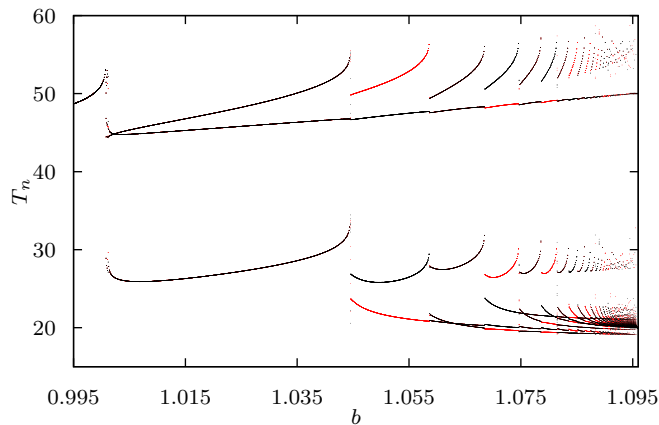


FIG. 11. Sampled return times between consecutive Poincaré events of $v_1 = -b$ (red) or $v_2 = -b$ (black) for varying b and fixed $(c, \varepsilon) = (-0.1, 0.1)$.

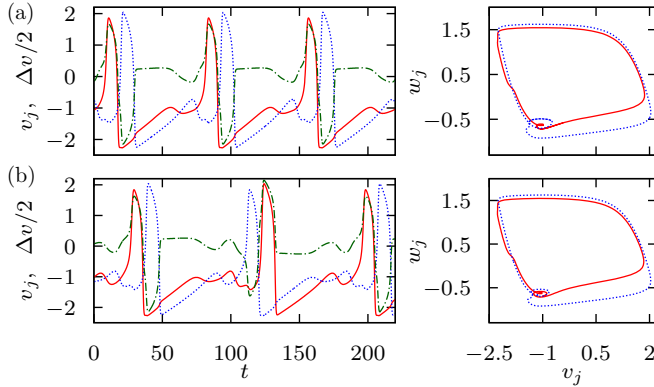


FIG. 12. Time traces and phase portraits of double leap-frogging at $b = 1.05$ (a) and triple leap-frogging at $b = 1.065$ (b). Other parameters are $(c, \varepsilon) = (-0.1, 0.1)$. Colors and line styles are as described in the caption of Fig. 4.

are successively either of the asymmetric type with fixed spiking order or of the type with the space-time symmetry and an alternating order of spiking, characterized by an even and odd number of leadership exchanges, respectively.

We have examined the stability regions of the double leap-frogging regime for varying c and different values of ε ; see Fig. 13. In contrast to the case of simple leap-frogging, these regions do not extend to a close vicinity of the degeneracy at $c = 0$. Under varying ε , their position with respect to the parameter b does not adapt to the canard transition $b_c(\varepsilon)$ of the symmetric oscillations (vertical dashed lines), as in case of the simple leap-frogging. The stability boundaries are outlined

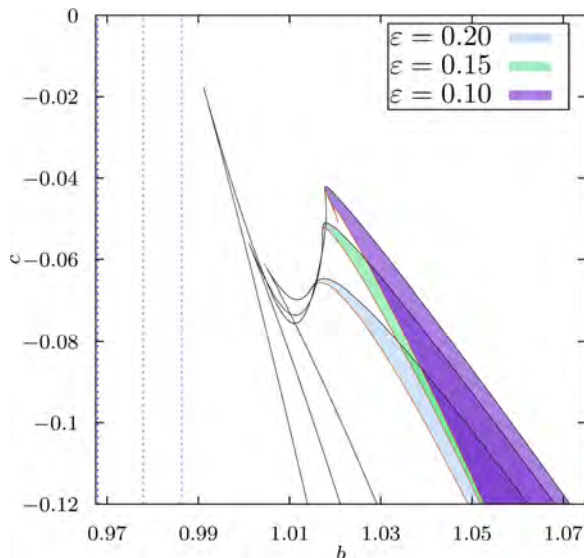


FIG. 13. Stability regions of the double leap-frog solutions in the (b, c) plane for fixed $\varepsilon \in \{0.2, 0.15, 0.1\}$ are presented in blue (bottom), green (middle), and purple (top), respectively. The left boundary of each region is given by a curve of period doubling bifurcations (orange), whereas the right one is provided by a fold curve (black). The vertical dashed lines of corresponding color indicate the location $b_c(\varepsilon)$ of the canard transition of the synchronous oscillations.

by curves of period doubling (orange) and curves of fold bifurcations (black) and do not involve any codimension-two bifurcations. This scenario for larger negative coupling, which is characterized by subsequent periodic patterns with different numbers of large relaxation oscillations and small loops, conforms, except for the different symmetry types, to the results of the asymptotic theory of mixed-mode oscillations at a folded node singularity.

IV. DISCUSSION AND OUTLOOK

In the present study, we have demonstrated that a variety of complex leap-frog patterns may emerge in a simple system comprised of two FitzHugh-Nagumo units with linear repulsive coupling in the fast variables. This complex dynamical scenario appears for parameter values in a vicinity of the canard transition of the uncoupled system and involves periodic solutions of different symmetry types. For larger repulsive coupling we obtain periodic regimes combining different numbers of small subthreshold and large relaxation oscillations, which resemble the general results for mixed-mode oscillations in slow-fast systems. For almost vanishing coupling, where the system gains an additional degeneracy, the situation is different. The stability region of the regime of simple leap frogging has the shape similar to a locking cone that approaches extremely close to the canard transition at vanishing coupling. Close to the tip of the cone, we have found a complex bifurcation scenario, which for decreasing ε is contracted to a close vicinity of the degenerate canard at $c = 0$. This contraction happens at a very fast and presumably exponential rate, such that already for moderately small values of ε a reliable numerical treatment became unfeasible and it would be a challenging task to perform an analytical study of this scenario in the singular limit $\varepsilon \rightarrow 0$.

Qualitatively, the onset of the leap-frog patterns may be explained as a result of a strong sensitivity to perturbations of the relaxation oscillation of a single FitzHugh-Nagumo unit just above the canard transition. There, already very small perturbations applied during the passage near the fold singularity of the slow manifold can deviate the trajectory away from the relaxation oscillation, giving rise to one or several loops conforming to subthreshold oscillations. Such a behavior of phase-sensitive excitability and the resulting response to excitations by noise of a single FitzHugh-Nagumo unit has been studied in Ref. [30]. Similar phenomena where the excitations arise from interactions in more complex networks have been studied in Ref. [31].

So far, the conditions relevant for the emergence of leap-frog patterns have mostly been considered within the context of neuroscience, especially in terms of relation to synchronized states. It has been known that such patterns cannot be obtained within the framework of weak-coupling theory for a pair of phase oscillators, because alternating order of firing cannot be described by reduction to an autonomous flow on the corresponding torus [32–34]. Thus, it was first believed that to observe the leap-frog solutions, one has to complement the phase oscillator dynamics by a complex synaptic coupling involving a finite synaptic time constant [12]. The suggested alternative has been to augment the simple phase dynamics by an additional negative phase branch

corresponding to strong hyperpolarization after the spiking event, as in case of the quadratic integrate-and-fire neuron model [12]. With regard to relaxation oscillators, the leap-frog patterns have first been observed as near-synchronous states where the complete phase synchronization is perturbed by *strong* inhibitory or excitatory coupling [13,14]. Later research focused on class I neural oscillators represented by Wang-Buzsáki [15] or Morris-Lecar model [12,35]. In both instances, it has been found that the appropriate inhibitory noninstantaneous synaptic dynamics is crucial for the onset of leap-frog dynamics. In particular, in the case of Morris-Lecar oscillators, such patterns are facilitated by the fact that the strong coupling causes the neurons to become transiently trapped in the subthreshold (excitable) state during a certain interval of the oscillation cycle, which allows for the exchange of the spiking order between the units [12]. In contrast to the above studies, we do not suggest a specific physiological mechanism, but discuss the general case of a system of *weakly*

coupled *excitable* units and show how the mechanism behind the exchange of leadership involves subthreshold oscillations, typically observed in class II neural oscillators [17,18,20]. In this sense our small negative linear coupling term can be seen as the essence of how qualitatively a local linearization of a more complicated functional dependence has to act to induce the leap-frog patterns.

ACKNOWLEDGMENTS

This work was supported by the Ministry of Education, Science, and Technological Development of Republic of Serbia under Project No. 171017, the DAAD Serbia-Germany Bilateral Project “Emergent Dynamics in Systems of Coupled Excitable Units,” as well as the DFG within the framework of Collaborative Research Center SFB 910. The authors thank O. E. Omel’chenko and N. Semenova for fruitful discussions.

-
- [1] R. C. Elson, A. I. Selverston, R. Huerta, N. F. Rulkov, M. I. Rabinovich, and H. D. I. Abarbanel, *Phys. Rev. Lett.* **81**, 5692 (1998).
- [2] R. Milo, S. Shen-Orr, S. Itzkovitz, N. Kashtan, D. Chklovskii, and U. Alon, *Science* **298**, 824 (2002).
- [3] E. Bullmore and O. Sporns, *Nat. Rev. Neurosci.* **10**, 186 (2009).
- [4] O. Sporns, *Networks of the Brain* (MIT Press, Cambridge, MA, 2011).
- [5] S. Song, P. J. Sjöström, M. Reigl, S. Nelson, and D. B. Chklovskii, *PLoS Biol.* **3**, e68 (2005).
- [6] A. Pikovsky, M. Rosenblum, and J. Kurths, *Synchronization, a Universal Concept in Nonlinear Science* (Cambridge University Press, Cambridge, UK, 2003).
- [7] E. M. Izhikevich, *Dynamical Systems in Neuroscience: The Geometry of Excitability and Bursting* (MIT Press, Cambridge, MA, 2007).
- [8] D. Terman, E. Lee, J. Rinzel, and T. Bem, *SIAM J. Appl. Dynam. Syst.* **10**, 1127 (2011).
- [9] G. Buzsáki, *Rhythms of the Brain* (Oxford University Press, Oxford, 2009).
- [10] P. Goel and G. B. Ermentrout, *Physica D (Amsterdam)* **163**, 191 (2002).
- [11] C. D. Acker, N. Kopell, and J. A. White, *J. Comp. Neurosci.* **15**, 71 (2003).
- [12] M. Oh and V. Matveev, *J. Comput. Neurosci.* **26**, 303 (2009).
- [13] A. Bose, N. Kopell, and D. Terman, *Physica D (Amsterdam)* **140**, 69 (2000).
- [14] Y. D. Sato and M. Shiino, *Phys. Rev. E* **75**, 011909 (2007).
- [15] S. K. Maran and C. C. Canavier, *J. Comput. Neurosci.* **24**, 37 (2008).
- [16] D. Terman, J. E. Rubin, and C. O. Diekmann, *Chaos* **23**, 046110 (2013).
- [17] M. Desroches, J. Guckenheimer, B. Krauskopf, C. Kuehn, H. M. Osinga, and M. Wechselberger, *SIAM Rev.* **54**, 211 (2012).
- [18] C. Kuehn, *Multiple Time Scale Dynamics* (Springer International Publishing, Switzerland, 2015).
- [19] E. N. Davison, Z. Aminzare, B. Dey, and N. E. Leonard, *Chaos* **29**, 033105 (2019).
- [20] M. Desroches, B. Krauskopf, and H. M. Osinga, *Chaos* **18**, 015107 (2008).
- [21] M. Krupa, B. Ambrosio, and M. A. Aziz-Alaoui, *Nonlinearity* **27**, 1555 (2014).
- [22] E. Köksal Ersöz, M. Desroches, and M. Krupa, *Physica D (Amsterdam)* **349**, 46 (2017).
- [23] M. N. Stolyarov, V. A. Romanov, and E. I. Volkov, *Phys. Rev. E* **54**, 163 (1996).
- [24] J. Guckenheimer, K. Hoffman, and W. Weckesser, *Int. J. Bifurcat. Chaos* **10**, 2669 (2000).
- [25] E. J. Doedel, and B. E. Oldeman, *AUTO-07P: Continuation and Bifurcation Software for Ordinary Differential Equations* (Concordia University, Montreal, 2012).
- [26] S. M. Baer and T. Erneux, *SIAM J. Appl. Math.* **46**, 721 (1986).
- [27] V. A. Makarov, V. I. Nekorkin, and M. G. Velarde, *Phys. Rev. Lett.* **86**, 3431 (2001).
- [28] B. Lindner, J. Garcia-Ojalvo, A. Neiman, and L. Schimansky-Geier, *Phys. Rep.* **392**, 321 (2004).
- [29] K. Shimizu, Y. Saito, M. Sekikawa, and N. Inaba, *Physica D (Amsterdam)* **241**, 1518 (2012).
- [30] I. Franović, O. E. Omel’chenko, and M. Wolfrum, *Chaos* **28**, 071105 (2018).
- [31] G. Ansmann, K. Lehnertz, and U. Feudel, *Phys. Rev. X* **6**, 011030 (2016).
- [32] M. Golubitsky, K. Josic, and E. Shea-Brown, *J. Nonlin. Sci.* **16**, 201 (2006).
- [33] E. M. Izhikevich, and Y. Kuramoto, *Weakly coupled oscillators, Encycl. Math. Phys.* **5**, 448 (2006).
- [34] F. C. Hoppensteadt and E. M. Izhikevich, *Weakly Connected Neural Networks* (Springer, New York, 1997).
- [35] *Frontiers of Applied and Computational Mathematics*, edited by D. Blackmore, A. Bose, and P. Petropoulos (World Scientific, Singapore, 2008).

Inverse stochastic resonance in a system of excitable active rotators with adaptive coupling

IVA BAČIĆ¹, VLADIMIR KLINSHOV², VLADIMIR NEKORKIN², MATJAŽ PERC³ and IGOR FRANOVIĆ^{1(a)}

¹ *Scientific Computing Laboratory, Center for the Study of Complex Systems, Institute of Physics Belgrade, University of Belgrade - Pregrevica 118, 11080 Belgrade, Serbia*

² *Institute of Applied Physics of the Russian Academy of Sciences - 46 Ulyanov Street, 603950 Nizhny Novgorod, Russia*

³ *Faculty of Natural Sciences and Mathematics, University of Maribor - Koroška cesta 160, SI-2000 Maribor, Slovenia*

received 17 September 2018; accepted in final form 8 November 2018

published online 11 December 2018

PACS 05.40.Ca – Noise

PACS 87.19.1n – Oscillations and resonance

Abstract – Inverse stochastic resonance is a phenomenon where an oscillating system influenced by noise exhibits a minimal oscillation frequency at an intermediate noise level. We demonstrate a novel generic scenario for such an effect in a multi-timescale system, considering an example of emergent oscillations in two adaptively coupled active rotators with excitable local dynamics. The impact of plasticity turns out to be twofold. First, at the level of multiscale dynamics, one finds a range of intermediate adaptivity rates that give rise to multistability between the limit cycle attractors and the stable equilibria, a condition necessary for the onset of the effect. Second, applying the fast-slow analysis, we show that the plasticity also plays a facilitatory role on a more subtle level, guiding the fast flow dynamics to parameter domains where the stable equilibria become focuses rather than nodes, which effectively enhances the influence of noise. The described scenario persists for different plasticity rules, underlying its robustness in the light of potential applications to neuroscience and other types of cell dynamics.

Copyright © EPLA, 2018

Introduction. – Noise in coupled excitable or bistable systems may induce two types of generic effects [1]. On the one hand, it can modify the deterministic behavior by acting non-uniformly on different states of the system, thus amplifying or suppressing some of its features. On the other hand, noise may give rise to completely novel forms of behavior, typically based on crossing the thresholds or separatrices, or involving enhanced stability of deterministically unstable structures. In neuronal systems, the constructive role of noise at different stages of information processing, referred to as “stochastic facilitation” [2,3], mainly comprises resonant phenomena. A classical example is the stochastic resonance [4], which allows for the detection of weak subthreshold periodic signals. A more recent development concerns the effect of inverse stochastic resonance (ISR) [3,5–12], where noise selectively reduces the spiking frequency of neuronal oscillators, converting the tonic firing into intermittent bursting-like activity or a short-lived transient followed

by a long period of quiescence. The name of the effect should be taken *cum grano salis*, because in contrast to stochastic resonance, it involves no additional external signal: one rather observes a non-monotonous dependence of the spiking rate on noise variance, whereby the oscillation frequency becomes minimal at a preferred noise level. Such an inhibitory effect of noise has recently been shown for cerebellar Purkinje cells [11], having explicitly demonstrated how the lifetimes of the spiking (“up”) and the silent (“down”) states [13–15] are affected by the noise variance. ISR has been indicated to play important functional roles in neuronal systems, including the reduction of spiking frequency in the absence of neuromodulators, suppression of pathologically long short-term memories, triggering of on-off tonic spiking activity and even optimization of information transfer along the signal propagation pathways [3,7,9,11].

So far, theoretical studies on ISR have mostly concerned the scenario where a single neuron exhibits bistable deterministic dynamics, featuring coexistence between a limit cycle and a stable equilibrium. Such bistability is

^(a)E-mail: franovic@ipb.ac.rs

typical for Type-II neurons below the subcritical Hopf bifurcation, *e.g.*, classical Hodgkin-Huxley and Morris-Lecar models [3,6–8]. There, applying noise induces switching between the metastable states, but at an intermediate noise level, one surprisingly finds a strong asymmetry of the associated switching rates, which makes the periods spent in the vicinity of equilibrium much longer than the periods of spiking activity.

An important open problem concerns conditions giving rise to ISR in coupled excitable systems, where noise influences the emergent oscillations. Here we address in detail this issue, as it may be crucial to understanding the prevalence of the effect in neural networks, whose activity depends on the interplay of excitability, coupling properties and noise. Synaptic dynamics typically involves the plasticity feature, which makes self-organization in neuronal systems a multi-timescale process: the short-term spiking activity unfolds on a quasi-static coupling configuration, while the slow adjustment of coupling weights depends on the time-averaged evolution of units.

Motivated by the findings in neuroscience, we focus on the onset of ISR in a simplified, yet paradigmatic system of two adaptively coupled stochastic active rotators with excitable local dynamics. Active rotators are canonical for Type-I excitability and may be seen as equivalent to the theta-neuron model. Adaptivity is introduced in a way that allows continuous interpolation between a spectrum of plasticity rules, including Hebbian learning and spike-time-dependent plasticity (STDP) [16–18].

We demonstrate a generic scenario for the plasticity-induced ISR, where the system’s multiscale structure, defined by the adaptivity rate, plays a crucial role. On a basic level, plasticity gives rise to multistable behavior involving coexisting stationary and oscillatory regimes. An additional subtlety, which we show by the fast-slow analysis, is that the plasticity promotes the resonant effect by guiding the fast flow toward the parameter region where the stable fixed points are focuses rather than nodes.

The paper is organized as follows. In the next section the details of the model and the numerical bifurcation analysis of the deterministic dynamics are presented. The third section contains the results on the ISR effect and the supporting conditions. In the fourth section the fast-slow analysis is applied to explain the mechanism by which plasticity enhances the system’s non-linear response to noise. Apart from providing a brief summary, in the last section we also discuss the prevalence of the observed effect.

Model and bifurcation analysis of deterministic dynamics. – Our model involves two stochastic active rotators interacting by adaptive couplings [19–22],

$$\begin{aligned}\dot{\varphi}_1 &= I_0 - \sin \varphi_1 + \kappa_1 \sin(\varphi_2 - \varphi_1) + \sqrt{D}\xi_1(t), \\ \dot{\varphi}_2 &= I_0 - \sin \varphi_2 + \kappa_2 \sin(\varphi_1 - \varphi_2) + \sqrt{D}\xi_2(t), \\ \dot{\kappa}_1 &= \epsilon(-\kappa_1 + \sin(\varphi_2 - \varphi_1 + \beta)), \\ \dot{\kappa}_2 &= \epsilon(-\kappa_2 + \sin(\varphi_1 - \varphi_2 + \beta)),\end{aligned}\quad (1)$$

where the phases $\{\varphi_1, \varphi_2\} \in S^1$, while the coupling weights $\{\kappa_1, \kappa_2\}$ are real variables.

The excitability parameters I_0 , which one may interpret as external bias currents in the context of neuroscience, are assumed to be identical for both units. For such a setup, the deterministic version of (1) possesses a Z_2 symmetry, being invariant to the exchange of units’ indices. The uncoupled units undergo a SNIPER bifurcation at $I_0 = 1$, with the values $I_0 < 1$ ($I_0 > 1$) corresponding to the excitable (oscillatory) regime. We consider the case of excitable local dynamics, keeping $I_0 = 0.95$ fixed throughout the paper, such that the oscillations may emerge only due to the coupling terms and/or noise. The scale separation between the fast dynamics of the phases and the slow dynamics of adaptation is adjusted by the parameter $\epsilon \ll 1$. The fast variables are influenced by independent white noise of variance D such that $\xi_i(t)\xi_j(t') = \delta_{ij}\delta(t-t')$ for $i, j \in \{1, 2\}$. Conceptually, adding stochastic input to the fast variables embodies the action of synaptic noise in neuronal systems [23].

The modality of the plasticity rule is specified by the parameter β , whose role may be understood by invoking the qualitative analogy between the adaptation dynamics in classical neuronal systems and the systems of coupled phase oscillators. This issue has first been addressed in [24–26], and a deeper analysis of the correspondence between the phase-dependent plasticity rules and the STDP has been carried out in [19]. In particular, it has been shown that the plasticity dynamics for $\beta = 3\pi/2$, where the stationary weights between the oscillators with smaller/larger phase differences increase/decrease, qualitatively resembles the Hebbian learning rule [25,26]. Nevertheless, when $\beta = \pi$, the coupling weights encode a causal relationship between the spiking of oscillators by changing in the opposite directions, in analogy to an STDP-like plasticity rule. Our interest lies with the β interval interpolating between these two limiting cases.

Using bifurcation analysis of the deterministic dynamics of (1), we first show how the modality of the plasticity rule influences the number of stationary states, and then explain how the onset of oscillations depends on adaptivity rate. The bifurcation diagram in fig. 1 indicates that the number and the stability of fixed points of (1) change with β in such a way that the system may possess two, four or six fixed points. Due to invariance to Z_2 symmetry, one always finds pairs of solutions sharing the same stability features. We consider the plasticity rules described by $\beta \in (3.298, 4.495)$, cf. the shaded region in fig. 1, where the system has two stable fixed points lying off the synchronization manifold $\varphi_1 = \varphi_2$, as well as four unstable fixed points. The bifurcations occurring at the boundaries of the relevant β interval are as follows. At $\beta = 3.298$, the system undergoes a supercritical symmetry-breaking pitchfork bifurcation giving rise to a pair of stable fixed points off the synchronization manifold. For $\beta = 4.495$, this pair of stable fixed points collides with a pair of unstable fixed points off

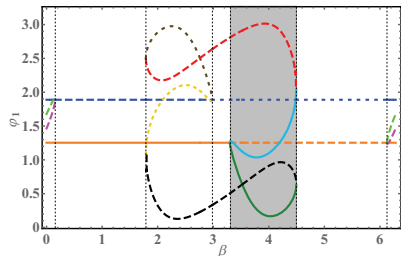


Fig. 1: (Color online) Bifurcation diagram for the fixed points of (1) with $D = 0$ under variation of β . Solid lines refer to stable fixed points, while dashed and dotted lines correspond to saddles of unstable dimension 1 and 2, respectively. Shading indicates the considered range of plasticity rules. The two fixed points independent on β belong to the synchronization manifold. The remaining parameters are $I_0 = 0.95, \epsilon = 0.05$.

the synchronization manifold, getting annihilated in two symmetry-related inverse fold bifurcations. Note that the weight levels typical for the two stable stationary states support effective unidirectional interaction, in a sense that one unit exerts a much stronger impact on the dynamics of the other unit than vice versa. When illustrating the effect of ISR, we shall mainly refer to the case $\beta = 4.2$. For this β , the two stable focuses of (1) at $D = 0$ are given by $(\varphi_1, \varphi_2, \kappa_1, \kappa_2) = (1.177, 0.175, 0.032, -0.92)$ and $(\varphi_1, \varphi_2, \kappa_1, \kappa_2) = (0.175, 1.177, -0.92, 0.032)$. Within the considered β interval, the two stable fixed points of the coupled system exhibit excitable behavior, responding to external perturbation by generating either the successive spikes or synchronized spikes [21].

The onset of oscillations for the deterministic version of (1) relies on the interplay between the plasticity rule, controlled by β , and the adaptation rate, characterized by ϵ . In fig. 2(a) are shown the results of parameter sweep indicating the variation of κ_1 variable, $\sigma_{\kappa_1} = \max(\kappa_1(t)) - \min(\kappa_1(t))$, within the (β, ϵ) parameter plane. The sweep indicates the maximal stability region of the two emerging periodic solutions, related by the exchange symmetry of units indices. The data are obtained by numerical continuation starting from a stable periodic solution, such that the final state reached for the given parameter set is used as initial conditions of the system dynamics for incremented parameter values. One observes that for fixed β , there exists an interval of timescale separation ratios $\epsilon \in (\epsilon_{min}, \epsilon_{max})$ admitting oscillations, see fig. 2(b). Within the given ϵ range, the system exhibits multistability where periodic solutions coexist with the two symmetry-related stable stationary states. The lower threshold for oscillations, ϵ_{min} , reduces with β , whereas the upper boundary value, ϵ_{max} , is found to grow as β is enhanced. Note that the waveform of oscillations also changes as ϵ is increased under fixed β . In particular, for smaller ϵ , the waveforms corresponding to the two units are rather different. Nevertheless, around $\epsilon \approx 0.06$ the system undergoes a pitchfork bifurcation of limit cycles, such that

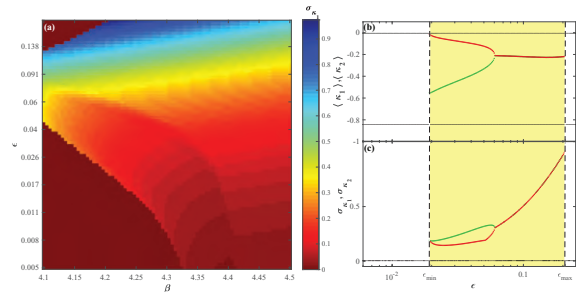


Fig. 2: (Color online) Onset of oscillations in (1) for $D = 0$. (a) Variation σ_{κ_1} of the coupling weight κ_1 in the (β, ϵ) -plane. (b) Mean coupling weights $\langle \kappa_1 \rangle(\epsilon)$ and $\langle \kappa_2 \rangle(\epsilon)$ for oscillatory (thick lines) and stationary states (thin lines) at $\beta = 4.2$. (c) Variation $\sigma_{\kappa_1}(\epsilon)$ and $\sigma_{\kappa_2}(\epsilon)$, presented as in (b). Shading in (b) and (c) indicates the ϵ interval admitting the stable periodic solutions.

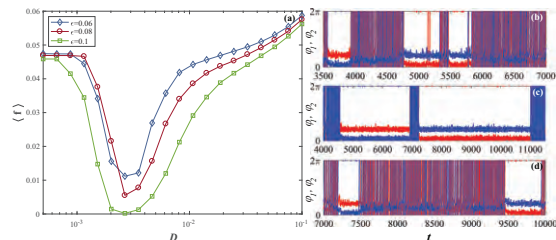


Fig. 3: (Color online) (a) Mean spiking rate $\langle f \rangle$ in terms of D for $\epsilon \in \{0.06, 0.08, 0.1\}$. The curves exhibit a characteristic minimum at an intermediate noise level. (b)–(d) Time traces $\varphi_1(t)$ and $\varphi_2(t)$ for noise levels below, at and above the resonant value. The remaining parameters are $I_0 = 0.95, \beta = 4.2, \epsilon = 0.06$.

the oscillatory solution gains the anti-phase space-time symmetry $\varphi_1(t) = \varphi_2(t + T/2), \kappa_1(t) = \kappa_2(t + T/2)$, where T denotes the oscillation period [21].

Numerical results on ISR. – Inverse stochastic resonance manifests itself as noise-mediated suppression of oscillations, whereby the frequency of noise-perturbed oscillations becomes minimal at a preferred noise level. For system (1), we find such an effect to occur generically for intermediate adaptivity rates, supporting multistability between the stationary and the oscillatory solutions, as described in the previous section. A family of curves describing the dependence of the oscillation frequency on noise variance $\langle f \rangle(D)$ for different ϵ values is shown in fig. 3. All the curves corresponding to $\epsilon \geq \epsilon_{min}(\beta)$ show a characteristic non-monotonous behavior, displaying a minimum at the optimal noise intensity. For weaker noise, the oscillation frequency remains close to the deterministic one, whereas for much stronger noise, the frequency increases above that of unperturbed oscillations. The displayed results are obtained by averaging over an ensemble of 1000 different stochastic realizations, having excluded the transient behavior, and having fixed a single set of initial conditions within the basin of attraction of the limit cycle attractor. Nevertheless, we have verified that the

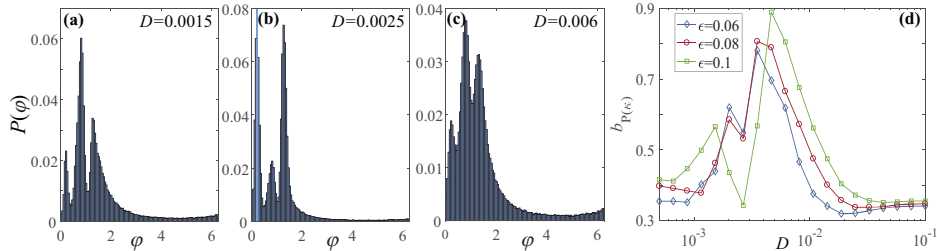


Fig. 4: (Color online) (a)–(c) Stationary distribution $P(\varphi_1)$ for the noise levels below, at and above the resonant value. System parameters are $I_0 = 0.95$, $\beta = 4.2$ and $\epsilon = 0.06$. From the three observable peaks, the middle one, prevalent in (a) and (c), refers to the metastable state associated to the oscillatory mode of (1) for $D = 0$. The two lateral peaks, dominant in (b), correspond to quasi-stationary states derived from the stable equilibria of the deterministic version of (1). (d) Bimodality coefficient for the stationary distribution of κ_1 , $b_{P(\kappa_1)}$, as a function of D . The three curves refer to $\epsilon = 0.06$ (diamonds), $\epsilon = 0.08$ (circles) and $\epsilon = 0.1$ (squares).

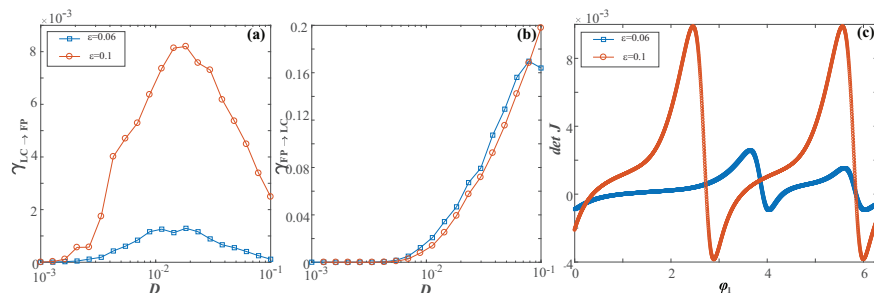


Fig. 5: (Color online) (a) and (b): transition rates from the stability basin of the limit cycle to the fixed point, $\gamma_{LC \rightarrow FP}(D)$ and vice versa, $\gamma_{FP \rightarrow LC}(D)$, numerically obtained for $\epsilon = 0.06$ (squares) and $\epsilon = 0.1$ (circles). The remaining parameters are $I_0 = 0.95$, $\beta = 4.2$. (c) Determinant of the Jacobian calculated along the limit cycle orbit as a function of the phase variable. The quantity provides an indication of the sensitivity of certain sections of the orbit to external perturbation. Blue and red colors correspond to $\epsilon = 0.06$ and $\epsilon = 0.1$, respectively.

qualitatively analogous results are obtained if for each realization of stochastic process one selects a set of random initial conditions lying within the stability basin of the periodic solution. The suppression effect of noise depends on the adaptivity rate, and is found to be more pronounced for faster adaptivity. Indeed, for smaller ϵ , $\varphi(t)$ series corresponding to the noise levels around the minimum of $\langle f \rangle(D)$ exhibit bursting-like behavior, whereas for larger ϵ , noise is capable of effectively quenching the oscillations, such that the minimal observed frequency approaches zero.

The core of the described effect concerns switching dynamics between the metastable states associated to coexisting attractors of the deterministic version of system (1). To illustrate this, in fig. 4 we have considered the stationary distributions of one of the phase variables, $P(\varphi)$, for the noise levels below, at and above the minimum of the $\langle f \rangle(D)$, having fixed the remaining parameters to $(\beta, \epsilon) = (4.2, 0.06)$. The distribution $P(\varphi)$ is characterized by two lateral peaks, reflecting the two symmetry-related quasi-stationary states, and the area around the central peak, corresponding to the oscillatory mode. For small noise $D = 0.0015$, see fig. 4(a), and very large noise $D = 0.006$, cf. fig. 4(c), the central peak of $P(\varphi)$ is expectedly prevalent compared to the two lateral peaks. Nevertheless, the switching dynamics for

$D = 0.0025$, the noise level about the minimum of $\langle f \rangle(D)$, is fundamentally different, and the corresponding distribution $P(\varphi)$ in fig. 4(b) shows that the system spends much more time in the quasi-stationary states than performing the oscillations. The onset of ISR in the dynamics of fast variables is accompanied by the increased bimodality of the stationary distribution of the couplings, see fig. 4(d).

In order to observe the non-monotonous response of the system's frequency to noise, the geometry of the phase space has to be asymmetrical with respect to the separatrix between the coexisting attractors in such a way that the limit cycle attractor lies much closer to the separatrix than the stationary states. Such structure of phase space gives rise to asymmetry in switching dynamics, whereby at the preferred noise level around the minimum of $\langle f \rangle(D)$, the transition rate from the stability basin of the limit cycle attractor to that of stationary states $\gamma_{LC \rightarrow FP}$ becomes much larger than the transition rate in the inverse direction, $\gamma_{FP \rightarrow LC}$. Figures 5(a) and (b) corroborate that the dependences $\gamma_{LC \rightarrow FP}(D)$ and $\gamma_{FP \rightarrow LC}(D)$ are qualitatively distinct: the former displays a maximum at the resonant noise level, whereas the latter just increases monotonously with noise. The fact that ISR is more pronounced for higher adaptivity rates is reflected in that the curve $\gamma_{LC \rightarrow FP}(D)$ for $\epsilon = 0.1$ lies substantially above that for $\epsilon = 0.06$, see fig. 5(a).

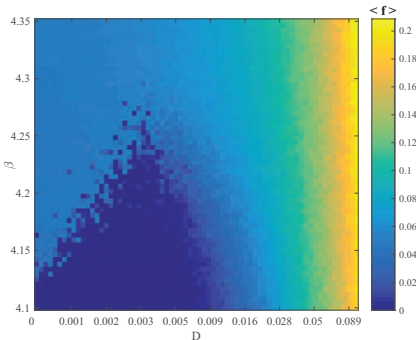


Fig. 6: (Color online) Mean spiking rate $\langle f \rangle$ as a function of β and D for fixed $\epsilon = 0.05$. The results evince the robustness of the ISR effect with respect to different plasticity rules.

To understand why the interplay of adaptivity rate and noise yields a stronger resonant effect for larger ϵ , we have investigated the susceptibility of the limit cycle attractor to external perturbation. In particular, fig. 5(c) shows how the determinant of the Jacobian calculated along the limit cycle orbit change for $\epsilon = 0.06$ (blue line) and $\epsilon = 0.1$ (red line), respectively. For smaller ϵ , one may identify two particular points where the determinant of the Jacobian is the largest, *i.e.*, where the impact of external perturbation is felt the strongest. This implies that noise is most likely to drive the systems trajectory away from the limit cycle attractor around these two sections of the orbit, which should lie closest to the boundary to the stability basins of the stationary states. Such a physical picture is maintained for larger ϵ , but one should stress that the sensitivity of limit cycle attractor to external perturbation substantially increases along the entire orbit, cf. fig. 5(c). In other words, faster adaptivity enhances the impact of noise, contributing to a more pronounced ISR effect. This point is addressed from another perspective in the next section.

We also examine the robustness of ISR to different modalities of the plasticity rule specified by β . Figure 6 shows how the average oscillation frequency changes with β and D for fixed $\epsilon = 0.05$. The non-linear response to noise, conforming to a resonant effect with a minimum of oscillation frequency at an intermediate noise level, persists in a wide range of β , essentially interpolating between the Hebbian-like and the STDP-like adaptive dynamics.

Fast-slow analysis: role of plasticity in the resonant effect. – Though ISR is observed for intermediate ϵ , here we show that the fast-slow analysis may still be applied to demonstrate a peculiar feature of the mechanism behind the resonant effect. In particular, we find that the plasticity enhances the resonant effect by driving the fast flow dynamics toward the parameter domain where the stationary state is a focus rather than a node. It is well known that the response to noise in multi-timescale systems qualitatively depends on the character of stationary states. Indeed, by using the sample-paths approach and other advanced techniques, it has already been shown

that such systems may exhibit fundamentally different scaling regimes with respect to noise variance and the scale-separation ratio [27,28]. Moreover, the resonant effects may typically be expected in the case in which quasi-stationary states are focuses [27], essentially because the local dynamics around the stationary state then involves an eigenfrequency.

Within the standard fast-slow analysis, one may either consider the layer problem, defined on the fast timescale, or the reduced problem, concerning the slow timescale [29]. For the layer problem, the fast flow dynamics $\varphi_1(t; \kappa_1, \kappa_2), \varphi_2(t; \kappa_1, \kappa_2)$ is obtained by treating the slow variables κ_1 and κ_2 as system parameters, whereas in the case of the reduced problem, determining the dynamics of the slow flow $(\kappa_1(t), \kappa_2(t))$ involves time-averaging over the stable regimes of the fast flow of the layer problem. The fast flow can in principle exhibit several attractors, which means that multiple stable sheets of the slow flow may emerge from the averaged dynamics on the different attractors of the fast flow. Our key point concerns the dynamics of the slow flow, which requires us to first classify the attractors of the fast flow.

The fast flow dynamics is given by

$$\begin{aligned}\dot{\varphi}_1 &= I_0 - \sin \varphi_1 + \kappa_1 \sin(\varphi_2 - \varphi_1), \\ \dot{\varphi}_2 &= I_0 - \sin \varphi_2 + \kappa_2 \sin(\varphi_1 - \varphi_2),\end{aligned}\quad (2)$$

where $\kappa_1, \kappa_2 \in [-1, 1]$ are considered as additional system parameters. One may formally obtain (2) by setting $\epsilon = 0$ in (1) with $D = 0$. We find that the fast flow is monostable for most of the (κ_1, κ_2) values, exhibiting either a stable equilibrium or a limit cycle attractor, see fig. 7(a). In general, the fast flow admits either two or four fixed points, and a more detailed physical picture, including the associated bifurcations, is presented in [21]. The stability region of the oscillatory regime, outlined by the red color, has been calculated by numerical continuation starting from a stable periodic solution. Bistability between a stable fixed point and a limit cycle is observed only in a small area near the main diagonal $\kappa_1 = \kappa_2$. Within the region featuring oscillatory regime, each periodic solution obtained for (κ_1, κ_2) above the main diagonal has a Z_2 symmetry-related counterpart below the diagonal. Typically, the periodic solutions emanate from SNIPER bifurcations, which make up two branches where either κ_1 or κ_2 are almost constant and close to zero.

Using the results from the analysis of the layer problem, our goal is to determine the vector fields corresponding to the stable sheets of the slow flow. We have numerically obtained the dynamics of the slow flow by a standard two-step approach [19,30]. First, for fixed values (κ_1, κ_2) , we have determined the time-averaged dynamics of the fast flow (2), $\langle \varphi_2 - \varphi_1 \rangle_t = h(\kappa_1, \kappa_2)$, whereby the averaging $\langle \cdot \rangle_t$ is carried out over a sufficiently long time interval, having excluded the transient behavior. As already indicated, such an average depends on the attractor of the fast flow for the given (κ_1, κ_2) . If the fast flow possesses

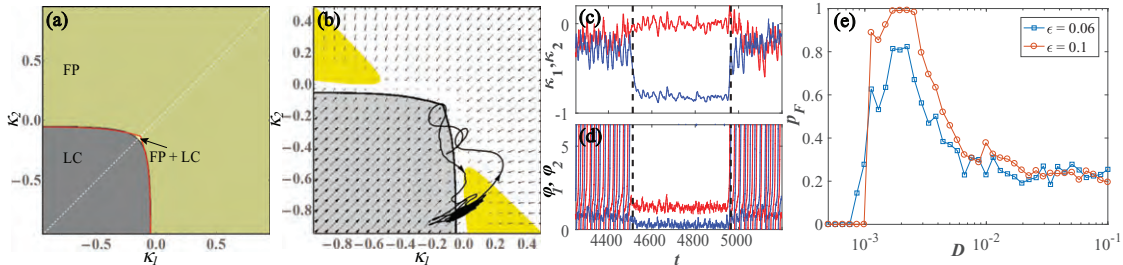


Fig. 7: (Color online) (a) Attractors of the fast flow (2) in terms of κ_1 and κ_2 , now treated as free parameters. The fast flow is typically monostable, admitting either a stable fixed point (FP) or a stable limit cycle (LC), apart from a small region of bistability (FP+LC) around the main diagonal. (b) Vector field of the slow flow (3) determined by considering only the stable regimes of the fast flow for $\beta = 4.2$, $I_0 = 0.95$. Within the yellow-highlighted regions, the stable fixed point of the fast flow is a focus rather than the node. The displayed orbit $(\kappa_1(t), \kappa_2(t))$ corresponds to a switching episode from the oscillatory state to the quasi-stationary state and back (evolution direction indicated by arrows). Panels (c) and (d) show the time traces of phases and couplings during the switching episode. (e) Conditional probability $p_F(D)$ for $\epsilon = 0.06$ (blue squares) and $\epsilon = 0.1$ (red circles).

a stable fixed point, then $\langle \varphi_2 - \varphi_1 \rangle_t = \varphi_2^* - \varphi_1^*$, which corresponds to the slow critical manifold of the system. For (κ_1, κ_2) where the attractor of the fast flow is a periodic solution, $\langle \varphi_2 - \varphi_1 \rangle_t$ amounts to the time average over the period. Averaging over a periodic attractor of the fast flow is a standard approximation [30], quite natural when describing the influence of oscillations in the fast flow to the dynamics of the slow flow.

As the second step, the obtained time averages are substituted into the coupling dynamics

$$\begin{aligned} \dot{\kappa}_1 &= \epsilon[-\kappa_1 + \sin(h(\kappa_1, \kappa_2) + \beta)], \\ \dot{\kappa}_2 &= \epsilon[-\kappa_2 + \sin(-h(\kappa_1, \kappa_2) + \beta)]. \end{aligned} \quad (3)$$

The system (3) allows one to determine the vector fields on the stable sheets of the slow flow, which correspond to the attractors of the fast flow. In fig. 7(b), the vector fields associated to each of the attractors (fixed point or limit cycle) are presented within its respective (κ_1, κ_2) stability region. In the small region of the (κ_1, κ_2) -plane supporting coexisting stable solutions of the fast flow, the corresponding vector field of the slow flow is given on multiple overlapping sheets, since the value of the average $f(\kappa_1, \kappa_2)$ depends on the initial conditions.

Within the above framework, one is able to explain a subtle influence of adaptivity on the mechanism behind the ISR. To this end, in fig. 7(b) we have projected a typical example of the $(\kappa_1(t), \kappa_2(t))$ trajectory of the full system (1) corresponding to a switching episode between the metastable states associated to a limit cycle attractor and a stable equilibrium of the deterministic system, see the time traces in figs. 7(c), (d). One observes that for the oscillating regime, the coupling dynamics always remains close to the SNIPER bifurcation of the fast flow, cf. fig. 7(a), which makes the oscillations quite susceptible to noise. Recall that the fast flow is typically monostable. Thus, switching events in the full system are naturally associated to the fast flow undergoing the SNIPER bifurcation: either a direct one, leading from the oscillatory to the stationary regime, or the inverse one, unfolding in the

opposite direction. For (κ_1, κ_2) values immediately after the SNIPER bifurcation toward the quiescent state, the stable equilibrium of the fast flow is a node. Nevertheless, for the noise levels where the effect of ISR is most pronounced, we find that the coupling dynamics guides the system into the region where the equilibrium is a stable focus rather than a node, see the yellow highlighted region in fig. 7(b). We have verified that this feature is a hallmark of the resonant effect by numerically calculating the conditional probability p_F that the events of crossing the SNIPER bifurcation are followed by the system's orbit visiting the (κ_1, κ_2) region where the stable equilibrium is a focus. The $p_F(D)$ dependences for two characteristic ϵ values at fixed $\beta = 4.2$ are plotted in fig. 7(e). One learns that $p_F(D)$ has a maximum for the resonant noise levels, where the corresponding curve $f(D)$ displays a minimum. In other words, the fact that the coupling dynamics drives the fast flow to the focus-associated regions of the (κ_1, κ_2) -plane results in trapping the phase variables for a longer time in the quasi-stationary (quiescent) state. Small noise below the resonant values is insufficient to drive the system to this region, whereas for too large a noise, the stochastic fluctuations completely take over, washing out the quasi-stationary regime. Note that for the faster adaptivity rate, the facilitatory role of coupling becomes more pronounced, as evinced by the fact that the curve $p_F(D)$ for $\epsilon = 0.1$ lies above the one for $\epsilon = 0.06$.

Discussion. – In the present paper, we have demonstrated a novel generic scenario for the onset of ISR, which involves an interplay between the local excitability feature and the adaptive dynamics of the couplings. For the example of two active rotators with coupling plasticity, we have shown that the spiking frequency corresponding to emergent oscillations varies non-monotonously with noise, displaying a minimum at a preferred noise level. Though the model *per se* is simplified, the underlying paradigm is relevant for combining the two core features of typical neuronal systems. The effect derives from the multi-timescale structure of the system, whereby the scale

separation between the local and the weight dynamics is tuned via adaptivity rate. Within a range of intermediate adaptivity rates, the deterministic dynamics of the full system exhibits multistability between the limit cycle attractors and the stable equilibria, each appearing in pairs due to the systems invariance to Z_2 symmetry. Applying the standard fast-slow analysis, we have shown that the resonant effect with noise is in fact plasticity-enhanced: plasticity promotes the impact of noise by guiding the fast flow toward the parameter domain where the stable equilibria become focuses instead of nodes. This mechanism increases the trapping efficiency by which the noise is able to deviate the systems trajectory from the metastable oscillatory states to the non-spiking regime. For faster adaptivity, the resonant effect is found to be more pronounced in a sense that the frequency dependence on noise shows deeper minima. Our scenario has proven to persist in a wide range of plasticity rules, interpolating between the cases analogous to Hebbian learning and STDP.

In earlier studies, observation of ISR has mostly been confined to Type-II neurons with intrinsic bistable dynamics, as in case of Hodgkin-Huxley or Morris-Lecar neurons near the subcritical Hopf bifurcation [3,6–9]. Even in case of networks, the macroscopic ISR effect has been linked to dynamical features of single units, only being modulated by the details of synaptic dynamics and the network topology [10]. In contrast to that, our results show that ISR may not rely on bistability of local dynamics, but may rather emerge due to the facilitatory role of coupling, here reflected in the interplay of multiscale dynamics and plasticity. Another distinction from most of the previous studies is that our scenario concerns Type-I units. For this class of systems, it is known that the dependence of the oscillating frequency of a single unit with noise is just monotonous [3,12], so that the resonant effect can only be observed in case of coupled units. So far, the latter case has been analyzed only once [5], but the underlying scenario is different from ours insofar as it involves static, rather than the adaptive couplings, and the effect *per se* is confined to a narrow region of the parameter space.

Quite recently, the onset of ISR has been reported for a single Fitzhugh-Nagumo oscillator [12], which is the first observation of the effect for Type-II neuron model in the vicinity of the supercritical Hopf bifurcation. Similar to the scenario we elaborated, ISR there also derives from the multiscale structure of the system. However, the actual mechanism behind the effect is associated to phase-sensitive (non-uniform) excitability of a limit cycle orbit conforming to relaxation oscillations [12]. These findings and the results here suggest that ISR may indeed provide a generic means of controlling and optimizing the firing rate in multi-timescale systems, which can be applied to neuronal activity, calcium signaling and other types of cell dynamics.

IF and IB would like to thank M. WOLFRUM and S. YANCHUK for useful discussions. The work of VK on

the third section was supported by the Russian Science Foundation, grant No. 16-42-01043. The work of VN on the fourth section was supported by the Russian Science Foundation, grant No. 14-12-01358.

REFERENCES

- [1] LINDNER B., GARCIA-OJALVO J., NEIMAN A. and SCHIMANSKY-GEIER L., *Phys. Rep.*, **392** (2004) 321.
- [2] MCDONNELL M. D. and WARD L. M., *Nat. Rev. Neurosci.*, **12** (2011) 415.
- [3] SCHMERL B. A. and MCDONNELL M. D., *Phys. Rev. E*, **88** (2013) 052722.
- [4] GAMMAITONI L., HÄNGGI P., JUNG P. and MARCHESONI F., *Rev. Mod. Phys.*, **70** (1998) 223.
- [5] GUTKIN B. S., JOST J. and TUCKWELL H. C., *EPL*, **81** (2008) 20005.
- [6] TUCKWELL H. C., JOST J. and GUTKIN B. S., *Phys. Rev. E*, **80** (2009) 031907.
- [7] UZUNTARLA M., CRESSMAN J. R., OZER M. and BARRETO E., *Phys. Rev. E*, **88** (2013) 042712.
- [8] UZUNTARLA M., *Phys. Lett. A*, **377** (2013) 2585.
- [9] UZUNTARLA M., TORRES J. J., SO P., OZER M. and BARRETO E., *Phys. Rev. E*, **95** (2017) 012404.
- [10] UZUNTARLA M., BARRETO E. and TORRES J. J., *PLoS Comput. Biol.*, **13** (2017) e1005646.
- [11] BUCHIN A., RIEUBLAND S., HÄUSSER M., GUTKIN B. S. and ROTH A., *PLoS Comput. Biol.*, **12** (2016) e1005000.
- [12] FRANOVIĆ I., OMEL'CHENKO O. E. and WOLFRUM M., *Chaos*, **28** (2018) 071105.
- [13] HAHN T. T. G., MCFARLAND J. M., BERBERICH S., SAKMANN B. and MEHTA M. R., *Nat. Neurosci.*, **15** (2012) 1531.
- [14] FRANOVIĆ I. and KLINSHOV V., *Chaos*, **28** (2018) 023111.
- [15] FRANOVIĆ I. and KLINSHOV V., *EPL*, **116** (2016) 48002.
- [16] SONG S., MILLER K. D. and ABBOTT L. F., *Nat. Neurosci.*, **3** (2000) 919.
- [17] FROEMKE R. C. and DAN Y., *Nature*, **416** (2002) 433.
- [18] WANG H.-X., GERKIN R. C., NAUEN D. W. and BI G.-Q., *Nat. Neurosci.*, **8** (2005) 187.
- [19] LÜCKEN L., POPOVYCH O. V., TASS P. A. and YANCHUK S., *Phys. Rev. E*, **93** (2016) 032210.
- [20] KASATKIN D. V. and NEKORKIN V. I., *Radiophys. Quantum Electron.*, **58** (2016) 877.
- [21] BAČIĆ I., YANCHUK S., WOLFRUM M. and FRANOVIĆ I., *Eur. Phys. J. ST*, **227** (2018) 1077.
- [22] KASATKIN D., YANCHUK S., SCHÖLL E. and NEKORKIN V., *Phys. Rev. E*, **96** (2017) 062211.
- [23] DESTEXHE A. and RUDOLPH-LILITH M., *Neuronal Noise* (Springer, New York) 2012.
- [24] MAISTRENKO Y. L., LYSYANSKY B., HAUPTMANN C., BURLYKO O. and TASS P., *Phys. Rev. E*, **75** (2007) 066207.
- [25] AOKI T. and AOYAGI T., *Phys. Rev. Lett.*, **102** (2009) 034101.
- [26] AOKI T. and AOYAGI T., *Phys. Rev. E*, **84** (2011) 066109.
- [27] BERGLUND N. and GENTZ B., *Noise-Induced Phenomena in Slow-Fast Dynamical Systems* (Springer, Berlin) 2006.
- [28] LAING C. and LORD G. J. (Editors), *Stochastic Methods in Neuroscience* (Oxford University Press, London) 2009.
- [29] KUEHN C., *Multiple Time Scale Dynamics* (Springer International Publishing, Switzerland) 2015.
- [30] SHILNIKOV A., *Int. J. Bifurcat. Chaos*, **18** (2008) 2141.

Inverse stochastic resonance in a system of excitable active rotators with adaptive coupling

IVA BAČIĆ¹, VLADIMIR KLINSHOV², VLADIMIR NEKORKIN², MATJAŽ PERC³ and IGOR FRANOVIĆ^{1(a)}

¹ *Scientific Computing Laboratory, Center for the Study of Complex Systems, Institute of Physics Belgrade, University of Belgrade - Pregrevica 118, 11080 Belgrade, Serbia*

² *Institute of Applied Physics of the Russian Academy of Sciences - 46 Ulyanov Street, 603950 Nizhny Novgorod, Russia*

³ *Faculty of Natural Sciences and Mathematics, University of Maribor - Koroška cesta 160, SI-2000 Maribor, Slovenia*

received 17 September 2018; accepted in final form 8 November 2018

published online 11 December 2018

PACS 05.40.Ca – Noise

PACS 87.19.1n – Oscillations and resonance

Abstract – Inverse stochastic resonance is a phenomenon where an oscillating system influenced by noise exhibits a minimal oscillation frequency at an intermediate noise level. We demonstrate a novel generic scenario for such an effect in a multi-timescale system, considering an example of emergent oscillations in two adaptively coupled active rotators with excitable local dynamics. The impact of plasticity turns out to be twofold. First, at the level of multiscale dynamics, one finds a range of intermediate adaptivity rates that give rise to multistability between the limit cycle attractors and the stable equilibria, a condition necessary for the onset of the effect. Second, applying the fast-slow analysis, we show that the plasticity also plays a facilitatory role on a more subtle level, guiding the fast flow dynamics to parameter domains where the stable equilibria become focuses rather than nodes, which effectively enhances the influence of noise. The described scenario persists for different plasticity rules, underlying its robustness in the light of potential applications to neuroscience and other types of cell dynamics.

Copyright © EPLA, 2018

Introduction. – Noise in coupled excitable or bistable systems may induce two types of generic effects [1]. On the one hand, it can modify the deterministic behavior by acting non-uniformly on different states of the system, thus amplifying or suppressing some of its features. On the other hand, noise may give rise to completely novel forms of behavior, typically based on crossing the thresholds or separatrices, or involving enhanced stability of deterministically unstable structures. In neuronal systems, the constructive role of noise at different stages of information processing, referred to as “stochastic facilitation” [2,3], mainly comprises resonant phenomena. A classical example is the stochastic resonance [4], which allows for the detection of weak subthreshold periodic signals. A more recent development concerns the effect of inverse stochastic resonance (ISR) [3,5–12], where noise selectively reduces the spiking frequency of neuronal oscillators, converting the tonic firing into intermittent bursting-like activity or a short-lived transient followed

by a long period of quiescence. The name of the effect should be taken *cum grano salis*, because in contrast to stochastic resonance, it involves no additional external signal: one rather observes a non-monotonous dependence of the spiking rate on noise variance, whereby the oscillation frequency becomes minimal at a preferred noise level. Such an inhibitory effect of noise has recently been shown for cerebellar Purkinje cells [11], having explicitly demonstrated how the lifetimes of the spiking (“up”) and the silent (“down”) states [13–15] are affected by the noise variance. ISR has been indicated to play important functional roles in neuronal systems, including the reduction of spiking frequency in the absence of neuromodulators, suppression of pathologically long short-term memories, triggering of on-off tonic spiking activity and even optimization of information transfer along the signal propagation pathways [3,7,9,11].

So far, theoretical studies on ISR have mostly concerned the scenario where a single neuron exhibits bistable deterministic dynamics, featuring coexistence between a limit cycle and a stable equilibrium. Such bistability is

^(a)E-mail: franovic@ipb.ac.rs

typical for Type-II neurons below the subcritical Hopf bifurcation, *e.g.*, classical Hodgkin-Huxley and Morris-Lecar models [3,6–8]. There, applying noise induces switching between the metastable states, but at an intermediate noise level, one surprisingly finds a strong asymmetry of the associated switching rates, which makes the periods spent in the vicinity of equilibrium much longer than the periods of spiking activity.

An important open problem concerns conditions giving rise to ISR in coupled excitable systems, where noise influences the emergent oscillations. Here we address in detail this issue, as it may be crucial to understanding the prevalence of the effect in neural networks, whose activity depends on the interplay of excitability, coupling properties and noise. Synaptic dynamics typically involves the plasticity feature, which makes self-organization in neuronal systems a multi-timescale process: the short-term spiking activity unfolds on a quasi-static coupling configuration, while the slow adjustment of coupling weights depends on the time-averaged evolution of units.

Motivated by the findings in neuroscience, we focus on the onset of ISR in a simplified, yet paradigmatic system of two adaptively coupled stochastic active rotators with excitable local dynamics. Active rotators are canonical for Type-I excitability and may be seen as equivalent to the theta-neuron model. Adaptivity is introduced in a way that allows continuous interpolation between a spectrum of plasticity rules, including Hebbian learning and spike-time-dependent plasticity (STDP) [16–18].

We demonstrate a generic scenario for the plasticity-induced ISR, where the system’s multiscale structure, defined by the adaptivity rate, plays a crucial role. On a basic level, plasticity gives rise to multistable behavior involving coexisting stationary and oscillatory regimes. An additional subtlety, which we show by the fast-slow analysis, is that the plasticity promotes the resonant effect by guiding the fast flow toward the parameter region where the stable fixed points are focuses rather than nodes.

The paper is organized as follows. In the next section the details of the model and the numerical bifurcation analysis of the deterministic dynamics are presented. The third section contains the results on the ISR effect and the supporting conditions. In the fourth section the fast-slow analysis is applied to explain the mechanism by which plasticity enhances the system’s non-linear response to noise. Apart from providing a brief summary, in the last section we also discuss the prevalence of the observed effect.

Model and bifurcation analysis of deterministic dynamics. – Our model involves two stochastic active rotators interacting by adaptive couplings [19–22],

$$\begin{aligned}\dot{\varphi}_1 &= I_0 - \sin \varphi_1 + \kappa_1 \sin(\varphi_2 - \varphi_1) + \sqrt{D}\xi_1(t), \\ \dot{\varphi}_2 &= I_0 - \sin \varphi_2 + \kappa_2 \sin(\varphi_1 - \varphi_2) + \sqrt{D}\xi_2(t), \\ \dot{\kappa}_1 &= \epsilon(-\kappa_1 + \sin(\varphi_2 - \varphi_1 + \beta)), \\ \dot{\kappa}_2 &= \epsilon(-\kappa_2 + \sin(\varphi_1 - \varphi_2 + \beta)),\end{aligned}\quad (1)$$

where the phases $\{\varphi_1, \varphi_2\} \in S^1$, while the coupling weights $\{\kappa_1, \kappa_2\}$ are real variables.

The excitability parameters I_0 , which one may interpret as external bias currents in the context of neuroscience, are assumed to be identical for both units. For such a setup, the deterministic version of (1) possesses a Z_2 symmetry, being invariant to the exchange of units’ indices. The uncoupled units undergo a SNIPER bifurcation at $I_0 = 1$, with the values $I_0 < 1$ ($I_0 > 1$) corresponding to the excitable (oscillatory) regime. We consider the case of excitable local dynamics, keeping $I_0 = 0.95$ fixed throughout the paper, such that the oscillations may emerge only due to the coupling terms and/or noise. The scale separation between the fast dynamics of the phases and the slow dynamics of adaptation is adjusted by the parameter $\epsilon \ll 1$. The fast variables are influenced by independent white noise of variance D such that $\xi_i(t)\xi_j(t') = \delta_{ij}\delta(t-t')$ for $i, j \in \{1, 2\}$. Conceptually, adding stochastic input to the fast variables embodies the action of synaptic noise in neuronal systems [23].

The modality of the plasticity rule is specified by the parameter β , whose role may be understood by invoking the qualitative analogy between the adaptation dynamics in classical neuronal systems and the systems of coupled phase oscillators. This issue has first been addressed in [24–26], and a deeper analysis of the correspondence between the phase-dependent plasticity rules and the STDP has been carried out in [19]. In particular, it has been shown that the plasticity dynamics for $\beta = 3\pi/2$, where the stationary weights between the oscillators with smaller/larger phase differences increase/decrease, qualitatively resembles the Hebbian learning rule [25,26]. Nevertheless, when $\beta = \pi$, the coupling weights encode a causal relationship between the spiking of oscillators by changing in the opposite directions, in analogy to an STDP-like plasticity rule. Our interest lies with the β interval interpolating between these two limiting cases.

Using bifurcation analysis of the deterministic dynamics of (1), we first show how the modality of the plasticity rule influences the number of stationary states, and then explain how the onset of oscillations depends on adaptivity rate. The bifurcation diagram in fig. 1 indicates that the number and the stability of fixed points of (1) change with β in such a way that the system may possess two, four or six fixed points. Due to invariance to Z_2 symmetry, one always finds pairs of solutions sharing the same stability features. We consider the plasticity rules described by $\beta \in (3.298, 4.495)$, cf. the shaded region in fig. 1, where the system has two stable fixed points lying off the synchronization manifold $\varphi_1 = \varphi_2$, as well as four unstable fixed points. The bifurcations occurring at the boundaries of the relevant β interval are as follows. At $\beta = 3.298$, the system undergoes a supercritical symmetry-breaking pitchfork bifurcation giving rise to a pair of stable fixed points off the synchronization manifold. For $\beta = 4.495$, this pair of stable fixed points collides with a pair of unstable fixed points off

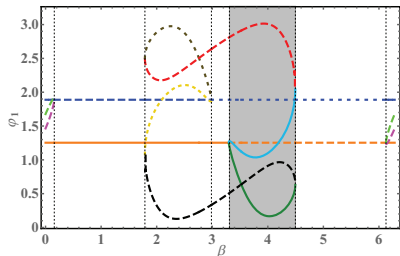


Fig. 1: (Color online) Bifurcation diagram for the fixed points of (1) with $D = 0$ under variation of β . Solid lines refer to stable fixed points, while dashed and dotted lines correspond to saddles of unstable dimension 1 and 2, respectively. Shading indicates the considered range of plasticity rules. The two fixed points independent on β belong to the synchronization manifold. The remaining parameters are $I_0 = 0.95, \epsilon = 0.05$.

the synchronization manifold, getting annihilated in two symmetry-related inverse fold bifurcations. Note that the weight levels typical for the two stable stationary states support effective unidirectional interaction, in a sense that one unit exerts a much stronger impact on the dynamics of the other unit than vice versa. When illustrating the effect of ISR, we shall mainly refer to the case $\beta = 4.2$. For this β , the two stable focuses of (1) at $D = 0$ are given by $(\varphi_1, \varphi_2, \kappa_1, \kappa_2) = (1.177, 0.175, 0.032, -0.92)$ and $(\varphi_1, \varphi_2, \kappa_1, \kappa_2) = (0.175, 1.177, -0.92, 0.032)$. Within the considered β interval, the two stable fixed points of the coupled system exhibit excitable behavior, responding to external perturbation by generating either the successive spikes or synchronized spikes [21].

The onset of oscillations for the deterministic version of (1) relies on the interplay between the plasticity rule, controlled by β , and the adaptation rate, characterized by ϵ . In fig. 2(a) are shown the results of parameter sweep indicating the variation of κ_1 variable, $\sigma_{\kappa_1} = \max(\kappa_1(t)) - \min(\kappa_1(t))$, within the (β, ϵ) parameter plane. The sweep indicates the maximal stability region of the two emerging periodic solutions, related by the exchange symmetry of units indices. The data are obtained by numerical continuation starting from a stable periodic solution, such that the final state reached for the given parameter set is used as initial conditions of the system dynamics for incremented parameter values. One observes that for fixed β , there exists an interval of timescale separation ratios $\epsilon \in (\epsilon_{min}, \epsilon_{max})$ admitting oscillations, see fig. 2(b). Within the given ϵ range, the system exhibits multistability where periodic solutions coexist with the two symmetry-related stable stationary states. The lower threshold for oscillations, ϵ_{min} , reduces with β , whereas the upper boundary value, ϵ_{max} , is found to grow as β is enhanced. Note that the waveform of oscillations also changes as ϵ is increased under fixed β . In particular, for smaller ϵ , the waveforms corresponding to the two units are rather different. Nevertheless, around $\epsilon \approx 0.06$ the system undergoes a pitchfork bifurcation of limit cycles, such that

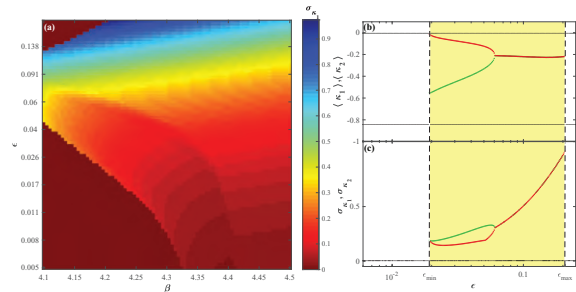


Fig. 2: (Color online) Onset of oscillations in (1) for $D = 0$. (a) Variation σ_{κ_1} of the coupling weight κ_1 in the (β, ϵ) -plane. (b) Mean coupling weights $\langle \kappa_1 \rangle(\epsilon)$ and $\langle \kappa_2 \rangle(\epsilon)$ for oscillatory (thick lines) and stationary states (thin lines) at $\beta = 4.2$. (c) Variation $\sigma_{\kappa_1}(\epsilon)$ and $\sigma_{\kappa_2}(\epsilon)$, presented as in (b). Shading in (b) and (c) indicates the ϵ interval admitting the stable periodic solutions.

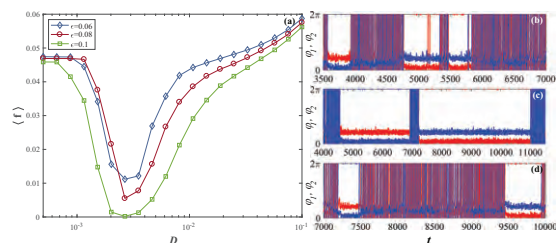


Fig. 3: (Color online) (a) Mean spiking rate $\langle f \rangle$ in terms of D for $\epsilon \in \{0.06, 0.08, 0.1\}$. The curves exhibit a characteristic minimum at an intermediate noise level. (b)–(d) Time traces $\varphi_1(t)$ and $\varphi_2(t)$ for noise levels below, at and above the resonant value. The remaining parameters are $I_0 = 0.95, \beta = 4.2, \epsilon = 0.06$.

the oscillatory solution gains the anti-phase space-time symmetry $\varphi_1(t) = \varphi_2(t + T/2), \kappa_1(t) = \kappa_2(t + T/2)$, where T denotes the oscillation period [21].

Numerical results on ISR. – Inverse stochastic resonance manifests itself as noise-mediated suppression of oscillations, whereby the frequency of noise-perturbed oscillations becomes minimal at a preferred noise level. For system (1), we find such an effect to occur generically for intermediate adaptivity rates, supporting multistability between the stationary and the oscillatory solutions, as described in the previous section. A family of curves describing the dependence of the oscillation frequency on noise variance $\langle f \rangle(D)$ for different ϵ values is shown in fig. 3. All the curves corresponding to $\epsilon \geq \epsilon_{min}(\beta)$ show a characteristic non-monotonous behavior, displaying a minimum at the optimal noise intensity. For weaker noise, the oscillation frequency remains close to the deterministic one, whereas for much stronger noise, the frequency increases above that of unperturbed oscillations. The displayed results are obtained by averaging over an ensemble of 1000 different stochastic realizations, having excluded the transient behavior, and having fixed a single set of initial conditions within the basin of attraction of the limit cycle attractor. Nevertheless, we have verified that the

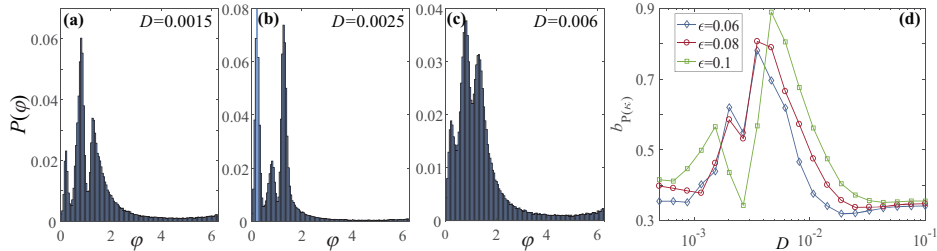


Fig. 4: (Color online) (a)–(c) Stationary distribution $P(\varphi_1)$ for the noise levels below, at and above the resonant value. System parameters are $I_0 = 0.95$, $\beta = 4.2$ and $\epsilon = 0.06$. From the three observable peaks, the middle one, prevalent in (a) and (c), refers to the metastable state associated to the oscillatory mode of (1) for $D = 0$. The two lateral peaks, dominant in (b), correspond to quasi-stationary states derived from the stable equilibria of the deterministic version of (1). (d) Bimodality coefficient for the stationary distribution of κ_1 , $b_{P(\kappa_1)}$, as a function of D . The three curves refer to $\epsilon = 0.06$ (diamonds), $\epsilon = 0.08$ (circles) and $\epsilon = 0.1$ (squares).

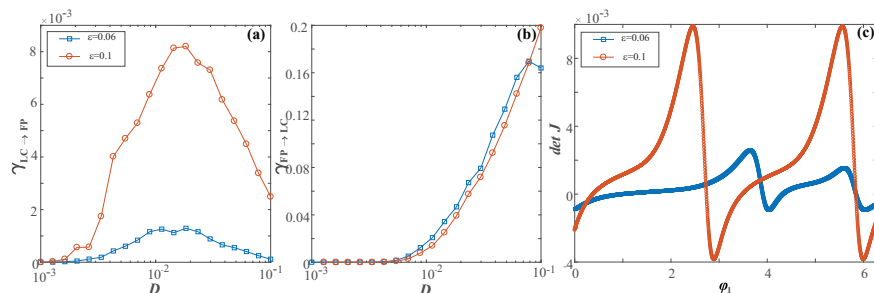


Fig. 5: (Color online) (a) and (b): transition rates from the stability basin of the limit cycle to the fixed point, $\gamma_{LC \rightarrow FP}(D)$ and vice versa, $\gamma_{FP \rightarrow LC}(D)$, numerically obtained for $\epsilon = 0.06$ (squares) and $\epsilon = 0.1$ (circles). The remaining parameters are $I_0 = 0.95$, $\beta = 4.2$. (c) Determinant of the Jacobian calculated along the limit cycle orbit as a function of the phase variable. The quantity provides an indication of the sensitivity of certain sections of the orbit to external perturbation. Blue and red colors correspond to $\epsilon = 0.06$ and $\epsilon = 0.1$, respectively.

qualitatively analogous results are obtained if for each realization of stochastic process one selects a set of random initial conditions lying within the stability basin of the periodic solution. The suppression effect of noise depends on the adaptivity rate, and is found to be more pronounced for faster adaptivity. Indeed, for smaller ϵ , $\varphi(t)$ series corresponding to the noise levels around the minimum of $\langle f \rangle(D)$ exhibit bursting-like behavior, whereas for larger ϵ , noise is capable of effectively quenching the oscillations, such that the minimal observed frequency approaches zero.

The core of the described effect concerns switching dynamics between the metastable states associated to coexisting attractors of the deterministic version of system (1). To illustrate this, in fig. 4 we have considered the stationary distributions of one of the phase variables, $P(\varphi)$, for the noise levels below, at and above the minimum of the $\langle f \rangle(D)$, having fixed the remaining parameters to $(\beta, \epsilon) = (4.2, 0.06)$. The distribution $P(\varphi)$ is characterized by two lateral peaks, reflecting the two symmetry-related quasi-stationary states, and the area around the central peak, corresponding to the oscillatory mode. For small noise $D = 0.0015$, see fig. 4(a), and very large noise $D = 0.006$, cf. fig. 4(c), the central peak of $P(\varphi)$ is expectedly prevalent compared to the two lateral peaks. Nevertheless, the switching dynamics for

$D = 0.0025$, the noise level about the minimum of $\langle f \rangle(D)$, is fundamentally different, and the corresponding distribution $P(\varphi)$ in fig. 4(b) shows that the system spends much more time in the quasi-stationary states than performing the oscillations. The onset of ISR in the dynamics of fast variables is accompanied by the increased bimodality of the stationary distribution of the couplings, see fig. 4(d).

In order to observe the non-monotonous response of the system's frequency to noise, the geometry of the phase space has to be asymmetrical with respect to the separatrix between the coexisting attractors in such a way that the limit cycle attractor lies much closer to the separatrix than the stationary states. Such structure of phase space gives rise to asymmetry in switching dynamics, whereby at the preferred noise level around the minimum of $\langle f \rangle(D)$, the transition rate from the stability basin of the limit cycle attractor to that of stationary states $\gamma_{LC \rightarrow FP}$ becomes much larger than the transition rate in the inverse direction, $\gamma_{FP \rightarrow LC}$. Figures 5(a) and (b) corroborate that the dependences $\gamma_{LC \rightarrow FP}(D)$ and $\gamma_{FP \rightarrow LC}(D)$ are qualitatively distinct: the former displays a maximum at the resonant noise level, whereas the latter just increases monotonously with noise. The fact that ISR is more pronounced for higher adaptivity rates is reflected in that the curve $\gamma_{LC \rightarrow FP}(D)$ for $\epsilon = 0.1$ lies substantially above that for $\epsilon = 0.06$, see fig. 5(a).

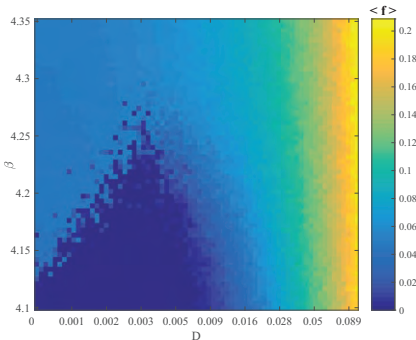


Fig. 6: (Color online) Mean spiking rate $\langle f \rangle$ as a function of β and D for fixed $\epsilon = 0.05$. The results evince the robustness of the ISR effect with respect to different plasticity rules.

To understand why the interplay of adaptivity rate and noise yields a stronger resonant effect for larger ϵ , we have investigated the susceptibility of the limit cycle attractor to external perturbation. In particular, fig. 5(c) shows how the determinant of the Jacobian calculated along the limit cycle orbit change for $\epsilon = 0.06$ (blue line) and $\epsilon = 0.1$ (red line), respectively. For smaller ϵ , one may identify two particular points where the determinant of the Jacobian is the largest, *i.e.*, where the impact of external perturbation is felt the strongest. This implies that noise is most likely to drive the systems trajectory away from the limit cycle attractor around these two sections of the orbit, which should lie closest to the boundary to the stability basins of the stationary states. Such a physical picture is maintained for larger ϵ , but one should stress that the sensitivity of limit cycle attractor to external perturbation substantially increases along the entire orbit, cf. fig. 5(c). In other words, faster adaptivity enhances the impact of noise, contributing to a more pronounced ISR effect. This point is addressed from another perspective in the next section.

We also examine the robustness of ISR to different modalities of the plasticity rule specified by β . Figure 6 shows how the average oscillation frequency changes with β and D for fixed $\epsilon = 0.05$. The non-linear response to noise, conforming to a resonant effect with a minimum of oscillation frequency at an intermediate noise level, persists in a wide range of β , essentially interpolating between the Hebbian-like and the STDP-like adaptive dynamics.

Fast-slow analysis: role of plasticity in the resonant effect. – Though ISR is observed for intermediate ϵ , here we show that the fast-slow analysis may still be applied to demonstrate a peculiar feature of the mechanism behind the resonant effect. In particular, we find that the plasticity enhances the resonant effect by driving the fast flow dynamics toward the parameter domain where the stationary state is a focus rather than a node. It is well known that the response to noise in multi-timescale systems qualitatively depends on the character of stationary states. Indeed, by using the sample-paths approach and other advanced techniques, it has already been shown

that such systems may exhibit fundamentally different scaling regimes with respect to noise variance and the scale-separation ratio [27,28]. Moreover, the resonant effects may typically be expected in the case in which quasi-stationary states are focuses [27], essentially because the local dynamics around the stationary state then involves an eigenfrequency.

Within the standard fast-slow analysis, one may either consider the layer problem, defined on the fast timescale, or the reduced problem, concerning the slow timescale [29]. For the layer problem, the fast flow dynamics $\varphi_1(t; \kappa_1, \kappa_2), \varphi_2(t; \kappa_1, \kappa_2)$ is obtained by treating the slow variables κ_1 and κ_2 as system parameters, whereas in the case of the reduced problem, determining the dynamics of the slow flow $(\kappa_1(t), \kappa_2(t))$ involves time-averaging over the stable regimes of the fast flow of the layer problem. The fast flow can in principle exhibit several attractors, which means that multiple stable sheets of the slow flow may emerge from the averaged dynamics on the different attractors of the fast flow. Our key point concerns the dynamics of the slow flow, which requires us to first classify the attractors of the fast flow.

The fast flow dynamics is given by

$$\begin{aligned}\dot{\varphi}_1 &= I_0 - \sin \varphi_1 + \kappa_1 \sin(\varphi_2 - \varphi_1), \\ \dot{\varphi}_2 &= I_0 - \sin \varphi_2 + \kappa_2 \sin(\varphi_1 - \varphi_2),\end{aligned}\quad (2)$$

where $\kappa_1, \kappa_2 \in [-1, 1]$ are considered as additional system parameters. One may formally obtain (2) by setting $\epsilon = 0$ in (1) with $D = 0$. We find that the fast flow is monostable for most of the (κ_1, κ_2) values, exhibiting either a stable equilibrium or a limit cycle attractor, see fig. 7(a). In general, the fast flow admits either two or four fixed points, and a more detailed physical picture, including the associated bifurcations, is presented in [21]. The stability region of the oscillatory regime, outlined by the red color, has been calculated by numerical continuation starting from a stable periodic solution. Bistability between a stable fixed point and a limit cycle is observed only in a small area near the main diagonal $\kappa_1 = \kappa_2$. Within the region featuring oscillatory regime, each periodic solution obtained for (κ_1, κ_2) above the main diagonal has a Z_2 symmetry-related counterpart below the diagonal. Typically, the periodic solutions emanate from SNIPER bifurcations, which make up two branches where either κ_1 or κ_2 are almost constant and close to zero.

Using the results from the analysis of the layer problem, our goal is to determine the vector fields corresponding to the stable sheets of the slow flow. We have numerically obtained the dynamics of the slow flow by a standard two-step approach [19,30]. First, for fixed values (κ_1, κ_2) , we have determined the time-averaged dynamics of the fast flow (2), $\langle \varphi_2 - \varphi_1 \rangle_t = h(\kappa_1, \kappa_2)$, whereby the averaging $\langle \cdot \rangle_t$ is carried out over a sufficiently long time interval, having excluded the transient behavior. As already indicated, such an average depends on the attractor of the fast flow for the given (κ_1, κ_2) . If the fast flow possesses

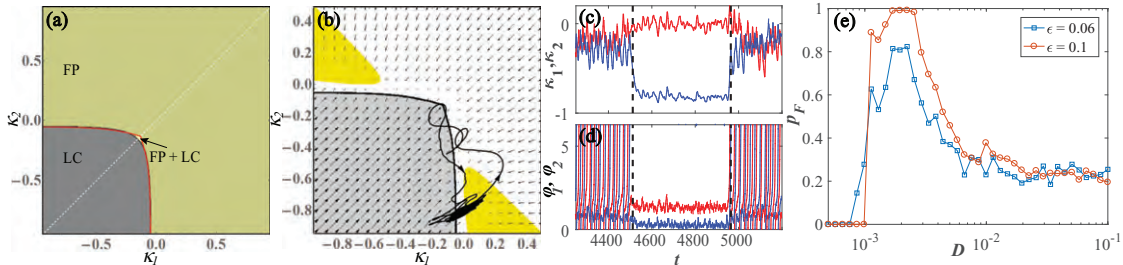


Fig. 7: (Color online) (a) Attractors of the fast flow (2) in terms of κ_1 and κ_2 , now treated as free parameters. The fast flow is typically monostable, admitting either a stable fixed point (FP) or a stable limit cycle (LC), apart from a small region of bistability (FP+LC) around the main diagonal. (b) Vector field of the slow flow (3) determined by considering only the stable regimes of the fast flow for $\beta = 4.2, I_0 = 0.95$. Within the yellow-highlighted regions, the stable fixed point of the fast flow is a focus rather than the node. The displayed orbit $(\kappa_1(t), \kappa_2(t))$ corresponds to a switching episode from the oscillatory state to the quasi-stationary state and back (evolution direction indicated by arrows). Panels (c) and (d) show the time traces of phases and couplings during the switching episode. (e) Conditional probability $p_F(D)$ for $\epsilon = 0.06$ (blue squares) and $\epsilon = 0.1$ (red circles).

a stable fixed point, then $\langle \varphi_2 - \varphi_1 \rangle_t = \varphi_2^* - \varphi_1^*$, which corresponds to the slow critical manifold of the system. For (κ_1, κ_2) where the attractor of the fast flow is a periodic solution, $\langle \varphi_2 - \varphi_1 \rangle_t$ amounts to the time average over the period. Averaging over a periodic attractor of the fast flow is a standard approximation [30], quite natural when describing the influence of oscillations in the fast flow to the dynamics of the slow flow.

As the second step, the obtained time averages are substituted into the coupling dynamics

$$\begin{aligned} \dot{\kappa}_1 &= \epsilon[-\kappa_1 + \sin(h(\kappa_1, \kappa_2) + \beta)], \\ \dot{\kappa}_2 &= \epsilon[-\kappa_2 + \sin(-h(\kappa_1, \kappa_2) + \beta)]. \end{aligned} \quad (3)$$

The system (3) allows one to determine the vector fields on the stable sheets of the slow flow, which correspond to the attractors of the fast flow. In fig. 7(b), the vector fields associated to each of the attractors (fixed point or limit cycle) are presented within its respective (κ_1, κ_2) stability region. In the small region of the (κ_1, κ_2) -plane supporting coexisting stable solutions of the fast flow, the corresponding vector field of the slow flow is given on multiple overlapping sheets, since the value of the average $f(\kappa_1, \kappa_2)$ depends on the initial conditions.

Within the above framework, one is able to explain a subtle influence of adaptivity on the mechanism behind the ISR. To this end, in fig. 7(b) we have projected a typical example of the $(\kappa_1(t), \kappa_2(t))$ trajectory of the full system (1) corresponding to a switching episode between the metastable states associated to a limit cycle attractor and a stable equilibrium of the deterministic system, see the time traces in figs. 7(c), (d). One observes that for the oscillating regime, the coupling dynamics always remains close to the SNIPER bifurcation of the fast flow, cf. fig. 7(a), which makes the oscillations quite susceptible to noise. Recall that the fast flow is typically monostable. Thus, switching events in the full system are naturally associated to the fast flow undergoing the SNIPER bifurcation: either a direct one, leading from the oscillatory to the stationary regime, or the inverse one, unfolding in the

opposite direction. For (κ_1, κ_2) values immediately after the SNIPER bifurcation toward the quiescent state, the stable equilibrium of the fast flow is a node. Nevertheless, for the noise levels where the effect of ISR is most pronounced, we find that the coupling dynamics guides the system into the region where the equilibrium is a stable focus rather than a node, see the yellow highlighted region in fig. 7(b). We have verified that this feature is a hallmark of the resonant effect by numerically calculating the conditional probability p_F that the events of crossing the SNIPER bifurcation are followed by the system's orbit visiting the (κ_1, κ_2) region where the stable equilibrium is a focus. The $p_F(D)$ dependences for two characteristic ϵ values at fixed $\beta = 4.2$ are plotted in fig. 7(e). One learns that $p_F(D)$ has a maximum for the resonant noise levels, where the corresponding curve $f(D)$ displays a minimum. In other words, the fact that the coupling dynamics drives the fast flow to the focus-associated regions of the (κ_1, κ_2) -plane results in trapping the phase variables for a longer time in the quasi-stationary (quiescent) state. Small noise below the resonant values is insufficient to drive the system to this region, whereas for too large a noise, the stochastic fluctuations completely take over, washing out the quasi-stationary regime. Note that for the faster adaptivity rate, the facilitatory role of coupling becomes more pronounced, as evinced by the fact that the curve $p_F(D)$ for $\epsilon = 0.1$ lies above the one for $\epsilon = 0.06$.

Discussion. – In the present paper, we have demonstrated a novel generic scenario for the onset of ISR, which involves an interplay between the local excitability feature and the adaptive dynamics of the couplings. For the example of two active rotators with coupling plasticity, we have shown that the spiking frequency corresponding to emergent oscillations varies non-monotonously with noise, displaying a minimum at a preferred noise level. Though the model *per se* is simplified, the underlying paradigm is relevant for combining the two core features of typical neuronal systems. The effect derives from the multi-timescale structure of the system, whereby the scale

separation between the local and the weight dynamics is tuned via adaptivity rate. Within a range of intermediate adaptivity rates, the deterministic dynamics of the full system exhibits multistability between the limit cycle attractors and the stable equilibria, each appearing in pairs due to the systems invariance to Z_2 symmetry. Applying the standard fast-slow analysis, we have shown that the resonant effect with noise is in fact plasticity-enhanced: plasticity promotes the impact of noise by guiding the fast flow toward the parameter domain where the stable equilibria become focuses instead of nodes. This mechanism increases the trapping efficiency by which the noise is able to deviate the systems trajectory from the metastable oscillatory states to the non-spiking regime. For faster adaptivity, the resonant effect is found to be more pronounced in a sense that the frequency dependence on noise shows deeper minima. Our scenario has proven to persist in a wide range of plasticity rules, interpolating between the cases analogous to Hebbian learning and STDP.

In earlier studies, observation of ISR has mostly been confined to Type-II neurons with intrinsic bistable dynamics, as in case of Hodgkin-Huxley or Morris-Lecar neurons near the subcritical Hopf bifurcation [3,6–9]. Even in case of networks, the macroscopic ISR effect has been linked to dynamical features of single units, only being modulated by the details of synaptic dynamics and the network topology [10]. In contrast to that, our results show that ISR may not rely on bistability of local dynamics, but may rather emerge due to the facilitatory role of coupling, here reflected in the interplay of multiscale dynamics and plasticity. Another distinction from most of the previous studies is that our scenario concerns Type-I units. For this class of systems, it is known that the dependence of the oscillating frequency of a single unit with noise is just monotonous [3,12], so that the resonant effect can only be observed in case of coupled units. So far, the latter case has been analyzed only once [5], but the underlying scenario is different from ours insofar as it involves static, rather than the adaptive couplings, and the effect *per se* is confined to a narrow region of the parameter space.

Quite recently, the onset of ISR has been reported for a single Fitzhugh-Nagumo oscillator [12], which is the first observation of the effect for Type-II neuron model in the vicinity of the supercritical Hopf bifurcation. Similar to the scenario we elaborated, ISR there also derives from the multiscale structure of the system. However, the actual mechanism behind the effect is associated to phase-sensitive (non-uniform) excitability of a limit cycle orbit conforming to relaxation oscillations [12]. These findings and the results here suggest that ISR may indeed provide a generic means of controlling and optimizing the firing rate in multi-timescale systems, which can be applied to neuronal activity, calcium signaling and other types of cell dynamics.

IF and IB would like to thank M. WOLFRUM and S. YANCHUK for useful discussions. The work of VK on

the third section was supported by the Russian Science Foundation, grant No. 16-42-01043. The work of VN on the fourth section was supported by the Russian Science Foundation, grant No. 14-12-01358.

REFERENCES

- [1] LINDNER B., GARCIA-OJALVO J., NEIMAN A. and SCHIMANSKY-GEIER L., *Phys. Rep.*, **392** (2004) 321.
- [2] MCDONNELL M. D. and WARD L. M., *Nat. Rev. Neurosci.*, **12** (2011) 415.
- [3] SCHMERL B. A. and MCDONNELL M. D., *Phys. Rev. E*, **88** (2013) 052722.
- [4] GAMMAITONI L., HÄNGGI P., JUNG P. and MARCHESONI F., *Rev. Mod. Phys.*, **70** (1998) 223.
- [5] GUTKIN B. S., JOST J. and TUCKWELL H. C., *EPL*, **81** (2008) 20005.
- [6] TUCKWELL H. C., JOST J. and GUTKIN B. S., *Phys. Rev. E*, **80** (2009) 031907.
- [7] UZUNTARLA M., CRESSMAN J. R., OZER M. and BARRETO E., *Phys. Rev. E*, **88** (2013) 042712.
- [8] UZUNTARLA M., *Phys. Lett. A*, **377** (2013) 2585.
- [9] UZUNTARLA M., TORRES J. J., SO P., OZER M. and BARRETO E., *Phys. Rev. E*, **95** (2017) 012404.
- [10] UZUNTARLA M., BARRETO E. and TORRES J. J., *PLoS Comput. Biol.*, **13** (2017) e1005646.
- [11] BUCHIN A., RIEUBLAND S., HÄUSSER M., GUTKIN B. S. and ROTH A., *PLoS Comput. Biol.*, **12** (2016) e1005000.
- [12] FRANOVIĆ I., OMEL'CHENKO O. E. and WOLFRUM M., *Chaos*, **28** (2018) 071105.
- [13] HAHN T. T. G., MCFARLAND J. M., BERBERICH S., SAKMANN B. and MEHTA M. R., *Nat. Neurosci.*, **15** (2012) 1531.
- [14] FRANOVIĆ I. and KLINSHOV V., *Chaos*, **28** (2018) 023111.
- [15] FRANOVIĆ I. and KLINSHOV V., *EPL*, **116** (2016) 48002.
- [16] SONG S., MILLER K. D. and ABBOTT L. F., *Nat. Neurosci.*, **3** (2000) 919.
- [17] FROMKE R. C. and DAN Y., *Nature*, **416** (2002) 433.
- [18] WANG H.-X., GERKIN R. C., NAUEN D. W. and BI G.-Q., *Nat. Neurosci.*, **8** (2005) 187.
- [19] LÜCKEN L., POPOVYCH O. V., TASS P. A. and YANCHUK S., *Phys. Rev. E*, **93** (2016) 032210.
- [20] KASATKIN D. V. and NEKORKIN V. I., *Radiophys. Quantum Electron.*, **58** (2016) 877.
- [21] BAČIĆ I., YANCHUK S., WOLFRUM M. and FRANOVIĆ I., *Eur. Phys. J. ST*, **227** (2018) 1077.
- [22] KASATKIN D., YANCHUK S., SCHÖLL E. and NEKORKIN V., *Phys. Rev. E*, **96** (2017) 062211.
- [23] DESTEXHE A. and RUDOLPH-LILITH M., *Neuronal Noise* (Springer, New York) 2012.
- [24] MAISTRENKO Y. L., LYSYANSKY B., HAUPTMANN C., BURLYKO O. and TASS P., *Phys. Rev. E*, **75** (2007) 066207.
- [25] AOKI T. and AOYAGI T., *Phys. Rev. Lett.*, **102** (2009) 034101.
- [26] AOKI T. and AOYAGI T., *Phys. Rev. E*, **84** (2011) 066109.
- [27] BERGLUND N. and GENTZ B., *Noise-Induced Phenomena in Slow-Fast Dynamical Systems* (Springer, Berlin) 2006.
- [28] LAING C. and LORD G. J. (Editors), *Stochastic Methods in Neuroscience* (Oxford University Press, London) 2009.
- [29] KUEHN C., *Multiple Time Scale Dynamics* (Springer International Publishing, Switzerland) 2015.
- [30] SHILNIKOV A., *Int. J. Bifurcat. Chaos*, **18** (2008) 2141.

Stimulus-evoked activity in clustered networks of stochastic rate-based neurons

Igor Franović^{1,a} and Vladimir Klinshov^{2,b}

¹ Scientific Computing Laboratory, Center for the Study of Complex Systems, Institute of Physics Belgrade, University of Belgrade, Pregrevica 118, 11080 Belgrade, Serbia

² Institute of Applied Physics of the Russian Academy of Sciences, 46 Ulyanov Street, 603950 Nizhny Novgorod, Russia

Received 29 April 2018 / Received in final form 22 June 2018

Published online 12 December 2018

Abstract. Understanding the effect of network connectivity patterns on the relation between the spontaneous and the stimulus-evoked network activity has become one of the outstanding issues in neuroscience. We address this problem by considering a clustered network of stochastic rate-based neurons influenced by external and intrinsic noise. The bifurcation analysis of an effective model of network dynamics, comprised of coupled mean-field models representing each of the clusters, is used to gain insight into the structure of metastable states characterizing the spontaneous and the induced dynamics. We show that the induced dynamics strongly depends on whether the excitation is aimed at a certain cluster or the same fraction of randomly selected units, whereby the targeted stimulation reduces macroscopic variability by biasing the network toward a particular collective state. The immediate effect of clustering on the induced dynamics is established by comparing the excitation rates of a clustered and a homogeneous random network.

1 Introduction

Characterizing the structure of spontaneous emergent activity in neuronal populations, and the fashion in which it is modulated by the sensory stimuli, is fundamental to understanding the principles of information processing in the cortex. The generic patterns of spontaneous cortical dynamics, called slow rate fluctuations or UP–DOWN states, involve switching between the episodes of elevated neuronal and synaptic activity, and the stages of relative quiescence [1–3]. Alternation between UP and DOWN states is orchestrated by coherent action of individual neurons, with the observed rates typically lying in the range from 0.1 to 2 Hz [3]. Slow rate fluctuations give rise to macroscopic variability in the cortex [4,5], underlying in vivo activity during quiet wakefulness, sleep or under anesthesia [1,6,7], and even featuring in various in vitro preparations [8,9]. Our paper focuses on the open issues concerning the ingredients that affect the relationship between the stimulus-evoked and the ongoing

^a e-mail: franovic@ipb.ac.rs

^b e-mail: vladimir.klinshov@ipfran.ru

dynamics of neural assemblies, as well as the way the induced activity depends on the stimulus.

The research on induced patterns in sensory cortical areas has surprisingly shown that regardless of the type of stimuli, these patterns exhibit remarkable similarity to those of the idling activity [10–13]. In fact, the onset of UP–DOWN states has been recorded while performing perceptual tasks, but has also been found crucial to pyramidal neurons of neocortex, where it facilitates certain forms of learning and memory consolidation [1,14–17]. Such data evince that typical evoked activity patterns are drawn from a limited “vocabulary” already present within the spontaneous dynamics [10], whereby the sampling ability is pinned by the form of sensory stimuli. The striking similarity between the ongoing and the induced cortical activity is now considered as a generic feature of cortical dynamics, verified at increasing levels of structural complexity [18]. Certain experimental studies have linked the similarity to nontrivial properties of cortical connectivity, suggesting that it confines the pool of potential activity patterns [18]. By this paradigm, the structure of patterns reflects the modular (clustered) architecture of cortical networks, whereby certain patterns are activated by stimulating particular local subcircuits, known as the leader sites [19]. Conceptually, investigating the impact of clustered topology on different aspects of collective dynamics is biologically plausible [5,20], as recent research indicates strong prevalence of clustered over the homogeneous connectivity in cortical networks [21–24]. Clustering has already been shown to enable task-specialization, maintaining of high levels of neuronal activity, or adaptation to certain types of stimuli [25,26].

Here, we examine how the interplay of modular network architecture and noise influences the relation between the spontaneous and induced macroscopic activity, as well as how the macroscopic variability is affected by the different types of network stimulation. We analyze a model of a clustered network of noisy rate-based neurons [27–29], employing a second-order effective model of collective dynamics to gain insight into the structure of network’s metastable states. While the spontaneous activity consists of noise-induced fluctuations between the metastable states, we show that the specific type of stimulation, targeted at a certain cluster, biases the network toward a particular state, thereby reducing the macroscopic variability.

The origin of macroscopic variability, as an emergent network phenomenon, has so far been treated within two different frameworks, one associating slow rate fluctuations to deterministic networks, where balanced massive excitation and inhibition render the collective dynamics highly sensitive to fluctuations, and the other, which ties the slow rate fluctuations to multistability in attractor model networks, such that switching between coexisting states emerges due to noise, whose action amounts to a finite-size effect. In our recent paper [27], we have applied the latter approach, comparing the switching dynamics in clustered networks relative to random (statistically uniform) networks with the same average connectivity, having shown that clustering promotes multistability, thereby enhancing the switching phenomenon and its robustness. Here, the use of effective model of collective dynamics derived in [27] is extended to capture the response of random and clustered networks to external stimuli. In case of clustered networks, we compare the effects of two different stimulation protocols, including (i) the targeted stimulation, where an increased bias current is introduced only to units in a certain cluster, and (ii) the distributed stimulation, where the same fraction of randomly selected neurons is excited. It is found that due to modular architecture, the two stimulation scenarios may give rise to fundamentally different responses of the network.

The paper is organized as follows. In Section 2, we introduce the model of network dynamics and present the effective model of its macroscopic behavior. Section 3 contains the bifurcation analysis of the effective model of a clustered network in

the thermodynamic limit, applying it to anticipate the induced dynamics of the network. In Section 4, we compare the numerical results to the predictions of the mean-field model. Section 5 provides a brief summary and discussion on the obtained results.

2 Network dynamics: full and the effective model

We consider an m -cluster network comprised of N neurons, assuming random connectivity both within and between the clusters. The intra-cluster connectivity, specified by connectedness probability p_{in} , is more dense than the cross-connectivity p_{out} , whereby the degree of topological heterogeneity is characterized by the clustering parameter $g = p_{\text{in}}/p_{\text{out}}$. Larger g implies stronger clustering, such that the limiting case $g = 1$ describes the non-clustered (homogeneous random) network, while the case $g \rightarrow \infty$ corresponds to a network of uncoupled clusters. The clustering algorithm involves rewiring of a sparse random network, and thus preserves the average connectedness probability, set to a biologically plausible level $p = 0.2$. The parameters p_{in} and p_{out} can be linked to p via $p_{\text{in}} = \frac{gm}{m-1+g}p$ and $p_{\text{out}} = \frac{m}{m-1+g}p$, which allows one to explicitly compare the relevant parameter domains between the homogeneous and the clustered network.

The local dynamics follows a stochastic rate model [27–31]

$$\frac{dr_{X_i}}{dt} = -\lambda_X r_{X_i} + H(v_{X_i}) + \sqrt{2D}\xi_{X_i}(t), \tag{1}$$

where r_{X_i} is the firing rate of neuron i from cluster X , λ_X defines the rates relaxation time, and H is the nonlinear gain function, whose argument is the total input to a neuron v_{X_i} . The latter is given by $v_{X_i} = u_{X_i} + I_X + \sqrt{2B}\eta_{X_i}(t)$, where u_{X_i} is the synaptic input $u_{X_i} = \kappa \sum_Y \sum_j a_{YXji} r_{Y_j}$ and I_X denotes the external bias current. The coupling scheme is specified by the adjacency matrix $a_{YXji} \in \{0, 1\}$, such that a_{YXji} stands for the link projecting from neuron j in cluster Y to neuron i in cluster X . Coupling weights are assumed to be homogeneous and scale with the network size as $\kappa = K_{YX}/N$. The random perturbations in the microscopic dynamics derive from two distinct sources of noise. In particular, the external noise, characterized by B , and the intrinsic noise, described by D , are introduced to account for the action of synaptic and ion-channel noise, respectively. All the associated fluctuations are independent and are given by Gaussian white noise.

Note that the form (1) is quite general, in a sense that by choosing different H , one may interpolate between different classes of models, including Wilson–Cowan or Hopfield model. From a broader perspective, a plausible gain function should meet three simple requirements: it should drop to zero for sufficiently small input, exhibit saturation for large enough input, and just be monotonous for intermediate input values. Here, the form of H

$$\mathcal{H}(U) = \begin{cases} 0, & U \leq 0, \\ 3U^2 - 2U^3, & 0 < U < 1, \\ 1, & U \geq 1. \end{cases} \tag{2}$$

is selected to make the analysis of macroscopic dynamics analytically tractable [27–29]. Note that the qualitative physical picture associated to the collective multi-stable behavior in assemblies of neurons with rate-based dynamics does not depend

on the particular choice of the gain function. This point has been extensively elaborated in [30], and we have also numerically verified that the results presented here persist for the Heaviside-like gain function.

2.1 Effective model of clustered network dynamics

The effective model of network dynamics is comprised of coupled mean-field models representing the activities of particular clusters. Typically, the effective models of network behavior concern either the case of random sparse connectivity or the case of full connectivity. In this context, our model can be seen as interpolating between the two standard scenarios, featuring dense intra-cluster connectivity and sparse inter-cluster connections. The applied mean-field approach involves a Gaussian closure hypothesis [32–35], such that the collective dynamics of each cluster X is described by the mean-rate R_X and the associated variance S_X

$$R_X = \frac{1}{N_X} \sum_i r_{Xi} \equiv \langle r_{Xi} \rangle S_X = \langle r_{Xi}^2 \rangle - R_X^2, \quad (3)$$

where $\langle \cdot \rangle$ denotes averaging over the neurons within the given cluster. For each of the clusters, we use the bottom-up approach to obtain the second-order stochastic equations of macroscopic behavior. With the detailed derivation of the effective model already provided in [27], here we only briefly outline the two main steps necessary to carry out the appropriate averaging over the microscopic dynamics, namely the Ansatz on local variables and the Taylor expansion of \mathcal{H} function.

The Ansatz on local variables consists in writing r_{Xi} as $r_{Xi} = R_X + \sqrt{S_X} \rho_{Xi}$ [36], where $\{\rho_{Xi}\}$ is a set of variables satisfying $\langle \rho_{Xi} \rangle = 0$, $\langle \rho_{Xi}^2 \rangle = 1$, as readily follows from definition (3). The introduced Ansatz is applied to rewrite the total input to a neuron as $v_{xi} = U_X + \delta v_{Xi}$, where

$$U_X = I_X + \kappa \sum_Y p_{YX} N_Y R_Y \quad (4)$$

presents the assembly-averaged input to cluster X , p_{YX} denotes the connectedness probability from cluster Y to cluster X , and N_Y is the size of cluster Y . The deviation δv_{Xi} from the average input U_X consists of two terms:

$$\delta v_{Xi} = \kappa \sum_Y R_Y \nu_{YXi} + \kappa \sum_Y \sqrt{S_Y} \sigma_{YXi}. \quad (5)$$

The first term accounts for the topological effect associated to the deviation $\nu_{YXi} = \sum_j a_{YXji} - p_{YX} N_Y$ from the average number of connections $p_{YX} N_Y$, whereas the second term captures the effect of local rate fluctuations, contained within the factor $\sigma_{YXi} = \sum_j a_{YXji} \rho_{Yj}$. Equations (4) and (5) allow one to average the terms containing the gain function by developing $H(v_{Xi})$ about U_X up to second order. This leads to $H(v_{Xi}) = H_{0X} + H_{1X} \delta v_{Xi} + H_{2X} \delta v_{Xi}^2$, having introduced notation $H_{0X} \equiv H(U_X)$, $H_{1X} = \frac{dH}{dv_{Xi}}(U_X)$, $H_{2X} = \frac{1}{2} \frac{d^2H}{dv_{Xi}^2}(U_X)$.

Following a number of intermediate steps elaborated in [27], one arrives at the effective model of network dynamics stated in terms of interacting finite-size mean-field models describing the cluster dynamics. The effective model is given by

$$\begin{aligned} \frac{dR_X}{dt} &= -\lambda_X R_X + H_{0X} + 2B_X H_{2X} + H_{2X} \sum_Y K_{YX}^2 p_{YX} N_Y (R_Y^2 + S_Y) / N^2 \\ &\quad + \sqrt{\Psi_X} \beta(t) + \sqrt{\Omega_X} \eta, \\ \frac{dS_X}{dt} &= -2\lambda_X S_X + 2B_X H_{1X}^2 + 2D_X, \end{aligned} \tag{6}$$

and involves three types of finite-size effects, including the small deterministic correction term, the effective “macroscopic” noise of intensity Ψ_X , as well as the quenched randomness, accounting for the fact that each particular network realization features distinct deviations from the average connectivity degree. The macroscopic noise is multiplicative

$$\Psi_X = \frac{1}{N} (2D_X + 2B_X H_{1X}^2) + \frac{1}{N} H_{1X}^2 \sum_Y K_{YX}^2 p_{YX} \frac{N_Y}{N_X} S_Y, \tag{7}$$

and incorporates three terms: the first two describe how the local external and intrinsic noise are translated to macroscopic level, whereas the third one reflects the impact of local fluctuations in the input arriving to each neuron in the cluster. At variance with the time-varying stochastic term featuring $\beta(t)$, the effect of quenched randomness in (6) is characterized by a constant random term of magnitude $\Omega_X = \frac{1}{N} H_{1X}^2 \sum_Y K_{YX}^2 p_{YX} \frac{N_Y}{N_X} R_Y^2$, with η being just a constant random number $\mathcal{N}(0, 1)$.

In the S_X dynamics, for simplicity we omit all the finite-size effects, including the deterministic correction and the stochastic terms. One may do so because the variance S_X only affects the $\mathcal{O}(1/N)$ terms in the dynamics of R_X .

3 Bifurcation analysis of the effective model in the thermodynamic limit

In this section, we carry out the bifurcation analysis of the system (6) in the limit $N \rightarrow \infty$ to characterize the response of a clustered network to external stimuli. Our focus is on the scenario of targeted stimulation, where an increased bias current is applied to a certain cluster, while the rest of the network remains unperturbed. The stimulation is provided in the form of a rectangular pulse, whose duration Δ is sufficiently long such that the network is allowed to reach the new metastable state. Our analysis will address the issues of why the evoked states of the network are similar to those occurring within the spontaneous activity, and how the stimulus biases the network dynamics to a particular collective state. Note that the system (6) holds for networks of an arbitrary number of clusters of arbitrary sizes, but for simplicity we consider the case of m equal clusters of size $N_c = N/m$.

In our previous study, the model (6) has been analyzed in case where the entire network receives homogeneous external current I . Here, we deal with inhomogeneous stimulation, conforming to a paradigm with l clusters delivered the current I_A , whereas the remaining ones are influenced by I_B . One is interested into solutions where the mean activity of the unperturbed clusters equals R_B , whereas the state of

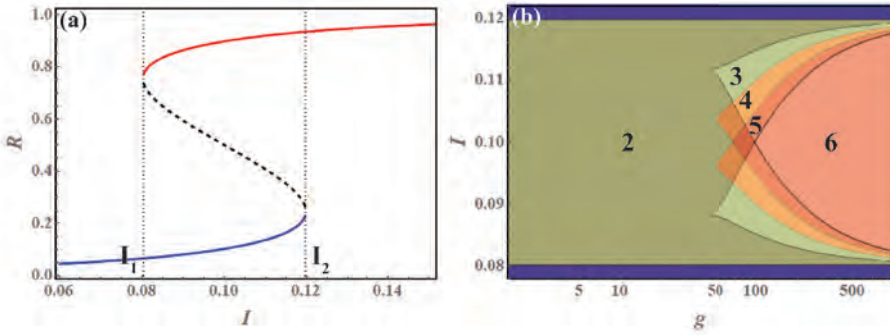


Fig. 1. (a) Bifurcation diagram $R(I)$ for the non-clustered network subjected to homogeneous stimulation. The network parameters are $\alpha = 0.8$, $B = 0.004$, $D = 0.02$ and $g = 1$. (b) Bifurcation diagram for the clustered network $m = 5$ influenced by the homogeneous stimulation: bias current I against logarithm of the clustering coefficient g . The numbers indicate how many coexisting attractors exist within the given region.

the excited clusters R_A may be different. Neglecting the finite-size effects $\mathcal{O}(1/N)$, it follows that the network dynamics is given by

$$\begin{aligned} \frac{dR_A}{dt} &= -R_A - 2U_A(R_A, R_B)^3 + 3U_A(R_A, R_B)^2 + 6B(1 - 2U_A(R_A, R_B)) \\ \frac{dR_B}{dt} &= -R_B - 2U_B(R_A, R_B)^3 + 3U_B(R_A, R_B)^2 + 6B(1 - 2U_B(R_A, R_B)), \end{aligned} \quad (8)$$

where the average input to the two subsets of clusters reads

$$\begin{aligned} U_A(R_A, R_B) &= I_A + \frac{\alpha}{m-1+g} \left[(g+l-1)R_A + (m-l)R_B \right] \\ U_B(R_A, R_B) &= I_B + \frac{\alpha}{m-1+g} \left[lR_A + (g+m-l-1)R_B \right], \end{aligned} \quad (9)$$

having $\alpha = Kp$ denote the network coupling parameter.

Prior to analyzing the induced dynamics of the network, let us briefly consider the spontaneous activity, which is in this framework represented by a setup with homogeneous bias currents $I_A = I_B = I$. In case of a non-clustered network ($g = 1$), one observes bistability in a certain interval $I \in [I_1, I_2]$ [29], provided the coupling parameter α is sufficiently large. The corresponding bifurcation diagram $R(\alpha)$ in Figure 1a contains two stable branches associated to the UP and DOWN states of the network. Introducing sufficiently strong clustering promotes multistability, giving rise to network states which do not exist in the non-clustered case. The increased number of network levels derives from the states with broken symmetry, where subsets of clusters may lie in their respective high or low states [27]. For such inhomogeneous collective states, the system symmetry is reduced from the permutation group Σ_m (permutation of all cluster indices), to a subgroup of the type $\Sigma_l \otimes \Sigma_{m-l}$, where $l \in \{1, 2, \dots, m-1\}$. Given that each cluster may either lie in the low or the high state, the maximal multistability of a network comprised of m clusters is $m+1$. To provide an example, in Figure 1b is shown a bifurcation diagram in the (g, I) plane for a modular network $m = 5$. There, one observes that maximal multistability is facilitated by the clustering parameter $g \gtrsim 100$.

Note that the external noise B acts in (8) as a bifurcation parameter, influencing the number and position of stationary states in the thermodynamic limit. Figure 2a

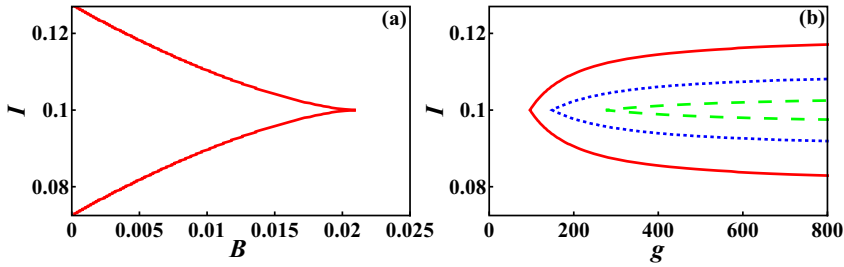


Fig. 2. (a) Bifurcation diagram in the (B, I) for the non-clustered network subjected to homogeneous stimulation. The remaining parameters are $\alpha = 0.8$, $D = 0.02$ and $g = 1$. (b) Shift of the maximal multistability region in the (g, I) plane for a clustered network $m = 5$. The red solid lines outline the maximal multistability domain for noise level $B = 0.004$, whereas the blue dotted lines and the green dashed lines correspond to $B = 0.01$ and $B = 0.015$, respectively.

shows the bifurcation diagram referring to spontaneous activity of the non-clustered network in the (B, I) plane, obtained under fixed connectivity $\alpha = 0.8$. The bistability region again lies between two branches of fold bifurcations (red curves) that meet at the cusp point, where a pitchfork bifurcation occurs. One finds that for fixed I , there always exists a B value above which a non-clustered network can no longer support bistable behavior. For the spontaneous dynamics of a clustered network, it can be shown that the region of maximal multistability in the (g, I) plane, bounded by two curves of fold bifurcations intersecting at the pitchfork bifurcation, reduces and shifts toward stronger clustering under increasing B , cf. Figure 2b. In other words, for higher external noise, one requires larger clustering in order to observe maximal multistability in the network.

To investigate the scenario of a targeted stimulation, we analyze the network’s response by looking into solutions of (8) for $l = 1$, such that the stimulated cluster occupies the state different from the remaining clusters. The clustering coefficient g and the stimulation current I_A are considered as control parameters, while the remaining parameters $\alpha = 0.8$, $B = 0.004$, and $I_B = 0.1$ are such that the spontaneous dynamics of the associated homogeneous random network with $I = I_B$ pertains to bistability region in Figure 1a. The (g, I_A) bifurcation diagram explaining the action of targeted stimulation is plotted in Figure 3a. For $I_A \approx I_B$ and strong enough clustering, the network possesses four stable steady states, which can readily be traced in the limit of ultimate clustering $g \rightarrow \infty$. Indeed, suppose that a network is decomposed into a set of non-interacting clusters, and that I_A and I_B lie within the interval $[I_1, I_2]$ from Figure 1a. Then, each of the clusters is bistable, which gives exactly four stable steady states in the full system (8). The area of maximal multistability, where both the stimulated cluster and the resting network may either occupy the low or the high state, extends to moderate clustering $g \sim 100$. In Figure 3b, the four stable steady states of the effective model are denoted by O_{LL} , O_{LH} , O_{HL} and O_{HH} . Note that the first and second index refer to states of the stimulated cluster and the rest of the network, respectively, whereby L/H indicates the low/high level, and U denotes the unstable state.

As the stimulation I_A increases, the system undergoes a saddle-node bifurcation in which the states O_{LH} and O_{UH} are annihilated, see the curve C_1 in Figure 3a. Then the system passes to the area with 3 stable steady states, with the corresponding phase portrait shown in Figure 3c. Further growth of I_A causes the states O_{LL} and O_{UL} to collide, cf. the curve C_2 in Figure 3a, such that the system becomes bistable, as corroborated by the phase portrait in Figure 3d. For small g , very strong simulation I_A leads to a collision and disappearance of the steady states O_{HL}

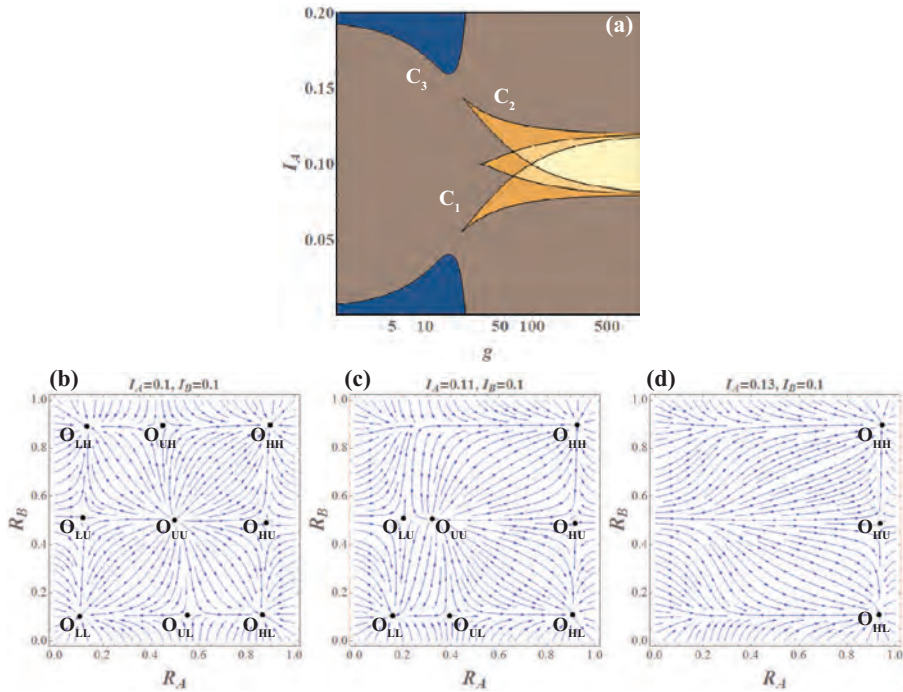


Fig. 3. (a) Bifurcation diagram $I_A(g)$ of system (8), with the number of coexisting solutions indicated for particular regions. The remaining parameters are fixed to $\alpha = 0.8$, $B = 0.004$, $D = 0.02$, $m = 5$ and $I_B = 0.1$. (b–d) Phase portraits associated to system (8) under increasing I_A .

and O_{HU} , see the curve C_3 in Figure 3a, whereby the system becomes monostable. Note that the decrease of I_A (targeted inhibition) gives rise to a similar scenario. When I_A is systematically reduced, the system first becomes tristable with coexisting states O_{LL} , O_{LH} and O_{HH} , then bistable and eventually passes to monostability domains.

4 Numerical results: targeted vs. distributed stimulation

In this section, our aim is to first explicitly demonstrate that the effective model (8) can successfully predict the response of a clustered network in case of targeted stimulation. Nevertheless, we shall also show an interesting effect evincing that the response of modular networks to external stimulation is strongly dependent on the character of stimulation, i.e. the fashion in which it is distributed to neurons within the network.

In Figure 4, the response of a clustered network $m = 5$ to a targeted stimulation is compared against the induced dynamics of the effective model analyzed in Section 3. Note that the numerical experiments concerning the full system (1) have been carried out on a relatively small network comprised of $N = 300$ neurons, which corresponds to only 60 neurons per cluster, having fixed the noise levels to $D = 0.02$ and $B = 0.004$. Given the relatively small cluster size, one would expect strong fluctuations in the network dynamics. Nevertheless, it will be shown that even under such conditions, the mean-field analysis performed in case of thermodynamic limit still remains qualitatively valid, in a sense of being able to qualitatively capture the induced behavior of the network.

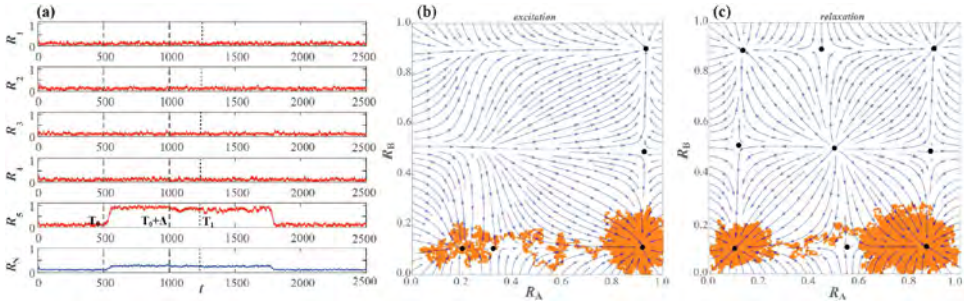


Fig. 4. (a) Response of a clustered network ($m = 5$) to a stimulus of intensity I_A and duration Δ introduced to cluster 5 at the moment T_0 . Notation $R_i, i \in [1, 5]$ refers to mean-rates of particular clusters, whereas R_N stands for the collective network activity. Panels (b) and (c) show excitation and relaxation processes of the network in the (R_A, R_B) plane, respectively. The system’s orbit is superimposed on the vector field of the effective model (8), obtained for $(I_A, I_B) = (0.12, 0.1)$ in (b) and $I_A = I_B = 0.1$ in (c). The remaining parameters are $g = 250, B = 0.004, D = 0.02$.

The scenario of targeted stimulation unfolds in such a way that before introducing the stimulation, all the clusters occupy the low state and are influenced by the same current $I_A = I_B = 0.1$. Then, at the moment $T_0 = 500$, a rectangular pulse of elevated bias current $I_A = 0.12$ is introduced solely to cluster 5. The pulse is maintained for a sufficiently long time $\Delta = 500$, such that the network is allowed to reach the new metastable state. Note that during the stimulation, I_A lies very close to the bifurcation curve C_2 from Figure 3a. Therefore the state O_{LL} is weakly stable, and the finite-size fluctuations may easily drive the system away from it, as indicated by the time traces in Figure 4a. In Figure 4b, we have plotted the excitation orbit of the network in the (R_A, R_B) plane in order to demonstrate that the system switches between the metastable states anticipated by the effective model (8). In particular, the vector field provided in the background presents the flow of system (8) for $(I_A, I_B) = (0.12, 0.1)$. One observes that the network rapidly leaves the vicinity of the state O_{LL} and switches to O_{HL} , conforming to the path where a single cluster, described by R_A , is perturbed by the stimulation, whereas the remaining clusters, associated to R_B , remain unaffected.

We have also examined the relaxation process of the network after the termination of the stimulus at $t = T_0 + \Delta$. In Figure 4c, the relaxation orbit is plotted against the vector field of the system (8) for $I_A = I_B = 0.1$. As predicted by the effective model, the state O_{HL} lies far from bifurcations, which makes it relatively stable, in a sense that the network may spend quite a long time in its vicinity. However, the fluctuations induced by the finite-size effect eventually drive the network back to the homogeneous DOWN state O_{LL} .

The dependence of the networks response on the stimulation magnitude I_A is illustrated in Figure 5. The response is characterized by the "excitation rate" γ , defined as the average fraction of excited neurons at the moment $T_0 + \Delta$ just after the stimulus has ceased, having performed averaging over an ensemble of 80 stochastic realizations. Since the targeted stimulation may only give rise to excitation of a single cluster, γ in this case is merely the probability of cluster excitation. The response function $\gamma(I_A)$ exhibits threshold-like behavior, with the rising stage triggered at $I_A \approx 0.11$ and completed at $I_A \approx 0.12$, cf. the blue solid line with empty circles. Note that the latter value is in perfect agreement with the prediction of the bifurcation diagram in Figure 3a. For large I_A , the excitation rate saturates at $\gamma = 1/m = 0.2$, which implies that only a single cluster is excited regardless of how large I_A becomes.

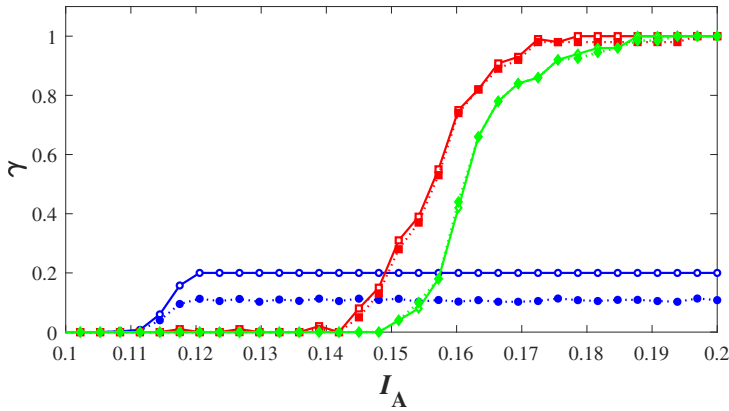


Fig. 5. Excitation rate, i.e. fraction of excited clusters γ in terms of I_A for the different stimulation scenarios. The circles and squares refer to targeted and distributed stimulation of a clustered network ($m = 5, g = 250$), respectively, whereas the diamonds indicate the response of a homogeneous random network ($g = 1$). The empty symbols connected by solid lines denote γ values at the moment $T_0 + \Delta$ when the stimulation is terminated. The solid symbols connected by the dotted lines show γ at the moment T_1 after the stimulation has ceased, cf. Figure 4a. The remaining network parameters are $B = 0.004$, $D = 0.02$ and $I_B = 0.1$.

In general, the persistence of the elevated state does not depend on the applied stimulation magnitude I_A , but is rather determined by the relaxation speed of the state the network occupies at the moment $T_0 + \Delta$ when the stimulation is terminated. In order to analyze the features of the relaxation process, we have measured the excitation rate γ at a later moment $T_1 = 1250$, sufficiently long after the excitation pulse has ceased, cf. the blue dotted line connecting the filled circles in Figure 5. Since in the case of targeted stimulation one always encounters the same excited state with only a single cluster perturbed, it is natural to expect proportionality between the excitation rate immediately after the stimulation (moment $T_0 + \Delta$) and at a later moment T_1 . Our results corroborate that the elevated state may indeed persist considerably longer than the triggering pulse.

As already announced, we also report on an interesting finding that the induced dynamics of modular networks strongly depends on the applied stimulation protocol. In particular, suppose that instead of a targeted stimulation, one introduces an elevated bias current to the same fraction of neurons as in a single cluster, but just randomly distributed over the network. We refer to such a scenario as “distributed stimulation”. In this instance, for sufficiently large stimulation I_A , the network may reach states where substantially more than a single cluster is elicited, in spite of relatively large clustering coefficient g .

The network excitation rate as a function of I_A for the case of distributed stimulation is indicated by the solid red line with empty squares in Figure 5. One immediately realizes that the impact of the distributed stimulation is quite distinct from that of the targeted one in two aspects: (i) the I_A threshold where it starts to excite a single cluster is significantly larger than for the targeted stimulation and (ii) for sufficiently strong stimulation I_A , all the clusters may cross to high state.

To gain a deeper insight into how the network’s response is shaped by clustering, we consider an additional scenario, where a certain fraction of neurons is stimulated in a homogeneous random network $g = 1$. To allow the comparison, we have perturbed the same fraction of units as in the clustered network, but here one cannot distinguish between the targeted and the distributed stimulation protocols

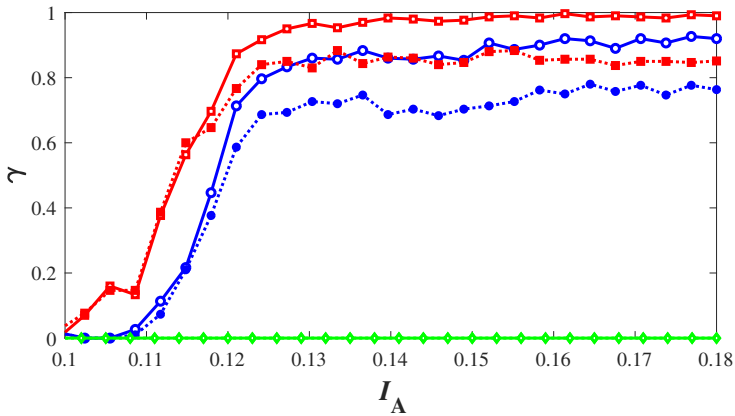


Fig. 6. Dependence of excitation rate γ on the applied current I_A for levels of external noise B where the network cannot exhibit maximal multistability. The green diamonds concern the response of a homogeneous random network $g = 1$ in case where the effective model exhibits only the DOWN state ($B = 0.028, D = 0.02, I_B = 0.1$). The blue circles and the red squares refer cases of a targeted and distributed stimulation of a clustered network $m = 5$, respectively. In the thermodynamic limit, the parameters of the clustered network facilitate bistable dynamics between the homogeneous UP and DOWN states ($B = 0.018, D = 0.02, g = 60, I_B = 0.1$). The solid/empty symbols are used the same way as in Figure 5.

because any subset of units is equivalent. The ensuing excitation rate, plotted in Figure 5 by the solid green line, indicates a response substantially distinct from that of a clustered network in case of targeted stimulation, but reminiscent of the induced dynamics typical for the distributed stimulation. This is so because the homogeneous network possesses only two metastable states, namely the homogeneous DOWN and UP states, which implies that one cannot excite only a certain fraction of units, but can rather excite the entire network. As the DOWN state vanishes at the bifurcation curve C_3 in Figure 3a, the guaranteed excitation of the network is observed only if I_A lies sufficiently close to this curve. The associated threshold current corresponds to the saturation of the excitation rate observed at $I_A \approx 0.19$ in Figure 5.

As already indicated, the external noise influences the multistable dynamics of both the homogeneous and the clustered networks. In Figure 6, it is examined how the excitation rate changes if the level of external noise B is increased such that the network can no longer exhibit maximal multistability in the thermodynamic limit. For the non-clustered network, we have considered the case where the deterministic dynamics is monostable, admitting only the DOWN state. As expected, stimulating a fraction of neurons with arbitrary strong external current cannot switch the network to the UP state, cf. the green diamonds in Figure 6. For the clustered network $m = 5$, the external noise B and the clustering coefficient g have been set such that the deterministic dynamics exhibits only bistability between the homogeneous UP and DOWN states. For both the scenarios of the targeted and distributed stimulation protocols, the excitation rate exhibits a threshold-like behavior, ultimately reaching the network-wide UP state for a sufficiently strong stimulation. As predicted by the effective model, the targeted stimulation can no longer bring the network to a heterogeneous state where only a single cluster is excited.

5 Summary and discussion

In the present paper, we have analyzed the induced dynamics of a clustered network subjected to two types of stimulation protocols, the targeted stimulation and the distributed stimulation. In the former case, it has explicitly been demonstrated that the effective model, describing the macroscopic dynamics in terms of coupled mean-field models associated to each of the clusters, may accurately capture the networks response, predicting the metastable state reached by the network.

An interesting finding is that the response of a clustered network strongly depends on the applied stimulation protocol. In particular, in case of a targeted stimulation, under sufficiently strong clustering, one typically observes that only the targeted cluster is activated, whereas the remaining clusters are unaffected by the perturbation. Nevertheless, for the distributed stimulation, applying a sufficiently strong excitation may result in much richer dynamics, where different forms of elevated states, including a network-wide high state, may be reached.

Concerning the immediate impact of the modular network architecture, we have established that the response of a clustered network is drastically different from that of a statistically homogeneous one even if the same number of randomly selected units is stimulated. In particular, given the same stimulation magnitude, the excitation rate of the homogeneous random network turns out to be substantially lower than that of a clustered network. This distinction derives from the fact that a non-clustered network cannot exhibit heterogeneous states. As expected, the differences in behavior of the non-clustered and clustered networks vanish for sufficiently strong stimuli, where the network-wide excitation becomes the prevalent scenario regardless of the network structure. In case of a non-clustered network, the reduced model has been shown to provide a good estimate of the threshold current that guarantees reaching the elevated state.

The external noise has been found to play a nontrivial role with respect to the excitation process, because it affects the features of the network's multistable behavior in the thermodynamic limit. This is a consequence of the fact that the macroscopic noise derived from the local external noise is multiplicative [37]. The associated changes in the multistability have been shown to substantially influence the excitation rates in clustered networks for both the stimulation protocols, as well as in the scenario where the stimulus acts on a certain fraction of neurons in a non-clustered network.

For the particular stimulation protocol, the properties of the relaxation process are found not to be determined by the intensity of excitation, but rather by the state of the network at the moment the stimulation is terminated. One should note that instances of prolonged relaxation have been observed, especially in the case of distributed stimulation under higher intensities of the applied current, which facilitate excitation to the homogeneous UP state. The lifetimes of the metastable states are also influenced by the level of the external noise, and the underlying effects provide an interesting topic for future studies. In particular, the impact of multistability on the relaxation process may consist in inducing nonlinear dependencies of relaxation times on the noise level, which can manifest as noise-enhanced stability of metastable states [38,39].

Within the present study, we have explained by the effective model, and corroborated numerically, why the induced dynamics of a clustered network resembles the spontaneous one, further demonstrating how the stimulation biases the network toward a particular collective state. Recent experimental research indicates that the external stimulation reduces both the macroscopic and the microscopic neuronal variability [10,40,41], the latter being associated to randomness in local dynamics, viz. the spiking series of individual units. While our results may indeed account for the stimulation-induced decrease of macroscopic variability, one cannot

infer anything regarding the microscopic variability, since we apply a rate-based neuron model. In this context, it would be of interest to consider in detail the induced dynamics of a clustered network of spiking neurons via an effective model, especially given that the numerical results in [5,13,20] already link the stimulated activity with reduction of both the macroscopic and microscopic neuronal variability.

This work is supported by the Ministry of Education, Science and Technological Development of Republic of Serbia under project No. 171017, by the Russian Foundation for Basic Research under project No. 17-02-00904, and by the Russian Science Foundation under project No. 16-42-01043.

References

1. T.T.G. Hahn, J.M. McFarland, S. Berberich, B. Sakmann, M.R. Mehta, *Nat. Neurosci.* **15**, 1531 (2012)
2. G. Buzsáki, C.A. Anastassiou, C. Koch, *Nat. Rev. Neurosci.* **13**, 407 (2012)
3. V.V. Vyazovskiy, K.D. Harris, *Nat. Rev. Neurosci.* **14**, 443 (2013)
4. M.R. Cohen, A. Kohn, *Nat. Neurosci.* **14**, 811 (2011)
5. A. Litwin-Kumar, B. Doiron, *Nat. Neurosci.* **15**, 1498 (2012)
6. C.C.H. Petersen, T.T.G. Hahn, M. Mehta, A. Grinvald, B. Sakmann, *Proc. Natl. Acad. Sci. U.S.A.* **100**, 13638 (2003)
7. D. Millman, S. Mihalas, A. Kirkwood, E. Niebur, *Nat. Phys.* **6**, 801 (2010)
8. J. Anderson et al., *Nat. Neurosci.* **3**, 617 (2000)
9. R. Cossart, D. Aronov, R. Yuste, *Nature* **423**, 283 (2003)
10. A. Luczak, P. Barthó, K.D. Harris, *Neuron* **62**, 413 (2009)
11. A. Luczak, P. Barthó, K.D. Harris, *J. Neurosci.* **33**, 1684 (2013)
12. D.L. Ringach, *Curr. Opin. Neurobiol.* **19**, 439 (2009)
13. G. Deco, E. Hugues, *PLoS Comput. Biol.* **8**, e1002395 (2012)
14. D. Ji, M.A. Wilson, *Nat. Neurosci.* **10**, 100 (2007)
15. S. Diekelmann, J. Born, *Nat. Rev. Neurosci.* **11**, 114 (2010)
16. D. Miyamoto et al., *Science* **352**, 1315 (2016)
17. G. Rothschild, E. Eban, L.M. Frank, *Nat. Neurosci.* **20**, 251 (2017)
18. J.L. Vincent et al. *Nature* **447**, 83 (2007)
19. V. Pasquale, S. Martinoia, M. Chiappalone, *Sci. Rep.* **7**, 9080 (2017)
20. B. Doiron, A. Litwin-Kumar, *Front. Comput. Neurosci.* **8**, 56 (2014)
21. S. Song, P. Sjöström, M. Reigl, S. Nelson, D. Chklovskii, *PLoS Biol.* **3**, e68 (2005)
22. S. Lefort, C. Tamm, J.-C.F. Sarria, C.C.H. Petersen, J.C. Floyd Sarria, C.C.H. Petersen, *Neuron* **61**, 301 (2009)
23. R. Perin, M. Telefont, H. Markram, *Front. Neuroanat.* **7**, 1 (2013)
24. V.V. Klinshov, J.N. Teramae, V.I. Nekorkin, T. Fukai, *PLoS One* **9**, e94292 (2014)
25. S.B. Hofer, H. Ko, B. Pichler, J. Vogelstein, H. Ros et al., *Nat. Neurosci.* **14**, 1045 (2011)
26. H. Ko, S.B. Hofer, B. Pichler, K.A. Buchanan, P.J. Sjöström, T.D. Mrsic-Flogel, *Nature* **473**, 87 (2011)
27. I. Franović, V. Klinshov, *Chaos* **28**, 023111 (2018)
28. I. Franović, V. Klinshov, *Europhys. Lett.* **116**, 48002 (2016)
29. V. Klinshov, I. Franović, *Phys. Rev. E* **92**, 062813 (2015)
30. H. Hasegawa, *Phys. Rev. E* **75**, 051904 (2007)
31. R.A. Anderson, S. Musallam, B. Pesaran, *Curr. Opin. Neurobiol.* **14**, 720 (2004)
32. B. Lindner, J. Garcia-Ojalvo, A. Neiman, L. Schimansky-Geier, *Phys. Rep.* **392**, 321 (2004)
33. M.A. Zaks, X. Sailer, L. Schimansky-Geier, A.B. Neiman, *Chaos* **15**, 026117 (2005)
34. I. Franović, K. Todorović, N. Vasović, N. Burić, *Phys. Rev. E* **87**, 012922 (2013)

35. I. Franović, K. Todorović, N. Vasović, N. Burić, *Phys. Rev. E* **89**, 022926 (2014)
36. A.N. Burkitt, *Biol. Cybern.* **95**, 1 (2006)
37. S. Ciuchi, F. de Pasquale, B. Spagnolo, *Phys. Rev. E* **47**, 3915 (1993)
38. N.V. Agudov, A.A. Dubkov, B. Spagnolo, *Physica A* **325**, 144 (2003)
39. G. Augello, D. Valentia, B. Spagnolo, *Eur. Phys. J. B* **78**, 225 (2010)
40. L. Mazzucato, A. Fontanini, G. La Camera, *J. Neurosci.* **35**, 8214 (2015)
41. I.-C. Lin, M. Okun, M. Carandini, K.D. Harris, *Neuron* **87**, 644 (2015)

Noise-induced switching in two adaptively coupled excitable systems

Iva Bačić¹, Serhiy Yanchuk², Matthias Wolfrum³, and Igor Franović^{1,a}

¹ Scientific Computing Laboratory, Center for the Study of Complex Systems, Institute of Physics Belgrade, University of Belgrade, Pregrevica 118, 11080 Belgrade, Serbia

² Institute of Mathematics, Technische Universität Berlin, Straße des 17. Juni 136, 10623 Berlin, Germany

³ Weierstrass Institute, Mohrenstrasse 39, 10117 Berlin, Germany

Received 30 April 2018 / Received in final form 19 June 2018

Published online 12 December 2018

Abstract. We demonstrate that the interplay of noise and plasticity gives rise to slow stochastic fluctuations in a system of two adaptively coupled active rotators with excitable local dynamics. Depending on the adaptation rate, two qualitatively different types of switching behavior are observed. For slower adaptation, one finds alternation between two modes of noise-induced oscillations, whereby the modes are distinguished by the different order of spiking between the units. In case of faster adaptation, the system switches between the metastable states derived from coexisting attractors of the corresponding deterministic system, whereby the phases exhibit a bursting-like behavior. The qualitative features of the switching dynamics are analyzed within the framework of fast-slow analysis.

1 Introduction

In many complex systems, ranging from biology, physics and chemistry to social sciences and engineering, the interaction patterns are not static, but are rather affected by the states of constituent units [1–4]. This gives rise to complex feedback mechanisms, where the coupling weights adapt to dynamical processes at the units, which in turn influences the evolution of units itself. Modeling of such systems is based on the paradigm of adaptive networks, where self-organization unfolds both at the level of coupling weights and the collective states of the units, typically involving a separation of characteristic timescales. The faster and the slower timescales are naturally associated to the dynamics of units and couplings, respectively, such that the short-term evolution of the units occurs on a quasi-static network, whereas the slow changes in coupling weights depend on the time-averaged dynamics of the units. An important example of adaptive connectivity is provided by neuronal systems, where the strength of synaptic couplings is adjusted to the underlying spiking activity via spike-time-dependent plasticity (STDP), a temporally asymmetric form of Hebbian learning [5],

^a e-mail: franovic@ipb.ac.rs

promoting causal relationship between the spikes of pre- and postsynaptic neurons [6–8].

Motivated by the research on neuronal systems, in the present paper we study a simplified model which incorporates the basic ingredients of neurodynamics, such as excitability, plasticity and noise. The considered system consists of two adaptively coupled active rotators, whose intrinsic dynamics is set to excitable regime and subjected to noise. The plasticity rule is introduced in such a way that one may continuously interpolate between the coupling dynamics characteristic to Hebbian learning and STDP. We demonstrate that the interplay of plasticity and noise may facilitate two qualitatively different forms of slow stochastic fluctuations, depending on the adaptation rate. While for slower adaptation the self-organized dynamics consists of switching between the two modes of noise-induced oscillations, in case of faster adaptation, the switching dynamics comprises metastable states associated to attractors of the deterministic system.

In the context of neuroscience, one may compare the considered system to a binary neuron motif. It is well known that the same structural motif, defined at the level of anatomy, can support multiple functional motifs [9–12], characterized by different weight configurations and potentially distinct directions of information flow. In these terms, our study will show that the co-effect of plasticity and noise may (i) contribute to the emergence of different functional motifs on top of the given structural one and (ii) trigger slow alternation between the functional motifs.

So far, the co-effects of noise and the STDP plasticity rule have been analyzed in systems of two coupled neural oscillators, as well as in networks of oscillators. In case of two units, multistability between different weight configurations has been found, surprisingly indicating that noise may stabilize configurations of strong bidirectional coupling absent in the deterministic system [13]. At variance with this, our study concerns excitable local dynamics and explicitly addresses the slow stochastic fluctuations between metastable states. For networks of adaptively coupled neural or phase oscillators, the previous research has mainly focused on the impact of plasticity on the synchronization behavior. In the absence of noise, several generic forms of macroscopic dynamics have been identified, including desynchronized or partially synchronized states with weak couplings, as well as cluster states [14–18]. In presence of noise, an interesting effect of self-organized noise resistance to desynchronization has been reported in the case of a network of neural oscillators [19]. In networks of excitable units, the STDP rule has been shown to give rise to oscillating coupling configurations that facilitate switching between strongly and weakly synchronized states [20–22].

The paper is organized as follows. The details of the model are introduced in Section 2. An overview of the underlying deterministic dynamics, characterizing the impact of plasticity on the stationary states and the onset of emergent oscillations, is provided in Section 3. Section 4 is dedicated to a fast–slow analysis of the deterministic dynamics, whereas in Section 5 are explained the features of the two generic types of switching behavior. In Section 6 we provide a summary of our main results.

2 Model

We consider a system of two stochastic active rotators interacting by adaptive couplings, where the dynamics of the phases $\{\varphi_1(t), \varphi_2(t)\}$ and the coupling weights $\{\kappa_1(t), \kappa_2(t)\}$ is given by

$$\begin{aligned}
 \dot{\varphi}_1 &= I_0 - \sin \varphi_1 + \kappa_1 \sin(\varphi_2 - \varphi_1) + \sqrt{D}\xi_1 \\
 \dot{\varphi}_2 &= I_0 - \sin \varphi_2 + \kappa_2 \sin(\varphi_1 - \varphi_2) + \sqrt{D}\xi_2 \\
 \dot{\kappa}_1 &= \epsilon(-\kappa_1 + \sin(\varphi_2 - \varphi_1 + \beta)) \\
 \dot{\kappa}_2 &= \epsilon(-\kappa_2 + \sin(\varphi_1 - \varphi_2 + \beta)),
 \end{aligned} \tag{1}$$

where $\varphi_1, \varphi_2 \in S^1$, while κ_1 and κ_2 are real variables. The rotators are assumed to be identical, having their local dynamics governed by the excitability parameter I_0 , which gives rise to a SNIPER bifurcation at $I_0 = 1$. We focus on the excitable regime, such that $I_0 = 0.95$ is kept fixed throughout the paper. In this case, the uncoupled system always converges to a steady state, whereas the collective dynamics emerges due to interaction and noise. The parameter $\epsilon \ll 1$ defines the scale separation between the fast dynamics of the phases and the slow dynamics of adaptation. White noise of variance D acts only within the subspace of fast variables, whereby the terms $\xi_1(t)$ and $\xi_2(t)$ are independent ($\xi_i(t)\xi_j(t') = \delta_{ij}\delta(t-t')$ for $i, j \in \{1, 2\}$). In the context of neuroscience, I_0 can be interpreted as external bias current, whereas the impact of stochastic terms is analogous to that of synaptic noise. Note that the deterministic version of (1) is symmetric with respect to the exchange of indices $1 \leftrightarrow 2$.

The plasticity rule is controlled by the parameter β , which allows one to interpolate between the different adaptation modalities. The analogy between the adaptivity dynamics in classical neuronal systems and the systems of coupled phase oscillators has been addressed in [14,23,24], whereas a deeper analysis of the correspondence between the phase-dependent plasticity rules and the STDP has been provided in [13]. From these studies, it follows that the scenario found for $\beta = 3\pi/2$, where the stationary weights increase for smaller phase differences and decrease for larger ones (“like-and-like” form of behavior), qualitatively resembles the Hebbian learning rule [23,24]. Nevertheless, in the case $\beta = \pi$, the two coupling weights always change in opposite directions, which may be interpreted as promoting an STDP-like plasticity rule. In the present paper, we are interested in the β interval between these two limit cases, since it admits two coexisting excitable fixed points.

3 Deterministic dynamics of the full system

In this section, we analyze the details of the *deterministic* dynamics of the full system (1), considering first the stationary states and the associated excitability feature, and then focusing on the scenario that gives rise to emergent oscillations.

3.1 Stationary states and excitable dynamics

Fixed points $(\varphi_1^*, \varphi_2^*, \kappa_1^*, \kappa_2^*)$ of the complete system (1) for $D = 0$ are given by the solutions of the following set of equations:

$$\begin{aligned} \sin \varphi_1^* - \sin(\varphi_2^* - \varphi_1^* + \beta) \sin(\varphi_2^* - \varphi_1^*) &= I_0, \\ \sin \varphi_2^* - \sin(\varphi_1^* - \varphi_2^* + \beta) \sin(\varphi_1^* - \varphi_2^*) &= I_0, \end{aligned} \tag{2}$$

with

$$\begin{aligned} \kappa_1^* &= \sin(\varphi_2^* - \varphi_1^* + \beta), \\ \kappa_2^* &= \sin(\varphi_1^* - \varphi_2^* + \beta). \end{aligned} \tag{3}$$

Equation (2) can be solved numerically for any fixed parameter set, or numerical path-following can be applied in order to study the dependence of the fixed points on the parameters.

The bifurcation diagram in Figure 1 shows how the number and stability of fixed points of the full system change with β . In particular, depending on β , there may be two, four or six fixed points. Due to symmetry, the solutions always appear in pairs of points sharing the same stability features. Since our study concerns plasticity rules which support excitable fixed points, we have confined the analysis to the interval $\beta \in (3.298, 4.495)$, where the system has *two stable* fixed points, which lie off the synchronization manifold $\varphi_1 = \varphi_2$. Apart from that, there are also four unstable

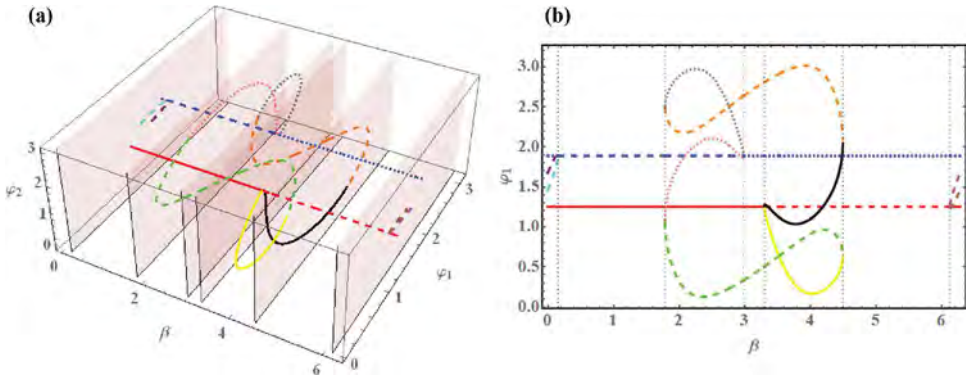


Fig. 1. (a) Bifurcation diagram for the fixed points of system (1) with $D = 0$ in the $(\beta, \varphi_1, \varphi_2)$ space. (b) Projection of the bifurcation diagram to (β, φ_1) plane. The two fixed points independent on β belong to the synchronization manifold: the red (blue) one is always longitudinally stable (unstable). The solid lines denote stable fixed points, whereas the dashed and dotted lines denote saddles of unstable dimension 1 and 2, respectively.

fixed points. The bifurcations associated to the boundaries of the given β interval are as follows: at $\beta = 3.298$ the system undergoes a supercritical symmetry-breaking pitchfork bifurcation where a symmetry related pair of two stable fixed points off the synchronization manifold is created, whereas at $\beta = 4.495$, this pair meets another pair of unstable fixed points off the synchronization manifold such that both are annihilated in symmetry related inverse saddle-node bifurcations. For instance, at $\beta = 4.1$, one finds the symmetry related pair of stable foci given by $(\varphi_1, \varphi_2, \kappa_1, \kappa_2) = (1.177, 0.175, 0.032, -0.92)$ and $(\varphi_1, \varphi_2, \kappa_1, \kappa_2) = (0.175, 1.177, -0.92, 0.032)$. Note that these weight levels support effective master-slave configurations, where one unit exerts a much stronger influence on the other unit than vice versa.

The two stable asymmetric fixed points in the interval $\beta \in (3.298, 4.495)$ are excitable, and may exhibit several different types of response to external perturbations, see the classification in Figure 2. Introducing the perturbations by setting different initial conditions, we plot in Figure 2 the phase dynamics in the fast subspace while keeping the weights (κ_1, κ_2) fixed. Note that in the case where both units respond with a single spike, the order of firing is such that the unit with larger initial phase $\varphi_i(0), i \in \{1, 2\}$ fires first.

3.2 Onset of oscillations

The onset of emergent oscillations in system (1) with $D = 0$ depends on the interplay between the plasticity rule, specified by β , and the speed of adaptation, characterized by ϵ . A parameter scan indicating the variation of κ_1 , $A_{\kappa_1} = \max(\kappa_1(t)) - \min(\kappa_1(t))$ in terms of (β, ϵ) is shown in Figure 3a. The results are obtained by numerical continuation beginning from a stable periodic solution, such that the final state reached for a certain set of (β, ϵ) values provides the initial conditions for the simulation of the system at incremented parameter values. By this method, we have determined the maximal stability region of the periodic solution.

One finds that for a fixed β , there actually exists an interval of timescales separation $\epsilon \in (\epsilon_{min}, \epsilon_{max})$ admitting oscillations, cf. Figure 3b. The periodic solutions in this interval coexist with the two symmetry-related stable stationary states. One observes that the threshold ϵ_{min} reduces with β , whereas the upper boundary value ϵ_{max} grows with increasing β . The detailed bifurcation mechanisms behind the onset

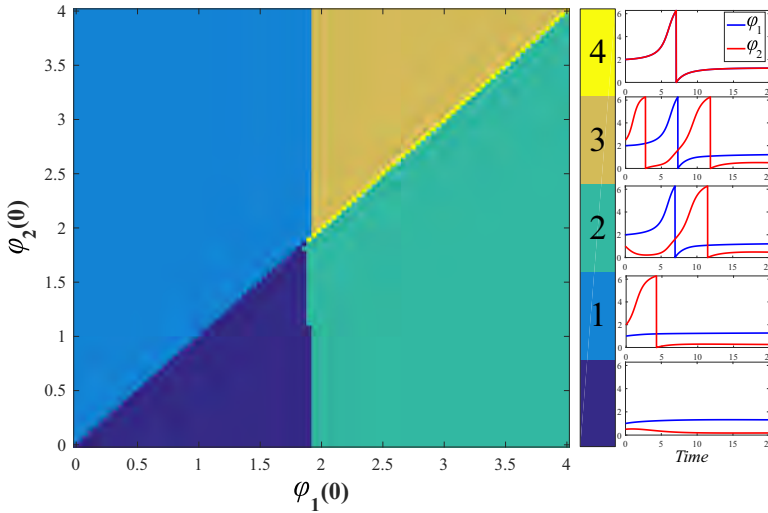


Fig. 2. Modalities of the response to external perturbation for system (1) with $D = 0$. The system parameters are $I_0 = 0.95$, $\epsilon = 0.01$ and $\beta = 4.212$, whereas the initial conditions for the coupling weights are set to $\kappa_1(0) = -0.0077$, $\kappa_2(0) = -0.846$. Depending on the initial phases $(\varphi_1(0), \varphi_2(0))$, one may observe the following regimes: (0) no spikes; (1) the unit with larger $\varphi(0)$ emits one spike and the other does not; (2) both units emit a single spike, with the unit with larger $\varphi(0)$ firing first; (3) the unit with larger $\varphi(0)$ emits two spikes and the other unit emits one; (4) both units spike synchronously.

of oscillations and multistability are beyond the scope of this paper, and essentially involve an interplay between the fast and slow variables.

Enhancing ϵ under fixed β gives rise to a supercritical symmetry-breaking pitchfork bifurcation of limit cycles, indicated by PFL in Figure 3b. Below the bifurcation, the phases $\varphi_1(t)$ and $\varphi_2(t)$ maintain a small phase-shift, while the oscillation profiles $\kappa_i(t), i \in \{1, 2\}$ are rather different, see Figures 3d and 3e, respectively. Above the bifurcation, the system gains the anti-phase space-time symmetry $\varphi_1(t) = \varphi_2(t + T/2), \kappa_1(t) = \kappa_2(t + T/2)$ where T denotes the oscillation period, cf. the associated waveforms in Figures 3g and 3f.

4 Slow-fast analysis of the deterministic dynamics

The deterministic dynamics in case of slow adaptation, corresponding to a strong timescale separation between the fast and slow variables, may be analyzed within the framework of standard fast-slow analysis. In general, one may either consider the layer problem, defined on the fast timescale, or the reduced problem, which concerns the slow timescale. Within the layer problem, the aim is to determine the fast flow dynamics $\varphi_1(t; \kappa_1, \kappa_2), \varphi_2(t; \kappa_1, \kappa_2)$ by treating the slow variables κ_1 and κ_2 as parameters, whereas the reduced problem consists in determining the dynamics of the slow flow $(\kappa_1(t), \kappa_2(t))$ (reduced flow) assuming that the fast flow of the layer problem is either at a stable equilibrium or at the averaged value of a stable regime.

In this section, we first investigate the fast layer problems. Depending on the values of the slow variables (κ_1, κ_2) , the fast flow can exhibit several attractors, such that multiple sheets of the slow flow emerge from the averaged dynamics on the different attractors of the fast flow.

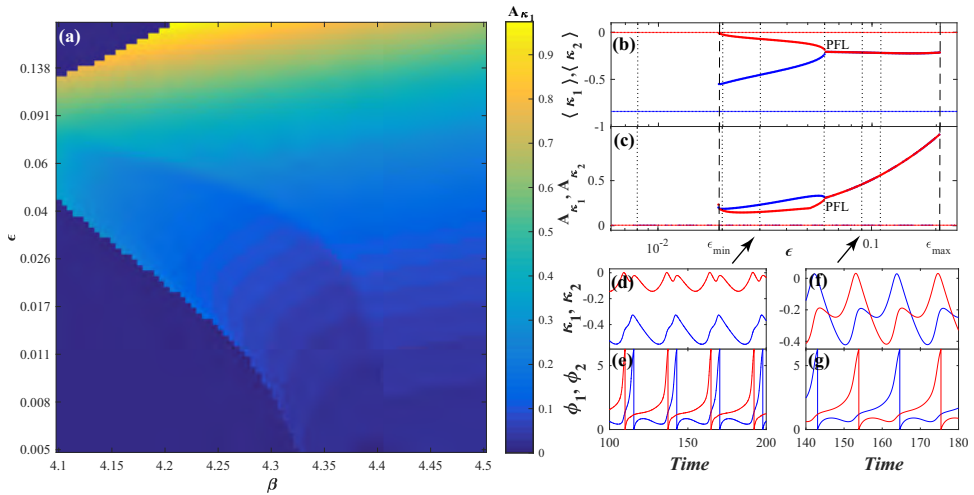


Fig. 3. Onset of oscillations in the full system (1) for $D = 0$. In panel (a) is shown how the variation A_{κ_1} of coupling weight κ_1 changes in the (β, ϵ) plane. Panel (b) shows how the mean coupling weights $\langle \kappa_1 \rangle$ and $\langle \kappa_2 \rangle$ of oscillatory states (thick lines) change with ϵ under fixed $\beta = 4.212$. The thin solid lines indicate the stationary state. In panel (c) are plotted the analogous dependencies for variation of the oscillation. The dotted lines in (b) and (c) indicate the ϵ values corresponding to the time traces in Figure 7, whereas the dashed lines indicate the boundaries of the ϵ region supporting the stable periodic solutions. The symmetry-breaking pitchfork bifurcation of limit cycles is denoted by PFL. In panels (d)–(g) are shown the waveforms of periodic solutions without and with the anti-phase space-time symmetry, obtained for $\epsilon = 0.03$ and $\epsilon = 0.09$, respectively (see the arrows). The excitability parameter is fixed to $I_0 = 0.95$.

4.1 Dynamics of the fast flow

Within the layer problem, one studies the dynamics of the fast variables

$$\begin{aligned} \dot{\varphi}_1 &= I_0 - \sin \varphi_1 + \kappa_1 \sin(\varphi_2 - \varphi_1) \\ \dot{\varphi}_2 &= I_0 - \sin \varphi_2 + \kappa_2 \sin(\varphi_1 - \varphi_2), \end{aligned} \tag{4}$$

where $\kappa_1, \kappa_2 \in [-1, 1]$ are considered as additional system parameters. Formally, system (4) is obtained by setting $\varepsilon = 0$ in (1) for $D = 0$.

The numerically obtained bifurcation diagram in Figure 4a shows that the fast flow is monostable for most of the (κ_1, κ_2) values, possessing either an equilibrium or a limit cycle attractor. The stability boundary of the periodic solution (red curves) has been obtained by the method of numerical continuation where, beginning from a stable periodic solution, the initial conditions for incremented parameter values are given by the final state reached for the previous set of (β, ϵ) values. The coexistence between a stable fixed point, lying on the synchronization manifold, and a limit cycle is found within a small region near the diagonal, see Figure 4a. Let us first classify the fixed points of the fast flow and then examine the scenarios that give rise to oscillations.

It can be shown that the fast flow admits either two or four fixed points, with the associated regions indicated in Figure 4b. In particular, two fixed points FP1 and FP2 on the synchronization manifold are *independent* on κ_1 and κ_2 . They are given by $(\varphi_1^*, \varphi_2^*) = (\arcsin I_0, \arcsin I_0)$ and $(\varphi_1^*, \varphi_2^*) = (\pi - \arcsin I_0, \pi - \arcsin I_0)$. One may also find two additional fixed points off the synchronization manifold, referred

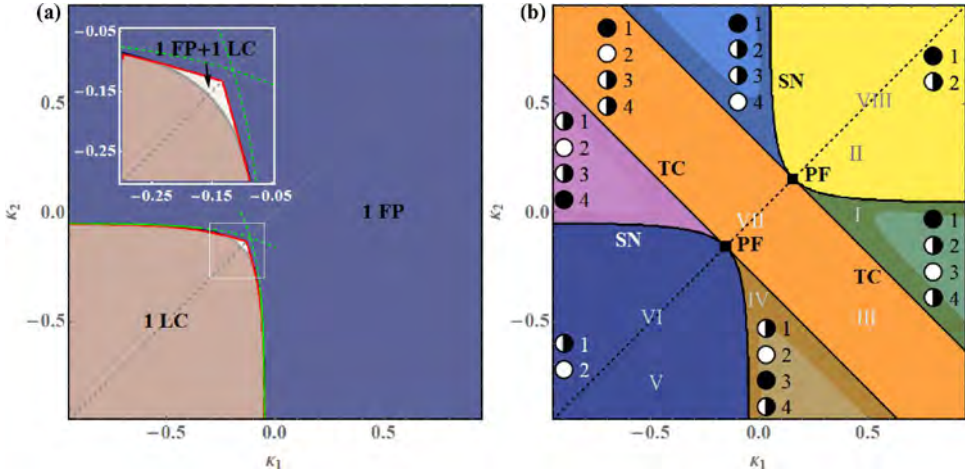


Fig. 4. (a) Attractors of the fast flow (4) in terms of κ_1 and κ_2 , now considered as parameters. The fast flow is typically monostable, supporting either a stable fixed point (FP) or a stable limit cycle (LC), apart from a small region around the main diagonal, where it exhibits bistable behavior. The green dashed curves indicate approximations of two branches of SNIPER bifurcations, obtained by the method described in the text. The red lines correspond to the numerically determined stability boundaries of the oscillatory solution. (b) Classification of the fixed points of the fast flow (4). The fixed points are labeled the same way as in the main text, with their stability indicated as follows: full circles denote stable fixed points, semi-full circles represent saddle points and white circles correspond to doubly unstable fixed points. Within the four light-shaded triangular-shaped regions, the doubly unstable fixed point is a focus, rather than a node. The notation I–VIII refers to parameter values corresponding to the phase portraits in Figure 5.

to as FP3 and FP4 in Figure 4b. The bifurcations affecting the number and stability of the fixed points, beginning from the lower left region of the (κ_1, κ_2) plane, can be summarized as follows. Along the main diagonal $\kappa_1 = \kappa_2$, we find two points of supercritical pitchfork bifurcations (PF), where from the symmetric fixed points the saddles FP3 and FP4 appear and disappear. Off the main diagonal, the pitchforks are unfolded into curves of saddle-node (SN) and transcritical bifurcations (TC), see Figure 4b.

The (κ_1, κ_2) region featuring stable oscillations almost completely matches the lower left domain admitting two unstable fixed points. Within this region, each periodic solution obtained for (κ_1, κ_2) above the main diagonal $\kappa_1 = \kappa_2$ has a counterpart in the domain below the main diagonal, related to it by the exchange symmetry of units indices. Typically, the periodic solutions emerge via SNIPER bifurcations, comprising two branches where either κ_1 or κ_2 remain almost constant and close to zero. In both cases, the two fixed points that collide and disappear are FP3 and FP4. Nevertheless, such scenarios cannot be maintained in the small (κ_1, κ_2) region admitting coexistence between a fixed point and a limit cycle, because the SNIPER bifurcation is accompanied by a change in the number of fixed points. Our findings suggest that near the main diagonal, the limit cycle emerges via a heteroclinic bifurcation, where an orbit connects two saddles lying off the synchronization manifold (not shown). Note that the orbit of the limit cycle follows the unstable manifold of the saddle point FP2 on the synchronization manifold. To the left or the right of the main diagonal, instead of a heteroclinic bifurcation, one finds homoclinic bifurcations, whereby a saddle point, either FP3 or FP4, touches the limit cycle orbit. The schematic phase portraits indicating the stable and unstable manifolds of the fixed points and the limit

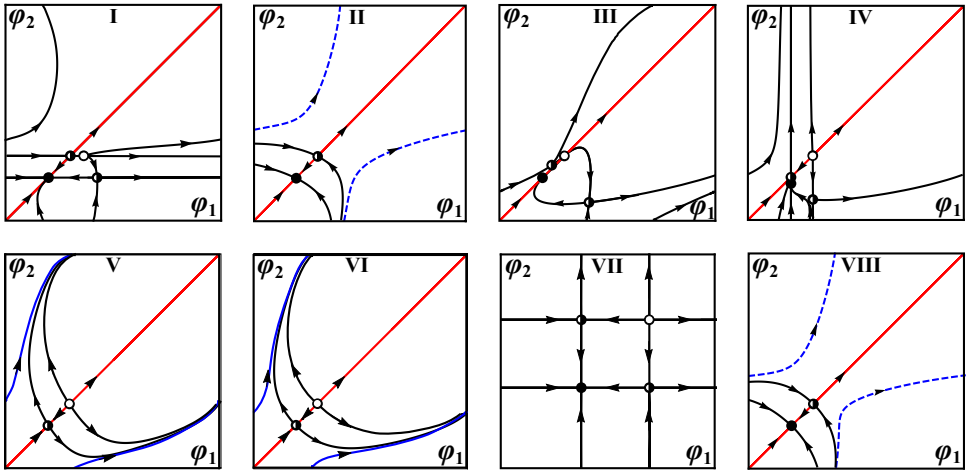


Fig. 5. Schematic phase portraits corresponding to the characteristic regimes of the fast flow. The panels I–VIII refer to representative parameter values indicated in Figure 4b. Also, the stability of fixed points is presented the same way as in Figure 4b. The invariant synchronization manifold is denoted by the red color, whereas the orbit of a stable/unstable limit cycle is indicated by the solid/dashed blue lines.

cycle for the characteristic regimes of the fast flow, denoted by I–VIII in Figure 4b, are illustrated in Figure 5.

The two branches of SNIPER bifurcations may readily be approximated for small values of κ_1 and κ_2 by a simple scheme, which amounts to reducing the fast flow to a normal form of saddle-node bifurcation. Suppose first that $\kappa_1 \ll 1$ and $I_0 - 1 \ll 1$. More specifically, let $\xi \ll 1$ be a small parameter such that $I_0 - 1 = \xi$ (close to the threshold) and $\kappa_1 = \gamma\xi$, i.e. γ is a rescaling parameter of κ_1 , allowing for a zoom in the neighborhood of zero. Then, the steady states are given by the system

$$\begin{aligned} 1 + \xi - \sin \varphi_1 + \xi\gamma \sin(\varphi_2 - \varphi_1) &= 0, \\ 1 + \xi - \sin \varphi_2 + \kappa_2 \sin(\varphi_1 - \varphi_2) &= 0. \end{aligned} \tag{5}$$

The first equation in the zeroth order approximation leads to $\varphi_1 = \pi/2$. Hence, using the perturbation approach, we have

$$\varphi_1^* = \frac{\pi}{2} + \sqrt{\xi}\Psi_1 + \dots; \quad \varphi_2^* = \Psi_2 + \dots, \tag{6}$$

where the $\sqrt{\xi}$ scaling follows from the Taylor expansion of the function $\sin \varphi_1$ at $\pi/2$. Inserting (6) into (5), one obtains the system of equations for Ψ_1 and Ψ_2

$$\begin{aligned} 1 + \frac{1}{2}\Psi_1^2 - \gamma \cos \Psi_2 &= 0, \\ 1 - \sin \Psi_2 + \kappa_2 \cos \Psi_2 &= 0. \end{aligned} \tag{7}$$

From system (7), it is not difficult to see that the saddle-node bifurcation takes place if the condition $1 - \gamma \cos \Psi_2 = 0$ is satisfied. This leads to the parametric representation $\kappa_1 = \xi\gamma = \frac{I_0 - 1}{\cos \Psi_2}$, $\kappa_2 = \frac{\sin \Psi_2 - 1}{\cos \Psi_2}$, of the saddle-node curve for small κ_1 values, where Ψ_2 plays the role of the parameter along the curve. An analogous approach may be used to capture the second branch of saddle-node bifurcations, cf. the green dashed lines in Figure 4a.

4.2 Dynamics of the slow flow

We have numerically obtained the dynamics of the slow flow by applying a two-step approach. First, for fixed values (κ_1, κ_2) , we determine the time-averaged dynamics of the fast flow (4), $\langle \varphi_2 - \varphi_1 \rangle_t = f(\kappa_1, \kappa_2)$. Here, the averaging $\langle \cdot \rangle_t$ is performed over a sufficiently large time interval, having eliminated a transient. Hence, this average depends on the attractor of the fast flow for the given (κ_1, κ_2) . In particular, if the fast flow possesses a stable fixed point, then $\langle \varphi_2 - \varphi_1 \rangle_t = \varphi_2^* - \varphi_1^*$, where $(\varphi_1^*, \varphi_2^*)$ is a solution of

$$\begin{aligned} I_0 - \sin \varphi_1^* + \kappa_1 \sin (\varphi_2^* - \varphi_1^*) &= 0 \\ I_0 - \sin \varphi_2^* + \kappa_2 \sin (\varphi_1^* - \varphi_2^*) &= 0. \end{aligned} \tag{8}$$

This procedure just results in determining the slow critical manifold of the system. In case when the attractor of the fast flow is periodic, $\langle \varphi_2 - \varphi_1 \rangle_t$ presents the time average over the period. Averaging approximation in case of a periodic attractor of the fast flow constitutes a standard approach [13,25], rather natural for describing the influence of oscillations in the fast flow on the dynamics of the slow flow. At the second stage, the obtained time-averages are substituted into the dynamics of the weights

$$\begin{aligned} \dot{\kappa}_1 &= \epsilon[-\kappa_1 + \sin(f(\kappa_1, \kappa_2) + \beta)] \\ \dot{\kappa}_2 &= \epsilon[-\kappa_2 + \sin(-f(\kappa_1, \kappa_2) + \beta)]. \end{aligned} \tag{9}$$

The system (9) is used to determine the vector field of the slow flow by taking into account only the attractors of the fast flow, such that the vector field associated to each attractor is plotted within its respective stability region, cf. Figure 6.

In regions of the (κ_1, κ_2) plane where there are coexisting stable solutions of the fast flow, the corresponding vector field of the slow flow is given on multiple overlapping sheets, since the value of the average $f(\kappa_1, \kappa_2)$ depends on the initial conditions. In our case, this occurs only in a small region of coexistence between an equilibrium and a stable limit cycle.

One should single out two important features of the slow flow: (i) it exhibits two symmetry-related fixed points in the green and blue regions in Figure 6, and (ii) the slow vector field is pointed in opposite directions close to the boundary between the fast oscillatory regime (orange region) and the steady states of the fast flow (blue, green and white regions). The latter in particular implies that interesting effects occur close to the border of the oscillatory and the steady state regime of the fast flow. Moreover, adding noise gives rise to fluctuations around this boundary, which leads to switching between the quasi-stationary and the fast spiking dynamics. Such effects are studied in more detail within the next section.

5 Switching dynamics

Our main observation in this section is that the interplay of plasticity and noise induces slow stochastic fluctuations (switching dynamics), mediating two qualitatively different scenarios depending on the speed of adaptation. The latter include (i) switching between two modes of *noise-induced* oscillations for slower adaptation (small $\epsilon \simeq 0.01$) and (ii) switching between multiple coexisting attractors of the deterministic dynamics for faster adaptation (intermediate $\epsilon \simeq 0.05$).

In case (i), the impact of noise is twofold: on a short timescale, it gives rise to spiking dynamics, whereas on a long time scale, it induces random transitions between

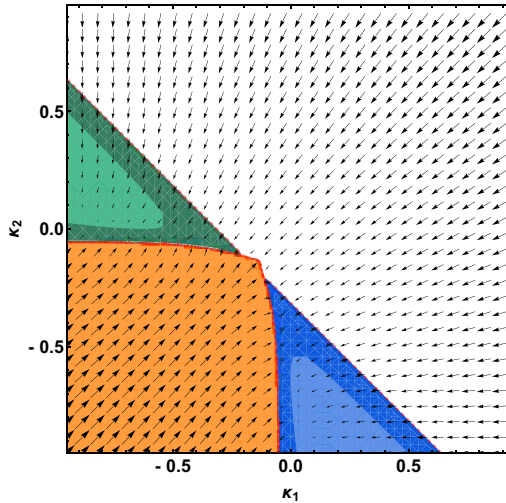


Fig. 6. Vector field of the slow flow obtained by taking into account only stable attractors of the fast flow for $\beta = 4.212$, $I_0 = 0.95$. The color coding is as follows: orange color denotes the region associated to the stable limit cycle of the fast flow, white stands for the stable fixed point of the fast flow FP1, whereas blue and green color correspond to the two stable fixed points FP3 and FP4. Within the light-shaded regions, FP3 and FP4 are foci rather than nodes, cf. Figure 4b.

the two oscillatory modes. In case (ii), the switching dynamics comprises metastable states derived from two fixed points, as well as two limit cycles associated to emergent oscillations of the corresponding deterministic system. The key difference between the effects (i) and (ii) is that for slower adaptation, the system switches between the oscillatory modes that do not exist as deterministic attractors. Moreover, the two generic types of switching are characterized by distinct phase dynamics: for slower adaptation, one finds alternation of patterns with different order of spiking between the units, whereas for faster adaptation, the phases effectively exhibit bursting behavior, involving a succession between episodes of spiking and relative quiescence. An overview on how the typical dynamics of couplings changes with ϵ at fixed β is provided in Figure 7. Note that the difference between the average coupling weights of the stable periodic solutions of the deterministic system are much smaller than a typical distance between the coupling levels for the stationary states. The prevalence of metastable states is affected by ϵ so that intermediate adaptation favors oscillatory modes, whereas the fast adaptation apparently promotes the two quasi-stationary states. In the next two subsections, we provide further insight into the mechanisms behind the switching dynamics using the results of the fast-slow analysis.

5.1 Switching dynamics under slow adaptation

As already indicated, ϵ is here taken sufficiently small, such that it cannot facilitate emergent oscillations in the full system (1). For $\epsilon \simeq 0.01$ and under appropriate noise levels, one observes noise-induced oscillations [26]. The latter arise via a scenario involving a multiple-timescale stochastic bifurcation, whereby noise acts only within the fast subsystem of (1). The onset of oscillations under increasing D occurs in two stages. In the first stage, the phase dynamics gradually exhibits more induced spikes,

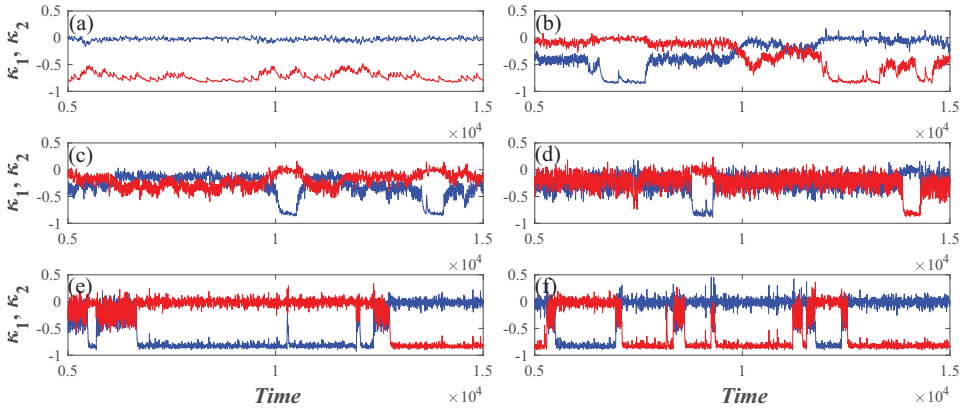


Fig. 7. Switching dynamics under variation of ϵ . The time traces $(\kappa_1(t), \kappa_2(t))$ are obtained for fixed $I_0 = 0.95$, $D = 0.006$, $\beta = 4.212$, whereas ϵ assumes the following values: (a) $\epsilon = 0.008$, (b) $\epsilon = 0.02$, (c) $\epsilon = 0.03$, (d) $\epsilon = 0.06$, (e) $\epsilon = 0.09$, (f) $\epsilon = 0.11$.

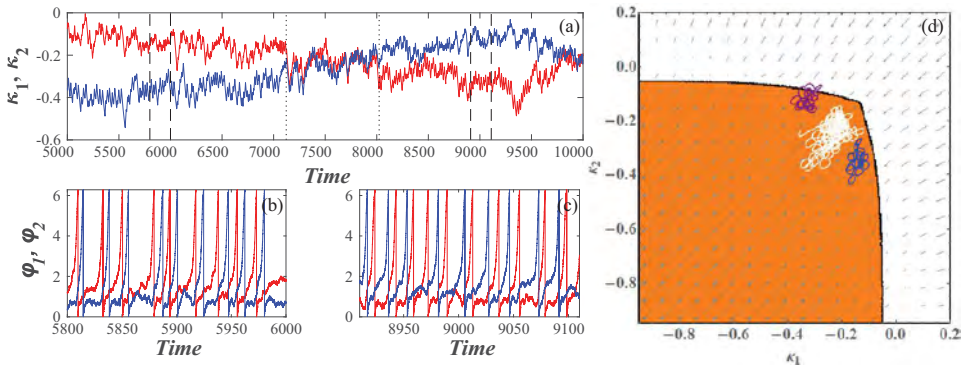


Fig. 8. Switching dynamics between the two modes of noise-induced oscillations. Time traces of the weights are shown in panel (a), whereas panel (b) and (c) display the corresponding time traces of the phases during the intervals between the dashed lines in panel (a). In panel (d), the $(\kappa_1(t), \kappa_2(t))$ projections of the orbits associated to each of the two modes (blue color), as well as the switching episode, shown in white, are superimposed to the vector field of the slow flow from Figure 6. The shaded area corresponds to the stable limit cycle. The system parameters are $I_0 = 0.95$, $\beta = 4.212$, $\epsilon = 0.01$, $D = 0.009$.

such that the stationary distributions of phases eventually acquire a longer tail reflecting the occurrence of spikes (not shown). Nevertheless, the stationary distributions $P(\kappa_i)$ change appreciably only at the second stage, which takes place for sufficiently large D . Such a change accompanies the emergence of coupling oscillations. Note that the system (1) actually exhibits *two modes* of noise-induced oscillations, characterized by the different order of firing between the two units, cf. the time traces of phase dynamics and the associated evolution of couplings in Figure 8a.

It is interesting to examine whether the vector field of the slow flow from Section 4.2 can be used to explain the slow stochastic fluctuations of the coupling weights. To this end, we have superimposed the $(\kappa_1(t), \kappa_2(t))$ orbits of the two noise-induced modes, as well as a switching episode, to a vector field of the slow flow from Figure 6. Note that the orbits typically lie close to the boundary outlining the transition between the two attractors of the fast flow, featuring non-negligible coupling weights. Moreover, the two modes are confined to small areas of the (κ_1, κ_2) plane

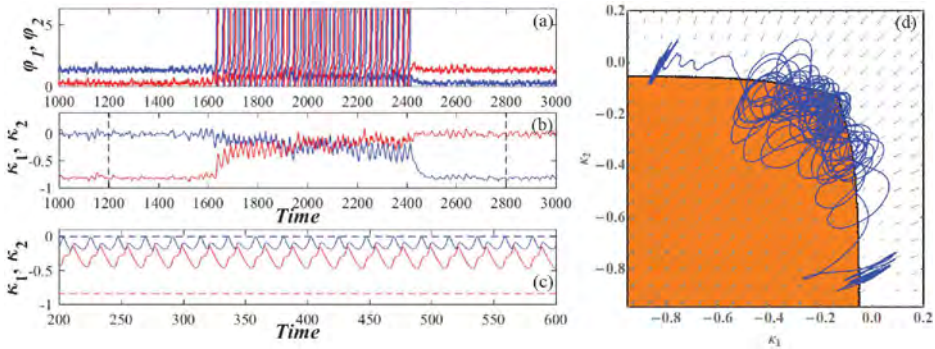


Fig. 9. Time traces of the phases (a) and weights (b) associated to noise-induced switching between the coexisting attractors of the deterministic system. The results are obtained for $I_0 = 0.95$, $\beta = 4.212$, $\epsilon = 0.05$, $D = 0.004$. In panel (c) is provided the deterministic dynamics of weights obtained for the same parameter values. In panel (d), the $(\kappa_1(t), \kappa_2(t))$ orbit corresponding to the interval between the dashed lines in (b) is super-imposed on the vector field of the slow flow cf. Figure 6.

symmetrical with respect to the main diagonal $\kappa_1 = \kappa_2$, whereas the switching episode virtually takes place on the diagonal. Apparently, the noise-induced modes occupy regions where the oscillations in the fast flow emerge via homoclinic bifurcations, rather than the SNIPER scenario. Nonetheless, the switching episode seems to involve the domain featuring coexistence of the two stable sheets of the slow vector field. Within these sheets, which correspond to two attractors of the fast flow (a stable node and a stable limit cycle), the vector fields are oriented in opposite directions, thereby contributing to switching.

5.2 Switching dynamics for faster adaptation

In case of faster adaptation associated to intermediate ϵ , the switching dynamics involves four metastable states, derived from the attractors of the deterministic system. The deterministic multistable behavior includes two symmetry-related stationary states, as well as two symmetry-related limit cycles. Note that while the two stable steady states exist for arbitrary small ϵ and are therefore visible in the slow flow in Figure 6, the oscillatory solutions disappear for small ϵ and hence cannot be observed in the slow flow. The two oscillatory regimes are characterized by the same phase shift, but the reverse order of firing between the two units. Influenced by noise, the phases effectively engage in bursting behavior, manifesting slow stochastic fluctuations between episodes of intensive spiking activity and periods of relative quiescence, see Figure 9a. For a fixed noise level, the prevalence of metastable states, defined by transition probabilities between them, changes with adaptation speed. One observes that for $\epsilon \simeq 0.05$, the oscillatory dynamics is preferred, whereas for $\epsilon \simeq 0.1$, the quasi-stationary states are more ubiquitous.

A comparison of the (κ_1, κ_2) orbits displaying switching dynamics and the vector field of the slow flow from Figure 6 again shows that the former is confined to the criticality region at the boundary between the stationary and oscillatory regimes in the fast flow, cf. Figure 9. One should remark on how the transitions between the different metastable states take place. In particular, from Figure 9b, it is clear that there can be no direct transitions between the two quasi-stationary states, but they rather have to be mediated by the system passing through the oscillatory states. Also, the transition from oscillatory to quasi-stationary states typically occurs

once the couplings approach a master-slave-like configuration, where the coupling in one direction is much stronger than the other one. This scenario coincides with the SNIPER bifurcation of the fast flow described in Section 4.1. The scenario of transition between the two metastable oscillatory states resembles closely the one from Section 5.2.

6 Summary

In the present study, we have analyzed a system of two adaptively coupled active rotators with excitable intrinsic dynamics, demonstrating that the interplay of plasticity and noise may give rise to slow stochastic fluctuations. Two qualitatively different types of self-organized behavior have been identified, depending on the adaptation speed. For slower adaptation, the switching dynamics consists of an alternation between two modes of noise-induced oscillations, associated to a preferred order of spiking between the two units. In this case, noise plays a twofold role: on one hand, it perturbs the excitable local dynamics giving rise to oscillations on a short timescale, whereas on the other hand, it elicits the alternation between the two oscillatory states on a long timescale. The underlying phase dynamics shows slow switching between two patterns distinguished by the different order in which the units are spiking. In case of faster adaptation, the coupling becomes capable of eliciting emergent oscillations in the deterministic system [27]. The latter then exhibits complex multistable behavior, involving two stationary and two oscillatory regimes. Under the influence of noise, the system undergoes switching between these four different metastable states, whose prevalence at fixed noise level depends on the speed of adaptation. The deterministic attractors associated to metastable states are related by the Z_2 symmetry. Thus, a mismatch in excitability parameters would lead to symmetry-breaking, whereby a small mismatch would induce a bias in switching dynamics, whereas a larger mismatch, corresponding to a scenario with one excitable and one oscillatory unit, would completely alter the observed dynamics.

Though the underlying phenomena are not found in the singular limit of infinite scale separation, the fast-slow analysis we have applied still allows one to explain the qualitative features of both considered types of switching behavior. Studying the layer problem, and in particular the vector field of the slow flow, has enabled us to gain insight into the metastable states and the transitions between them. It has been demonstrated that the coupling dynamics is always in a state of “criticality”, being confined to the boundary between the stationary and oscillatory regimes of the fast flow.

Given that excitability, plasticity and noise are inherent ingredients of neuronal systems, the obtained results can be interpreted in the context of neuroscience. It is well known that the backbone of neural networks is made up of binary and ternary neuron motifs, whereby the structural motifs typically support multiple functional motifs, essentially characterized by the weight configuration and the underlying direction of the information flow. With this in mind, the scenario of switching under slow adaptation may be important, because it implies that a binary motif can display slow alternation between two effectively unidirectional weight configurations, promoting opposite direction of information flow. For faster adaptation, one finds multistability between unidirectional coupling and bidirectional coupling of moderate strength. Nonetheless, the underlying phase dynamics, if extended to networks, may be considered as a paradigm for UP-DOWN states, typical for cortical dynamics [28,29]. Thus, it would be of interest to examine the impact of plasticity in networks of noisy excitable units, where one may expect different types of emergent behavior, such as cluster, non-synchronized and partially synchronized states, depending on the frustration of local dynamics and the impact of noise.

We thank S. Eydam for useful discussions. This work was supported by the Ministry of Education, Science and Technological Development of Republic of Serbia under project No. 171017, the DAAD Serbia-Germany Bilateral Project “Emergent Dynamics in Systems of Coupled Excitable Units”, as well as the DFG within the framework of Collaborative Research Center SFB 910.

Author contribution statement

I.F. and S.Y. conceived the model and defined the analysis of noise-induced switching as the main goal of the research. S.Y. and M.W. developed the general framework to investigating the deterministic fast-slow problem and the bifurcation analysis of the associated reduced systems. I.B. obtained all the numerical results, whereas I.B. and I.F. carried out the bifurcation analysis, identified the two types of noise-induced switching behavior and made the main contribution to writing the manuscript. All the authors discussed the findings and participated in interpretation of the results.

References

1. F. Sorrentino, E. Ott, Phys. Rev. Lett. **100**, 114101 (2008)
2. F. Vazquez, V.M. Eguiluz, M.S. Miguel, Phys. Rev. Lett. **100**, 108702 (2008)
3. N. Caporale, Y. Dan, Ann. Rev. Neurosci. **31**, 25 (2008)
4. C. Furusawa, K. Kaneko, Phys. Rev. Lett. **90**, 088102 (2003)
5. D.O. Hebb, *The Organization of Behavior: a Neuropsychological Approach* (John Wiley & Sons, New York, 1949)
6. S. Song, K.D. Miller, L.F. Abbott, Nat. Neurosci. **3**, 919 (2000)
7. R.C. Froemke, Y. Dan, Nature (London) **416**, 433 (2002)
8. H.-X. Wang, R.C. Gerkin, D.W. Nauen, G.-Q. Bi, Nat. Neurosci. **8**, 187 (2005)
9. O. Sporns, R. Kotter, PLoS Biol. **2**, e369 (2004)
10. I. Franović, V. Miljković, Chaos Soliton. Fract. **44**, 122 (2011)
11. I. Franović, V. Miljković, Chaos Soliton. Fract. **45**, 527 (2012)
12. I. Franović, V. Miljković, EPL **92**, 68007 (2011)
13. L. Lüchen, O.V. Popovych, P.A. Tass, S. Yanchuk, Phys. Rev. E **93**, 032210 (2016)
14. Y.L. Maistrenko, B. Lysyansky, C. Hauptmann, O. Burylko, P.A. Tass, Phys. Rev. E **75**, 066207 (2007)
15. P. Seliger, S.C. Young, L.S. Tsimring, Phys. Rev. E **65**, 041906 (2002)
16. M. Li, S. Guan, C.-H. Lai, New J. Phys. **12**, 103032 (2010)
17. P.S. Skardal, D. Taylor, J.G. Restrepo, Physica D **267**, 27 (2014)
18. D. Kasatkin, S. Yanchuk, E. Schöll, V. Nekorkin, Phys. Rev. E **96**, 062211 (2017)
19. O.V. Popovych, S. Yanchuk, P.A. Tass, Sci. Rep. **3**, 2926 (2013)
20. K. Mikkelsen, A. Imparato, A. Torcini, Phys. Rev. Lett. **110**, 208101 (2013)
21. D. Millman, S. Mihalas, A. Kirkwood, E. Niebur, Nat. Phys. **6**, 801 (2010)
22. A. Levina, J.M. Herrmann, T. Geisel, Phys. Rev. Lett. **102**, 118110 (2009)
23. T. Aoki, T. Aoyagi, Phys. Rev. Lett. **102**, 034101 (2009)
24. T. Aoki, T. Aoyagi, Phys. Rev. E **84**, 066109 (2011)
25. A. Shilnikov, Int. J. Bifurc. Chaos **18**, 2141 (2008)
26. S.-J. Wang, G. Ouyang, J. Guang, M. Zhang, Phys. Rev. Lett. **116**, 018101 (2016)
27. Q. Ren, K.M. Kolwankar, A. Samal, J. Jost, Phys. Rev. E **86**, 056103 (2012)
28. T.T.G. Hahn, J.M. McFarland, S. Berberich, B. Sakmann, M.R. Mehta, Nat. Neurosci. **15**, 1531 (2012)
29. V.V. Vyazovskiy, K.D. Harris, Nat. Rev. Neurosci. **14**, 443 (2013)